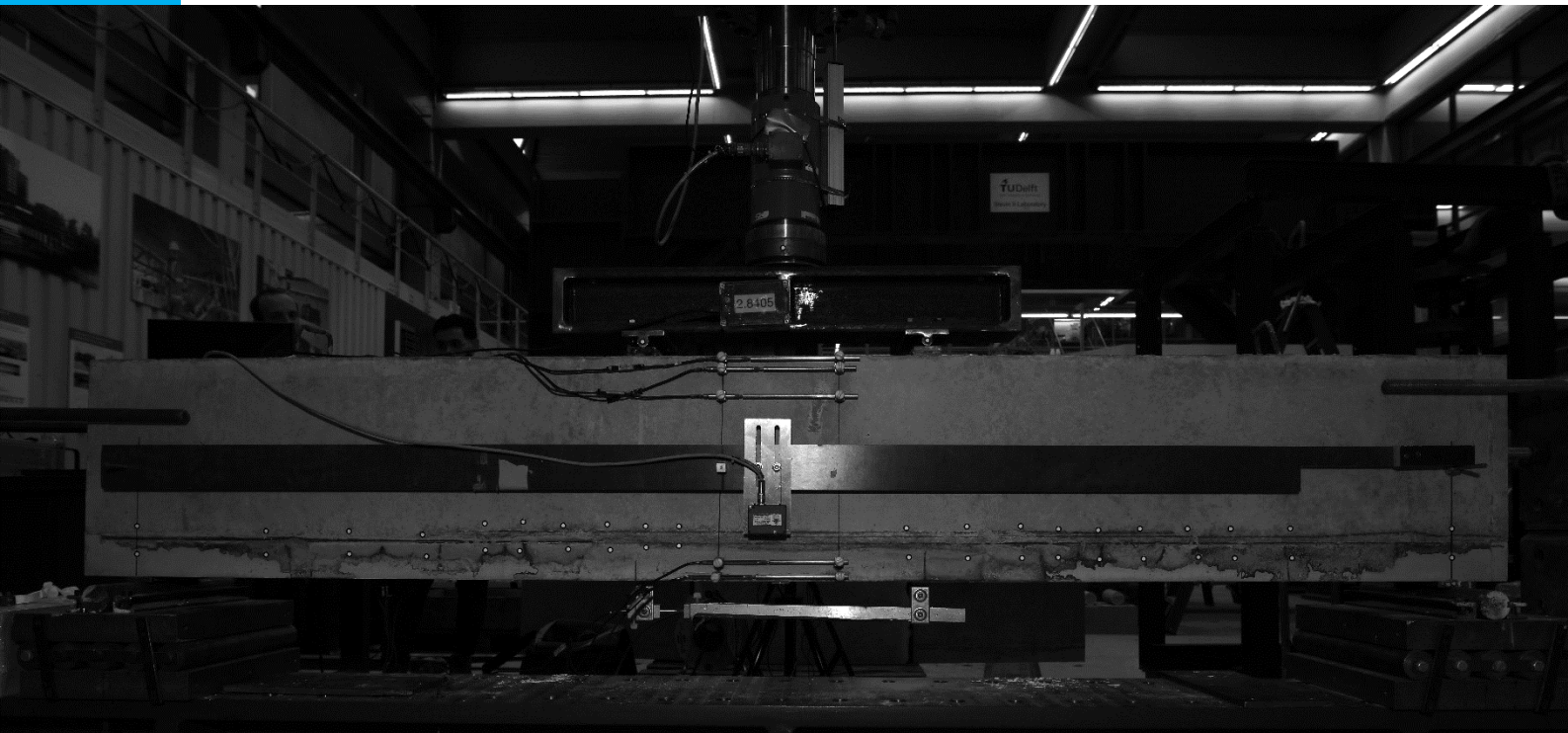


# Flexural Crack-width Controlling Behavior of Hybrid R/SHCC Beams

Enhancement of crack-width control of 400mm hybrid beam  
with a SHCC layer of 70mm

**B. Bougarchouh**





# Flexural Crack-width control of hybrid R/SHCC beams

Enhancement of crack-width control of 400mm hybrid beam with a  
SHCC layer of 70mm

By

B.Bougarchouh

in partial fulfilment of the requirements for the degree of

**Master of Science**

in Structural Engineering

at the Delft University of Technology,

to be defended publicly on 12-11-2024

Supervisor:	Mrs. dr. ir. M. Lukovic,	TU Delft
Thesis committee:	Dr. M.A. (Mariana) Popescu,	TU Delft
	Ir. H.J. (Jelle) Bezemer,	TU Delft
	Ir. S. (Shozab) Mustafa,	TU Delft

An electronic version of this thesis is available at <http://repository.tudelft.nl/>

---

# Preface

---

I am pleased to present my master's thesis, submitted in partial fulfilment of the requirements for the degree of Master of Science in Structural Engineering at Delft University of Technology. After first praising and thanking God, the most High, I would like to take this moment to show my gratitude to some very important people who directly or indirectly contributed to this work.

Firstly, my sincere thanks go to the chair of this thesis, Dr. Mladena Lukovic. I am deeply grateful for your support in introducing me to this topic, your confidence in my work, and your guidance and availability throughout the project. I could not have asked for a better mentor. I am also very thankful to my daily supervisor, Jelle Bezemer. Your support has been invaluable; from assisting with experimental work to offering constructive and insightful feedback on the report. Your high aspirations, dedication and hard work are truly admirable and inspiring.

I also wish to extend my thanks to Dr. Mariana Popescu. Although your involvement in the project was ultimately less extensive than initially planned, your feedback and support were nonetheless invaluable. I also want to thank Shozab for his guidance during the first three months of the project, as well as the lab staff—Albert, Ake, Ton, and Maiko—for their assistance.

Finally, I owe a deep debt of gratitude to my family for their unwavering support.

I am proud of the final result and can only hope that this thesis contributes to your understanding of the topic. All that remains for me to say; enjoy reading!

*B.Bougarchouh  
Rotterdam, October 2024*

---

# Abstract

---

Crack-width control of concrete structures, a serviceability limit state (SLS) criteria, could be governing in design calculations over ultimate limit state (ULS). To ensure adequate crack-width control, additional steel reinforcement is often used, which, while essential for SLS, is redundant for ULS purposes, thereby increasing the environmental impact due to excessive steel use. In efforts to reduce the amount of steel reinforcement required in RC beams, a series of MSc thesis studies at TU Delft have explored the potential of incorporating a layer of Strain-Hardening Cementitious Composites (SHCC) in the tension zone of beams, creating what are known as hybrid Reinforced concrete/SHCC (R/SHCC) beams. SHCC is a composite material that, through its specific composition and fiber incorporation, exhibits the ability to form multiple fine cracks when subjected to tensile stresses, offering an effective solution for enhancing crack-width control. Huang [1] demonstrated the effectiveness of a 70mm thick SHCC layer in a 200mm high hybrid R/SHCC beam. Singh [2] investigated the role of interface preparation on the crack-width control performance and found that both smooth and grooved SHCC-concrete interfaces provide similar flexural crack-width control in a 200mm high hybrid R/SHCC beam with a 70mm thick SHCC layer. Bezemer [3] explored the effectiveness of a 70mm thick SHCC layer in hybrid R/SHCC beams of more practical heights of 300mm and 400mm, revealing an anticipated decline in the layer's flexural crack-width control efficiency as beam height increased.

The current study investigates the effect of three key parameters on crack width control: (1) the SHCC-concrete interface, ranging from a smooth interface to a profiled interface coated with Vaseline; (2) the rebar-SHCC bond, weakened by changing from ribbed to smooth rebars; and (3) the SHCC type, varying from PVA-based SHCC to PE-based SHCC. Additionally, the effect of curing time is examined. The beams, with a total height of 400mm and a 70mm thick SHCC layer, are tested experimentally in a four-point bending set-up to generate a constant bending moment region (CBMR), allowing for the study of flexural cracks. Digital Image Correlation (DIC) is performed to evaluate the crack patterns and the crack-widths. The performance of the beams is assessed by checking its capability to restrict crack-widths below the 0.2mm and 0.3mm crack-width limits.

The experimental results demonstrate that the use of a Vaseline-coated profiled SHCC-conventional concrete (SHCC-CC) interface enhances the crack-width controlling ability of hybrid R/SHCC beams compared to a smooth interface. The beam with this profiled interface demonstrates a significant increase in the load, expressed as a percentage of the yield load, at which the 0.2mm and 0.3mm crack-width limits are exceeded of 37.6% and 22.7%, respectively, compared to the beam with a smooth interface. This improvement is attributed to the interface's ability to show controlled delamination (as a result of the mechanical interlock provided by the shear keys) over the full length of the region of interest (as a result of the chemical debond facilitated by the Vaseline coating).

The use of smooth rebars significantly compromises the crack-width controlling ability of hybrid R/SHCC beams, as the beam with smooth rebars experiences a decrease in the load, expressed as a percentage of the yield load, at which the 0.2mm and 0.3mm crack-width limits are exceeded of 51.0% and 35.7%, respectively, compared to the beam with ribbed rebars. This reduction in performance can be attributed to the weakening of the reinforcement-SHCC bond, which relies solely on chemical adhesion and friction with smooth rebars. This limitation hinders the activation of SHCC and leads to rapid localization of cracks within the SHCC. Despite the application of a Vaseline-coated profiled SHCC-concrete interface in both beams, the benefits of the Vaseline-coated profiled

interface observed in the beam with ribbed rebars were not realized in the beam with smooth rebars, indicating that a sufficient bond strength is a prerequisite for effective crack-width control.

PE-SHCC improves crack-width control in hybrid R/SHCC beams compared to PVA-SHCC when used in combination with smooth rebars. The beam with PE-SHCC exhibits an increase in the load, expressed as a percentage of the yield load, at which the 0.2mm and 0.3mm crack-width limits are exceeded of 6.0% and 14.9%, respectively, compared to the beam with PVA-SHCC. This improvement can likely be attributed to the larger ductility of PE-SHCC and the superior reinforcement-SHCC bond strength in PE-SHCC, which facilitates greater activation of the SHCC. However, it remains uncertain whether these findings can be extended to the use of ribbed rebars, as the superior reinforcement-SHCC bond strength in PE-SHCC may lead to an excessively high bond strength which could hinder strain redistribution.

The experimental results also demonstrate that curing time significantly influences the crack-width controlling ability of hybrid R/SHCC beams, with the beam tested at a later age (85 days of SHCC age) showing superior crack-width control compared to the beam tested by Bezemer [3] at 55 days of SHCC age. Specifically, there is an increase in the load, expressed as a percentage of the yield load, at which the 0.2mm and 0.3mm crack-width limits are exceeded in the beam tested at 85 days of SHCC age of 10.6% and 5.5%, respectively, compared to the beam tested at 55 days of SHCC age. This improvement is attributed to two factors: (1) the tensile properties of SHCC degrade over time, delaying crack localization, and (2) the SHCC-CC interface bond strengthens over time, resulting in less pronounced delamination. Consequently, while less SHCC is activated, the ability of SHCC to serve as effective reinforcement is enhanced.

In conclusion, the current study demonstrates that crack-width control in hybrid R/SHCC beams can be significantly improved by employing a roughened interface and utilizing ribbed rebars instead of smooth rebars when working with PVA-SHCC. Additionally, when using smooth rebars, opting for PE-SHCC enhances crack-width control. The current study also shows that hybrid R/SHCC beams of more practical height can effectively control crack-widths beyond reinforcement yielding when implementing the proposed design adjustments.

---

# Samenvatting

---

Het beperken van scheurwijdtes in betonnen constructies, een criterium voor de bruikbaarheidsgrenstoestand (SLS), kan in sommige gevallen bepalend zijn in ontwerpberekeningen ten opzichte van de uiterste grenstoestand (ULS). Om beperkte scheurwijdtes te waarborgen, wordt vaak extra staalwapening toegepast. Deze extra wapening is echter alleen noodzakelijk voor SLS-doeleinden en overbodig voor ULS, wat bijdraagt aan een hogere milieu-impact door overmatig staalgebruik. Om de hoeveelheid benodigde staalwapening in gewapende betonnen balken (RC-balken) te verminderen, hebben diverse MSc-onderzoeken aan de TU Delft het potentieel onderzocht van het integreren van een laag Strain-Hardening Cementitious Composites (SHCC) in de trekzone van balken, waardoor zogenoemde hybride gewapend beton/SHCC-balken (R/SHCC-balken) ontstaan. SHCC is een composiet dat, door zijn specifieke samenstelling en vezeltoevoeging, onder trekspanningen in staat is meerdere fijne scheuren te vormen en daarmee een effectieve oplossing biedt voor het beter beperken van scheurwijdtes. Huang [1] toonde de effectiviteit aan van een 70mm dikke SHCC-laag in een 200mm hoge hybride R/SHCC-balk. Singh [2] onderzocht de invloed van de SHCC-beton interface op scheurwijdtes en ontdekte dat zowel gladde als geprofileerde SHCC-betoninterfaces vergelijkbare prestaties leverden in het beperken van scheurwijdtes in een 200mm hoge hybride R/SHCC-balk met een 70mm dikke SHCC-laag. Bezemer [3] onderzocht de effectiviteit van een 70mm dikke SHCC-laag in hybride R/SHCC-balken met praktischere hoogtes van 300mm en 400mm, waarbij een verwachte afname in de efficiëntie van de SHCC-laag werd waargenomen naarmate de balkhoogte toenam.

In het huidige onderzoek worden drie belangrijke parameters bestudeerd voor hun invloed op scheurwijdtebeperking: (1) de SHCC-betoninterface, variërend van een gladde interface tot een geprofileerde interface gecoat met Vaseline; (2) de wapening-SHCC-verbinding, verzwakt door ribbelstaven te vervangen door gladde staven; en (3) het type SHCC, variërend van PVA-gebaseerde SHCC naar PE-gebaseerde SHCC. Ook het effect van uithardingstijd wordt onderzocht. De balken, met een totale hoogte van 400mm en een 70mm dikke SHCC-laag, worden experimenteel getest in een vierpuntsbuigopstelling om een gebied met een constant buigmoment (CBMR) te creëren, waardoor buigscheuren kunnen worden onderzocht. Met behulp van Digital Image Correlation (DIC) worden de scheurpatronen en scheurwijdtes geëvalueerd. De prestaties van de balken worden beoordeeld door te kijken of de scheurwijdtes onder de limieten van 0.2mm en 0.3mm blijven.

Uit de experimentele resultaten blijkt dat het gebruik van een geprofileerde SHCC-betoninterface met een Vaselinecoating de beperking van scheurwijdte van hybride R/SHCC-balken aanzienlijk verbetert ten opzichte van een gladde interface. De balk met deze geprofileerde interface vertoont een significante toename in de belasting, uitgedrukt als percentage van de vloeikracht, waarbij de 0.2mm- en 0.3mm-limieten worden overschreden met respectievelijk 37,6% en 22,7%, vergeleken met de balk met een gladde interface. Deze verbetering wordt toegeschreven aan de mogelijkheid van de interface om gecontroleerde delaminatie te vertonen (door de mechanische vergrendeling van de groeven) over de volledige lengte van het CBMR (mogelijk gemaakt door de chemische onthechting van de lagen door de Vaselinecoating).

Het gebruik van gladde wapening vermindert aanzienlijk de beperking van scheurwijdtes van hybride R/SHCC-balken. De balk met gladde staven ervaart een daling in de belasting, uitgedrukt als

percentage van de vloeikracht, waarbij de 0.2mm- en 0.3mm-limieten worden overschreden met respectievelijk 51,0% en 35,7% ten opzichte van de balk met ribbelstaven. Deze prestatievermindering kan worden toegeschreven aan de verzwakking van de wapening-SHCC-verbinding, die enkel berust op chemische hechting en wrijving bij gladde staven. Deze beperking belemmert de activatie van SHCC en leidt tot snelle scheurlocalisatie binnen de SHCC. Ondanks de toepassing van een geprofileerde SHCC-betoninterface met vaselinecoating in beide balken, werden de voordelen van deze geprofileerde interface met vaseline in de balk met ribbelstaven niet gerealiseerd, wat erop wijst dat een voldoende sterke hechting noodzakelijk is voor effectieve scheurwijdtebeperking.

PE-SHCC verbetert de beperking van scheurwijdtes in hybride R/SHCC-balken vergeleken met PVA-SHCC, wanneer deze wordt gebruikt in combinatie met gladde staven. De balk met PE-SHCC vertoont een toename in de belasting, uitgedrukt als percentage van de vloeikracht, waarbij de 0.2mm- en 0.3mm-limieten worden overschreden met respectievelijk 6,1% en 14,9%, vergeleken met de balk met PVA-SHCC. Deze verbetering kan waarschijnlijk worden toegeschreven aan de grotere vervormbaarheid van PE-SHCC en de superieure hechting tussen wapening en SHCC in PE-SHCC, wat een grotere activatie van de SHCC mogelijk maakt. Het blijft echter onzeker of deze bevindingen ook gelden bij het gebruik van ribbelstaven, aangezien de superieure hechting tussen wapening en SHCC in PE-SHCC kan leiden tot een te hoge hechtingssterkte die de spanningsherverdeling in de wapening zou kunnen belemmeren.

Uit de experimentele resultaten blijkt ook dat de uithardingstijd de beperking van scheurwijdte in hybride R/SHCC-balken aanzienlijk beïnvloedt. De balk die werd getest op latere leeftijd (SHCC-leeftijd van 85 dagen) vertoonde een betere scheurwijdtebeperking dan de balk getest door Bezemer [3] op een SHCC-leeftijd van 55 dagen. Specifiek is er een toename in de belasting, uitgedrukt als percentage van de vloeikracht, waarbij de 0.2mm- en 0.3mm-limieten worden overschreden met respectievelijk 10,6% en 5,5% vergeleken met de balk getest op 55 dagen. Deze verbetering wordt toegeschreven aan twee factoren: (1) de treksterkte-eigenschappen van SHCC verminderen met de tijd, waardoor scheurlocalisatie wordt uitgesteld, en (2) de hechting tussen SHCC en conventioneel beton neemt met de tijd toe, wat resulteert in minder duidelijk waarneembare delaminatie. Hierdoor wordt, hoewel minder SHCC wordt geactiveerd, de effectiviteit van SHCC om te fungeren als wapening vergroot.

Samenvattend toont dit onderzoek aan dat scheurwijdtebeperking in hybride R/SHCC-balken aanzienlijk kan worden verbeterd door een geprofileerde interface met een Vaselinecoating te gebruiken en ribbelstaven in plaats van gladde staven toe te passen bij het gebruik van PVA-SHCC. Bovendien blijkt dat bij gebruik van gladde staven PE-SHCC de scheurwijdtebeperking verbetert. Het onderzoek toont ook aan dat hybride R/SHCC-balken met een praktischere hoogte effectief scheurwijdtes kunnen beperken voorbij het vloeipunt van de wapening met de voorgestelde ontwerpaanpassingen.

---

# Contents

---

Preface .....	i
Abstract .....	ii
Samenvatting.....	iv
Contents .....	vi
List of Figures.....	viii
List of Tables.....	xv
1 Introduction.....	1
1.1. Background.....	1
1.2. Problem statement.....	1
1.3. Research objective and questions .....	2
1.4. Research hypothesis.....	2
1.5. Methodology .....	2
1.6. Research scope.....	3
1.7. Thesis outline .....	4
2. Literature study .....	5
2.1. Strain Hardening Cementitious Composite (SHCC) .....	5
2.1.1. Properties .....	5
2.1.2. Mix composition .....	6
2.1.3. Bonding of reinforcement-SHCC .....	14
2.1.4. Limitations of SHCC .....	15
2.2. Cracking in hybrid R/SHCC beams .....	19
2.3.1 Hybrid R/SHCC beams vs conventional RC beams.....	19
2.3.2. Influence of SHCC-concrete interface bond .....	24
2.3.3. Influence of reinforcement-SHCC bond .....	29
2.3.4. Influence of fiber-type.....	31
2.3. Concluding remarks.....	32
3. Design of beams .....	35
3.1 Motivation for design of beams .....	35
3.2 Overview beam dimensions and lay-out .....	36
3.2.1 Beam PVA-RR-SI.....	36
3.2.2 Beam PVA-RR-VPI .....	36
3.2.3 Beam PVA-SR-VPI.....	38
3.2.4 Beam PE-SR-VPI.....	39
3.3 Material properties .....	40
4. Experimental program.....	42
4.2. Pre-study .....	42
4.3. Sample preparation .....	43
4.3.1. Formwork .....	43
4.3.2. SHCC-layer .....	43
4.3.3. CC layer.....	44
4.3.4. Material samples .....	45

4.3.5.	Remarks after demolding .....	45
4.4.	Experimental methods .....	46
4.4.1.	Digital Image Correlation (DIC) .....	46
4.4.2.	Linear Variable Data Transformers (LVDTs) .....	49
5.	Results .....	50
5.1.	Hybrid R/SHCC beams .....	50
5.1.1	Beam PVA-RR-SI .....	50
5.1.2	Beam PVA-RR-VPI .....	58
5.1.3	Beam PVA-SR-VPI .....	67
5.1.4	Beam PE-SR-VPI .....	76
5.2	Material tests .....	85
5.2.1	Compression tests .....	85
5.2.2	Tensile tests .....	86
6.	Comparison and discussion .....	92
6.1	Verification with earlier studies .....	92
6.2	Influence of curing time .....	95
6.3	Influence of SHCC-CC interface roughness .....	98
6.4	Influence of reinforcement-SHCC bond .....	101
6.5	Influence of SHCC-type .....	103
6.6	Efficiency of all tested beams .....	106
6.7	Behavior outside CBMR .....	107
6.7.1	Cracking behavior .....	107
6.7.2	Delamination & Slip outside CBMR .....	111
7.	Conclusion and recommendation .....	114
7.1	Conclusions .....	114
7.2	Recommendations .....	117
8.	Bibliography .....	120
A.	Top view profiled interface .....	126
B.	Design checks .....	127
B.1.	Concrete cover .....	127
B.2.	Flexural capacity .....	127
B.3.	Shear capacity .....	128
C.	Comparison GOM data and LVDT data .....	130
C.1	Beam PVA-RR-SI .....	130
C.2	Beam PVA-RR-VPI .....	130
C.3	Beam PVA-SR-VPI .....	131
C.4	Beam PE-SR-VPI .....	132

---

# List of Figures

---

FIG. 1.1: CRACK-WIDTH LIMITS ACCORDING TO EUROCODE [7].....	4
FIG. 1.2: THESIS OUTLINE .....	4
FIG. 2.1: TYPICAL STRESS-STRAIN CURVE SHCC [9].....	5
FIG. 2.2: FIBER-BRIDGING STRESS VS CRACK OPENING DISPLACEMENT OF OILED AND UNOILED PVA FIBER [12] .....	7
FIG. 2.3: : STRESS-STRAIN CURVE OF SHCC-PVA AND SHCC-PE [14] .....	8
FIG. 2.4: CLASSIFICATION OF FIBER ORIENTATION. (A) 1D, (B) 2D RANDOM, (C) 2D ORGANIZED, (D) 3D [19].....	9
FIG. 2.5: EFFECT OF MEMBER THICKNESS ON TENSILE PROPERTIES OF SHCC [20].....	9
FIG. 2.6: INFLUENCE OF S/C RATIO ON TENSILE STRENGTH (A) AND STRAIN (B) OF SHCC AS FOUND BY [21].....	10
FIG. 2.7: EFFECT OF W/C RATIO ON PROPERTIES OF SHCC [22].....	11
FIG. 2.8: EFFECT OF LIMESTONE INCORPORATION IN SHCC ON STRESS-STRAIN RELATION OF SHCC [26].....	12
FIG. 2.9: EFFECT OF INCORPORATION OF LIMESTONE IN SHCC ON FIBER-MATRIX BOND [27] .....	13
FIG. 2.10: REINFORCEMENT-MATRIX BOND STRENGTH OF RIBBED REBARS IN SHCC AND CC FOR DIFFERENT BOND LENGTHS [35].....	14
FIG. 2.11: REINFORCEMENT-MATRIX BOND STRENGTH FOR SMOOTH REBARS IN SHCC AND CC [36].....	15
FIG. 2.12: ENERGY CONSUMPTION PER 1000 KG OF STEEL REINFORCED CONCRETE AND SHCC [41].....	16
FIG. 2.13: EFFECT OF TIME ON THE DUCTILITY OF PVA-SHCC [43].....	17
FIG. 2.14: EFFECT OF TEMPERATURE ON TENSILE PROPERTIES OF PVA-SHCC [47] .....	18
FIG. 2.15: OVERVIEW OF STUDIES ON THE EFFECT OF TEMPERATURE ON TENSILE PROPERTIES OF PVA-SHCC [46] .....	18
FIG. 2.16: CROSS-SECTIONS OF BEAMS (LEFT) AND TEST SETUP (RIGHT) AS USED BY [49] .....	19
FIG. 2.17: LOAD-DEFLECTION CURVES (LEFT) AND LOAD-CRACK WIDTH CURVES (RIGHT) OF BEAMS TESTED BY [49].....	20
FIG. 2.18: (A) CROSS-SECTION OF BEAMS OF GROUP I [1] .....	(B) CROSS-SECTION OF BEAMS OF GROUP II [1] 20
FIG. 2.19: TEST SET-UP AS USED BY [1] .....	21
FIG. 2.20: LOAD DEFLECTION-CRACK WIDTH CURVES FOR BEAMS OF GROUP I (LEFT) AND LOAD DEFLECTION-CRACK WIDTH CURVES FOR BEAMS OF GROUP II (RIGHT) [1] .....	21
FIG. 2.21: (A) CROSS-SECTION OF 300MM BEAMS, (B) TEST SETUP OF 300MM BEAMS, (C) CROSS-SECTION OF 400MM BEAMS, (D) TEST SETUP OF 400MM BEAMS [3] .....	22
FIG. 2.22: LOAD-DEFLECTION-CRACK WIDTH CURVES OF 300MM BEAMS (LEFT) AND LOAD-DEFLECTION-CRACK WIDTH CURVES OF 300MM BEAMS (RIGHT) .....	23
FIG. 2.23: PHOTOS OF INTERFACE CONDITIONS AS REALIZED BY [52].....	24
FIG. 2.24: LOAD-DEFLECTION-CRACK WIDTH CURVES OF BEAMS TESTED BY (LEFT) AND BAR GRAPH OF LOADS AT WHICH ALL BEAMS TESTED EXCEEDED 0.3MM CRACK WIDTH (RIGHT) [52].....	25
FIG. 2.25: DETAILED OVERVIEW OF TEST SET-UP, CROSS-SECTION OF BEAMS AND INTERFACE DETAILS AS EMPLOYED BY [53] .....	26
FIG. 2.26: LOAD-DEFLECTION-CRACK WIDTH CURVES (LEFT) AND OVERVIEW 0.3MM CW-LIMIT LOAD AND DEFORMATION (RIGHT) [53] .....	27
FIG. 2.27: COMPARISON OF (A) AVERAGE CRACK WIDTHS AND (B) NUMBER OF CRACKS BETWEEN ALL TESTED BEAMS [53] .....	27
FIG. 2.28: DEVELOPMENT OF THE MAXIMUM CRACK WIDTH FOR ALL THE SIMULATED BEAMS [53] .....	28
FIG. 2.29: CONTOURS OF PRINCIPAL TENSILE STRAINS AT VARIOUS DEFORMATION LEVELS AND TENSILE STRENGTHS [54] .....	29

FIG. 2.30: LOAD-DEFLECTION-CRACK WIDTH RESPONSE OF HYBRID BEAMS WITH VARYING FIBER TYPES [52].....	31
FIG. 2.31: CRACKING PATTERN AT ULTIMATE LOAD OF HYBRID BEAMS WITH VARYING FIBER TYPES [52].....	31
FIG. 3.1: SIDE VIEW OF BEAM PVA-RR-SI.....	36
FIG. 3.2: CROSS-SECTIONAL VIEW OF BEAM PVA-RR-SI WITH (LEFT) SECTION AA AND (RIGHT) SECTION BB.....	36
FIG. 3.3: SIDE VIEW OF BEAM PVA-RR-VPI.....	37
FIG. 3.4: CROSS-SECTIONAL OVERVIEW OF BEAM PVA-RR-VPI WITH (LEFT) SECTION AA AND (RIGHT) SECTION BB ...	37
FIG. 3.5: : SIDE VIEW OF BEAM PVA-SR-VPI.....	38
FIG. 3.6: CROSS-SECTIONAL OVERVIEW OF BEAM PVA-SR-VPI WITH (LEFT) SECTION AA AND (RIGHT) SECTION BB ...	38
FIG. 3.7: SIDE VIEW OF BEAM PE-SR-VPI.....	39
FIG. 3.8: CROSS-SECTIONAL OVERVIEW OF BEAM PE-SR-VPI WITH (LEFT) SECTION AA AND (RIGHT) SECTION BB .....	39
FIG. 3.9: INGREDIENTS USED IN PVA-SHCC. FROM LEFT TO RIGHT: CEM III/B, LIMESTONE, PVA FIBERS, SUPERPLASTICIZER AND WATER .....	40
FIG. 3.10: INGREDIENTS USED IN PVA-SHCC. FROM LEFT TO RIGHT: CEM III/B, LIMESTONE, PE FIBERS, SILICA FUME, SUPERPLASTICIZER AND WATER .....	40
FIG. 4.1: FRESH (LEFT) AND HARDENED (RIGHT) STATE OF PROFILED INTERFACES .....	42
FIG. 4.2: PROFILED INTERFACES AFTER DEMOLDING .....	43
FIG. 4.3: WOODEN MOLDS USED TO CAST THE BEAMS.....	43
FIG. 4.4: (A) LEVELLING TOOL (B) SILICONE MOLD USED TO CREATE PROFILED INTERFACE (C) BEAM MOLDS COVERED AFTER SHCC LAYER CASTING INTERFACE .....	44
FIG. 4.5: (A) VASELINE USED ON TOP OF PROFILED INTERFACE (B) VIBRATION NEEDLE USED TO VIBRATE CC LAYER (C) BEAM MOLDS COVERED AFTER CC LAYER CASTING .....	45
FIG. 4.6: MOLDS FOR CUBES AND DOGBONES .....	45
FIG. 4.7: TEST SETUP .....	46
FIG. 4.8: SPECKLE PATTERN. FIRST SURFACE IS PAINTED WHITE (TOP LEFT), THEN SPECKLES ARE SPRAYED ON WHITE SURFACE (TOP RIGHT). SKETCH OF SPECKLE PATTERN ON BEAM WITH DEFINITION OF THE CONSTANT BENDING MOMENT REGION (BOTTOM).....	47
FIG. 4.9: CORRELATABLE STICKERS (TOP) AND SKETCH OF CORRELATABLE STICKERS ON BEAM (BOTTOM).....	47
FIG. 4.10: VON-MISES STRAINS OVER CBMR.....	48
FIG. 4.11: CLOSELY SPACED CRACKS.....	48
FIG. 4.12: SIDE VIEW OF BEAM WITH ALL LVDTs AND LASER MOUNTED TO ROD.....	49
FIG. 4.13: CONFIGURATION OF LVDTs. (TOP) SIDE VIEW AND (BOTTOM) BOTTOM VIEW .....	49
FIG. 5.1: LOAD-DEFLECTION RESPONSE OF BEAM PVA-RR-SI.....	50
FIG. 5.2: COMPARISON OF LASER MEASUREMENTS WITH DIC MEASUREMENTS OF BEAM PVA-RR-SI.....	51
FIG. 5.3: COMPARISON OF THE MEASUREMENTS OF ALL HORIZONTALLY PLACED LVDTs WITH THE DIC MEASUREMENTS OF BEAM PVA-RR-SI .....	51
FIG. 5.4: CRACKING BEHAVIOR OF BEAM PVA-RR-SI AT A LOAD OF 18kN. TOP LEFT: LOAD-LEVEL ON LOAD-DEFLECTION CURVE. TOP RIGHT: CONTOUR PLOT VON-MISES STRAINS. BOTTOM LEFT: SCATTER PLOT OF ALL CRACKS. BOTTOM RIGHT: CRACK-WIDTH DISTRIBUTION OF CRACKS IN SHCC. ....	52
FIG. 5.5: CRACKING BEHAVIOR OF BEAM PVA-RR-SI AT A LOAD OF 29kN. TOP LEFT: LOAD-LEVEL ON LOAD-DEFLECTION CURVE. TOP RIGHT: CONTOUR PLOT VON-MISES STRAINS. BOTTOM LEFT: SCATTER PLOT OF ALL CRACKS. BOTTOM RIGHT: CRACK-WIDTH DISTRIBUTION OF CRACKS IN SHCC. ....	52
FIG. 5.6: CRACKING BEHAVIOR OF BEAM PVA-RR-SI AT A LOAD OF 37kN. TOP LEFT: LOAD-LEVEL ON LOAD-DEFLECTION CURVE. TOP RIGHT: CONTOUR PLOT VON-MISES STRAINS. BOTTOM LEFT: SCATTER PLOT OF ALL CRACKS. BOTTOM RIGHT: CRACK-WIDTH DISTRIBUTION OF CRACKS IN SHCC. ....	53
FIG. 5.7: CRACKING BEHAVIOR OF BEAM PVA-RR-SI AT A LOAD OF 46kN. TOP LEFT: LOAD-LEVEL ON LOAD-DEFLECTION CURVE. TOP RIGHT: CONTOUR PLOT VON-MISES STRAINS. BOTTOM LEFT: SCATTER PLOT OF ALL CRACKS. BOTTOM RIGHT: CRACK-WIDTH DISTRIBUTION OF CRACKS IN SHCC. ....	53

FIG. 5.8: CRACKING BEHAVIOR OF BEAM PVA-RR-SI AT A LOAD OF 56kN. TOP LEFT: LOAD-LEVEL ON LOAD-DEFLECTION CURVE. TOP RIGHT: CONTOUR PLOT VON-MISES STRAINS. BOTTOM LEFT: SCATTER POT OF ALL CRACKS. BOTTOM RIGHT: CRACK-WIDTH DISTRIBUTION OF CRACKS IN SHCC. ....	54
FIG. 5.9: CRACKING BEHAVIOR OF BEAM PVA-RR-SI AT A LOAD OF 60kN. TOP LEFT: LOAD-LEVEL ON LOAD-DEFLECTION CURVE. TOP RIGHT: CONTOUR PLOT VON-MISES STRAINS. BOTTOM LEFT: SCATTER PLOT OF ALL CRACKS. BOTTOM RIGHT: CRACK-WIDTH DISTRIBUTION OF CRACKS IN SHCC .....	54
FIG. 5.10: CRACKING BEHAVIOR OF BEAM PVA-RR-SI AT A LOAD OF 70kN. TOP LEFT: LOAD-LEVEL ON LOAD-DEFLECTION CURVE. TOP RIGHT: CONTOUR PLOT VON-MISES STRAINS. BOTTOM LEFT: SCATTER PLOT OF ALL CRACKS. BOTTOM RIGHT: CRACK-WIDTH DISTRIBUTION OF CRACKS IN SHCC. ....	55
FIG. 5.11: CRACKING BEHAVIOR OF BEAM PVA-RR-SI AT A LOAD OF 93kN. TOP LEFT: LOAD-LEVEL ON LOAD-DEFLECTION CURVE. TOP RIGHT: CONTOUR PLOT VON-MISES STRAINS. BOTTOM LEFT: SCATTER PLOT OF ALL CRACKS. BOTTOM RIGHT: CRACK-WIDTH DISTRIBUTION OF CRACKS IN SHCC. ....	55
FIG. 5.12: LOAD - MAX.CW - DEFLECTION CURVE OF BEAM PVA-RR-SI .....	56
FIG. 5.13: DELAMINATION (LEFT) AND SLIP (RIGHT) OF INTERFACE OF BEAM PVA-RR-SI FOR THREE MEASURING POINTS .....	56
FIG. 5.14: CONTOUR PLOTS OF VERTICAL STRAINS AT SEVERAL LOAD LEVELS OF BEAM PVA-RR-SI .....	57
FIG. 5.15: LOAD-DEFLECTION RESPONSE OF BEAM PVA-RR-VPI .....	58
FIG. 5.16: COMPARISON OF THE MEASUREMENTS OF LVDT2 (LEFT) AND LVDT3 (RIGHT) WITH THE DIC MEASUREMENTS OF BEAM PVA-RR-VPI .....	58
FIG. 5.17: CRACKING BEHAVIOR OF BEAM PVA-RR-VPI AT A LOAD OF 19kN. TOP LEFT: LOAD-LEVEL ON LOAD-DEFLECTION CURVE. TOP RIGHT: CONTOUR PLOT VON-MISES STRAINS. BOTTOM LEFT: SCATTER PLOT OF ALL CRACKS. BOTTOM RIGHT: CRACK-WIDTH DISTRIBUTION OF CRACKS IN SHCC. ....	59
FIG. 5.18: CRACKING BEHAVIOR OF BEAM PVA-RR-VPI AT A LOAD OF 32kN. TOP LEFT: LOAD-LEVEL ON LOAD-DEFLECTION CURVE. TOP RIGHT: CONTOUR PLOT VON-MISES STRAINS. BOTTOM LEFT: SCATTER PLOT OF ALL CRACKS. BOTTOM RIGHT: CRACK-WIDTH DISTRIBUTION OF CRACKS IN SHCC. ....	60
FIG. 5.19: CRACKING BEHAVIOR OF BEAM PVA-RR-VPI AT A LOAD OF 43kN. TOP LEFT: LOAD-LEVEL ON LOAD-DEFLECTION CURVE. TOP RIGHT: CONTOUR PLOT VON-MISES STRAINS. BOTTOM LEFT: SCATTER PLOT OF ALL CRACKS. BOTTOM RIGHT: CRACK-WIDTH DISTRIBUTION OF CRACKS IN SHCC. ....	60
FIG. 5.20: CRACKING BEHAVIOR OF BEAM PVA-RR-VPI AT A LOAD OF 53kN. TOP LEFT: LOAD-LEVEL ON LOAD-DEFLECTION CURVE. TOP RIGHT: CONTOUR PLOT VON-MISES STRAINS. BOTTOM LEFT: SCATTER PLOT OF ALL CRACKS. BOTTOM RIGHT: CRACK-WIDTH DISTRIBUTION OF CRACKS IN SHCC. ....	61
FIG. 5.21: CRACKING BEHAVIOR OF BEAM PVA-RR-VPI AT A LOAD OF 64kN. TOP LEFT: LOAD-LEVEL ON LOAD-DEFLECTION CURVE. TOP RIGHT: CONTOUR PLOT VON-MISES STRAINS. BOTTOM LEFT: SCATTER PLOT OF ALL CRACKS. BOTTOM RIGHT: CRACK-WIDTH DISTRIBUTION OF CRACKS IN SHCC. ....	61
FIG. 5.22: CRACKING BEHAVIOR OF BEAM PVA-RR-VPI AT A LOAD OF 71kN. TOP LEFT: LOAD-LEVEL ON LOAD-DEFLECTION CURVE. TOP RIGHT: CONTOUR PLOT VON-MISES STRAINS. BOTTOM LEFT: SCATTER PLOT OF ALL CRACKS. BOTTOM RIGHT: CRACK-WIDTH DISTRIBUTION OF CRACKS IN SHCC. ....	62
FIG. 5.23: CRACKING BEHAVIOR OF BEAM PVA-RR-VPI AT A LOAD OF 80kN. TOP LEFT: LOAD-LEVEL ON LOAD-DEFLECTION CURVE. TOP RIGHT: CONTOUR PLOT VON-MISES STRAINS. BOTTOM LEFT: SCATTER PLOT OF ALL CRACKS. BOTTOM RIGHT: CRACK-WIDTH DISTRIBUTION OF CRACKS IN SHCC. ....	62
FIG. 5.24: CRACKING BEHAVIOR OF BEAM PVA-RR-VPI AT A LOAD OF 86kN. TOP LEFT: LOAD-LEVEL ON LOAD-DEFLECTION CURVE. TOP RIGHT: CONTOUR PLOT VON-MISES STRAINS. BOTTOM LEFT: SCATTER PLOT OF ALL CRACKS. BOTTOM RIGHT: CRACK-WIDTH DISTRIBUTION OF CRACKS IN SHCC. ....	63
FIG. 5.25: CRACKING BEHAVIOR OF BEAM PVA-RR-VPI AT A LOAD OF 89kN. TOP LEFT: LOAD-LEVEL ON LOAD-DEFLECTION CURVE. TOP RIGHT: CONTOUR PLOT VON-MISES STRAINS. BOTTOM LEFT: SCATTER PLOT OF ALL CRACKS. BOTTOM RIGHT: CRACK-WIDTH DISTRIBUTION OF CRACKS IN SHCC. ....	63
FIG. 5.26: CRACKING BEHAVIOR OF BEAM PVA-RR-VPI AT A LOAD OF 90kN. TOP LEFT: LOAD-LEVEL ON LOAD-DEFLECTION CURVE. TOP RIGHT: CONTOUR PLOT VON-MISES STRAINS. BOTTOM LEFT: SCATTER PLOT OF ALL CRACKS. BOTTOM RIGHT: CRACK-WIDTH DISTRIBUTION OF CRACKS IN SHCC. ....	64

FIG. 5.27: LOAD - MAX.CW - DEFLECTION CURVE OF BEAM PVA-RR-VPI .....	64
FIG. 5.28: CONTOUR PLOTS OF VERTICAL STRAINS AT SEVERAL LOAD LEVELS OF BEAM PVA-RR-VPI.....	65
FIG. 5.29: DELAMINATION (LEFT) AND SLIP (RIGHT) OF INTERFACE OF BEAM PVA-RR-VPI FOR THREE MEASURING POINTS .....	65
FIG. 5.30:LOAD-DEFLECTION RESPONSE OF BEAM PVA-SR-VPI: (A) WHOLE EXPERIMENT AND (B) BEGINNING STAGE OF EXPERIMENT AND DEFLECTION-TIME RESPONSE OF BEAM PVA-SR-VPI: (C) WHOLE EXPERIMENT AND (D) BEGINNING STAGE OF EXPERIMENT .....	67
FIG. 5.31: CORRECTED LOAD-DEFLECTION RESPONSE OF BEAM PVA-SR-VPI .....	68
FIG. 5.32: COMPARISON OF THE MEASUREMENTS OF LVDT3 WITH THE DIC MEASUREMENTS OF BEAM PVA-SR-VPI.....	68
FIG. 5.33: CRACKING BEHAVIOR OF BEAM PVA-SR-VPI AT A LOAD OF 27kN. TOP LEFT: LOAD-LEVEL ON LOAD- DEFLECTION CURVE. TOP RIGHT: CONTOUR PLOT VON-MISES STRAINS. BOTTOM LEFT: SCATTER PLOT OF ALL CRACKS. BOTTOM RIGHT: CRACK-WIDTH DISTRIBUTION OF CRACKS IN SHCC. ....	69
FIG. 5.34: CRACKING BEHAVIOR OF BEAM PVA-SR-VPI AT A LOAD OF 33kN. TOP LEFT: LOAD-LEVEL ON LOAD- DEFLECTION CURVE. TOP RIGHT: CONTOUR PLOT VON-MISES STRAINS. BOTTOM LEFT: SCATTER PLOT OF ALL CRACKS. BOTTOM RIGHT: CRACK-WIDTH DISTRIBUTION OF CRACKS IN SHCC. ....	69
FIG. 5.35: CRACKING BEHAVIOR OF BEAM PVA-SR-VPI AT A LOAD OF 38kN. TOP LEFT: LOAD-LEVEL ON LOAD- DEFLECTION CURVE. TOP RIGHT: CONTOUR PLOT VON-MISES STRAINS. BOTTOM LEFT: SCATTER PLOT OF ALL CRACKS. BOTTOM RIGHT: CRACK-WIDTH DISTRIBUTION OF CRACKS IN SHCC. ....	70
FIG. 5.36: CRACKING BEHAVIOR OF BEAM PVA-SR-VPI AT A LOAD OF 44kN. TOP LEFT: LOAD-LEVEL ON LOAD- DEFLECTION CURVE. TOP RIGHT: CONTOUR PLOT VON-MISES STRAINS. BOTTOM LEFT: SCATTER PLOT OF ALL CRACKS. BOTTOM RIGHT: CRACK-WIDTH DISTRIBUTION OF CRACKS IN SHCC. ....	70
FIG. 5.37: CRACKING BEHAVIOR OF BEAM PVA-SR-VPI AT A LOAD OF 55kN. TOP LEFT: LOAD-LEVEL ON LOAD- DEFLECTION CURVE. TOP RIGHT: CONTOUR PLOT VON-MISES STRAINS. BOTTOM LEFT: SCATTER PLOT OF ALL CRACKS. BOTTOM RIGHT: CRACK-WIDTH DISTRIBUTION OF CRACKS IN SHCC. ....	71
FIG. 5.38: CRACKING BEHAVIOR OF BEAM PVA-SR-VPI AT A LOAD OF 59kN. TOP LEFT: LOAD-LEVEL ON LOAD- DEFLECTION CURVE. TOP RIGHT: CONTOUR PLOT VON-MISES STRAINS. BOTTOM LEFT: SCATTER PLOT OF ALL CRACKS. BOTTOM RIGHT: CRACK-WIDTH DISTRIBUTION OF CRACKS IN SHCC. ....	71
FIG. 5.39: CRACKING BEHAVIOR OF BEAM PVA-SR-VPI AT A LOAD OF 81N. TOP LEFT: LOAD-LEVEL ON LOAD- DEFLECTION CURVE. TOP RIGHT: CONTOUR PLOT VON-MISES STRAINS. BOTTOM LEFT: SCATTER PLOT OF ALL CRACKS. BOTTOM RIGHT: CRACK-WIDTH DISTRIBUTION OF CRACKS IN SHCC. ....	72
FIG. 5.40: CRACKING BEHAVIOR OF BEAM PVA-SR-VPI AT A LOAD OF 80kN. TOP LEFT: LOAD-LEVEL ON LOAD- DEFLECTION CURVE. TOP RIGHT: CONTOUR PLOT VON-MISES STRAINS. BOTTOM LEFT: SCATTER PLOT OF ALL CRACKS. BOTTOM RIGHT: CRACK-WIDTH DISTRIBUTION OF CRACKS IN SHCC. ....	72
FIG. 5.41: CRACKING BEHAVIOR OF BEAM PVA-SR-VPI AT A LOAD OF 87kN. TOP LEFT: LOAD-LEVEL ON LOAD- DEFLECTION CURVE. TOP RIGHT: CONTOUR PLOT VON-MISES STRAINS. BOTTOM LEFT: SCATTER PLOT OF ALL CRACKS. BOTTOM RIGHT: CRACK-WIDTH DISTRIBUTION OF CRACKS IN SHCC. ....	73
FIG. 5.42: LOAD - MAX.CW - DEFLECTION CURVE OF BEAM PVA-SR-VPI .....	73
FIG. 5.43: DELAMINATION (LEFT) AND SLIP (RIGHT) OF INTERFACE OF BEAM PVA-SR-VPI FOR FOUR MEASURING POINTS .....	74
FIG. 5.44: CONTOUR PLOTS OF VERTICAL STRAINS AT SEVERAL LOAD LEVELS OF BEAM PVA-SR-VPI .....	74
FIG. 5.45: LOAD-DEFLECTION RESPONSE OF BEAM PE-SR-VPI .....	76
FIG. 5.46: COMPARISON OF THE MEASUREMENTS OF LVDT1, LVDT2 AND LVDT3 WITH THE DIC MEASUREMENTS OF BEAM PE-SR-VPI.....	76
FIG. 5.47: CRACKING BEHAVIOR OF BEAM PE-SR-VPI AT A LOAD OF 19kN. TOP LEFT: LOAD-LEVEL ON LOAD- DEFLECTION CURVE. TOP RIGHT: CONTOUR PLOT VON-MISES STRAINS. BOTTOM LEFT: SCATTER PLOT OF ALL CRACKS. BOTTOM RIGHT: CRACK-WIDTH DISTRIBUTION OF CRACKS IN SHCC. ....	77
FIG. 5.48: : CRACKING BEHAVIOR OF BEAM PE-SR-VPI AT A LOAD OF 23kN. TOP LEFT: LOAD-LEVEL ON LOAD- DEFLECTION CURVE. TOP RIGHT: CONTOUR PLOT VON-MISES STRAINS. BOTTOM LEFT: SCATTER PLOT OF ALL CRACKS. BOTTOM RIGHT: CRACK-WIDTH DISTRIBUTION OF CRACKS IN SHCC. ....	78

FIG. 5.49: : CRACKING BEHAVIOR OF BEAM PE-SR-VPI AT A LOAD OF 32kN. TOP LEFT: LOAD-LEVEL ON LOAD-DEFLECTION CURVE. TOP RIGHT: CONTOUR PLOT VON-MISES STRAINS. BOTTOM LEFT: SCATTER PLOT OF ALL CRACKS. BOTTOM RIGHT: CRACK-WIDTH DISTRIBUTION OF CRACKS IN SHCC. ....	78
FIG. 5.50: : CRACKING BEHAVIOR OF BEAM PE-SR-VPI AT A LOAD OF 40kN. TOP LEFT: LOAD-LEVEL ON LOAD-DEFLECTION CURVE. TOP RIGHT: CONTOUR PLOT VON-MISES STRAINS. BOTTOM LEFT: SCATTER PLOT OF ALL CRACKS. BOTTOM RIGHT: CRACK-WIDTH DISTRIBUTION OF CRACKS IN SHCC. ....	79
FIG. 5.51: : CRACKING BEHAVIOR OF BEAM PE-SR-VPI AT A LOAD OF 43kN. TOP LEFT: LOAD-LEVEL ON LOAD-DEFLECTION CURVE. TOP RIGHT: CONTOUR PLOT VON-MISES STRAINS. BOTTOM LEFT: SCATTER PLOT OF ALL CRACKS. BOTTOM RIGHT: CRACK-WIDTH DISTRIBUTION OF CRACKS IN SHCC. ....	79
FIG. 5.52: : CRACKING BEHAVIOR OF BEAM PE-SR-VPI AT A LOAD OF 52kN. TOP LEFT: LOAD-LEVEL ON LOAD-DEFLECTION CURVE. TOP RIGHT: CONTOUR PLOT VON-MISES STRAINS. BOTTOM LEFT: SCATTER PLOT OF ALL CRACKS. BOTTOM RIGHT: CRACK-WIDTH DISTRIBUTION OF CRACKS IN SHCC. ....	80
FIG. 5.53: : CRACKING BEHAVIOR OF BEAM PE-SR-VPI AT A LOAD OF 62kN. TOP LEFT: LOAD-LEVEL ON LOAD-DEFLECTION CURVE. TOP RIGHT: CONTOUR PLOT VON-MISES STRAINS. BOTTOM LEFT: SCATTER PLOT OF ALL CRACKS. BOTTOM RIGHT: CRACK-WIDTH DISTRIBUTION OF CRACKS IN SHCC. ....	80
FIG. 5.54: : CRACKING BEHAVIOR OF BEAM PE-SR-VPI AT A LOAD OF 72kN. TOP LEFT: LOAD-LEVEL ON LOAD-DEFLECTION CURVE. TOP RIGHT: CONTOUR PLOT VON-MISES STRAINS. BOTTOM LEFT: SCATTER PLOT OF ALL CRACKS. BOTTOM RIGHT: CRACK-WIDTH DISTRIBUTION OF CRACKS IN SHCC. ....	81
FIG. 5.55: : CRACKING BEHAVIOR OF BEAM PE-SR-VPI AT A LOAD OF 82kN. TOP LEFT: LOAD-LEVEL ON LOAD-DEFLECTION CURVE. TOP RIGHT: CONTOUR PLOT VON-MISES STRAINS. BOTTOM LEFT: SCATTER PLOT OF ALL CRACKS. BOTTOM RIGHT: CRACK-WIDTH DISTRIBUTION OF CRACKS IN SHCC. ....	81
FIG. 5.56: : CRACKING BEHAVIOR OF BEAM PE-SR-VPI AT A LOAD OF 86N. TOP LEFT: LOAD-LEVEL ON LOAD-DEFLECTION CURVE. TOP RIGHT: CONTOUR PLOT VON-MISES STRAINS. BOTTOM LEFT: SCATTER PLOT OF ALL CRACKS. BOTTOM RIGHT: CRACK-WIDTH DISTRIBUTION OF CRACKS IN SHCC. ....	82
FIG. 5.57: LOAD - MAX.CW - DEFLECTION CURVE OF BEAM PE-SR-VPI.....	82
FIG. 5.58: DELAMINATION (LEFT) AND SLIP (RIGHT) OF INTERFACE OF BEAM PE-SR-VPI FOR FOUR MEASURING POINTS .....	83
FIG. 5.59: CONTOUR PLOTS OF VERTICAL STRAINS AT SEVERAL LOAD LEVELS OF BEAM PE-SR-VPI.....	83
FIG. 5.60: FAILURE OF SHCC-GLUE INTERFACE IN TENSILE TEST .....	87
FIG. 5.61: SOLUTIONS TO OVERCOME SHCC-GLUE FAILING. (1) STEEL ANGLES. (2) THIN GROOVES IN ONE DIRECTION. (3) THIN GROOVES IN BOTH DIRECTIONS. (4) THICK GROOVES IN BOTH DIRECTIONS. (5) THICK GROOVES IN BOTH DIRECTIONS + SCREWS .....	87
FIG. 5.62: STRESS-STRAIN-CRACK WIDTH CURVES OF PE-SHCC SPECIMENS OF SERIES 1. LEFT: DOGBONE 1 RIGHT: DOGBONE 2 (NO DIC) .....	88
FIG. 5.63: STEEL HAND USED IN SERIES 2 (LEFT) AND SKETCH OF DOGBONE GLUED IN THE STEEL HAND (RIGHT).....	88
FIG. 5.64: SHCC DETACHING FROM STEEL HAND (AT ITS FLAT PART) (LEFT) AND SHCC FAILURE OUTSIDE GAUGE AREA (RIGHT) .....	89
FIG. 5.65: STRESS-STRAIN CURVE OF PVA-SHCC DOGBONE THAT SHOWED SOME DUCTILITY.....	89
FIG. 5.66: STRESS-STRAIN CURVES OF PE-SHCC SPECIMENS OF SERIES 2. LEFT TO RIGHT: DOGBONE 1 TO DOGBONE 3	89
FIG. 5.67: STRESS-STRAIN-CRACK WIDTH CURVES OF ALL PE-SHCC SAMPLES .....	90
FIG. 5.68: CONTOUR PLOT OF VON-MISES STRAINS OF DOGBONE 1 OF SERIES 1 (LEFT) AND FAILURE OF DOGBONE 1 OF SERIES 1 (RIGHT) .....	90
FIG. 6.1: LOAD - MAX. CW - DEFLECTION CURVE OF BEAM RC400 (TESTED BY BEZEMER [4]) .....	92
FIG. 6.2: CRACKING BEHAVIOR OF BEAM HYRBRID400 AT A LOAD OF 49.8kN. LEFT: CONTOUR PLOT VON-MISES STRAINS. RIGHT: SCATTER PLOT OF ALL SHCC CRACKS .....	93
FIG. 6.3: CRACKING BEHAVIOR OF BEAM HYRBRID400 AT A LOAD OF 68.2kN. LEFT: CONTOUR PLOT VON-MISES STRAINS. RIGHT: SCATTER PLOT OF ALL SHCC CRACKS .....	93
FIG. 6.4: LOAD - MAX. CW - DEFLECTION CURVE OF BEAM HYRBRID400 (TESTED BY BEZEMER [4]).....	94

FIG. 6.5: COMPARISON OF LOAD - MAX. CW - DEFLECTION CURVES OF BEAMS PVA-RR-SI (55) AND PVA-RR-SI (85) ALONG WITH THE 0.2MM CRACK-WIDTH LIMIT (LEFT) AND 0.3MM CRACK-WIDTH LIMIT (RIGHT) .....	95
FIG. 6.6 COMPARISON OF NUMBER OF DEVELOPED CRACKS BETWEEN BEAMS PVA-RR-SI AND PVA-RR-VPI .....	96
FIG. 6.7: CONTOUR PLOT OF VON MISES STRAINS AT A LOAD OF 82kN FOR BEAM PVA-RR-SI (55) (LEFT) AND BEAM PVA-RR-VPI (85) (RIGHT) .....	96
FIG. 6.8: COMPARISON OF INTERFACE BEHAVIOR OF (LEFT) BEAM PVA-RR-SI (55) AND (RIGHT) BEAM PVA-RR-VPI AT A LOAD LEVEL OF 42kN.....	97
FIG. 6.9: COMPARISON LOAD - MAX. CRACK-WIDTH - DEFLECTION CURVES OF BEAMS PVA-RR-SI AND PVA-RR-VPI ALONG WITH THE 0.2MM CRACK-WIDTH LIMIT (LEFT) AND 0.3MM CRACK-WIDTH LIMIT (RIGHT) .....	98
FIG. 6.10: COMPARISON OF (A) NUMBER OF DEVELOPED CRACKS AND (B) AVERAGE CRACK-WITH BETWEEN BEAMS PVA-RR-SI AND PVA-RR-VPI.....	98
FIG. 6.11: CONTOUR PLOT OF VON MISES STRAINS AT A LOAD OF 72kN FOR BEAM PVA-RR-SI (LEFT) AND BEAM PVA-RR-VPI (RIGHT).....	99
FIG. 6.12: COMPARISON OF INTERFACE BEHAVIOR OF (A) BEAM PVA-RR-SI AND (B) BEAM PVA-RR-VPI AT DIFFERENT LOADS .....	100
FIG. 6.13: COMPARISON LOAD - MAX. CRACK-WIDTH - DEFLECTION CURVES OF BEAMS PVA-RR-VPI AND PVA-SR-VPI ALONG WITH THE 0.2MM CRACK-WIDTH LIMIT (LEFT) AND 0.3MM CRACK-WIDTH LIMIT (RIGHT) .....	101
FIG. 6.14: CONTOUR PLOT OF VON MISES STRAINS AT A LOAD OF 80kN FOR BEAM PVA-RR-VPI (LEFT) AND BEAM PVA-SR-VPI (RIGHT) .....	102
FIG. 6.15: COMPARISON OF (A) NUMBER OF DEVELOPED CRACKS BETWEEN BEAMS PVA-RR-VPI AND PVA-SR-VPI AND (B) AVERAGE CRACK-WITH BETWEEN BEAMS PVA-RR-VPI AND PVA-SR-VPI.....	102
FIG. 6.16: COMPARISON OF INTERFACE BEHAVIOR OF (LEFT) BEAM PVA-RR-VPI (55) AND (RIGHT) BEAM PVA-SR-VPI AT A LOAD LEVEL OF 71kN.....	102
FIG. 6.17: COMPARISON LOAD - MAX. CRACK-WIDTH - DEFLECTION CURVES OF BEAMS PVA-SR-VPI AND PE-SR-VPI ALONG WITH THE 0.2MM CRACK-WIDTH LIMIT (LEFT) AND 0.3MM CRACK-WIDTH LIMIT (RIGHT) .....	103
FIG. 6.18: COMPARISON OF (A) NUMBER OF DEVELOPED CRACKS BETWEEN BEAMS PVA-SR-VPI AND PE-SR-VPI AND (B) AVERAGE CRACK-WITH BETWEEN BEAMS PVA-SR-VPI AND PE-SR-VPI .....	104
FIG. 6.19: CONTOUR PLOT OF VON MISES STRAINS AT A LOAD OF 80kN FOR BEAM PVA-SR-VPI (LEFT) AND BEAM PE-SR-VPI (RIGHT) .....	104
FIG. 6.20: COMPARISON OF INTERFACE BEHAVIOR OF (LEFT) BEAM PVA-SR-VPI (55) AND (RIGHT) BEAM PE-SR-VPI AT A LOAD LEVEL OF 71kN.....	105
FIG. 6.21: EFFICIENCY OF ALL TESTED BEAMS EXPRESSED AS THE PERCENTAGE RELATIVE TO THE YIELD LOAD AT WHICH THE 0.2MM AND 0.3MM CRACK-WIDTH LIMITS ARE EXCEEDED. BEAMS RC AND PVA-RR-SI (55) ARE TESTED BY BEZEMER [3].....	106
FIG. 6.22: CRACKING BEHAVIOR OF BEAM PVA-RR-SI AT A LOAD OF 60kN WITH THE INCLUSION OF THE AREAS ADJACENT TO THE CBMR. TOP LEFT: LOAD-LEVEL ON LOAD-DEFLECTION CURVE. TOP RIGHT: CONTOUR PLOT VON-MISES STRAINS. BOTTOM LEFT: SCATTER PLOT OF ALL CRACKS. BOTTOM RIGHT: CRACK-WIDTH DISTRIBUTION OF CRACKS IN SHCC. ....	107
FIG. 6.23: CRACKING BEHAVIOR OF BEAM PVA-RR-SI AT A LOAD OF 41kN (OUTSIDE CBMR). TOP LEFT: LOAD-LEVEL ON LOAD-DEFLECTION CURVE. TOP RIGHT: CONTOUR PLOT VON-MISES STRAINS. BOTTOM LEFT: SCATTER PLOT OF ALL CRACKS. BOTTOM RIGHT: CRACK-WIDTH DISTRIBUTION OF CRACKS IN SHCC.....	108
FIG. 6.24: CRACKING BEHAVIOR OF BEAM PVA-RR-SI AT A LOAD OF 70kN (OUTSIDE CBMR). TOP LEFT: LOAD-LEVEL ON LOAD-DEFLECTION CURVE. TOP RIGHT: CONTOUR PLOT VON-MISES STRAINS. BOTTOM LEFT: SCATTER PLOT OF ALL CRACKS. BOTTOM RIGHT: CRACK-WIDTH DISTRIBUTION OF CRACKS IN SHCC.....	108
FIG. 6.25: LOAD - MAX.CW - DEFLECTION CURVE OF BEAM PVA-RR-SI (INCLUDING REGION OUTSIDE CBMR) .....	109
FIG. 6.26: CRACKING BEHAVIOR OF BEAM PE-SR-VPI AT A LOAD OF 52kN (OUTSIDE CBMR). TOP LEFT: LOAD-LEVEL ON LOAD-DEFLECTION CURVE. TOP RIGHT: CONTOUR PLOT VON-MISES STRAINS. BOTTOM LEFT: SCATTER PLOT OF ALL CRACKS. BOTTOM RIGHT: CRACK-WIDTH DISTRIBUTION OF CRACKS IN SHCC.....	109

FIG. 6.27: CRACKING BEHAVIOR OF BEAM PE-SR-VPI AT A LOAD OF 40kN WITH THE INCLUSION OF THE AREAS ADJACENT TO THE CBMR. TOP LEFT: LOAD-LEVEL ON LOAD-DEFLECTION CURVE. TOP RIGHT: CONTOUR PLOT VON-MISES STRAINS. BOTTOM LEFT: SCATTER PLOT OF ALL CRACKS. BOTTOM RIGHT: CRACK-WIDTH DISTRIBUTION OF CRACKS IN SHCC. ....	110
FIG. 6.28: LOAD - MAX.CW - DEFLECTION CURVE OF BEAM PVA-RR-SI (INCLUDING REGION OUTSIDE CBMR) .....	110
FIG. 6.29: DELAMINATION (LEFT) AND SLIP (RIGHT) OF BEAM PVA-RR-SI OUTSIDE CBMR.....	111
FIG. 6.30: DELAMINATION (LEFT) AND SLIP (RIGHT) OF BEAM PVA-RR-VPI OUTSIDE CBMR .....	111
FIG. 6.31: DELAMINATION (LEFT) AND SLIP (RIGHT) OF BEAM PVA-SR-VPI OUTSIDE CBMR .....	112
FIG. 6.32: DELAMINATION (LEFT) AND SLIP (RIGHT) OF BEAM PE-SR-VPI OUTSIDE CBMR.....	112
FIG. 7.1: RELATIVE INFLUENCE OF CERTAIN PARAMETERS ON THE LOAD AT WHICH THE 0.2MM AND 0.3MM CRACK-WIDTH LIMITS ARE EXCEEDED AS A PERCENTAGE OF THE YIELD LOAD IN THE 400MM HYBRID R/SHC BEAMS.....	116

---

# List of Tables

---

TABLE 2.1: MAJOR PHYSICAL PROPERTIES SHCC [10] .....	6
TABLE 2.2: MECHANICAL PROPERTIES OF COMMONLY USED FIBERS IN SHCC [11] .....	6
TABLE 2.3: MATRIX COMPOSITION OF SHCCs AS DESIGNED BY CUROSCU [14] .....	7
TABLE 2.4: : INFLUENCE OF SAND INCLUSION ON PROPERTIES OF SHCC [22] .....	11
TABLE 2.5: MIX COMPOSITION OF SHCC AND CC AS USED BY [49] .....	19
TABLE 2.6: MIX COMPOSITION OF SHCC AND CC AS USED BY [53] .....	26
TABLE 2.7: CONCISE SUMMARY OF LITERATURE STUDY WITH CONCLUDING REMARKS .....	32
TABLE 3.1: CLARIFICATION OF BEAM LABELS.....	36
TABLE 3.2 : PVA-BASED SHCC MIXTURE .....	40
TABLE 3.3: PE-BASED SHCC MIXTURE .....	40
TABLE 3.4: PROPERTIES OF USED FIBERS.....	41
TABLE 3.5: CC MIXTURE .....	41
TABLE 4.1: CONFIGURATIONS EMPLOYED TO CREATE PROFILED INTERFACE .....	42
TABLE 5.1: OVERVIEW BEAM PERFORMANCE OF BEAM PVA-RR-SI .....	57
TABLE 5.2: OVERVIEW BEAM PERFORMANCE OF BEAM PVA-RR-VPI.....	66
TABLE 5.3: OVERVIEW BEAM PERFORMANCE OF BEAM PVA-SR-VPI .....	75
TABLE 5.4: OVERVIEW BEAM PERFORMANCE OF BEAM PE-SR-VPI .....	84
TABLE 5.5: COMPRESSIVE STRENGTH OF CC BATCHES .....	85
TABLE 5.6: COMPRESSIVE STRENGTH OF SHCC .....	86
TABLE 5.7: OVERVIEW OF RESULTS OF TENSILE TESTS .....	91

# PART I

## General Introduction

---

# 1 Introduction

---

## 1.1. Background

In reinforced concrete (RC) structures, crack-width is a critical parameter to consider in Serviceability Limit State (SLS) calculations. Additional reinforcement is typically required to keep crack-widths smaller than a specified limit (e.g. 0.3mm), even though it may not be necessary for the structural safety (Ultimate Limit State, ULS) of the structure. This additional reinforcement, however, contributes significantly<sup>1</sup> to the environmental impact of RC structures, while the need for a more sustainable construction industry is emerging. Advancements in cement-based materials have led to the development of innovative Strain Hardening Cementitious Composites (SHCCs), which offer improved ductility and cracking behavior compared to conventional concrete [4]. This raises the question: can implementing SHCCs in concrete structures enhance crack-width control and potentially reduce the need for additional reinforcement to meet SLS-criteria?

SHCC is a special type of fiber-reinforced mortar-based composite that contains short and randomly distributed micro-fibers, typically comprising around 2% of the composite's volume, which result in superior ductility and crack-width controlling ability. When a microcrack forms, the tensile force is transferred to the fibers. In order for the crack-width to increase, the fibers must either be pulled out or broken, requiring a higher tensile force. Before the fibers are pulled out or broken, a new microcrack forms at another location, leading to increased deformation capacity [1]. This mechanism allows larger cracks to be "smeared out" into smaller cracks, effectively controlling crack-widths. SHCC typically exhibits a strain capacity which is approximately 500 times greater than that of conventional concrete for cracks smaller than 100 microns [5].

Implementing SHCC in the tension zone<sup>2</sup>, the zone prone to cracking, of a RC beam may eliminate the need for additional reinforcement to meet SLS-criteria. The effectiveness of such hybrid systems depends significantly on the interface between the two types of concrete: conventional concrete and SHCC. The implementation of a layer of SHCC in the tension zone of a RC beam already yielded promising results for beams with a height of 200mm and a SHCC-layer of 70mm with reinforcement being embedded in the SHCC-layer [1]. The crack-width control in the tested system was shown to be effective until yielding of the reinforcement. It has also been shown that interface roughness plays an insignificant role in 200mm hybrid beams as both smooth and rough interfaces between concrete and SHCC exhibit similar behavior and are able to effectively control crack-widths beyond reinforcement yielding [2].

## 1.2. Problem statement

The implementation of a 70mm SHCC-layer in beams with more practical heights of 300mm and 400mm has also shown promising results [3]. Similar to the findings with 200mm hybrid beams, the SHCC-layer significantly improved crack-width control compared to control beams without an SHCC-layer in the tension zone. However, as the height of the hybrid R/SHCC beams increased, an

---

<sup>1</sup> It is estimated that steel reinforcement contributes approximately 14-20% to the total environmental impact of a RC structure [6].

<sup>2</sup> Completely replacing concrete with SHCC is not feasible as this leads to a reduced cost-effectiveness, greater environmental impact and distinct shrinkage behavior. This will be elaborated on in [Chapter 2](#).

anticipated<sup>3</sup> reduction in the effectiveness of the 70mm SHCC layer in controlling crack-widths was observed, resulting in the crack-width limit of 0.3mm being exceeded before the reinforcement could yield. This outcome raises curiosity and suggests the need to explore design adjustments to potentially improve the crack-width controlling ability of these hybrid R/SHCC beams. [6] In light of this, the current research will focus on investigating and developing a system capable of limiting crack-widths up to the point of reinforcement yielding in hybrid R/SHCC beams.

### 1.3. Research objective and questions

This study aims to enhance the crack-width controlling ability of hybrid R/SHCC beams for practical applications. To guide this investigation, the following research questions are posed:

- ❖ 'How does the crack-width controlling ability of R/SHCC beams differ upon varying the roughness of the concrete-SHCC interface?'
- ❖ 'How does rebar roughness influence crack-width control in hybrid R/SHCC beams?'
- ❖ 'What is the impact of SHCC based on different fiber types on the crack-width control of hybrid R/SHCC beams?'

To address these questions, the study is organized around three main objectives:

- ❖ Investigate how different interface types effect the ability of the hybrid 400mm beam to control crack-widths. Specifically, the interface will be varied from very smooth to profiled coated with Vaseline<sup>4</sup>.
- ❖ Explore the impact of reducing the bond between the longitudinal reinforcement and the concrete. This will be achieved by utilizing ribbed and smooth rebars<sup>5</sup>.
- ❖ Examine the influence of SHCCs employing different fiber types on the cracking behavior. Specifically, two commonly used fibers in SHCC applications will be considered: Polyvinyl Alcohol (PVA) and Polyethylene (PE)<sup>6</sup>.

### 1.4. Research hypothesis

'The crack-width control in hybrid R/SHCC beams can be improved such that the 0.2mm crack-width limit is not exceeded up until reinforcement yielding by using a roughened concrete-SHCC interface, modifying the steel-SHCC bond, and choosing PE-based SHCC over PVA-based SHCC.'

### 1.5. Methodology

This study is conducted experimentally. The beam design choices are based on a comprehensive literature study. The literature study provides insights into the material SHCC and dives into various hybrid R/SHCC beams. To obtain conclusive results a total of four beams are casted and examined.

The design of the beams follow a particular sequence. The first beam serves as the reference and corresponds to one of the beams studied by Bezemer [3]. In the second beam, the SHCC-CC interface is altered from a smooth to a profiled interface treated with Vaseline. A pre-study is conducted to determine how to accomplish this desired interface. The third beam retains the same interface as

---

<sup>3</sup> The relative contribution of the 70mm SHCC-layer decreases as the height of the hybrid beams increased.

<sup>4,5,6</sup> The reason for selecting these integrations and alterations will become evident following the comprehensive literature review presented in [Chapter 2](#)

<sup>7</sup> A detailed description of each beam will be provided in [Chapter 0](#)

the second but features smooth longitudinal rebars instead of ribbed ones. The final beam has the same configuration as the third but will use PE-fibers in the SHCC instead of PVA-fibers.<sup>7</sup> This approach allows the study to capture the effects of individual parameter alterations and the combined impact of particular changes.

The beams are tested using a four-point bending configuration to create a constant bending moment region (CBMR), allowing for the study of a region with exclusively flexural cracks. Since the bending moment is still of great magnitude next to the CBMR, the cracks occurring next to this region will also be examined<sup>8</sup>. Besides the crack-widths, delamination of the concrete-SHCC interface is studied. This is done as varying the parameters under study may affect the delamination of the interface, thereby potentially compromising the structural integrity of the beams.

The beam dimensions and the material properties of SHCC and the conventional concrete are based on the previous studies, in particular the studies of Huang [1] and Bezemer [3].

Tensile tests are conducted on dogbone-shaped specimens to assess the tensile properties of the SHCCs, while compression tests are performed on cube-shaped specimens to evaluate the compressive strength of both the SHCCs and conventional concrete.

The experimental results are then compared and discussed. Given that the methodology used to determine crack-widths in this study differs slightly from the approach used in Bezemer's [3] study, a re-evaluation of Bezemer's [3] results will be undertaken to ensure a fair comparison. Finally, conclusions are drawn, and recommendations are provided to guide the practical application of R/SHCC beams.

### 1.6. Research scope

This thesis focuses on investigating and reassessing the effects of specific parameters on the crack-width controlling ability of hybrid R/SHCC beams, but it does not aim to optimize these parameters comprehensively. The study does not explore the creation or testing of an ideal rough interface; instead, it utilizes existing research on rough interfaces and selects a promising rough interface that has been shown to enhance crack control. This interface is then applied in a different configuration for further analysis.. Additionally, this research is limited to examining two conventional fiber types in SHCC—Polyvinyl Alcohol (PVA) and Polyethylene (PE)—and relies on previously developed SHCC mix designs that have been demonstrated to be effective in exhibiting strain-hardening properties. The scope is thus constrained to understanding the influence of these selected parameters, rather than exploring a wide range of interface types or SHCC mixtures. This research also does not focus on exploring various ways to alter reinforcement-SHCC bond. This approach ensures that the study remains focused and grounded in established practices, while still providing valuable insights into the specific configurations investigated.

To quantify the improvement in the beams' crack-controlling ability, the loads at which specific crack-width limits are exceeded are reported. In practical applications, various crack-width limits are applied depending on the environmental conditions and the relevant codes. In this study, the two

---

<sup>8</sup> The cracks next to the CBMR are not exclusively the result of a bending moment, since shear forces also act in that region.

strictest limits, the 0.2mm and 0.3mm crack-width limit, specified by the Eurocode [7] will be used, see Fig. 1.1.

Exposure Class	Reinforced members and prestressed members with unbonded tendons	Prestressed members with bonded tendons
	Quasi-permanent load combination	Frequent load combination
X0, XC1	0,4 <sup>1</sup>	0,2
XC2, XC3, XC4	0,3	0,2 <sup>2</sup>
XD1, XD2, XS1, XS2, XS3		Decompression
<b>Note 1:</b> For X0, XC1 exposure classes, crack width has no influence on durability and this limit is set to guarantee acceptable appearance. In the absence of appearance conditions this limit may be relaxed. <b>Note 2:</b> For these exposure classes, in addition, decompression should be checked under the quasi-permanent combination of loads.		

Fig. 1.1: Crack-width limits according to Eurocode [7]

### 1.7 Thesis outline

The structure of this thesis is illustrated in Fig. 1.2 and can be divided into three main parts. The first part begins with an introduction to the thesis background and presents the objective of this research, followed by a literature review. This review initially examines the general properties of SHCC and then explores studies related to hybrid R/SHCC beams.

The second part presents the experimental study conducted for this thesis. It starts by detailing the design of the beams, the testing methodology, and the approach used to assess the beams and material specimens and collect experimental data. The beam and material specimen results are then presented, noting that the tensile material test was conducted in two series. The first series did not produce any (satisfactory) results, prompting a second series using a different method. Following this, the beam test results are analysed and compared, emphasizing the influence of the studied parameters. In the final part of the thesis, conclusions are drawn from the experimental results, the thesis objective is revisited, and recommendations for future research are provided.

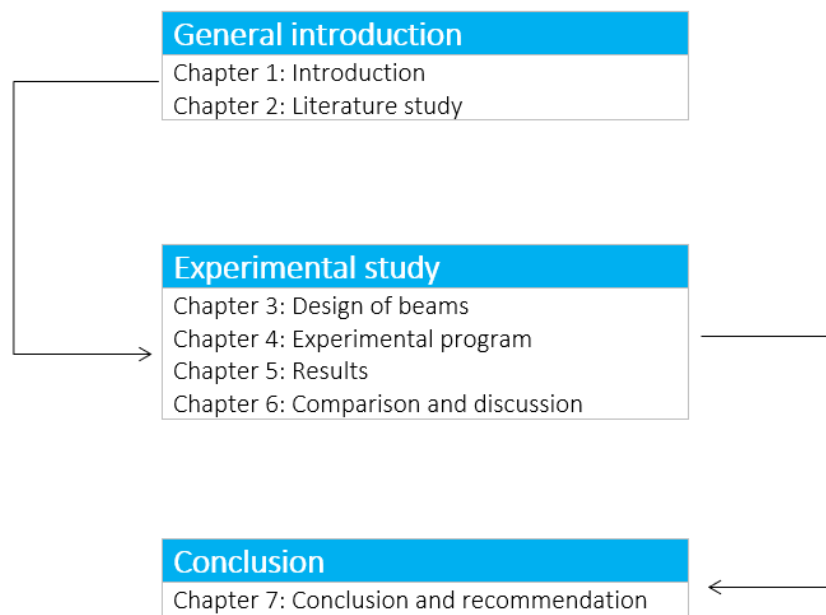


Fig. 1.2: Thesis outline

---

# 2. Literature study

---

## 2.1. Strain Hardening Cementitious Composite (SHCC)

### 2.1.1. Properties

SHCC is an innovative construction material renowned for its exceptional durability and enhanced tensile properties. Comprising a unique blend of cementitious matrices (involving the utilization of fine particles, predominantly fine sand fractions up to 300 $\mu$ m in size, and occasionally incorporating coarse sand fractions up to 3mm in size [5] and microfibers (around 2%)), SHCC exhibits the ability to undergo multiple cracking under tension while effectively maintaining load-carrying capacity.

The ability to undergo multiple cracking under tension, attributed to the fibers integrated in SHCC, enables the SHCC to provide enhanced crack-controlling behavior [4] and results in pseudo-strain hardening behavior. Upon the formation of a microcrack, the tensile force is transferred to the fibers. For the crack to widen, the fibers must either be pulled out or fractured, necessitating a higher tensile force. However, before the fibers reach this point, a new microcrack initiates at another location, inducing increased deformation [1]. This mechanism essentially causes larger cracks to ‘smear out’ into smaller cracks, effectively managing crack-width.

High deformability is a characteristic often associated with SHCC, exhibiting a tensile strain capacity typically ranging from 2-5% [8], significantly surpassing the tensile strain capacity of conventional concrete<sup>9</sup>. A representative stress-strain diagram for SHCC in tension is depicted in Fig. 2.1.

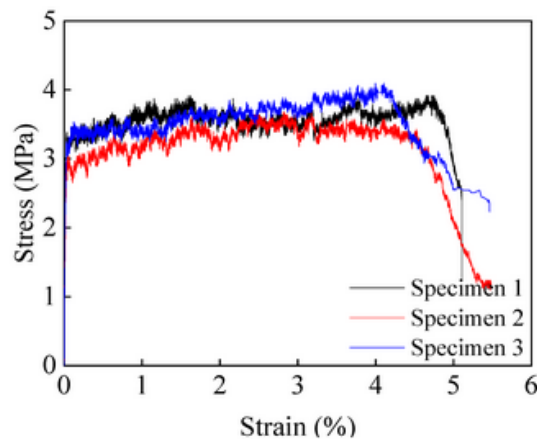


Fig. 2.1: Typical stress-strain curve SHCC [9]

---

<sup>9</sup> Roughly 0,01%

Table 2.1 shows a summary of major physical properties, with a broad range, of SHCC, as reported by [10].

Table 2.1: Major physical properties SHCC [10]

Compressive strength (MPa)	First crack strength (MPa)	Ultimate tensile strength (MPa)	Ultimate tensile strain (%)	Young's Modulus (GPa)	Flexural strength (MPa)	Density (g/cm <sup>3</sup> )
20 – 95	3 – 7	4 – 12	1 – 8	18 – 34	10 – 30	0.95 – 2,3

### 2.1.2. Mix composition

SHCC is typically composed of a binder (which usually is a cement-type), water, fibers and fine aggregates (usually sand or limestone powder). To enhance the SHCC-system superplasticizer is also often incorporated. Several studies have been conducted investigating the influence of the different constituents of SHCC to its properties.

#### Fibers

##### Fiber-type

The crack-bridging characteristic of SHCC is directly attributed to the presence of fibers within the matrix. A number of studies have been carried out to examine the impact of various fiber types on the material properties of SHCC. Several types of fibers have been incorporated into SHCC, each possessing distinct characteristics that contribute to the varied properties exhibited by SHCC [11].

Table 2.2: Mechanical properties of commonly used fibers in SHCC [11]

Type of fiber	Equivalent diameter (mm)	Specific gravity (kg/m <sup>3</sup> )	Tensile strength (MPa)	Young's modulus (GPa)	Ultimate elongation (%)
Polyvinyl alcohol (PVA)	0.027 to 0.66	1300	900 to 1600	23 to 40	7 to 8
Polyethylene (PE)	0.025 to 1.0	960	200 to 300	5.0	3.0
Polypropylene (PP)	0.02 to 0.40	950	550 to 760	3.5	15 to 25
Sisal	0.1 to 0.2	900	286 to 526	19	2.6 to 5.2
Jute	0.1 to 0.2	1030	160 to 440	35 to 48	0.6 to 0.9
Glass	0.005 to 0.15	2500	1000 to 2600	70 to 80	1.5 to 3.5
Steel	0.15 to 1.00	7840	345 to 3000	200	4 to 10

Two frequently employed types of fibers in SHCC are PVA-fibers and (HMW)PE-fibers. PVA-fibers fall under the category of high Young's modulus fibers. They are distinguished by a notably strong bonding affinity with the matrix due to their hydrophilic nature [11]. However, a drawback of PVA fibers is their surface roughness, which induces stress concentrations and harms the matrix during the pull-out process. To mitigate this issue, PVA fibers are coated with oil. This oil coating reduces both the frictional and chemical bonding with the cement paste [3]. Fig. 2.2 indicates the more ductile behavior of SHCC when oiled PVA fibers are used.

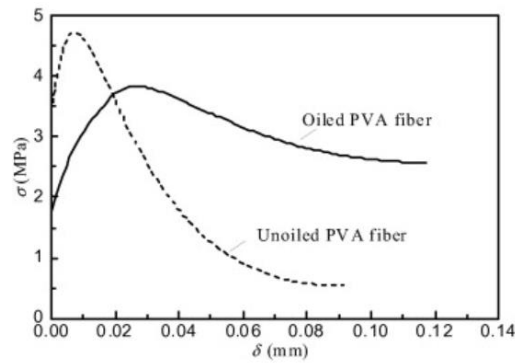


Fig. 2.2: Fiber-bridging stress vs crack opening displacement of oiled and unoiled PVA fiber [12]

On the other hand, (HMW)PE-fibers can elevate the load-bearing capacity of the composite material. Due to their comparatively weak bond with the cement matrix that is caused by their hydrophobic nature, PE fibers require a treatment procedure before incorporation into the composite. Plasma treatment, a surface modification technique that utilizes high-energy electrons, ions, and neutral particles generated by electrochemical discharge or high-frequency electromagnetic oscillation waves to bombard the surface of fibers, is commonly employed for this purpose [13]. This treatment enhances the bonding potential of PE fibers within the composite structure [11].

Curosu [14] investigated the influence of altering the fiber-type (from PVA to PE) in SHCC and the influences of strain-rates (the displacement rate was increased from 0.05mm/s to 20mm/s). The mix composition of the studied SHCC's are shown in Table 2.3<sup>10</sup>.

Table 2.3: Matrix composition of SHCCs as designed by Curoscu [14]

	<b>M1-PVA</b>	<b>M1-PE</b>	<b>M2-PE</b>
	[kg/m <sup>3</sup> ]	[kg/m <sup>3</sup> ]	[kg/m <sup>3</sup> ]
CEM I 42.5R-HS	505	505	-
CEM I 52.5 R-SR3/NA	-	-	1460
fly ash Steament H4	621	621	-
silica fume Elkem 971	-	-	292
quartz sand 0.06 - 0.2 mm	536	534	145
viscosity modifying agent	4.8	4.8	-
water	338	334	315
HRWRA ACE 30 (BASF)	10	25	-
HRWRA Glenium ACE 460 (BASF)	-	-	35
PVA fibers (2.00% by volume)	26	-	-
HDPE fibers (2.06% by volume)	-	20	20

HRWRA - high range water reducing agent (superplasticizer)

It was observed that, with the exception of the highest strain rate, SHCC-PVA exhibited superior properties compared to SHCC-PE for all other strain rates, as illustrated in Fig. 2.3. This discrepancy was attributed to two key factors: (1) SHCC-PE displayed inferior properties in its fresh state, and (2) the hydrophilic nature of PVA fibers facilitated the formation of a chemical bond with the surrounding cementitious matrix.

<sup>10</sup> M2-PE is a high strength SHCC containing PE-fibers and will for the sake of comparison not be reviewed.

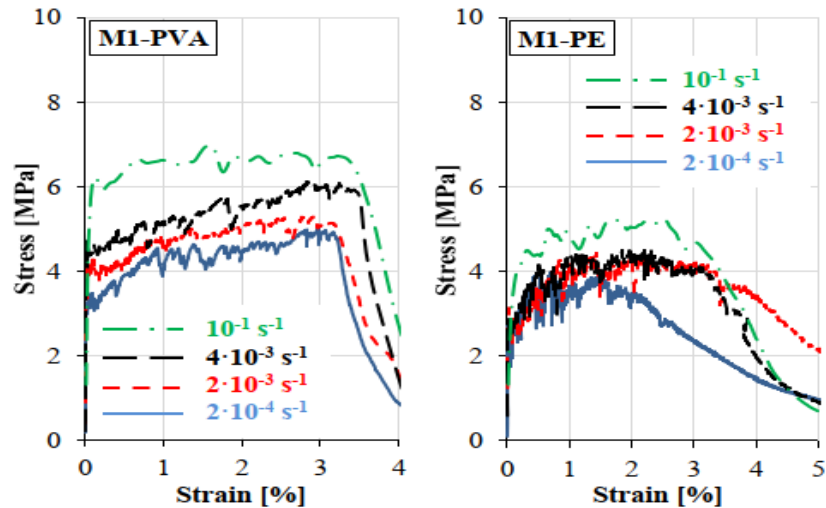


Fig. 2.3: : Stress-strain curve of SHCC-PVA and SHCC-PE [14]

However, in a parallel study conducted by Curosu et al. [15], the loading condition was altered from quasi-static to dynamic. In their findings, SHCC-PVA demonstrated significantly better performance under quasi-static loading conditions, while SHCC-PE exhibited superiority under dynamic loading conditions, aligning with the results obtained for the highest strain rate in the aforementioned study.

Under high strain rates, the robust bond between PVA and the cement matrix experienced a distinctive alteration, resulting in a reduced dynamic composite cracking strength. Conversely, the notably weak frictional bond between PE fibers and the cement matrix displayed better outcomes under high strain rates compared to its behavior under quasi-static loading.

#### *Fiber length and orientation*

The length and orientation of fibers within the SHCC matrix significantly influences its properties. Use of longer fibers improves the tensile strength and strain capacity of SHCC, as longer fibers exhibit better crack bridging effect [16]. This is attributed to the longer embedment length of a longer fiber [17]. However, workability becomes an issue when longer fibers are used [18]. The orientation of fibers is largely determined by the dimensions of the composite. In thinner SHCC members, where the thickness is small relative to the fiber length, fibers tend to orient in a 2D plane due to restricted rotational freedom (Fig. 2.4). Conversely, in elements where all three dimensions exceed the fiber length, fibers are more likely to orient in a 3D pattern [19].

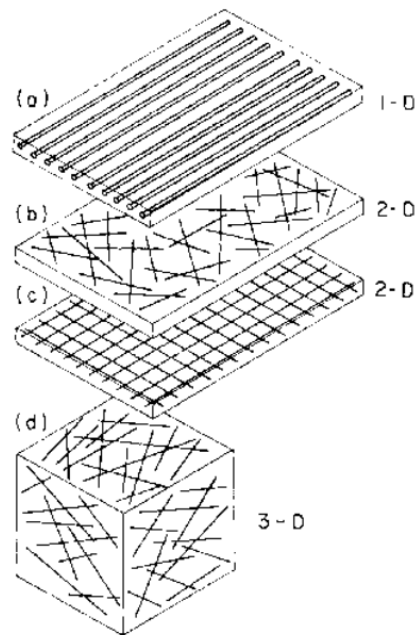


Fig. 2.4: Classification of fiber orientation. (a) 1D, (b) 2D random, (c) 2D organized, (d) 3D [19]

After numerically deriving the bridging relations for a single crack in SHCC specimens of varying thicknesses, Lu et al. [20] simulated an entire component to capture the multiple cracking process across different thicknesses. The study revealed that increasing the thickness from laboratory scale (10 to 15mm) to over 100mm resulted in a strength reduction of nearly 20% and a ductility decrease of almost 50%. A laboratory test on a dogbone specimen with a thickness of 13mm yielded a stress-strain relationship slightly superior to that of the numerically modelled component with a 15mm thickness, indicating the model's accuracy. These findings suggest the need for a reduction factor when predicting the mechanical properties of large SHCC members in real structures based on laboratory data.

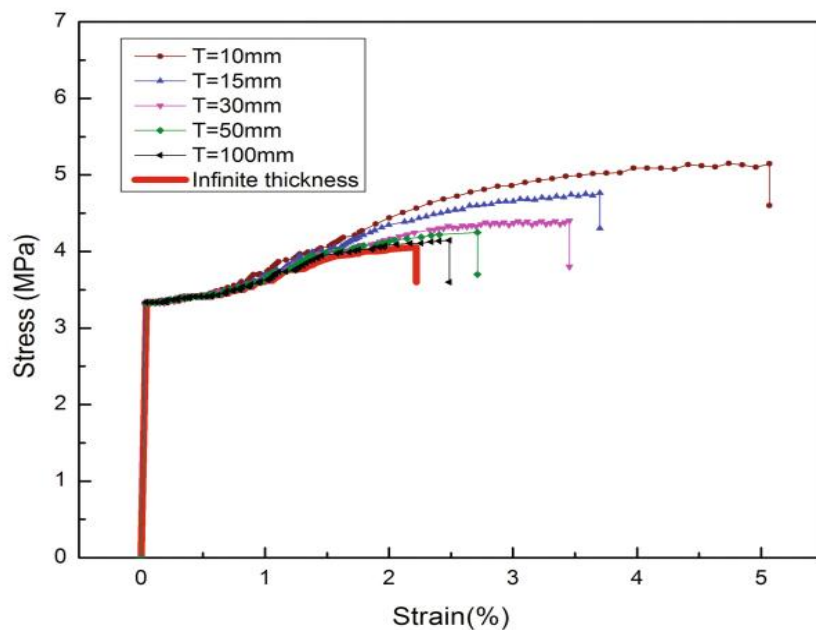


Fig. 2.5: Effect of member thickness on tensile properties of SHCC [20]

### Fine aggregates

The inclusion of fine aggregates is of major influence on the material characteristics of SHCC. In a study by Van Zijl [21], the influence of incorporating sand into the matrix was thoroughly explored. Five distinct mixtures were prepared: the first mixture integrated a sand/cement (s/c) ratio of 0.3, and the four remaining mixtures featured a s/c ratio of 0.5, 0.7, 1.0 and 1.5, respectively. The water/binder ratio was kept constant at 0.4.

The introduction of sand into the mixtures exhibited a significant detrimental effect on two key advantageous properties of SHCC: tensile strength and strain capacity. Transitioning from a s/c ratio of 0,3 to a ratio of 1,0 resulted in a reduction in tensile strength of 30%. Similarly, the strain capacity decreased with 60% upon increasing the s/c ratio from 0,3 to 1,0.

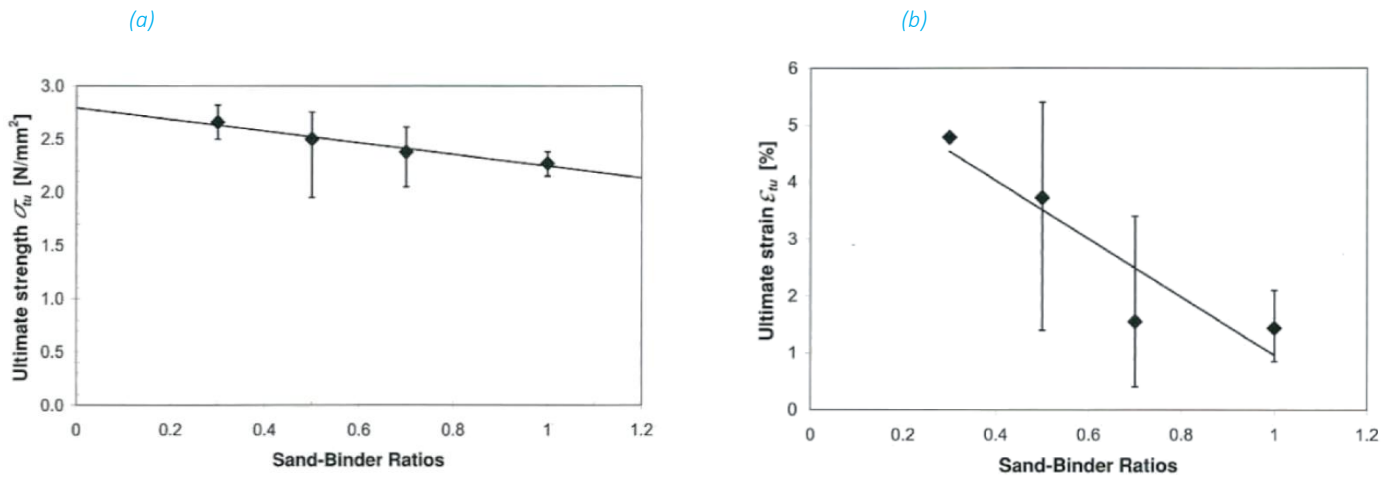


Fig. 2.6: Influence of s/c ratio on tensile strength (a) and strain (b) of SHCC as found by [21]

Conversely, the presence of sand had a positive, anticipated impact on both compressive strength and elastic modulus of the mixtures.

The impact of sand inclusion in the matrix was similarly evident in the research conducted by Li et al. [22]. In the study four distinct mixtures were prepared: the initial mixture featured a sand/cement (s/c) ratio of 0, the second mixture integrated a s/c ratio of 2, and the third and fourth mixtures employed a s/c ratio of 0.5. Among the latter, one mixture - labelled as Mix IIIb - incorporated polyethylene (PE) fibers with plasma-treatment<sup>11</sup>, while the other - labelled as Mix IIIa - utilized PE fibers without such treatment. This way also the influence of plasma-treatment of the PE-fibers was captured. An overview of the observed properties of these mixtures is presented in Table 2.4, aligning with the findings of Van Zijl [21]. Notably, the plasma treatment significantly augmented the properties of the mixture. However, the mixtures also contained different water/cement (w/c) ratio's. Mix I had a w/c ratio of 0.32, mix II had a w/c ratio of 0.45 and mix IIIa and mix IIIb had a w/c ratio of 0.35. Attributing the differences in matrix properties solely to the variation in the s/c ratio is not entirely accurate, as will be demonstrated in the following section.

<sup>11</sup> The reason for the plasma-treatment was elaborated in section 2.1.2

## 2. Literature study

Table 2.4: : Influence of sand inclusion on properties of SHCC [22]

Mix designation	$f'_c$ , Comp. strength (MPa)	$\sigma_{cu}$ , Tensile strength (MPa)	Strain capacity (%)	Deduced interfacial bond strength (MPa)	Average elastic modulus (GPa)
Mix I	65.6	4.7	5.60	0.70	20.3
Mix II	72.2	2.9	0.24	0.43	28.3
Mix IIIa	55.7	3.5	1.70	0.52	26.0
Mix IIIb	55.7 <sup>a</sup>	4.8	3.80	0.72	26.0 <sup>a</sup>

<sup>a</sup> Assumed same as Mix IIIa.

### Water/binder ratio

In the aforementioned study of Li et al. [22], the effect of altering the water content was also studied. It was found that, irrespective of the s/c ratio, a lower w/c ratio of 0,35 yielded superior matrix properties. However this effect diminished at higher s/c ratios, as can be observed in Fig. 2.7. For a s/c ratio of 1.0 a tensile strength increase of 29% and a fracture toughness<sup>12</sup> increase of 73% was observed. As is the case in conventional concrete, a lower w/c ratio will also negatively affect the workability of the mix.

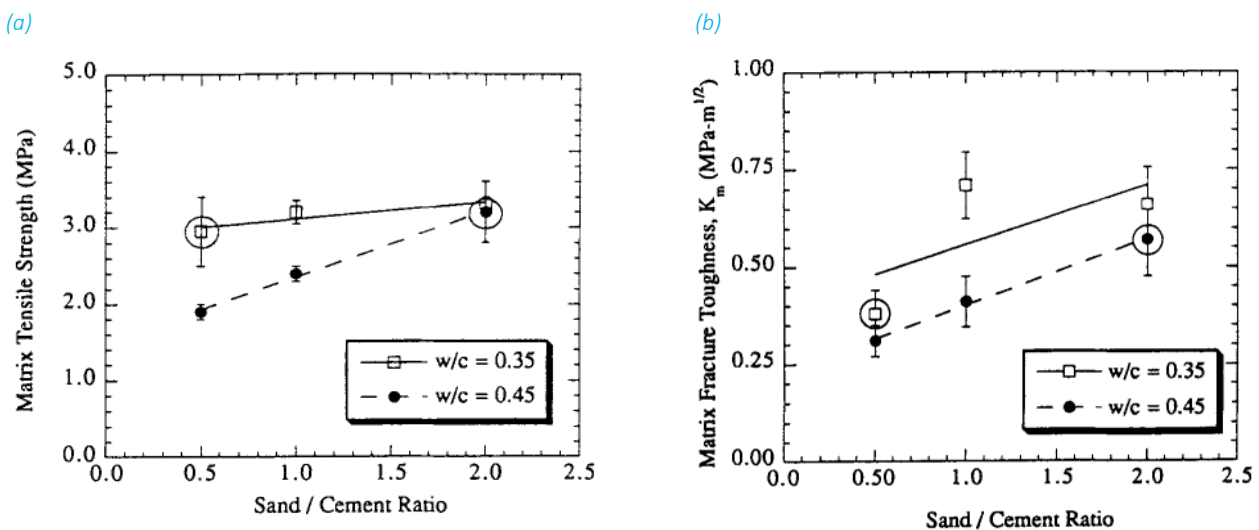


Fig. 2.7: Effect of w/c ratio on properties of SHCC [22]

The graphs also show that increasing the s/c ratio resulted in improved tensile properties, which contradicts the findings discussed earlier. One possible explanation for this discrepancy is the difference in the testing day. In the study by Van Zijl [21], the samples were tested after 14 days, whereas Li et al. [22] tested their samples at 28 days. With a higher s/c ratio, most shrinkage may have occurred by day 14, whereas in mixtures with a lower s/c ratio, shrinkage continues for a longer period. However, this explanation cannot be fully substantiated due to the lack of literature on the effect of sand inclusion on the tensile properties of SHCC at different ages.

<sup>12</sup> Greater fracture toughness is associated with an increased susceptibility to ductile fracture.

### Limestone

For nearly a decade, limestone has been a notable component in cement-based materials, with its advantages being extensively documented. Incorporating limestone into such materials brings about a range of benefits. Notably, these advantages encompass enhanced workability, accelerated cement hydration, improved microstructural characteristics, reduced porosity, and reduced drying shrinkage [23, 24].

Consequently, limestone powder has also found its place within SHCC systems. Numerous researchers have undertaken investigations into the impact of limestone incorporation in SHCC systems.

In a study by Yu & Leung [25], it was observed that substituting a portion of cement with limestone in PE-based SHCC led to enhanced tensile strength compared to a reference mix without limestone. This improvement in tensile strength manifested as an increase of approximately 36%, 55%, 51%, and 3% for limestone-to-cement ratios of 20%, 40%, 60%, and 80%, respectively. Hereby also indicating that after a certain content of limestone no enhancement in tensile behavior can be obtained. Meanwhile, the compressive strength demonstrated notable reduction solely in the mix where 80% of cement was replaced by limestone. In the remaining mixtures, the compressive strength remained relatively unaffected by the substitution.

A comparable pattern was observed by Qian et al. [26] in their investigation involving PVA-based SHCC. The study comprised four mixtures, each containing increasing amounts of limestone powder. As depicted in Fig. 2.8, it was noted that elevating the limestone powder content led to increased levels of tensile strength and ultimate tensile strain capacities. However, akin to the observations in the research by Yu & Leung [25], the enhancement in tensile behavior due to limestone powder reached a point of diminishing returns after a certain limestone powder content. This can be observed by comparing Mix M3 with Mix M4.

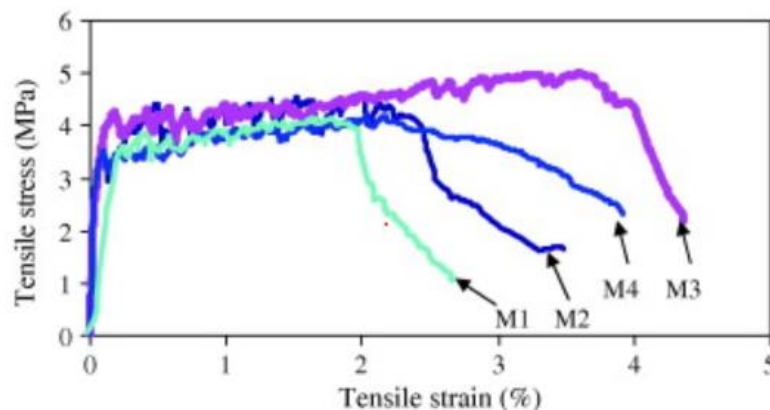


Fig. 2.8: *Effect of limestone incorporation in SHCC on stress-strain relation of SHCC* [26]

The reason behind the enhanced tensile strength in limestone-containing mixtures was linked to an enhanced bond between the fiber and matrix, driven by the porosity refinement effects of limestone. This enhanced fiber-matrix bond was similarly observed by Wang et al. [27], who conducted single fiber pull-out experiments. Refer to Fig. 2.9 for a visual representation of the influence of limestone incorporation on the bond strength between fibers and matrix, as well as on the pull-out energy of the fibers.

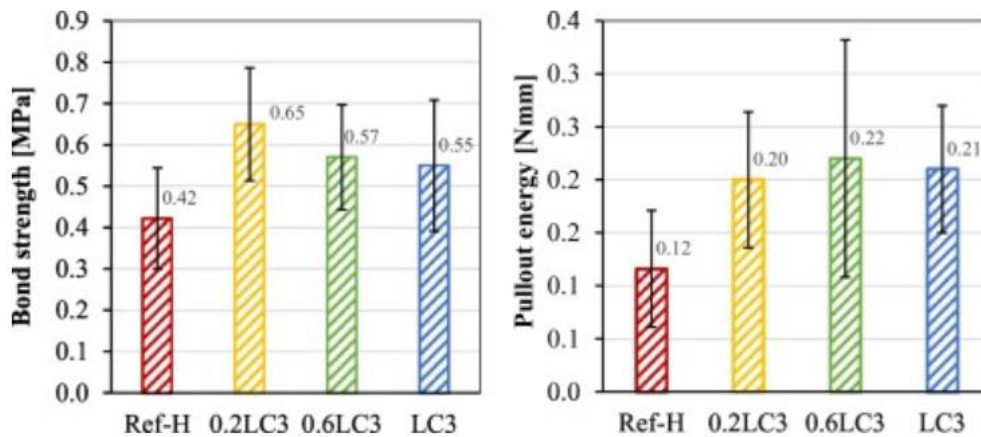


Fig. 2.9: *Effect of incorporation of limestone in SHCC on fiber-matrix bond* [27]

### Silica fume

Silica fume (SF), also known as microsilica, has been utilized in cementitious composites for some time. SF is a byproduct of silicon and ferrosilicon alloy production and plays a crucial role in (ultra-)high performance concrete ((U)HPC). Its ultra-fine particles fill the gaps between larger cement particles, enhancing both durability and strength. Rich in silicon dioxide ( $\text{SiO}_2$ ), SF undergoes a pozzolanic reaction with calcium hydroxide (CH) from cement hydration, forming additional calcium silicate hydrate (CSH), which increases the concrete's strength. Moreover, SF contributes to secondary hydrate production through its reaction with lime and CSH phases from primary hydration [28]. The inclusion of SF in concrete, however, is often risky in the aspect of its application to SHCC, because this additive of silica fume usually increases the brittleness of the cement matrix [29].

Therefore, the inclusion of SF in SHCC becomes particularly interesting. Wu et al. [20] explored the influence of SF on the tensile response and cracking behavior of PVA-SHCC. Their study revealed that increasing the SF content did not significantly influence the ultimate tensile strain of the SHCC. However, it was found that the first cracking stress was significantly affected by increasing the SF content, with a higher SF content yielding a higher first cracking stress. On the downside, an increase in SF also resulted in fewer cracks with larger average crack-widths, which undermines SHCC's ability to control crack-widths effectively.

### Superplasticizer

Superplasticizers are a specialized class of water reducers that can reduce water content by about 30% [30], distinguishing them from normal water reducers. Their key property is the ability to disperse cement particles effectively. In SHCC, which contains a high amount of cement, cement particle agglomeration can impair workability. The use of superplasticizers improves the workability of SHCC without requiring additional water. Additionally, the inclusion of superplasticizers allows for lower water-to-cement ( $w/c$ ) ratios, leading to higher concrete strength [31].

### 2.1.3. Bonding of reinforcement-SHCC

The bond between reinforcement and SHCC plays a crucial role in determining the load-carrying capacity and cracking pattern of SHCC-based structures. This bond strength is influenced by factors such as adhesion, friction, and mechanical interlocking, as elaborated by Tepfers [32]. Among these factors, mechanical interlocking stands as the primary contributor to the rebar-concrete bond in cracked concrete [32]. It heavily relies on the roughness of the rebar surface.

Numerous studies have been conducted to investigate the bond strength of reinforcement to SHCC and compare it with that of reinforcement to conventional concrete (CC). Lee et al. [33] discovered that due to the strain-hardening behavior of SHCC, the bond strength of **ribbed reinforcement** in SHCC increased by 45% compared to the bond strength in CC. This was attributed to SHCC's capability to (1) continuously contribute to load-carrying and (2) provide better confinement to the steel reinforcement, even after the formation of splitting cracks around the reinforcement. In a similar vein, Chen et al. [34] also confirmed the superior bond strength of ribbed reinforcement to SHCC compared to ribbed reinforcement to CC. This effect was again credited to (1) the crack-controlling behavior of SHCC; thanks to its multiple-cracking characteristics, even when splitting cracks appeared, micro-fibers bridged them, thus self-controlling the crack-width and (2) the friction between rebar and SHCC due to confinement of SHCC.

Similar to the studies conducted by Lee et al. [33] and Chen et al. [34], Cai et al. [35] also reported that the bond strength in SHCC is superior to that in CC. In their study, specimens of different sizes were constructed to investigate the influence of bond length, which was varied from 80mm to 220mm. The results, depicted in Fig. 2.10, revealed that for both bond lengths, the bond strength in SHCC was significantly superior to that in CC.

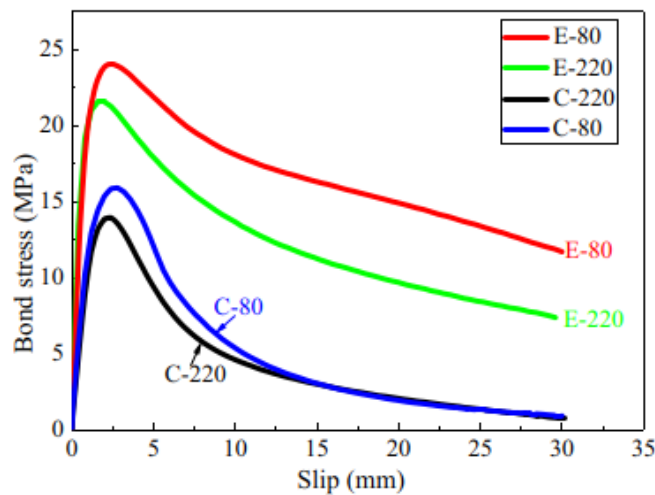


Fig. 2.10: Reinforcement-matrix bond strength of ribbed rebars in SHCC and CC for different bond lengths [35]

Deng et al. [36] conducted direct pull-out tests to investigate the bond strength between **smooth rebars** and SHCC. They reported that the bond strength for smooth steel rebar in SHCC is approximately 1.7 times higher than that in CC, as shown in Fig. 2.11<sup>13</sup>. This enhanced bond strength was attributed to the excellent interaction at the interface between SHCC and the smooth rebar.

<sup>13</sup> CIP12 is the curve for CC and EIP12 is curve for SHCC

In addition to the superior load-carrying and friction properties observed with ribbed rebars in SHCC, a key contributor to the bond force for smooth rebars was identified as *chemical adhesion*. The chemical adhesion between the cement and the smooth rebar was improved in SHCC due to (1) the absence of coarse aggregates and (2) the greater amount of binder in SHCC compared to CC. These factors contributed to the stronger bond between the smooth rebars and SHCC, ultimately leading to the observed higher bond strength in the direct pull-out tests.

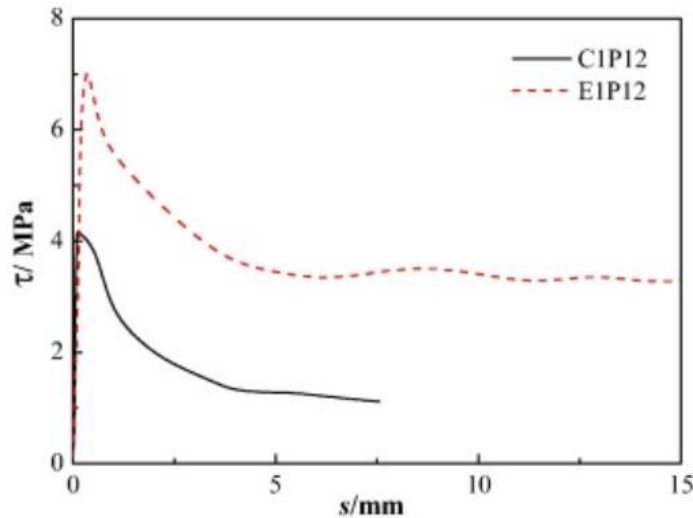


Fig. 2.11: Reinforcement-matrix bond strength for smooth rebars in SHCC and CC [36]

#### 2.1.4. Limitations of SHCC

As detailed in Section 2.1.2, the mix composition of SHCC differs significantly from that of conventional concrete (CC). While this distinctive composition yields several promising and advantageous properties to SHCC, as discussed in earlier sections, it also gives rise to certain drawbacks when compared to CC.

##### Shrinkage

The relatively larger binder content in SHCC and the absence of coarse aggregate, compared to CC, lead to a faster hardening process in SHCC. In the hardening process, water stored in capillary pores react with cement forming hydration products. As these pores deplete, suction occurs, causing them to constrict, ultimately resulting in shrinkage [37].

Furthermore, as cementitious composites are subjected to their environment, the loss of capillary water destined for cement hydration occurs due to a differential in relative humidity between the capillary pores and the external environment. This loss of water to the environment triggers shrinkage, known as drying shrinkage, and constitutes a primary factor contributing significantly to overall material shrinkage.. In conventional concrete (CC), the ultimate drying shrinkage strain typically ranges from  $400 \times 10^{-6}$  to  $600 \times 10^{-6}$  under standard drying conditions of 20 °C and 60% relative humidity. In contrast, SHCC exhibits a significantly higher ultimate drying shrinkage strain, approximately ranging from  $1200 \times 10^{-6}$  to  $1800 \times 10^{-6}$  under comparable drying conditions [38]. This substantial difference in shrinkage deformation increases the likelihood of shrinkage-induced cracking and development of eigen stresses when SHCC is employed in structural applications.

This limitation of SHCC particularly comes to play when SHCC is used in hybrid systems together with concrete, for example as an overlay.

Sustainability

Concrete poses significant environmental challenges, primarily attributable to the production of cement, a key ingredient. The cement manufacturing process is energy-intensive and releases substantial carbon dioxide (CO<sub>2</sub>) emissions, making it a major contributor to the environmental impact of concrete. The chemical transformation of limestone into clinker, the primary component of cement, releases CO<sub>2</sub> both from the combustion of fossil fuels and the breakdown of calcium carbonate. This process accounts for a substantial portion of the overall carbon footprint associated with concrete production. It has been suggested that the annual worldwide production of ordinary Portland cement (OPC) since 2000 has resulted in the emission of over 2.0 billion tons of CO<sub>2</sub>, corresponding with approximately 7% of the total global CO<sub>2</sub> emissions [39].

The environmental impact of SHCC should thus also be accounted for. As elaborated on in previous sections, SHCC has a distinct material composition compared to CC. With a higher proportion of cement, a primary contributor to the environmental impact of CC, SHCC is likely to have a more substantial environmental footprint. Additionally, the fibers, another significant component of SHCC, contribute significantly to its environmental impact. PVA-fibers, the predominantly used fiber-type in SHCC, possess a notable embodied carbon and energy footprint, stemming from its production that heavily relies on non-renewable resources such as natural gas and other fossil fuels [40]. Furthermore, the transportation of PVA fibers, given their non-global production, adds to this environmental impact.

Li [41] evaluated the LCA of for a bridge deck with conventional mechanical expansion joints versus one with SHCC link-slabs. Looking at the energy consumption in the production of each cubic meter of SHCC compared to the CC-system, it derived that the SHCC more than doubles the energy consumption for the CC-joint, as can be seen in Fig. 2.12. It can be seen that this greater energy consumption was a result of the consumption of PVA fibers and the use of superplasticizer.

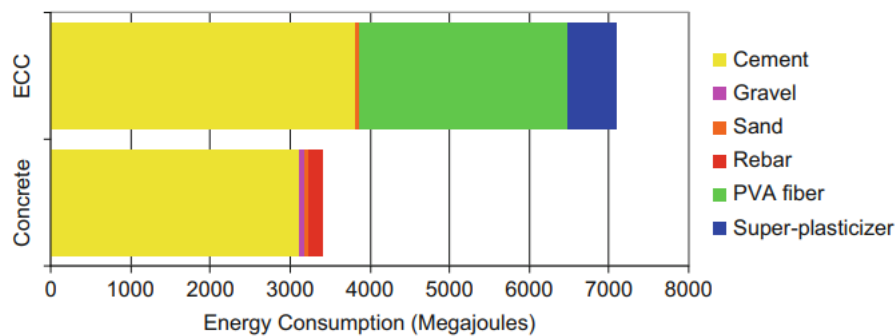


Fig. 2.12: Energy consumption per 1000 kg of steel reinforced concrete and SHCC [41]

However, when holistically reviewing the environmental impact of SHCC, it is essential to consider its durability. Incorporating SHCC into concrete systems could significantly extend the service life of the structure and reduce the need for maintenance, which is one of the most significant contributors to many life cycle impact categories. By minimizing maintenance requirements, SHCC not only enhances the sustainability of the structure but also reduces the total environmental footprint, balancing the initially higher embodied energy and carbon footprint associated with its materials [42].

### Time-dependent effect

To qualify as truly durable, a construction material must maintain consistent mechanical properties over time. To assess the long-term effectiveness of SHCC, Lepech et al. [43] conducted a series of direct tensile tests to evaluate the strain capacity over an extended period. The study observed that the peak strain capacity of approximately 5% was achieved around 10 days after casting (Fig. 2.13). As hydration continued, the strain capacity gradually decreased, reaching about 3% at 180 days. This reduction in strain capacity was attributed to the increased toughness of the matrix over time. However, since the tests were only conducted up to 180 days, there is no data available for longer periods. Based on the trend of the curve it is expected, though, that the reduction in strain capacity would begin to stabilize or flatten out after 180 days.

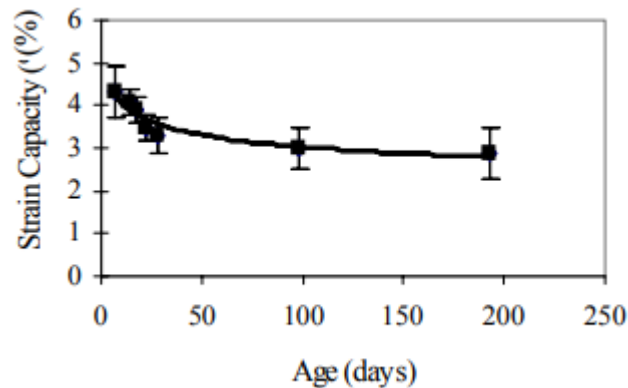


Fig. 2.13: Effect of time on the ductility of PVA-SHCC [43]

The tensile properties of PE-SHCC seem to be more stable over time compared to PVA-SHCC. In a study by Xu [44]<sup>14</sup> the tensile properties of PE-based SHCC were monitored for a period of one year. The tensile capacity after one year was found to have even increased compared to the 28-day tensile capacity. This stability was attributed to the hydrophobic nature of the PE fiber, which prevented the continued hydration process from affecting the frictional and chemical bonding with the cement paste.

### Fire resistance

The thermal exposure resistance of cementitious composites is a crucial property to ensure safety in scenarios such as fire outbreaks. (Ultra-)high performance concretes have shown vulnerability when exposed to elevated temperatures, often exhibiting spalling behavior. However, spalling has been found to be mitigated in SHCCs, particularly in PVA-SHCC, due to the formation of channels left behind after the PVA fibers melt. These channels help release internal steam pressure, reducing the risk of spalling [45]. Despite this advantage, the degradation of strain-hardening properties at high temperatures remains a significant concern, potentially compromising the material's performance under thermal stress.

The melting points of PVA fiber and PE fiber are 273°C and 150°C, respectively, making both PVA-SHCC and PE-SHCC vulnerable to thermal exposure [46]. Chen et al. [47] subjected PVA-SHCC to elevated temperatures up to 800°C. It was found that increasing the temperature from 20°C to 105°C resulted in improved strain-hardening properties (Fig. 2.14), though the elastic modulus was found to decrease. For the specimens subjected to temperatures between 250°C (approximately the melting point of PVA) and 800°C no strain hardening was observed at all; the material exhibited brittle failure immediately after the elastic region, similar to conventional concrete.

---

<sup>14</sup> As reviewed by [46]

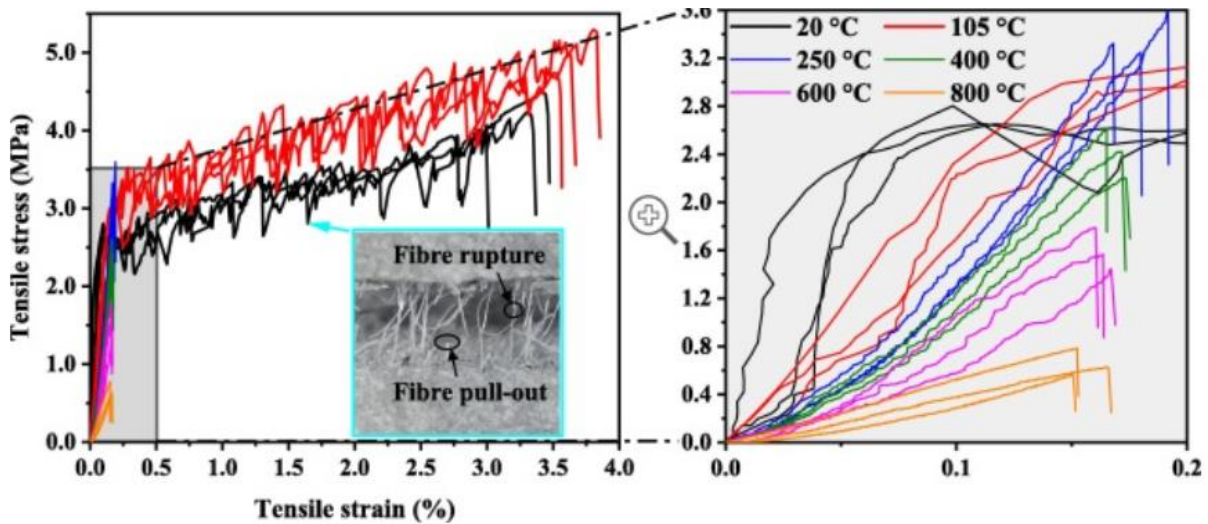


Fig. 2.14: Effect of temperature on tensile properties of PVA-SHCC [47]

Similar trends were also observed in other studies as reviewed by Yu et al. [46]. See Fig. 2.15 for an illustrative summary of the review.

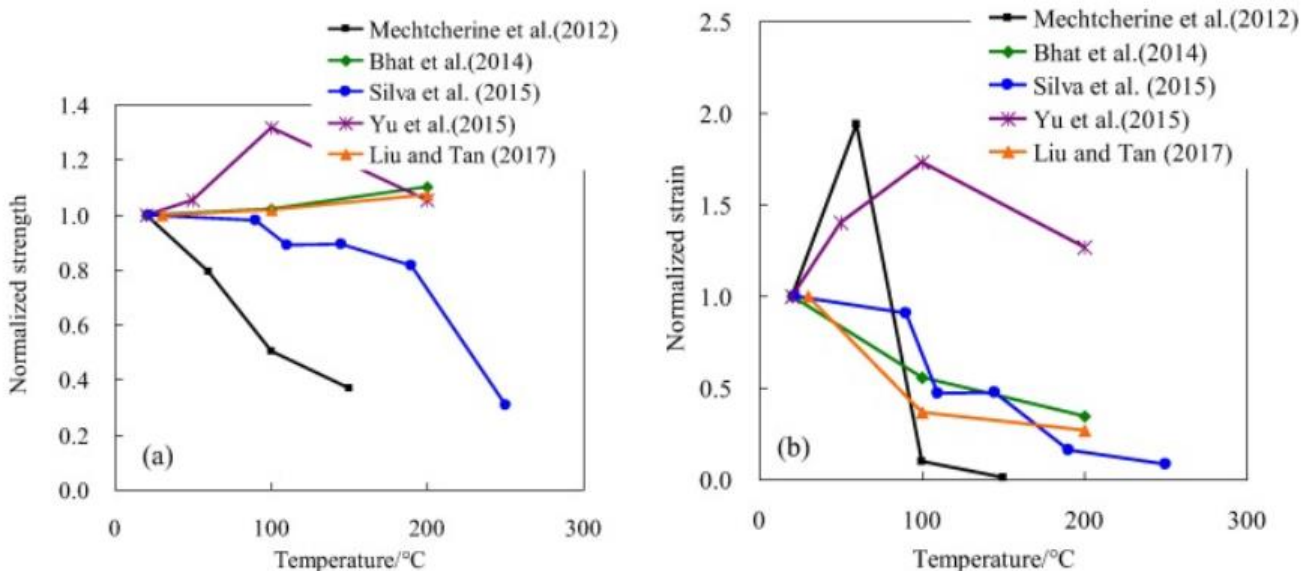


Fig. 2.15: Overview of studies on the effect of temperature on tensile properties of PVA-SHCC [46]

To mitigate the issue Wang et al. [45] partly substituted PVA fibers with carbon fibers, which melt at around 600 °C. However the researchers did not observe the residual tensile properties and only looked at the residual compressive strength (which improved with the substitution of PVA fibers for carbon fibers) and the susceptibility to spalling (which decreased with the substitution of PVA fibers for carbon fibers due to less needle-like channels being formed when fibers melt).

The thermal resistance of PE-SHCC has not been extensively studied, despite the fact that PE fibers have a lower melting point than PVA fibers. Luo et al. [48] investigated the residual behavior of high-strength SHCC made with Ultra-High-Molecular-Weight (UHMW) PE fibers after exposure to temperatures up to 200°C. The study found that at 50°C, the SHCC exhibited improved tensile behavior, at 100°C there was a slight reduction in the tensile properties. However, at 140°C, the tensile properties showed a significant reduction, and at 200°C, the composites displayed brittle behavior, indicating a severe degradation of their performance.

## 2.2. Cracking in hybrid R/SHCC beams

The preceding section has outlined the significant merits and drawbacks associated with SHCC. An ideal approach would involve combining SHCC and conventional concrete (CC) to form a hybrid system, thereby utilizing the beneficial material characteristics of SHCC and complementing each other's limitations. To explore this possibility, certain SHCC-concrete hybrid beams have undergone experimental and numerical testing in previous studies. This section will now present a comprehensive summary of the insights gained from those studies.

### 2.3.1 Hybrid R/SHCC beams vs conventional RC beams

*Khalil et al.* [49] investigated the influence of adding a 40mm ultra-high performance SHCC (UHP-SHCC) layer to a 200mm RC beam. Two groups of beams, consisting of five beams each, were subjected to monotonic and repeated loading respectively. Each group consisted of a control beam, with no UHP-SHCC layer, labelled as BSC/BRC and four beams with a UHP-SHCC layer with different reinforcement ratios incorporated in the UHP-SHCC layer, labelled as BS0/BR0, BS1, BR1, BS2/BR2, BS3/BR3 respectively. The mix composition of the UHP-SHCC and CC as used by Khalil et al. [49] can be seen in Table 2.5. The beam dimensions and experimental setup can be seen in Fig. 2.16.

Table 2.5: Mix composition of SHCC and CC as used by [49]

Ingredient (kg/m <sup>3</sup> )	UHP-SHCC	CC
Water	290	175
Cement (not specified)	1243	350
Silica Fume	223	-
Expansion agent	20	-
Sand	149	630
Coarse aggregate	-	1050
Superplasticizer	15	-
Air reducer	2,98	-
Fiber	19,5	-

The averaged tensile strength, ultimate tensile strain (strain at ultimate load) and the averaged compressive strength of the reinforced UHP-SHCC at the age of 28 days was reported to be 6.5 MPa, 0.45% and 78.8 MPa respectively. The average compressive strength of the used CC was determined to be 29 MPa. The Young's Moduli were not reported.

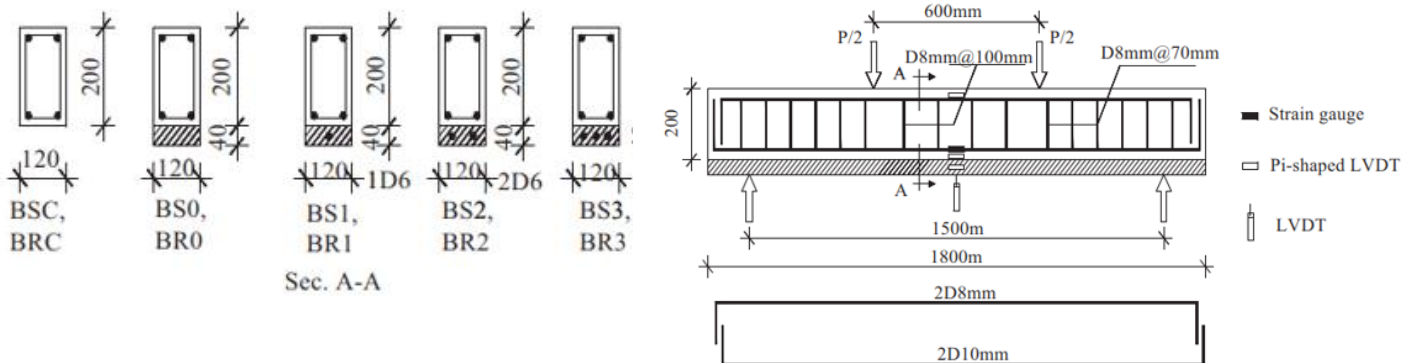


Fig. 2.16: Cross-sections of beams (left) and test setup (right) as used by [49]

## 2. Literature study

For the beams subjected to monotonic loading, both the load-carrying capacity and the cracking pattern, along with crack-widths, were documented. To measure crack-widths, a microscope was used to observe the maximum crack within the middle third of all beams, positioned at 20mm from the beam soffit in the CC.

Fig. 2.17 depicts that the inclusion of the 40mm SHCC layer had a notably positive impact on the capacity and cracking behavior of the beams. However, it is important to note that the capacity improvement can also be attributed to the increased height of the beam. At ultimate load, beams BS2 and BS3, which had reinforcement ratios of 1.2% and 1.8%, respectively, achieved up to a 82% reduction in crack-widths. Comparing the control beam (BSC) to the beam without reinforcement in the UHP-SHCC layer (BS0), it was observed that crack-widths at ultimate load were significantly reduced, reaching up to 70%.

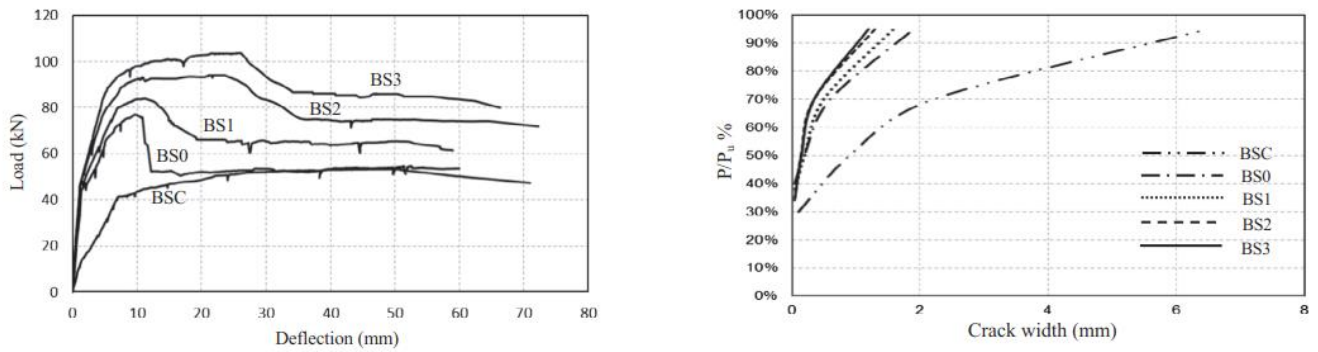


Fig. 2.17: Load-deflection curves (left) and load-crack width curves (right) of beams tested by [49]

Huang [1] conducted a study to investigate the impact of incorporating SHCC layers of 30mm and 70mm within a 200mm R/SHCC hybrid beam. The experimental setup involved two groups, each comprising three beams subjected to a four-point bending test. One beam in each group served as the control, containing no SHCC layer, while the other beams in each group included beams with SHCC layers – one containing self-healing agents – of 30mm and 70mm thickness, respectively.

It is worth noting that the mix composition of the SHCC layer and CC used in Huang's research was identical to the composition that will be utilized in the current study. Fig. 2.18 illustrates the beam dimensions, and Fig. 2.19 depicts the experimental setup employed in the study.

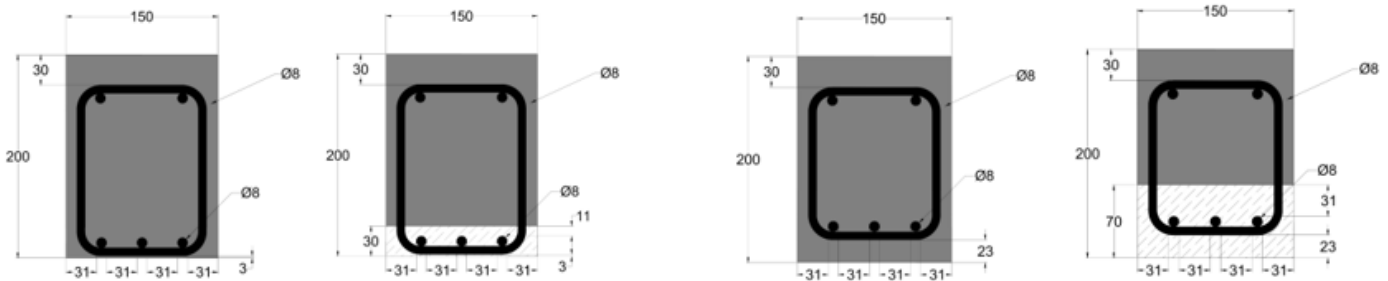


Fig. 2.18: (a) Cross-section of beams of group I [1]

(b) Cross-section of beams of group II [1]

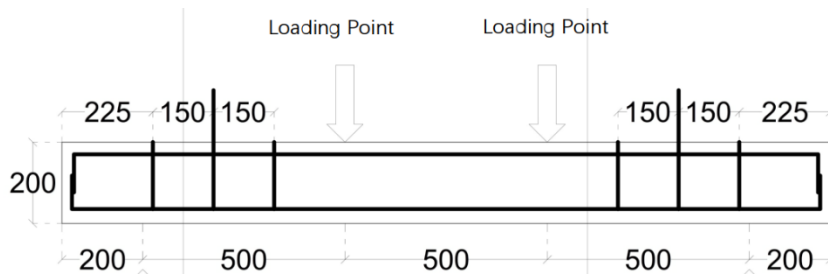


Fig. 2.19: Test set-up as used by [1]

In the study, it was observed that for beams with a 30mm SHCC layer, the maximum crack-width exceeded 0.3mm - crack-width limit as prescribed by Eurocode [50] - at 93% of their load bearing capacities (reaching 66kN and 67kN loads), while the control RC beam reached that crack-width at 95% of its load bearing capacity (at 61kN load), as shown in Fig. 2.20. On the other hand, for beams with a 70mm SHCC layer, the crack-widths exceeded 0.3mm at 92% (66kN) and 83% (62kN) of their load bearing capacities for SHCC and SHCC+SH (self-healing agents) beams, respectively. In contrast, the control beam's maximum crack-width exceeded 0.3mm at 60% of its capacity (35kN), as depicted in Fig. 2.20.

Thus the study revealed that the 70mm thick SHCC layer significantly improved crack-control ability, while the impact of the 30mm thick SHCC layer was minimal. However a non-normative concrete cover depth of 11mm was chosen for the beams with a 30mm SHCC-layer, which might have contributed to the beams' ineffectiveness of improving the crack-controlling behavior. The addition of self-healing agents in SHCC layers did not influence the crack-control ability of the SHCC layer nor the capacity of the SHCC-concrete composite beam.

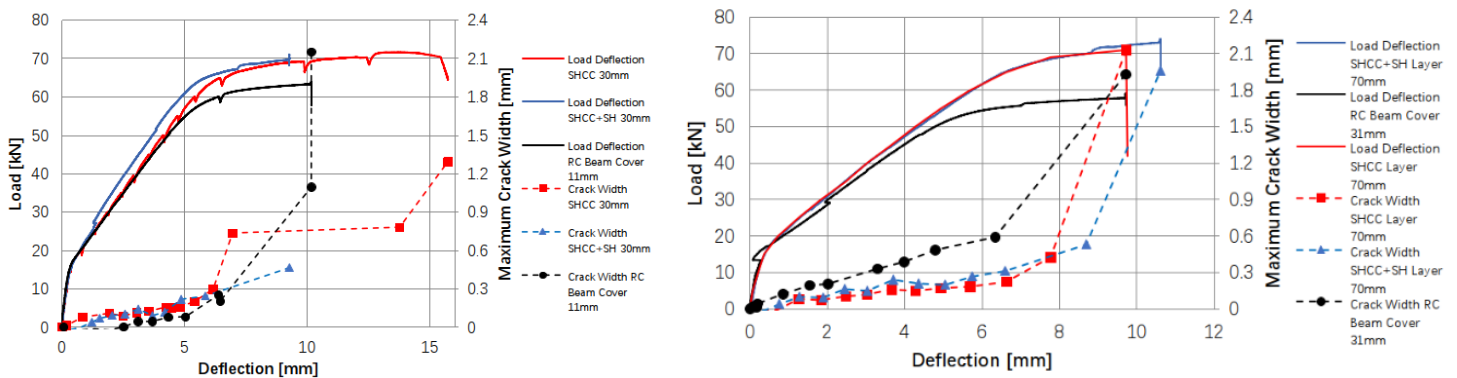


Fig. 2.20: Load deflection-crack width curves for beams of group I (left) and Load deflection-crack width curves for beams of group II (right) [1]

Jayanada [51] performed a numerical analysis on the beams studied by Huang [1] using the FEM-program Atena. The analysis aimed to replicate the experimental results obtained by Huang [1] by altering parameters such as the interface bond, mesh size, and steel-to-SHCC bond. The findings showed that the numerical analyses provided fairly accurate evaluations of the flexural capacity of the beams. However, they consistently underestimated the cracking response, showing a larger number of cracks and smaller crack-widths compared to Huang's [1] experimental results.

In an attempt to improve the accuracy of the cracking response evaluation, Jayanda [51] weakened the interface bond, refined the mesh size, and weakened the steel-to-SHCC bond. Despite these adjustments, no significant advancements in predicting the cracking behavior were achieved. The numerical analyses still fell short in accurately capturing the cracking behavior as observed in the

## 2. Literature study

experimental results by Huang [1], indicating the need for better numerical methods to predict the cracking behaviour of hybrid R/SHCC beams.

*Bezemer* [3] conducted a follow-up study building on the work performed by Huang [1] by investigating R/SHCC beams of more practical heights, incorporating a 70mm SHCC layer. The study considered beams of three different heights: 200mm (similar to Huang's study), 300mm<sup>15</sup>, and 400mm. For each height, two types of beams were studied and subjected to both numerical and experimental testing: a reference beam (a conventional RC beam) and a hybrid beam with a 70mm SHCC layer. The mix composition of the SHCC and the CC were kept identical to that used by Huang [1] and will be used in this study as well. Fig. 2.21 illustrates the cross-sections of the 300mm and 400mm beams and the experimental set-up.

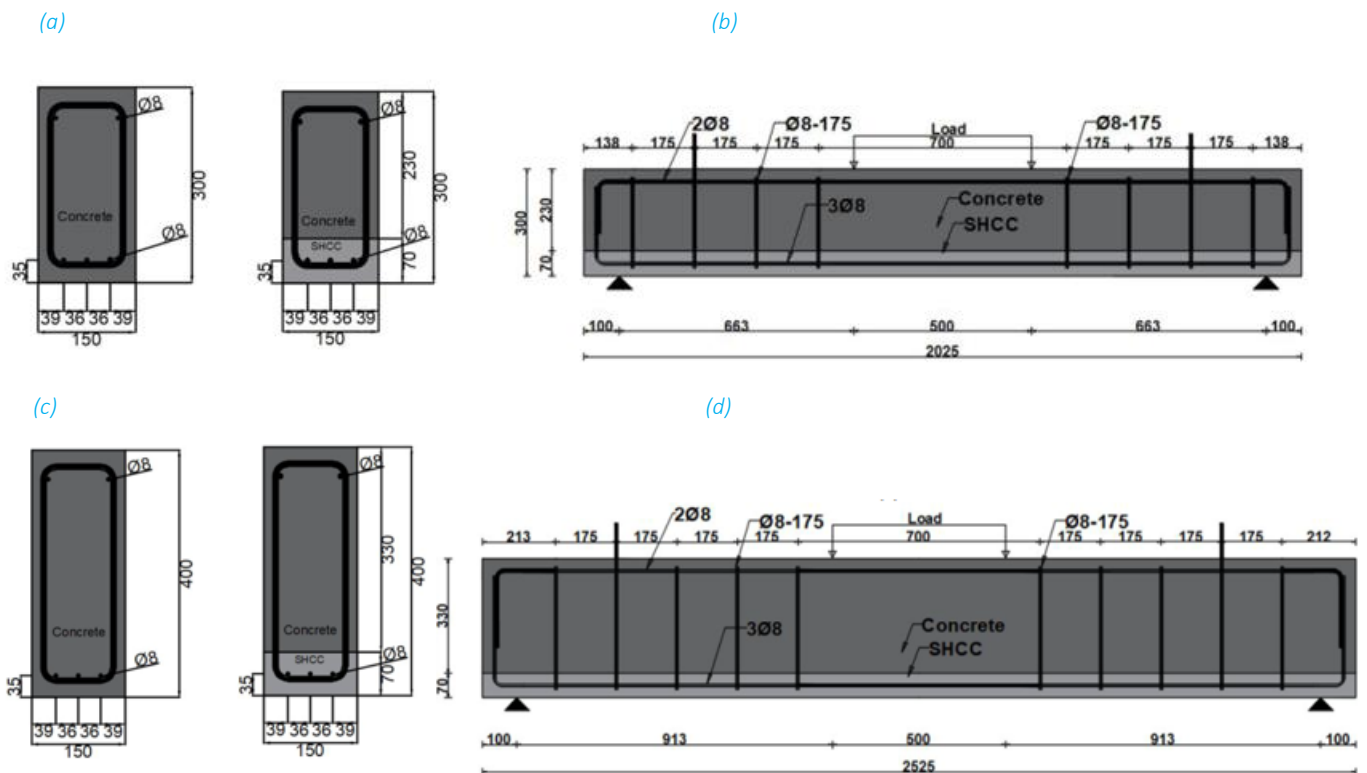


Fig. 2.21: (a) Cross-section of 300mm beams, (b) Test setup of 300mm beams, (c) Cross-section of 400mm beams, (d) Test setup of 400mm beams [3]

For the beams with heights of 300mm and 400mm, the crack-width limit of 0.3mm was reached without the start of reinforcement yielding. Nevertheless, a noteworthy enhancement in the ultimate SLS-load was observed in the hybrid beams when compared to the conventional RC beams.

As shown in Fig. 2.22<sup>16</sup>, the R/SHCC 300mm beam (labelled as H300) reached the 0.3mm crack-width limit at a load of 76.89kN (equivalent to 97.19% of the yielding load), while the control 300mm beam reached this limit at 52.67kN (78.35% of yielding load). This represented a substantial load increase of 24.22kN for the hybrid beam. In the case of the R/SHCC 400mm beam, the load at which the 0.3mm crack-width limit was reached in the hybrid beam was 19.97kN higher (at 69.92kN) compared to the RC400 beam (at 50.14kN), as depicted in Fig. 2.22. The hybrid beam demonstrated a relative

<sup>15</sup> The study also highlighted the influence of the altering the rebar-type from ribbed to Vaseline-covered smooth rebars in the 300mm high beam, but this will be discussed in section 2.3.3.

<sup>16</sup> The H300s beam will be discussed in section 2.3.3

## 2. Literature study

higher load capacity (91% of yielding load) at which the 0.3mm crack-width limit was reached, compared to the RC400 beam (77% of yielding load).

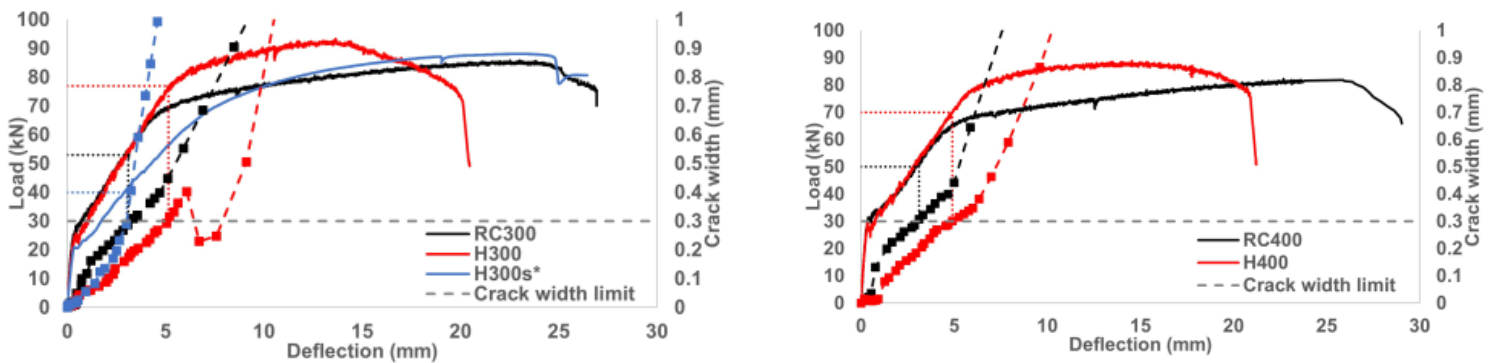


Fig. 2.22: Load-deflection-crack width curves of 300mm beams (left) and Load-deflection-crack width curves of 300mm beams (right)

As mentioned earlier, Bezemer [3] conducted a numerical study using the Delft Lattice Model, and the results demonstrated the model's accuracy in predicting the flexural capacity, deformation capacity, and cracking pattern for the hybrid beams. However, this accuracy diminished when increasing the beam's height. In particular, for the 400mm hybrid beam, the flexural capacity and deformation capacity were significantly overestimated, and an additional crack was observed in the cracking pattern compared to the experimental results of the conventional concrete (CC) beam. Regarding the load at which the 0.3mm crack-width limit was reached, the Delft Lattice Model proved to be quite accurate for all beams. However, for the 200mm hybrid beam, the 0.3mm crack-width limit was reached at a significantly higher deflection than in the experiments. This indicates the need for more optimized numerical methods to predict the crack-width of hybrid beams and the further experimental need for the study of hybrid beams.

To investigate the influence of bond strength at the interface on the numerical output, Bezemer [3] increased the bond strength for the 400mm hybrid beam. It was found that the deformation capacity decreased for the beam with the stronger concrete-SHCC interface. However, with this adjustment, the load at which the 0.3mm crack-width limit was reached and the flexural capacity were still significantly overestimated compared to the experimental results. Interestingly, the cracking pattern for the beam with the stronger concrete-SHCC interface closely resembled the experimental cracking pattern, with four cracks being propagated, unlike the beam with the weaker interface.

### 2.3.2. Influence of SHCC-concrete interface bond

Mustafa et al. [52] conducted research focusing on the influence of the interface<sup>17</sup> bond between the SHCC layer and conventional concrete layer on crack-width control. The mix composition of the SHCC and CC and the cross-section details were kept exactly the same as in the study of Huang [1]. The investigation encompassed both experimental and numerical analyses.

To study the effects of different interface conditions, Mustafa et al. varied the interface between smooth, profiled, partially debonded, and completely debonded interface. The profiled beam was designed to represent the strongest interface, characterized by mechanical interlock, achieved by pressing a grooved sheet into the SHCC-layer. On the other hand, the completely debonded interface represented the opposite extreme, where no composite action occurred between the SHCC and concrete layer. This was realized by using tape to cover the full length of the constant bending moment area.

To represent intermediary behavior, the smooth and partially debonded beams were created. The partially debonded interface was realized by placing 20mm wide strips of tape at 50mm intervals over the length of the constant bending moment area. Detailed images of the interface conditions can be observed in Fig. 2.23.



Fig. 2.23: Photos of interface conditions as realized by [52]

The study revealed that different interface properties had a significant impact on the cracking pattern observed in the beams. For the smooth and profiled interfaces, the load at which the 0.3mm allowable crack-width in SLS was reached showed minimal difference (only 3%), and it was approximately 77-80% higher compared to the control RC beam specimen. Moreover, it was noted that for these interfaces, the crack-width limit of 0.3mm was attained long after the reinforcement had yielded, indicating that the SLS criterion was no longer the governing factor. See Fig. 2.24 for the load-deflection-crack-width response of the four hybrid beams and a bar diagram of the loads at which the 0.3mm crack-width limit was reached. Increasing the surface roughness beyond this point did not lead to better crack-width control, as the crack growth was then controlled by the plasticity of the rebar after yielding.

This observation emphasized two key factors governing crack-width control in R/SHCC hybrid beams: the interface behavior and the yielding of the reinforcement. Prior to yielding, the interface properties play a crucial role in controlling crack-widths. However, once the reinforcement yielded, the plasticity of the rebar took over and governed the crack growth.

For specimens with a partially debonded interface, the load at which the maximum allowable crack-width in SLS was reached was 31.5% lower than that of the smooth interface and 38.5% higher than

<sup>17</sup> The influence of altering the fiber-type was also studied and will be touched upon in section 2.3.4

the control RC beam specimen. In contrast, for specimens with a completely debonded interface, the load at which the maximum allowable crack-width in SLS was reached was 61% lower than the smooth interface and only 13% higher than the control RC beam specimen, see Fig. 2.24.

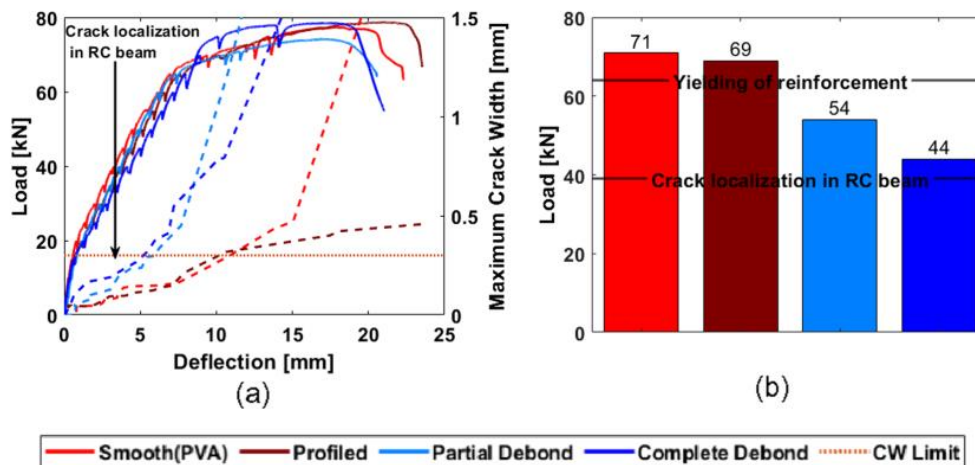


Fig. 2.24: Load-deflection-crack width curves of beams tested by (left) and Bar graph of loads at which all beams tested exceeded 0.3mm crack width (right) [52]

The Delft Lattice Model was employed for the numerical analysis, and with relatively straightforward inputs for the interface, the lattice model demonstrated promise in predicting and providing insights into the fracture behavior of the hybrid systems. It accurately simulated crack development, peak load, crack distribution, and final crack patterns. However, the model failed to properly capture the failure mode. In all simulated beams, maximum crack-widths exceeded 0.3mm only after the ultimate failure of the beam, regardless of the surface preparation. This behavior differed from the experimental observations.

From the numerical analysis, it was observed that failure occurred once the strain capacity of SHCC was reached, after which the SHCC could no longer bear additional tensile loads, leading to beam failure. This contrasted with the experimental observations, indicating a discrepancy in the model's representation of the failure mechanism. The model tended to overestimate the stiffness of the hybrid beams and underestimate the deformation capacity – as a consequence of the model's incapability of considering shrinkage of the SHCC –, consistent with the findings in Bezemer's [3] numerical study for the 200mm high beam.

*He et al.* [53] conducted both experimental and numerical research to investigate the impact of a profiled interface, achieved by creating shear keys, on the cracking behavior of a 200mm high R/SHCC hybrid beam integrated with a 10mm high SHCC-layer. A total of four beams were constructed, which included one conventional reinforced concrete beam and three hybrid R/SHCC beams. The three hybrid beams featured different interfaces: one with a smooth interface, one with a profiled interface, and one with a profiled interface treated with Vaseline. The mix composition of the SHCC and CC used in the study is presented in Table 2.6. The SHCC exhibited an average tensile strain capacity of 3.2% and an average tensile strength of 4.1 MPa. Additionally, the average compressive strengths of SHCC and concrete were 67.5 MPa and 47.5 MPa, respectively. For a visual representation of the studied beams and their interface details, refer to Fig. 2.25, which shows the cross-section details.

## 2. Literature study

Table 2.6: *Mix composition of SHCC and CC as used by [53]*

Ingredient (kg/m <sup>3</sup> )	SHCC	CC
Water	424	156
CEM I 52.5 R	-	260
CEM III/B 42.5 N	1060	-
Limestone powder	530	-
Sand	-	847
Gravel	-	1123
Superplasticizer	2	0,26
PVA fiber	26	-

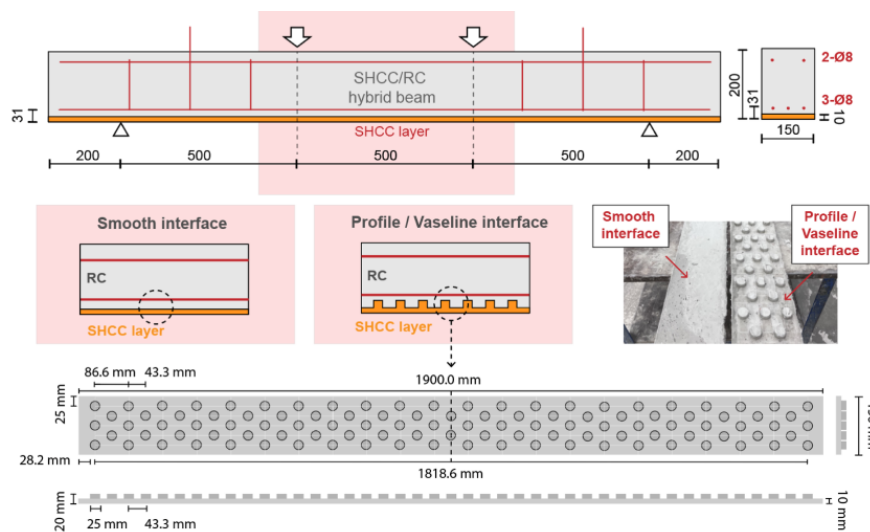


Fig. 2.25: *Detailed overview of test set-up, cross-section of beams and interface details as employed by [53]*

The load carrying capacity of all beams was observed to be quite similar, with only a 3 percent difference in the highest load value. As depicted in Fig. 2.26, the reference beam showed maximum crack-widths exceeding the 0.3mm limit at a load of 32.5kN. In contrast, the hybrid beams with smooth, profiled, and Vaseline-profiled interfaces effectively controlled crack-widths below 0.3mm until loads of 40.6kN, 53.3kN, and 51.0kN, respectively.

Notably, the loads at which a 0.3mm crack-width occurred in the profiled and Vaseline-profiled beams were higher than in the smooth beam. Additionally, the profiled and Vaseline-profiled beams exhibited 0.3mm-wide cracks at significantly larger deflections (6.2mm and 6.3mm, respectively) compared to the smooth beam, which reached the 0.3mm crack-width at only 3.6mm. This deflection value was only slightly higher than that of the reference beam, indicating that the crack-width control ability of the SHCC material was only marginally activated in the smooth beam.

## 2. Literature study

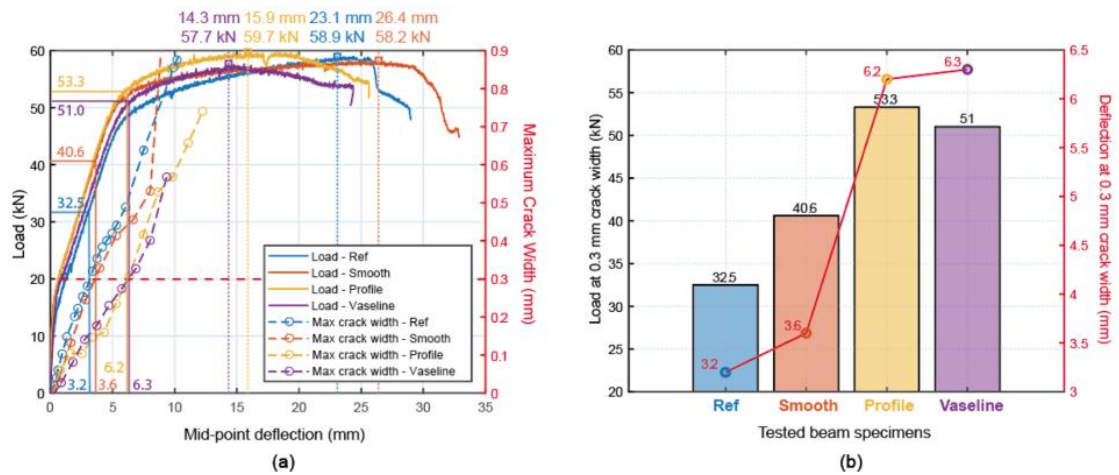


Fig. 2.26: Load-deflection-crack width curves (left) and overview 0.3mm cw-limit load and deformation (right) [53]

Upon comparing the cracking patterns of the different beams, it was evident that the smooth beam exhibited insignificant influence on the cracking behavior of the SHCC-layer. Branching of cracks from concrete to SHCC was observed only to a very limited extent. In contrast, the profiled beams displayed a distinct cracking behavior, with clear evidence of crack branching from the concrete to the SHCC layer. In comparison to the untreated profiled beam, the Vaseline-profiled interface beam showed superior cracking behavior, evident from the number of cracks and the lower crack-widths observed in the Vaseline-profiled beam.

Fig. 2.27 displays the correlation between average crack-width and deflection, as well as the number of cracks and deflection for all beams. The results indicate that the Vaseline-profiled beam demonstrated a maximum crack number approximately 160% higher than the profiled beam and an impressive tenfold increase compared to the smooth and reference beams. Notably, while both the reference and smooth beams stopped generating additional cracks at a deflection of around 3mm, the Vaseline-profiled beam continued to accumulate cracks until it reached its peak number at a deflection of 15mm. This deflection point significantly exceeded the 10-mm-deflection level at which the profiled beam ceased generating further cracks.

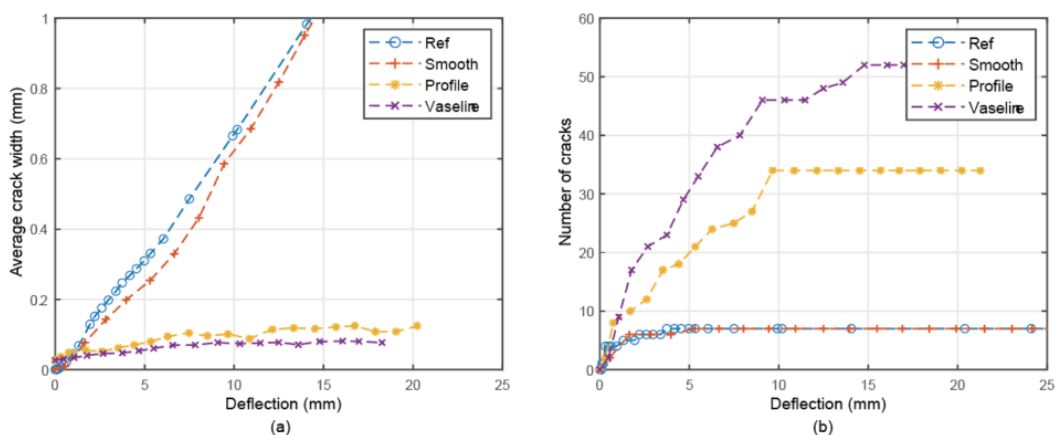


Fig. 2.27: Comparison of (a) average crack widths and (b) number of cracks between all tested beams [53]

Additionally, Fig. 2.27 highlights that the Vaseline-profiled beam exhibited the smallest average crack-width among the four tested beams, a direct consequence of its higher crack density, demonstrating that purposely weakening the interface indeed facilitated more activation of SHCC. In contrary, both the reference and smooth beams displayed an almost linear increase in average crack-widths with increasing deflection. This observation further reinforces the notion that a smooth interface in an SHCC/RC hybrid system is undesirable, as it fails to adequately activate the crack control ability of SHCC.

Similar to the investigations conducted by Bezemer [3] and Mustafa et al. [52], the numerical analysis in this study employed the Delft Lattice Model. Consistent with previous research, the lattice models demonstrated a high level of accuracy in simulating the load-deflection response and cracking behavior of the beams, albeit with a slight overestimation of beam stiffness<sup>18</sup>.

To investigate the influence of Vaseline application, the tensile strength of the interface elements in the profiled-interface beams was systematically varied, ranging from 75% to 10% of the tensile strength of the conventional concrete (CC). As depicted in Fig. 2.28, a decrease in the tensile strength resulted in an enhanced crack-width controlling capacity of the SHCC, in alignment with the experimental findings. Additionally, the reduction in tensile strength led to an increased number of damaged interface elements, indicating the formation of more cracks in the SHCC.

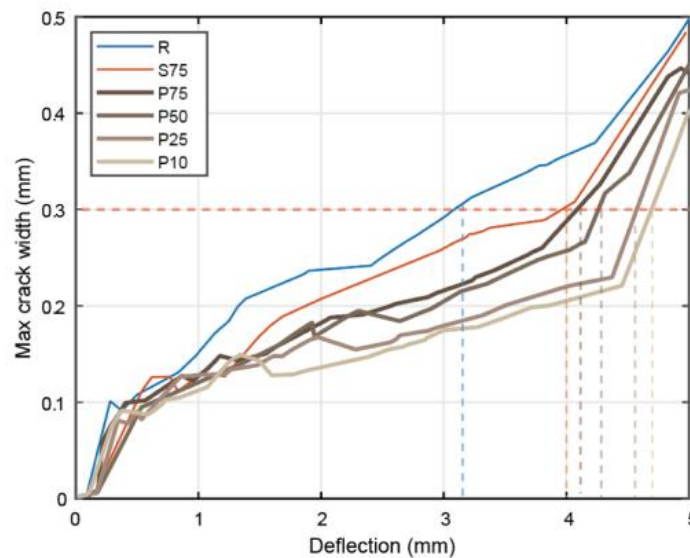


Fig. 2.28: Development of the maximum crack width for all the simulated beams [53]

<sup>18</sup> Which is in line with the studies of Bezemer [3] and Mustafa et al. [52]

### 2.3.3. Influence of reinforcement-SHCC bond

*Bandelt & Billington* [54] conducted a numerical investigation using the FEA-program Diana to examine the impact of bond behavior between steel reinforcement and SHCC. The analysis considered varying the interface from a perfect bond to a bond-slip model, along with adopting three different SHCC tensile strengths: 1.98 MPa, 2.20 MPa, and 2.42 MPa. It should be noted that the analysis did not involve hybrid R/SHCC beams, but beams solely made out of SHCC.

It was observed that the specimens where a bond-slip model was adopted, more cracks were able to form, as is most evident from the 12% deformation<sup>19</sup> contour plot shown in Fig. 2.29 where 3 dominant cracks can be observed for the bond-slip model compared to the 2 dominant cracks observed in the perfect bond model. Strain distribution in the reinforcement for bond-slip models tended to spread over a longer length, while perfect bond models exhibited concentrated strain at a localized section due to the strain compatibility between the reinforcement and SHCC.

Regarding the influence of SHCC tensile strength, it was observed that using higher SHCC tensile strengths resulted in fewer cracks forming and the anteceding of the localization of dominant cracks, as is evident from Fig. 2.29<sup>20</sup>. This occurred because deformation concentrated at specific locations before sufficient stress could accumulate to permit the formation of multiple cracks at other locations.

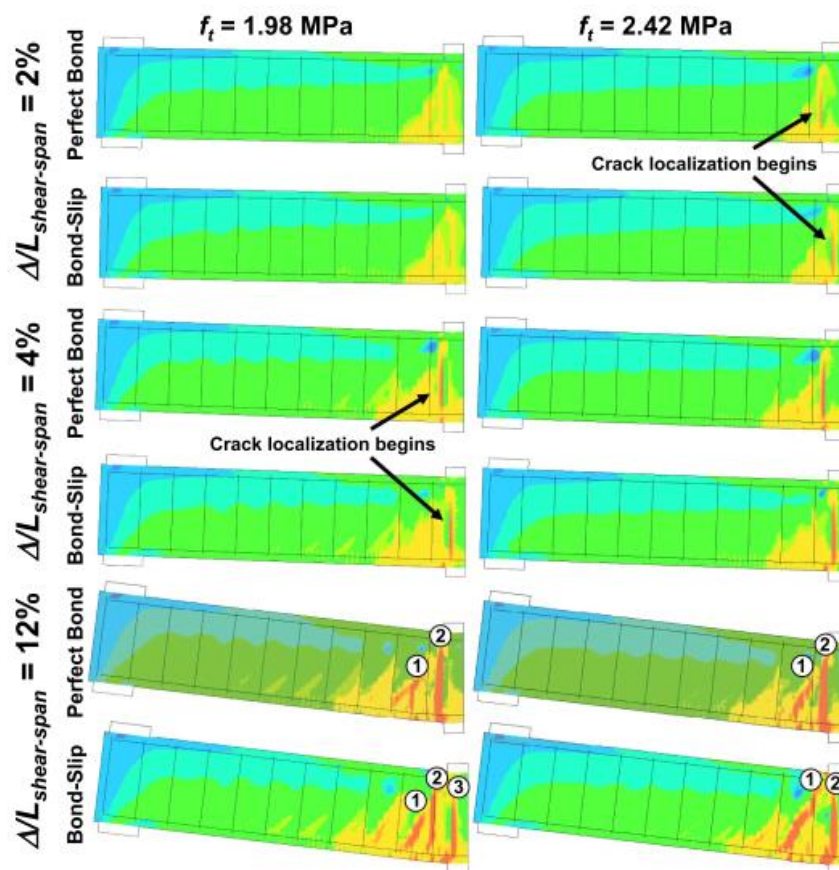


Fig. 2.29: Contours of principal tensile strains at various deformation levels and tensile strengths [54]

<sup>19</sup> The deformation was expressed as a percentage of the midspan-deflection / shear-span length

<sup>20</sup> The crack localization started at a deformation of 2% for  $f_t = 2,42$  MPa en 4% for  $f_t = 1,98$  MPa

In the aforementioned study conducted by *Bezemer* [3], in addition to investigating the influence of height scaling, the effect of weakening the reinforcement-SHCC bond was also examined. This was achieved by replacing the ribbed reinforcement rebars in the 300mm hybrid beam with smooth Vaseline-coated rebars.

Delamination of the rebars occurred, leading to a compromise in the crack-width controlling ability of the hybrid beam. The crack-width controlling ability of the hybrid beam with smooth Vaseline-treated rebars even performed worse than that of the conventional RC beam. This hybrid beam could only propagate a single dominant crack in the CC and a limited number of cracks in the SHCC layer. These observations indicated that excessively weakening the reinforcement-SHCC bond significantly reduced the activation of the SHCC material.

### 2.3.4. Influence of fiber-type

In the aforementioned study by *Mustafa et al.* [52], the investigation also extended to explore the impact of altering the fiber type. Specifically, a comparison was made between the smooth-interface beam with an SHCC-layer containing PVA fibers and another beam with an SHCC-layer containing HMPE fibers. The results, as illustrated in Fig. 2.30, indicated that both beams exhibited similar crack-controlling abilities. In both cases, the maximum cracks at the SHCC surface reached the 0.3mm limit after yielding of the reinforcement. Despite the higher ductility of the SHCC with HMPE fibers, it did not further enhance the cracking response of the beam, as crack-widths after reinforcement-yielding were influenced primarily by the plasticity of the reinforcement<sup>21</sup>.

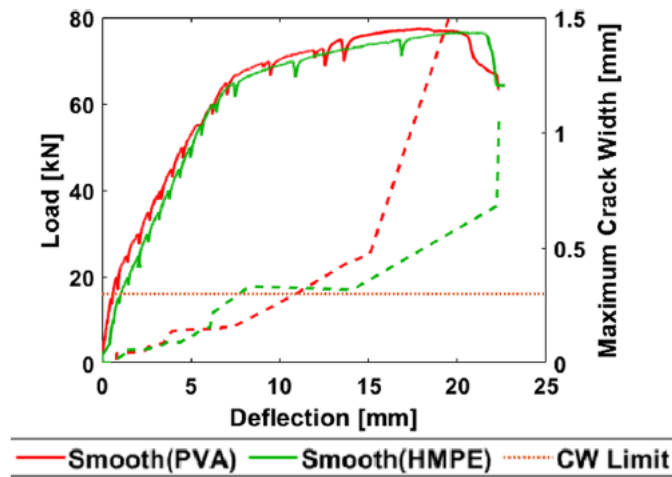


Fig. 2.30: Load-deflection-crack width response of hybrid beams with varying fiber types [52]

Nevertheless, upon comparing the cracking patterns, a notable distinction emerged. In the beam with an SHCC-layer containing HMPE fibers, the cracks tended to converge towards the localized cracks in the concrete, while in the beam with an SHCC-layer containing PVA fibers, the cracks in the SHCC-layer remained relatively straight, as illustrated in Fig. 2.31. Additionally, the beam with PVA fibers exhibited more evident debonding of the interface. These observations collectively suggested that using HMPE fibers enhances the bond at the interface, leading to a stronger interface connection.

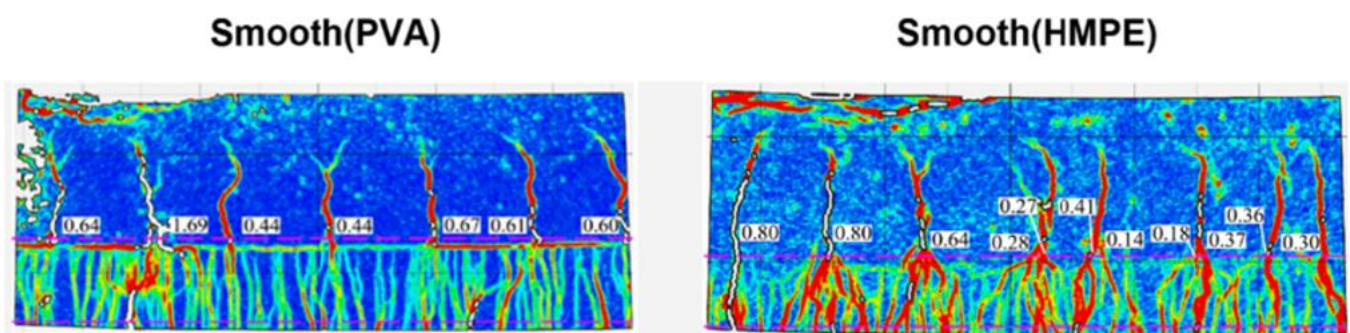


Fig. 2.31: Cracking pattern at ultimate load of hybrid beams with varying fiber types [52]

<sup>21</sup> Covered in [section 2.3.2](#)

### 2.3. Concluding remarks

The conclusions from the literature review are summarised in [Table 2.7](#).

Table 2.7: Concise summary of literature study with concluding remarks

		Conclusion
<b>SHCC</b>	<b>Mechanical properties</b>	SHCC exhibits the ability to undergo multiple cracking under tension, a characteristic attributed to the inclusion of fibers within the matrix. This unique behavior enables SHCC to display pseudo strain-hardening properties. As a result, SHCC can achieve tensile strain capacities ranging from 2-5%, significantly higher than that of CC (0.01%).
	<b>Mix composition</b>	<p>The two most commonly used fiber types in SHCCs are PVA fibers and PE fibers. PVA-SHCC demonstrates superior tensile properties under quasi-static loading conditions, while PE-SHCC tends to perform slightly better under dynamic loading conditions. Longer fibers are more effective in bridging cracks, enhancing the crack control capability of SHCC. However, the thickness of an SHCC member significantly impacts its tensile properties; as thickness increases, the fibers tend to orient in a 3D manner, which typically results in poorer tensile performance.</p> <p>The effect of the inclusion of fine aggregates on the tensile properties of SHCC is unsure. It seems at early age the inclusion of sand has a negative effect, whereas on longer term, the inclusion of sand may yield a benefit. The inclusion of limestone can enhance the matrix properties, although adding limestone at high volume fractions can ultimately lead to a decline in these properties.</p> <p>Adding silica fume to SHCC has no significant effect on its ductility, but it can negatively impact the first cracking stress, making the material less effective in resisting initial crack formation. Similar to CC, the addition of superplasticizers to SHCC improves its workability.</p>
	<b>Bonding of reinforcement-SHCC</b>	The bond between reinforcement and concrete is significantly stronger in SHCC than in CC, regardless of whether ribbed or smooth rebars are used. This might be attributed to the absence of aggregates in SHCC and confinement stemming from bridging splitting cracks.
	<b>Limitations of SHCC</b>	<p>SHCC exhibits more noticeable shrinkage compared to conventional concrete (CC). It is unsure what this implies for long-term structural behavior and creep behavior.</p> <p>SHCC involves higher initial energy consumption than CC, however it offers a longer lifespan and requires less maintenance.</p> <p>The long-term properties of SHCC are not yet fully understood. After one year, the tensile properties of PVA-SHCC tend to decrease, while PE-SHCC demonstrates more stable tensile properties over time.</p> <p>When exposed to high temperatures, the fibers in SHCC melt, which compromises its mechanical properties.</p>

Hybrid R/SHCC beams	Effect of implementing a SHCC-layer in tension zone	<p>Implementing an SHCC layer in the tension zone of beams of various heights significantly improved their crack-controlling behavior compared to control RC beams. For 200mm beams, the 0.3mm crack-width limit was not exceeded until after the rebars had yielded. However, in beams of more practical heights (300mm and 400mm), the effectiveness of a 70mm SHCC layer in controlling cracks was reduced, as anticipated.</p> <p>Therefore, it is of interest to study the effect of different parameters to enhance the crack-controlling ability of hybrid beams of more practical height.</p>
	Effect of SHCC-CC interface bond	<p>In a 200mm hybrid beam with a 70mm SHCC-layer, both partial and complete debonding of the CC-SHCC interface within the CBMR compromised the crack-controlling ability of the SHCC-layer. When comparing two beams—one with a smooth interface and the other with a profiled (grooved) interface—no significant difference was observed. Both beams exceeded the 0.3mm cw-limit after the reinforcement had yielded. Since crack control after yielding is primarily governed by the plasticity of the rebars, it was not possible to draw a definitive conclusion regarding the effectiveness of the different interface types in this scenario.</p> <p>However, in a 200mm hybrid beam with a 10mm SHCC-layer, using a profiled interface with shear keys treated with Vaseline over the full length of the beam showed better crack control compared to a smooth or untreated profiled interface. Since the thickness of the SHCC-layer was only 10mm the 3D effect (caused by fiber orientation) was less evident.</p> <p>Thus, it is of interest to investigate the effect of a profiled interface with shear keys treated with Vaseline specifically in the CBMR of a beam with a more practical height (and a higher SHCC-layer).</p>
	Influence of reinforcement-SHCC bond	<p>Weakening the reinforcement-SHCC bond in a numerical simulation of a beam made entirely of SHCC resulted in more cracks. Similarly, in a 300mm hybrid beam with a 70mm SHCC-layer, weakening the reinforcement-SHCC bond by applying Vaseline to smooth rebars undermined the beam's crack-controlling ability.</p> <p>Thus, it is of interest to study the effect of using smooth rebars without Vaseline on the crack-controlling ability of hybrid beams.</p>
	Influence of fiber-type	<p>No difference was observed in the crack-controlling ability of a 200mm beam containing a 70mm SHCC-layer with either PVA fibers or HMPE fibers. Both beams reached the 0.3mm crack-width limit after the reinforcement had yielded. Since the crack control was governed by the plasticity of the rebars post-yielding, no conclusive statement could be made about the potential differences between the two fiber types.</p> <p>Therefore, it is of interest to study the effect of fiber type in beams of more practical height to better understand their impact on crack-width control.</p>

# PART II

Experimental  
study

---

# 3. Design of beams

---

Four hybrid R/SHCC beams will be experimentally tested to achieve the research objective. One of the beams, will be in correspondence with the 400mm beam studied by Bezemer [3]. The material properties of the concrete and SHCC (with exception for the beam that will involve a SHCC-layer with PE fibers; SHCC-mixture was obtained from [55]), the beam dimensions and the reinforcement layout will all follow the 400mm hybrid beam studied by Bezemer [3]. An overview of the beam dimensions and layout is presented in [Section 3.2](#). [Section 3.3](#) provides the material properties of the SHCC mixtures and CC mixtures used.

## 3.1 Motivation for design of beams

To study the individual and combined effects of three key parameters—interface type, rebar-SHCC bond, and fiber type—a sequential approach is employed in altering these parameters.

First, the interface type is modified from a *very smooth*<sup>22</sup> surface to a rough, profiled interface treated with Vaseline. This specific interface configuration is selected based on its promising results in He's study [49] as discussed in [Section 2.3.2](#). Given the need to directly compare with the 400mm hybrid beam from Bezemer's study [4] and the focus on inspecting only flexural cracks, the interface alteration is limited to just beyond the constant bending moment region (CBMR). The presence of stirrups prevents the application of a silicone mold to create a profiled interface along the full length of the beam.

Next, a combination of the altered interface type and a weakened rebar-SHCC bond is studied by using smooth rebars. This is done because the literature review revealed that weakening the rebar-SHCC bond may enhance the cracking behavior of hybrid beams (see [Section 2.3.3](#)). This allows the direct study of the influence of weakening the rebar-SHCC bond on the cracking behavior, using the previous beam with a roughened interface as a reference. In this way, both the individual impact of the weakened bond and its combined effect with the roughened interface can be evaluated.

Finally, the fiber type is changed from PVA to PE. This alteration allows for the investigation of the individual effect of the fiber type on the cracking behavior, as well as the combined effect when the roughened interface, weakened rebar-SHCC bond, and altered fiber type are all present. This final design choice is based on the assumption that the influence of fiber type on cracking behavior remains consistent regardless of rebar type, given that the rebar-SHCC bond is weaker with smooth rebars compared to ribbed rebars, irrespective of the fiber type.

---

<sup>22</sup> An interface or surface is regarded as very smooth when casted against a steel, plastic or specially prepared wooden mold [50].

### 3.2 Overview beam dimensions and lay-out

Since three key parameters will be varied among the beams, the beams will be labelled in accordance to these parameters. The first part of each label refers to the fiber-type. The second part refers to the rebar-type. The last part refers to the interface-type. [Table 3.1](#) clarifies the labels of the beams.

Table 3.1: Clarification of beam labels

Parameter	Fiber type	Rebar type	Interface Type
Variation	PVA fibers or PE fibers	Rough Rebars or Smooth Rebars	Smooth Interface or Vaseline Profiled Interface
Label	PVA / PE	RR / SR	SI / VPI

#### 3.2.1 Beam PVA-RR-SI

Beam PVA-RR-SI will be a 400mm high hybrid R/SHCC beam with a 70mm thick SHCC layer, with a very smooth interface, rough longitudinal rebars and the SHCC-layer composed of PVA-fibers,. This will be the reference beam. This beam corresponds with one of the beams studied by Bezemer [3]. See [Fig. 3.1](#) and [Fig. 3.2](#) for a schematic sideview and the cross-section of beam PVA-RR-SI.

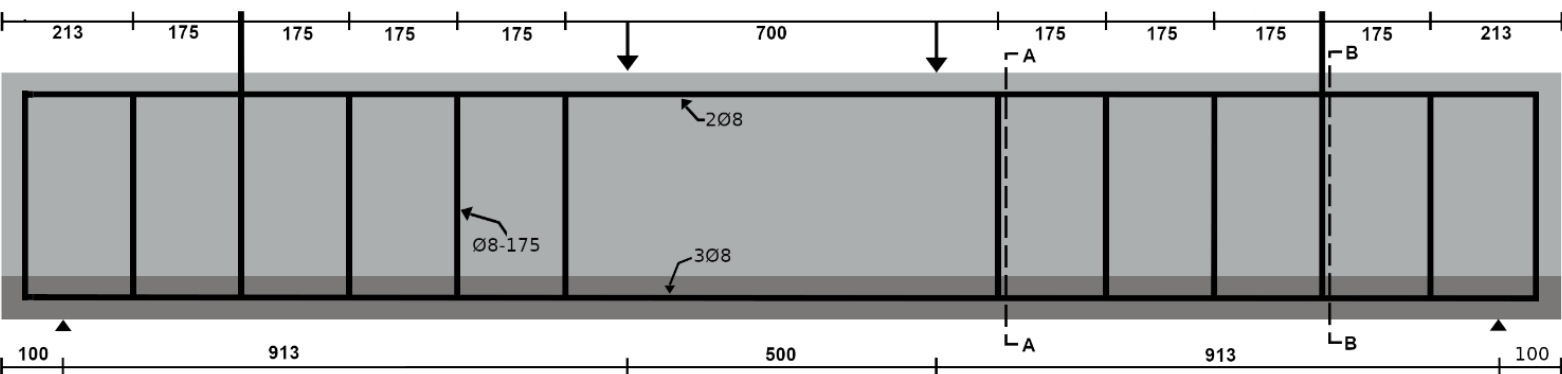


Fig. 3.1: Side view of beam PVA-RR-SI

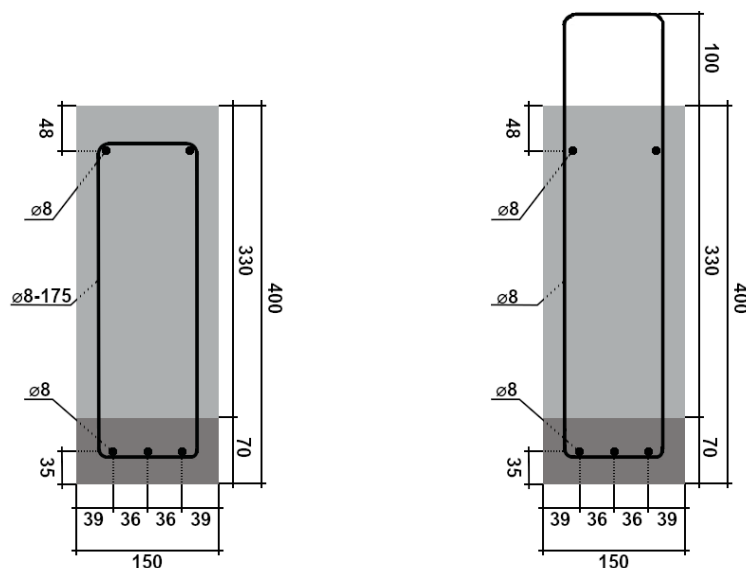


Fig. 3.2: Cross-sectional view of beam PVA-RR-SI with (left) Section AA and (right) Section BB

### 3.2.2 Beam PVA-RR-VPI

Beam PVA-RR-VPI will be a 400mm high hybrid R/SHCC beam with a 70mm thick SHCC layer, with a profiled interface treated with Vaseline (illustrated in yellow), rough longitudinal rebars and the SHCC-layer composed of PVA-fibers. This way the influence of the interface-type can be studied. See Fig. 3.3 and Fig. 3.4 for a schematic sideview and the cross-section of beam PVA-RR-VPI. A schematic top view of the SHCC layer can be found in Annex A.

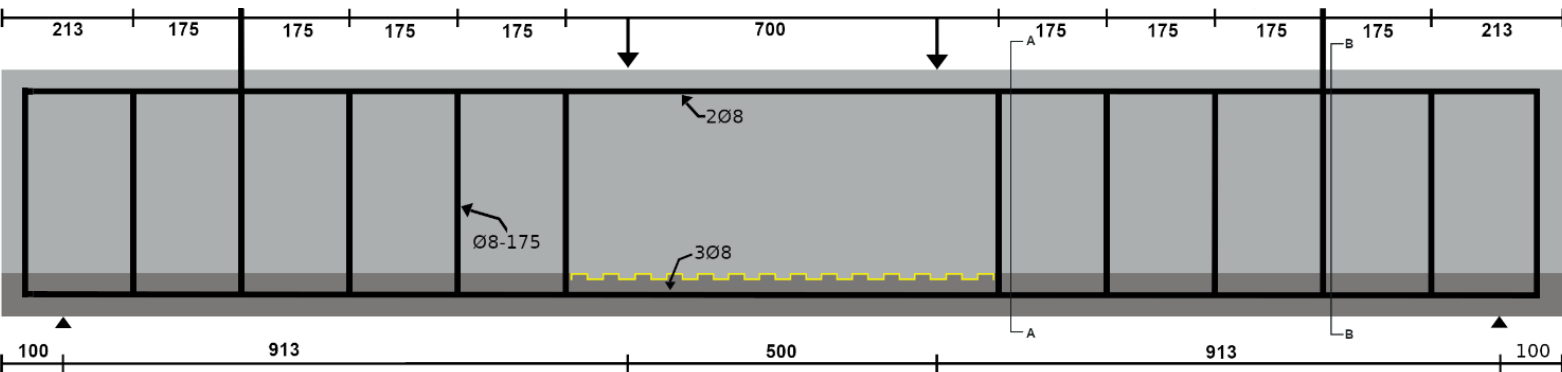


Fig. 3.3: Side view of beam PVA-RR-VPI

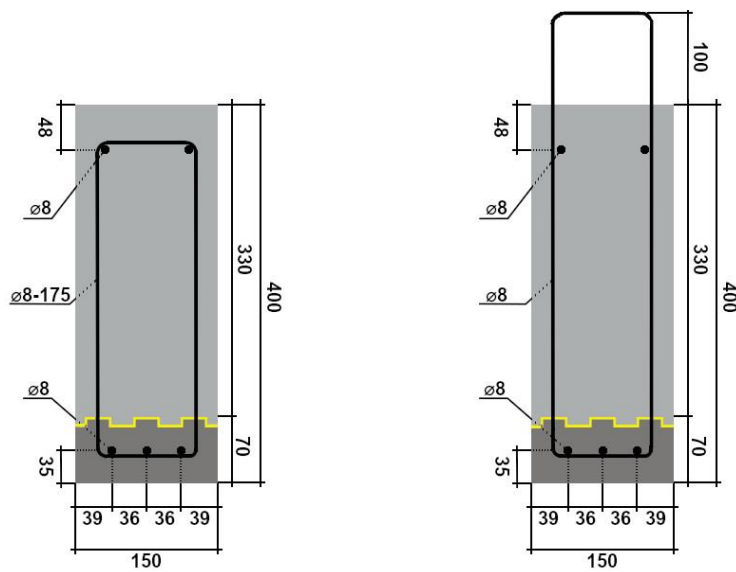


Fig. 3.4: Cross-sectional overview of beam PVA-RR-VPI with (left) Section AA and (right) Section BB

### 3.2.3 Beam PVA-SR-VPI

Beam PVA-SR-VPI will be a 400mm high hybrid R/SHCC beam with a 70mm thick SHCC layer, with a profiled interface treated with Vaseline (illustrated in yellow), smooth longitudinal rebars (illustrated in red) and the SHCC-layer composed of PVA-fibers. This way the influence of the reinforcement-SHCC bond can be studied. See

Fig. 3.5 and Fig. 3.6 for a schematic sideview and the cross-section of beam PVA-SR-VPI.

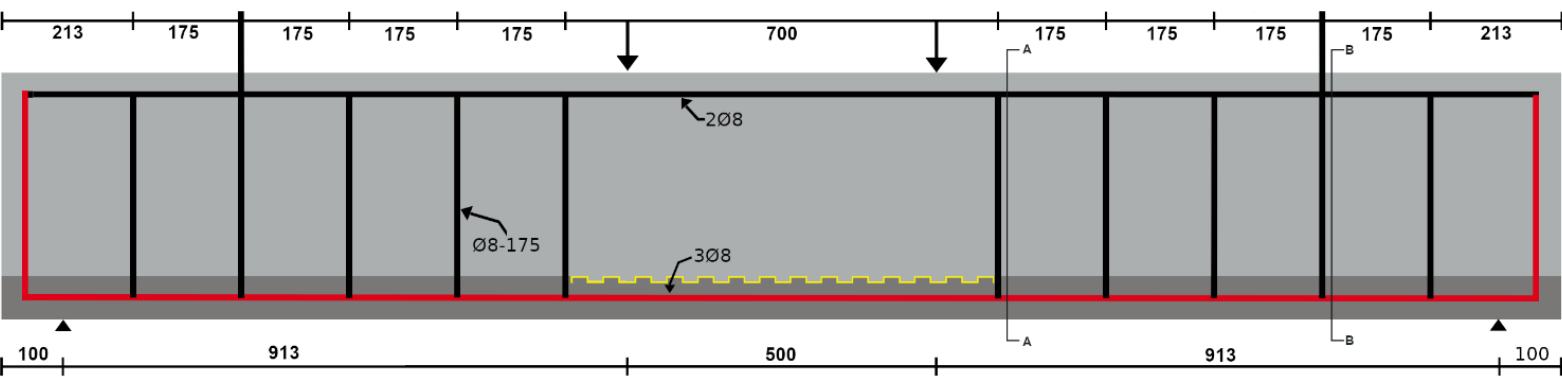


Fig. 3.5.: Side view of beam PVA-SR-VPI

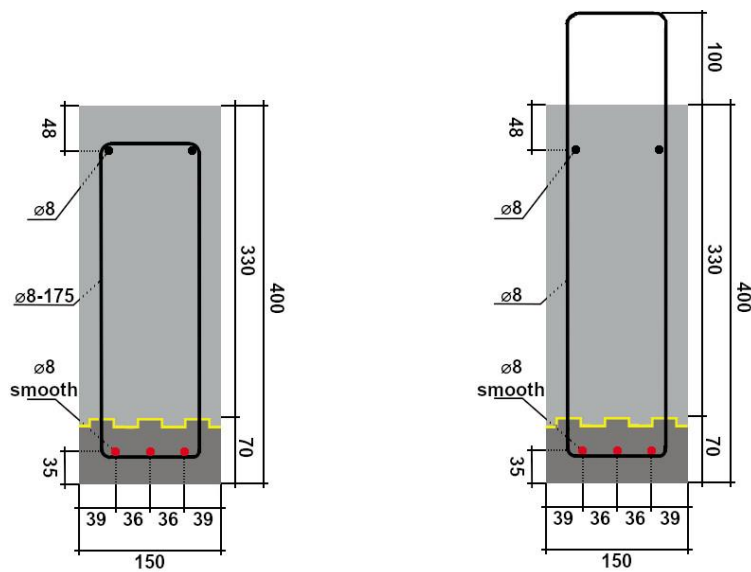


Fig. 3.6: Cross-sectional overview of beam PVA-SR-VPI with (left) Section AA and (right) Section BB

### 3.2.4 Beam PE-SR-VPI

Beam PE-SR-VPI will be a 400mm high hybrid R/SHCC beam with a 70mm thick SHCC layer, with a profiled interface treated with Vaseline (illustrated in yellow), smooth longitudinal rebars (illustrated in red) and the SHCC-layer composed of PE-fibers (illustrated with a darker grey colour). This way the influence of the fiber-type can be studied. See Fig. 3.7 and Fig. 3.8 for a schematic sideview and the cross-section of beam PE-SR-VPI.

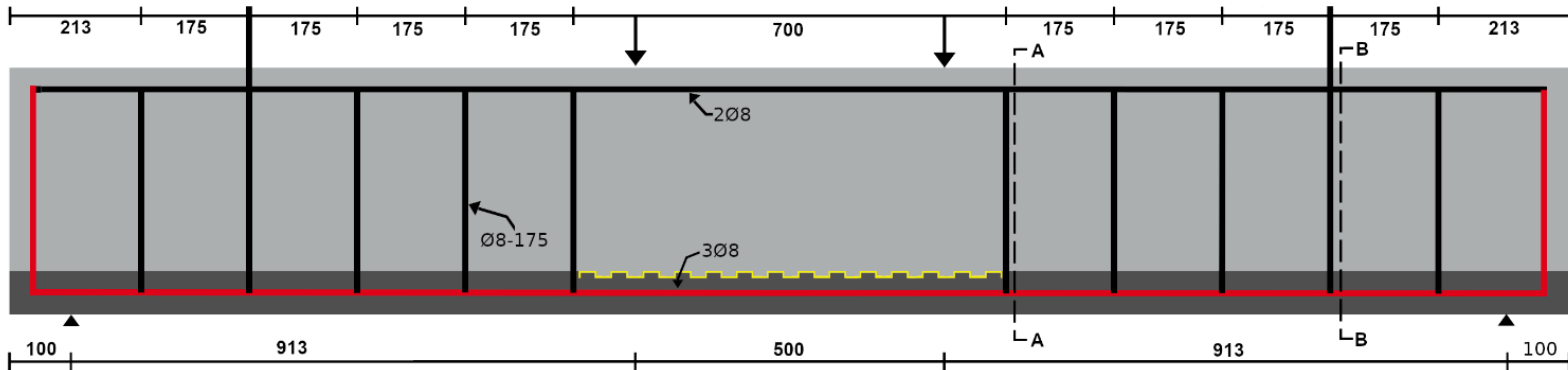


Fig. 3.7: Side view of beam PE-SR-VPI

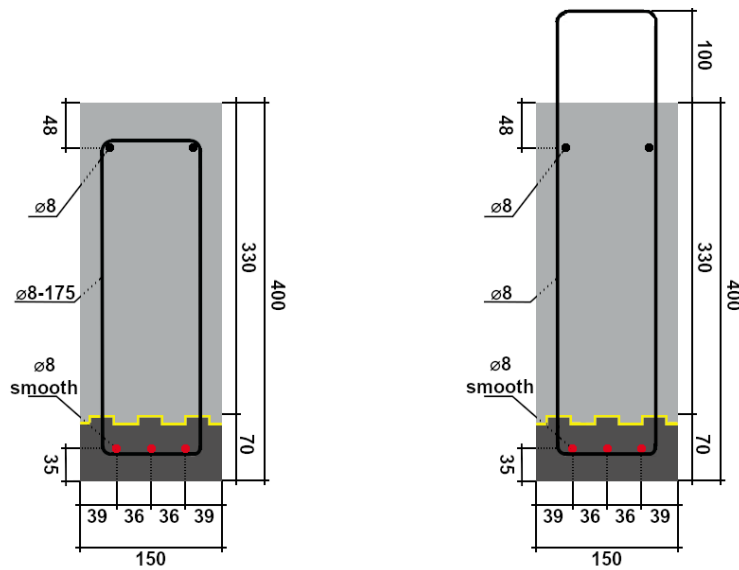


Fig. 3.8: Cross-sectional overview of beam PE-SR-VPI with (left) Section AA and (right) Section BB

### 3.3 Material properties

Table 3.2 shows the mixture composition of the PVA-SHCC and Fig. 3.9 shows the ingredients of the mixture. This mixture was developed in the study of Huang [1] and also used in the studies of Singh [2] and Bezemer [3]. Table 3.3 shows the mixture composition of the PE-SHCC and Fig. 3.10 shows the ingredients of the mixture. This mixture was developed in the study of Nuri [55]. The properties of the used fibers can be seen in Table 3.4. Lastly, Table 3.5 shows the mixture composition of the CC used in all beams.

Table 3.2 : PVA-based SHCC mixture

Ingredients	Dry weight (kg/m <sup>3</sup> )
CEM III B	790
Limestone powder	790
PVA fiber	26
Water	411
Superplasticizer	2,13



Fig. 3.9: Ingredients used in PVA-SHCC. From left to right: CEM III/B, limestone, PVA fibers, superplasticizer and water

Table 3.3: PE-based SHCC mixture

Ingredients	Dry weight (kg/m <sup>3</sup> )
CEM III B	841,8
Limestone powder	467,7
Silica fume	93,5
PE fiber	9,8
Water	374,1
Superplasticizer	3,5



Fig. 3.10: Ingredients used in PVA-SHCC. From left to right: CEM III/B, limestone, PE fibers, silica fume, superplasticizer and water

### 3. Design of beams

---

Table 3.4: *Properties of used fibers*

Fiber-type	Density (g/cm <sup>3</sup> )	Length (mm)	Ft (MPa)	E (GPa)
PVA	1.3	8	1600	40
PE	0.97	6	2700	120

Table 3.5: *CC mixture*

Ingredients	Dry weight (kg/m <sup>3</sup> )
CEM IB 52.5R	260
Sand 0.125-0.25mm	78.83
Sand 0.25-0.5	256.199
Sand 0.5-1mm	256.199
Sand 1-2mm	157.661
Sand 2-4mm	98.538
Sand 4-8mm	394.152
Gravel 8-16mm	729.181
Water	156
Superplasticizer	0.26

---

# 4. Experimental program

---

## 4.2. Pre-study

Prior to casting the beams, a preliminary study is conducted to evaluate the effectiveness of various methods for pressing down a mold to create the desired profiled interface. To replicate the conditions expected during the actual pressing of the molds onto the SHCC layer in the beams, a 70mm layer of SHCC (matching the height of the SHCC layer in the beams) is cast in a steel mold with a width of 150mm (the same width as the beams to be cast).

Several configurations were tested to determine the most effective approach. One method involved pressing down the silicone mold immediately after casting **(1)**. Doing this, the mold had difficulty staying in place, even with weights on top. Another configuration used two silicone molds placed a few minutes after casting: one without weights **(2)** and the other with weights on top **(3)**. To address concerns about the SHCC filling the relatively small holes (25mm in diameter) in the silicone mold, a foam mold with larger holes (50mm in diameter) was also tested and placed a few minutes after casting **(4)**. Additionally, small rectangular foam blocks (25x25mm) were pressed into the SHCC as another alternative **(5)**.

Table 4.1: Configurations employed to create profiled interface

Type of mold	When?	Weights on top?
Silicone mold with small holes	Directly after casting	Yes (1)
	Some minutes after casting	No (2)
		Yes (3)
Foam mold with big holes	Some minutes after casting	Yes (4)
Small foam blocks	Some minutes after casting	No (5)

Fig. 4.1 provides pictures of the different configurations after casting and the hardened state of the SHCC with the molds still in place.



Fig. 4.1: Fresh (left) and hardened (right) state of profiled interfaces

## 4. Experimental program

---

All configurations using the silicone mold yielded satisfactory results, with option 3 (placing the mold a few minutes after casting and adding weights on top) producing the smoothest profile. It was hardly possible to remove the foam mold, although the shear keys also formed well. Consequently, option 3 was chosen for further use.



Fig. 4.2: *Profiled interfaces after demolding*

## 4.3. Sample preparation

### 4.3.1. Formwork

Two wooden molds were constructed, each capable of holding two beams measuring 2525x150x400mm. Before placing the reinforcement cages, the molds were cleaned using a vacuum cleaner and then oiled. Plastic spacers were used to keep the steel reinforcement cages in position. Fig. 4.3 shows the molds for the four beams with the reinforcement cages in place.



Fig. 4.3: *Wooden molds used to cast the beams*

### 4.3.2. SHCC-layer

The SHCC was mixed in the *Imer Syntesi* mixer, with a volume capacity of 140L. During the mixing procedure, the cement and limestone powder were first dry-mixed for one minute. Gradually, the fibers were added to ensure even distribution throughout the mixture. The pre-mixed water and superplasticizer were then added incrementally while continuing to mix for 8-12 minutes until a uniform consistency was achieved. To guarantee the uniformity of the mixture, the mixer alternated

## 4. Experimental program

its orientation back and forth during the mixing process. Once the mixture was uniform and free of fiber clumps (checked by hand), the SHCC was cast into the molds.

During casting, a levelling tool was used to ensure a 70mm SHCC layer (Fig. 4.4). Once the layers were cast, the molds were placed on a vibration table. The mix was vibrated until it appeared smooth and air bubbles were no longer visible. In an attempt to make the interface of beam PVA-RR-SI very smooth, rather than smooth, a smooth foam is put on top of the interface during the vibration process. Then, in the three remaining beams, the silicone mold was pressed down into the SHCC layer to create the desired profile. The levelling tool was then again used to ensure the layer is 70mm. Finally, the SHCC was covered with foil to retain moisture and cured at room temperature for 14 days. This 14 day curing period, prior to casting the top conventional concrete layer, has been chosen to mitigate the differential shrinkage between SHCC and CC. Note, if the differential shrinkage is too high, it might lead to cracking due to internal restrains.

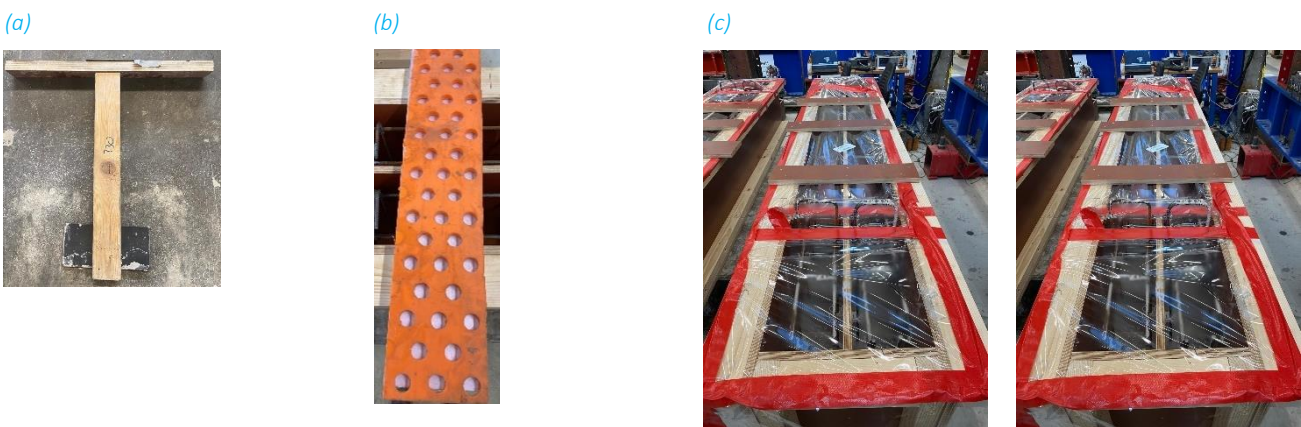


Fig. 4.4: (a) Levelling tool (b) Silicone mold used to create profiled interface (c) Beam molds covered after SHCC layer casting interface

### 4.3.3. CC layer

Before casting the conventional concrete layer, the silicone molds were removed, and the interfaces were prepared by vacuum cleaning and brushing with a steel brush to remove impurities and dust. The reinforcement was cleaned using a scraper with acetone. Finally, the interface was treated with a layer of Vaseline.

Initially, the aggregates were dry-mixed to ensure uniform distribution. Then, the cement was added to the mix. Lastly, the pre-mixed water with superplasticizer was added gradually until a uniform consistency was achieved. The concrete was then cast into the molds. For preparing the conventional concrete, due to the mixer's capacity limitations, four equal batches of concrete were mixed.

The concrete was vibrated using a vibration needle (see Fig. 4.5) to eliminate air bubbles. The top surface was then levelled, and the beams were covered with plastic sheets to retain moisture. The beams were cured at room temperature and demolded 71 days after casting the CC layer. The initial plan was to demold the beams 28 days after curing of the CC-layer, but due to an accident happening in the laboratory this had to be rescheduled until after inspection had given approval for the resumption of laboratory work.



Fig. 4.5: (a) Vaseline used on top of profiled interface (b) Vibration needle used to vibrate CC layer (c) Beam molds covered after CC layer casting

### 4.3.4. Material samples

In addition to the beams, material samples were cast to assess various material properties. For both types of SHCC, four cubes measuring 150x150x150mm and four dogbones with a gauge section of 110x60x60mm were cast. Each batch of conventional concrete included three cubes measuring 150x150x150mm and three prisms measuring 100x100x400mm.

The cubes were prepared for compressive tests, the dogbones for tensile tests, and the prisms were intended for evaluating Young's Modulus. The prisms were scheduled for testing only if significant differences were detected in the beams compared to the reference beam.



Fig. 4.6: Molds for cubes and dogbones

### 4.3.5. Remarks after demolding

After demolding, several observations were made that could potentially influence the response of the beams. Firstly, the SHCC layer in beam PVA-SR-VPI was found to be slightly thicker than 70mm outside of the CBMR, likely due to forgetting to use the levelling tool after pressing down the silicone mold. Secondly, a dent was found in the profiled interface of the same beam, probably caused by putting too much weights on that spot. The interface of beam PVA-RR-SI was intended to be very smooth. However, upon visual inspection (without the need of a surface scanner), this level of smoothness was not achieved. As a result, the interface is classified as smooth, making this beam an exact replica of the Hybrid400 beam tested in Bezemer's [3] study. Lastly, due to forgetting to insert wooden lats on top of the beams before sealing, the deformation of the molds was not restricted. As a result, the beams have a slightly wider top, with widths ranging between 150 mm and 160 mm. This slight difference in beam width at the top, can lead to slight differences in stiffness of the beams.

### 4.4. Experimental methods

To capture the structural response of the beams (i.e., the load-bearing capacity and the cracking response), the beams were subjected to a four-point bending test. The test setup is shown in Fig. 4.7. The beams were simply supported on steel plates placed on steel rollers. The load was generated by a 400kN hydraulic jack. To enable a 500mm constant bending moment region (CBMR), the load was distributed using a steel load spreader supported by a fixed roller and a free roller. The test was conducted in displacement control at a loading rate of 0.01mm/s.



Fig. 4.7: Test setup

Measurements were conducted using two methods: Digital Image Correlation (DIC) and Linear Variable Differential Transformers (LVDTs). DIC is a non-contact optical technique used to measure surface deformation, displacement, and strain of materials. This method involves capturing digital images of a material's surface before and after deformation. A random speckle pattern is applied to the surface, and the movement of these patterns is tracked using specialized software, in this study GOM correlate. Due to DIC's sensitivity to inaccuracies (stemming from the camera setup and speckle pattern quality), DIC measurements were validated using LVDTs. LVDTs measure displacement by detecting the difference between two predefined locations through the compression or relaxation of a spring.

#### 4.4.1. Digital Image Correlation (DIC)

2D in plane DIC measurements were performed on both sides of the beams. Photos were taken every five seconds with a Canon EOS 5DS R camera with 35mm fixed lenses. On one side, a speckle pattern was applied to the Constant Bending Moment Region (CBMR). This involved first painting the region white and then spraying a speckle pattern on the surface. The dots in the pattern needed to be large enough to be recognized by the GOM software, but not so large that they caused data loss.

Using GOM, the cracking pattern, crack-widths, and delamination of the interface in the CBMR were determined from this side. For two beams, PVA-RR-SI and PE-SR-VPI, the speckle pattern covered a 900mm region, allowing evaluations up to 200mm beyond the CBMR. For the other two beams, PVA-RR-VPI and PVA-SR-VPI, the pattern covered a 600mm region, matching the study region of Bezemer [3].

On the other side of the beams, correlatable stickers were placed around the interface along the full length of the beams to evaluate delamination outside the CBMR. Fig. 4.8 shows the applied speckle

#### 4. Experimental program

pattern on one side of the beam and Fig. 4.9 shows correlatable stickers on the opposite side of the beam.

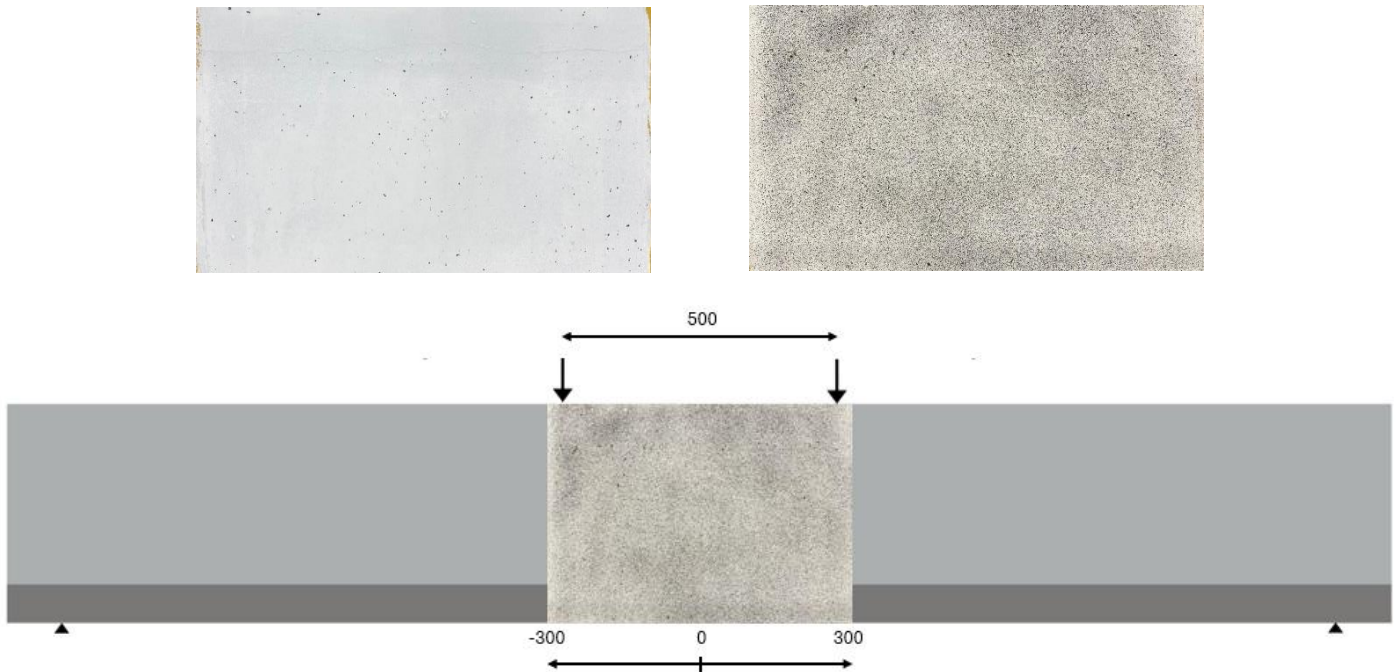


Fig. 4.8: *Speckle pattern. First surface is painted white (top left), then speckles are sprayed on white surface (top right). Sketch of speckle pattern on beam with definition of the constant bending moment region (bottom).*

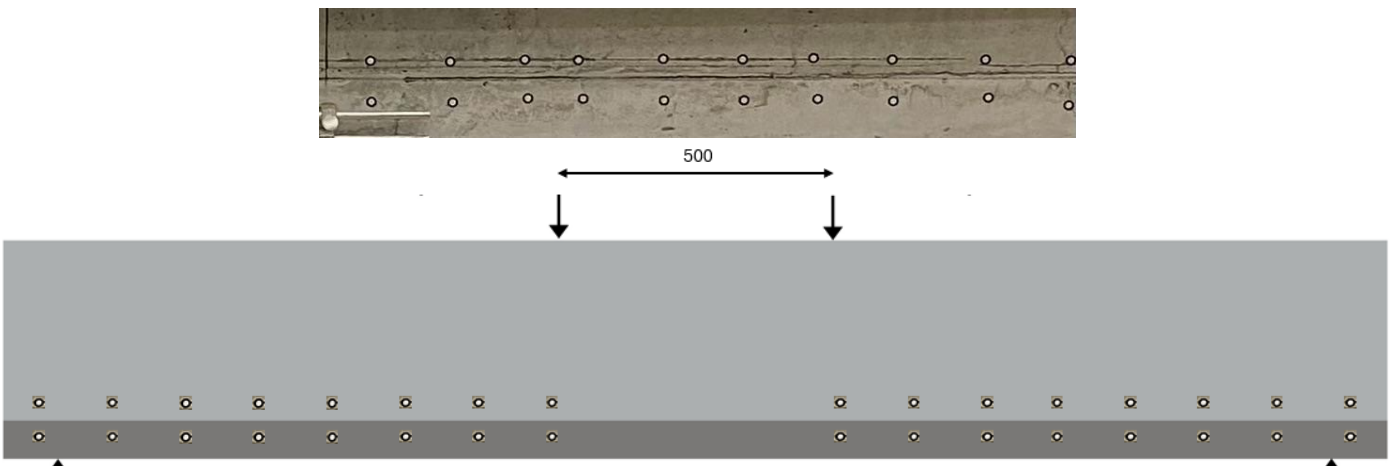


Fig. 4.9: *Correlatable stickers (top) and sketch of correlatable stickers on beam (bottom)*

In GOM, a surface area for evaluations was created. To verify the DIC data, point distances matching those of the LVDTs (see Section 4.4.2) were made. Two sections were defined: one near the bottom of the beam (2mm above the bottom) and one near the interface (2mm above the interface in the CC-layer). This approach was used because cracks are typically largest near the outer surface.

The precision in evaluating crack-widths is very high when cracks are visualized as Von-Mises strain localizations, as concluded by [56]. To evaluate crack-widths, Von-Mises strains were analysed across all load steps using selected photos taken during the experiment. These strains were determined over a cross-section along the length of the beam. A peak in the Von-Mises strain indicates the

## 4. Experimental program

presence of a crack. To determine the location, number, and widths of the cracks, the strain data corresponding to each section is passed through two filters. The first filter is defined as a threshold strain (labelled as threshold-strain in Fig. 4.10), above which any strain localization is considered a crack, while all strain values below that threshold are ignored and considered as noise of the DIC data. This threshold was determined by comparing the difference in strain between two photos in the unloaded state, accounting for the noise inherent in the camera outputs. This noise level was used to set the threshold.

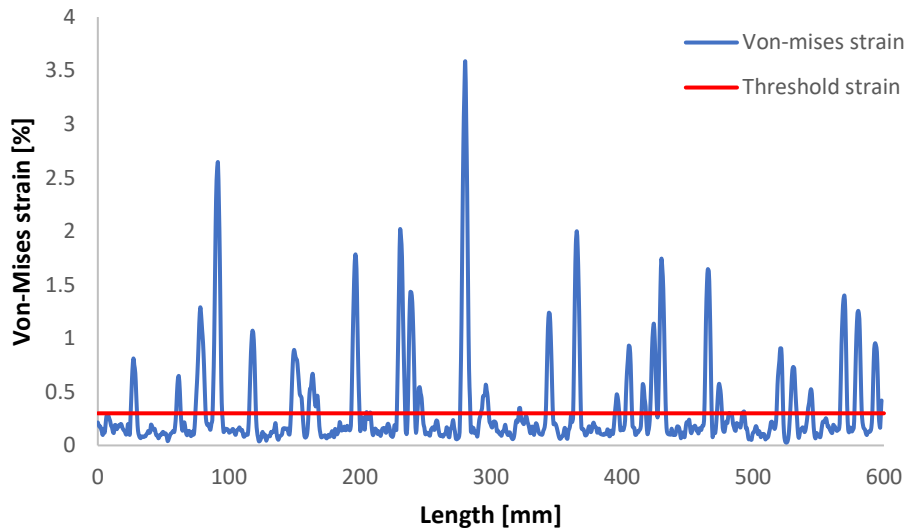


Fig. 4.10: Von-Mises strains over CBMR

Closely spaced cracks, however, cannot be distinguished by this filter alone, as shown in Fig. 4.11, where multiple peaks can be observed between the start and end of a crack localization. This behavior is typical of SHCC due to its dense micro-cracking characteristics. To prevent these fine cracks from being treated as one large crack, an additional filter is introduced. This second filter detects the local minima in the noise-free strain data and further divides the strain localizations at each minima to distinguish between closely spaced cracks.

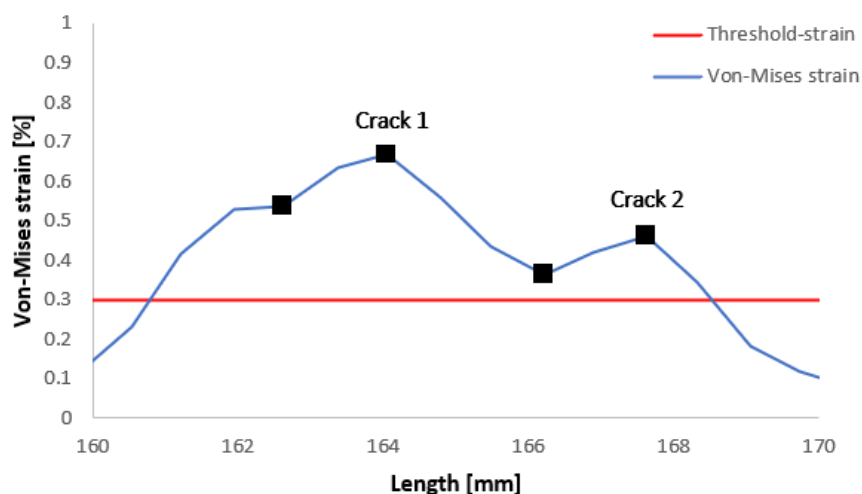


Fig. 4.11: Closely spaced cracks

The magnitude of the crack-widths were calculated by evaluating the difference in deformation between the starting point and the end point of a crack. Since the deformation is also subject to camera noise, a crack is only considered valid if its width exceeds a certain threshold, which was again

determined by comparing the deformation between two photos taken in the unloaded state of the beams. The crack-width calculations are automatized with a Matlab-script (inspired from the study of Mustafa et al. [52]).

#### 4.4.2. Linear Variable Data Transformers (LVDTs)

LVDTs were used to verify the DIC measurements (and because they are more accurate in measuring deformations). Six LVDTs were placed on each beam (see Fig. 4.12 and Fig. 4.13). All LVDTs had a measuring range of 200mm, except for LVDT3, which had a measuring range of 500mm. To capture the vertical deformation of the beam, a laser was mounted on a rod at the midsection of the beam. This rod was stabilized by supporting it on steel pins glued at the midsection of the beam above the supports, where no vertical displacement occurs. A steel plate was glued to the bottom of the beam, allowing the laser to measure the distance to the plate accurately (see Fig. 4.12).

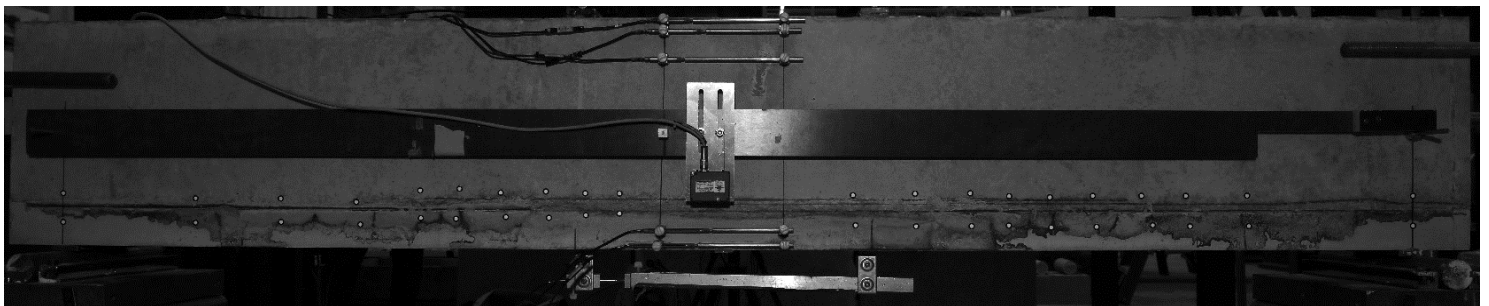


Fig. 4.12: Side view of beam with all LVDTs and laser mounted to rod

Fig. 4.13 show the location of all the LVDTs on the side face and bottom face of the beam, respectively.

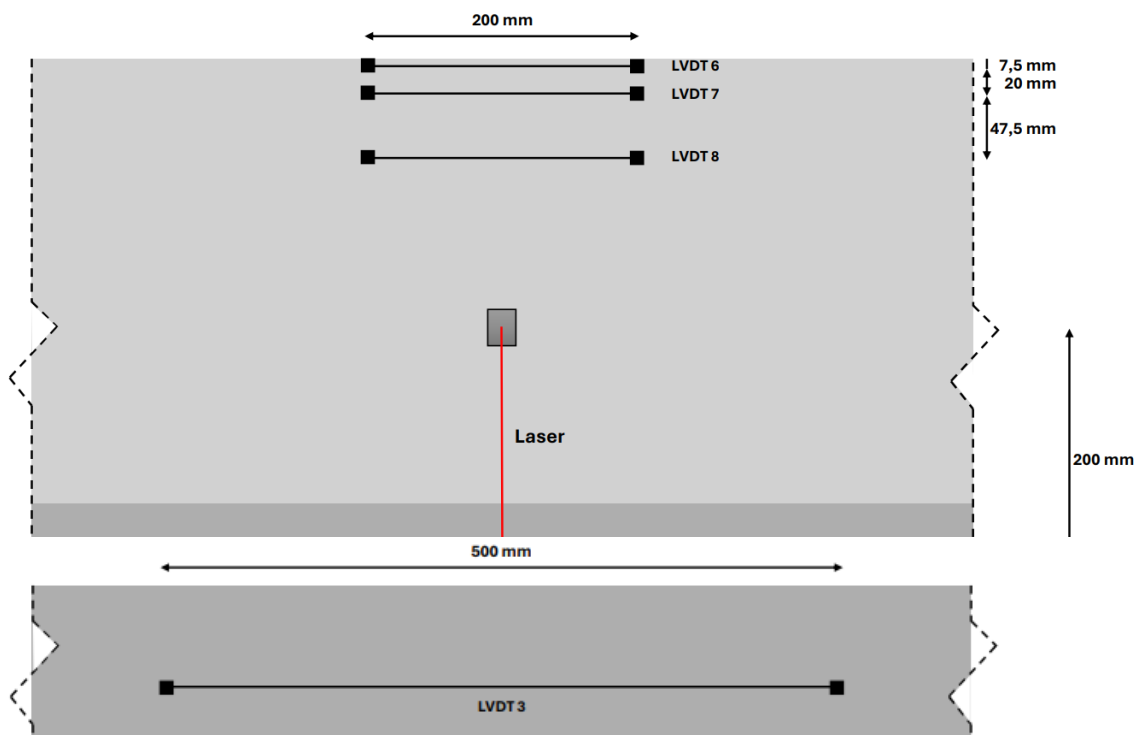


Fig. 4.13: Configuration of LVDTs. (Top) Side view and (Bottom) Bottom view

---

# 5. Results

---

## 5.1. Hybrid R/SHCC beams

The results of all beams are shown in the following order. For every beam, first, the load-deflection response is shown highlighting key characteristics of the beam response. Yielding is identified by drawing a tangent on the stabilized cracking stage and determining the load at which the load-deflection curve deviates from this tangent. Before presenting the crack development and the delamination of the SHCC-concrete interface, which are evaluated using DIC measurements, the DIC data is validated against the LVDT data.

Then, a step-by-step propagation of cracks in the CBMR of the beams is shown. Each load step is marked on the load-deflection curve with a red circle marker in the top left graph. Cracks are visualized in Von-Mises contour plots (top right graph), where the strain unit is given in percentage. In these plots, red striped lines indicate the sections where crack-widths in the CC and SHCC layers are measured. The crack-widths in the SHCC layer are represented in a scatter plot with small grey dots (bottom left graph). In addition, the CC cracks are shown with large black dots. The load step at which the cracks in the SHCC layer exceed the 0.2mm or the 0.3mm crack-width limit a red outline is visible. The distribution of crack-widths in the SHCC layer is depicted in a bar graph (bottom right graph).

Following this, the delamination and slip at the SHCC-concrete interface are quantitatively analysed at three predefined locations, supported by contour plots showing vertical strain to visualize delamination behavior. Finally, key performance indicators are summarized in a table..

### 5.1.1 Beam PVA-RR-SI

#### Load-deflection response

Fig. 5.1 illustrates the load-deflection response of beam PVA-RR-SI. The crack formation stage starts at a load of 27kN. Yielding of the reinforcement is observed at a load of 77.2kN and a deflection of 7.6mm. The ultimate load reaches 92.6kN, with the beam failing at a deflection of 25.2mm due to the rupture of the reinforcement bar(s).

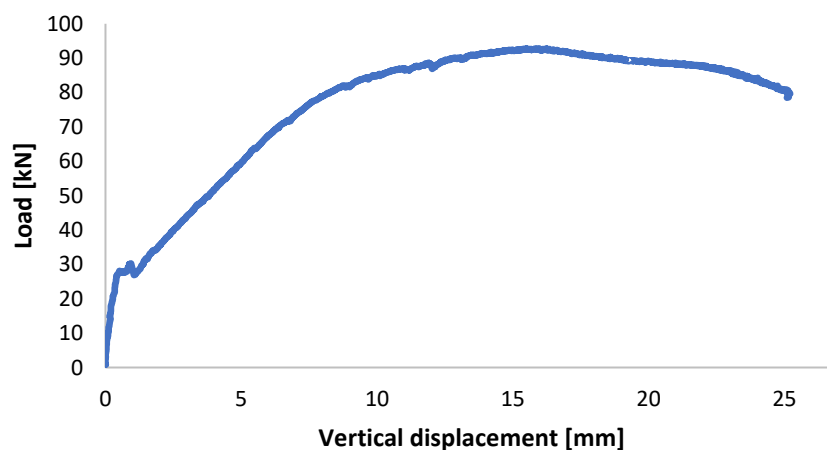


Fig. 5.1: Load-deflection response of beam PVA-RR-SI

### Validation GOM results

The DIC data are validated based on LVDT1, LVDT2, LVDT3 (placed in the tension zone) and the laser data, as these measurements show an accurate match (see Fig. 5.2 and Fig. 5.3). LVDT6, LVDT7, and LVDT8, which were positioned in the compression zone, exhibit only minimal strain. This led to a less accurate match during the non-linear stage (see Annex C).

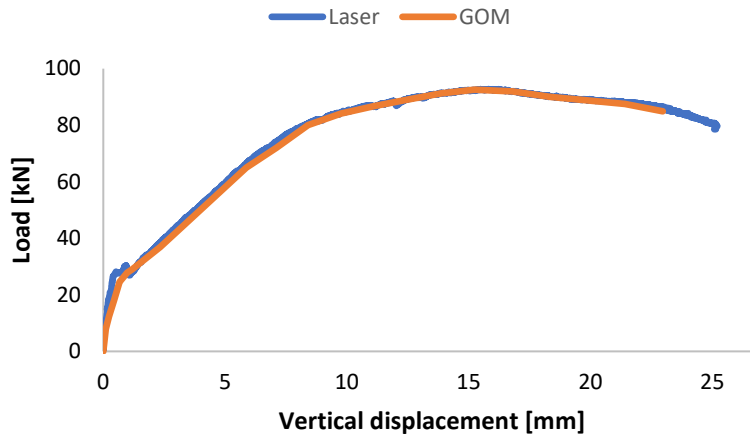


Fig. 5.2: Comparison of laser measurements with DIC measurements of beam PVA-RR-SI

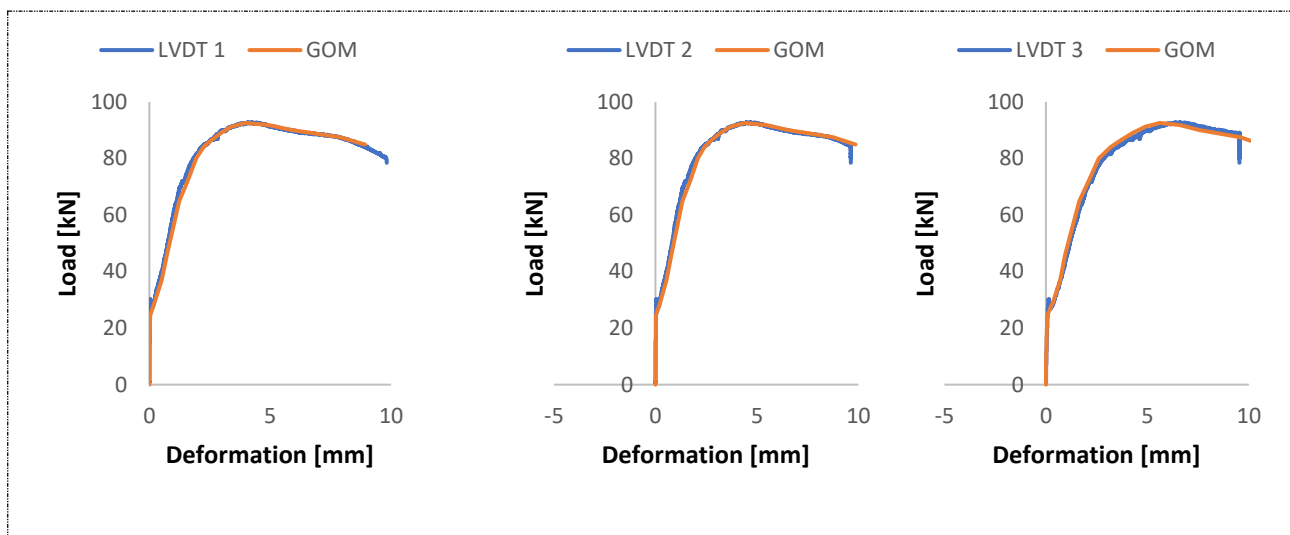


Fig. 5.3: Comparison of the measurements of all horizontally placed LVDTs with the DIC measurements of beam PVA-RR-SI

### Crack pattern development in CBMR

Fig. 5.4 to Fig. 5.11 shows the crack development of beam PVA-RR-SI. It can be observed (Fig. 5.4) that cracks are detected even before the crack formation stage begins. A probable reason for this is the widening of shrinkage induced micro-cracks. However, the presence of cracks prior to testing was not investigated. As the load increases, more cracks form and existing cracks widen. The widening of a crack also results in closing of adjacent cracks, as can be seen in Fig. 5.6 - Fig. 5.7, where cracks in the concrete layer close due to widening of an localized crack. At a load level of 65kN, the 0.2mm crack-width limit is exceeded (Fig. 5.9), and at a load level of 72kN, the 0.3mm crack-width limit is exceeded (Fig. 5.10). One crack propagates into the CC layer, and a strong activation of the SHCC around this propagated crack is observed. At the ultimate load, several cracks in the SHCC layer exceed the 0.3mm crack-width limit.

## 5. Results

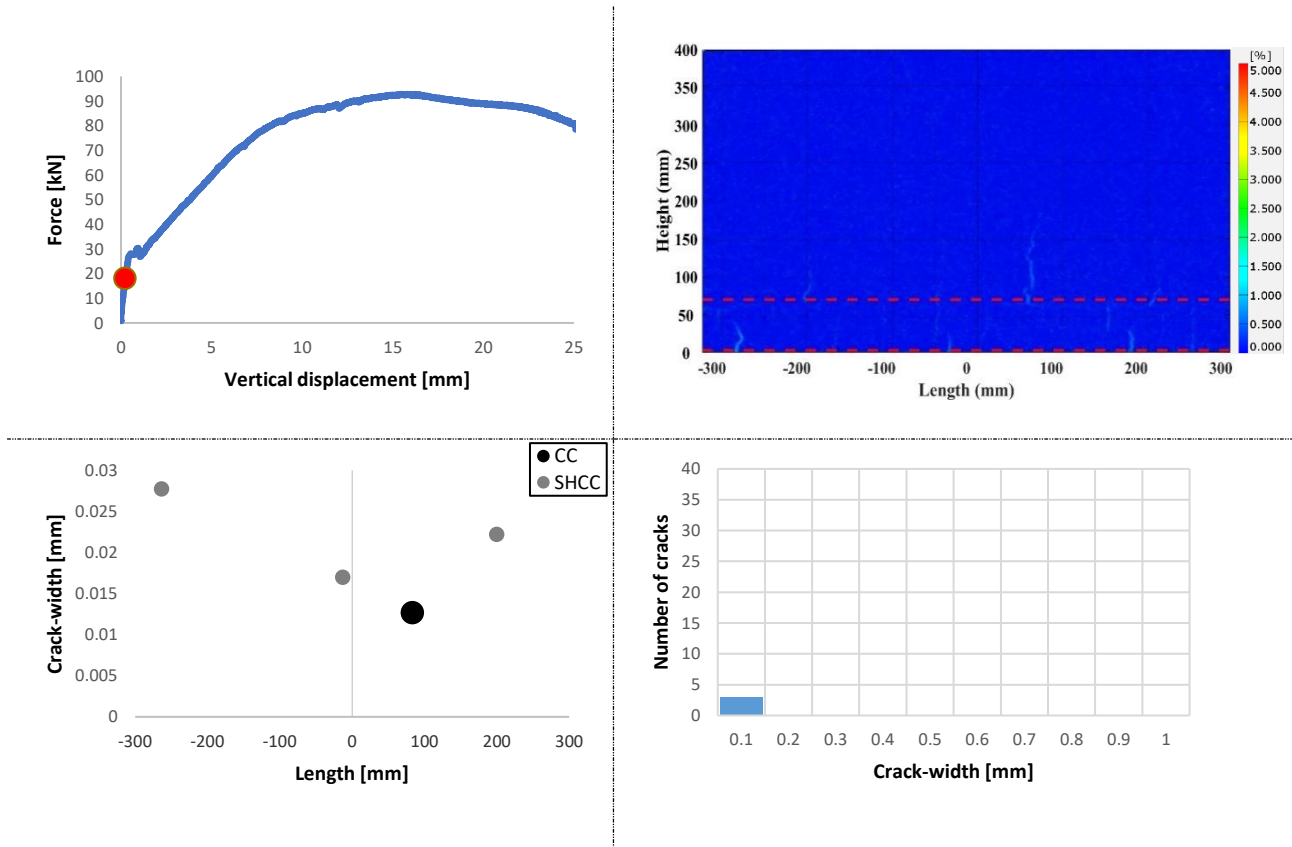


Fig. 5.4: Cracking behavior of beam PVA-RR-SI at a load of 18kN. Top left: Load-level on load-deflection curve. Top right: Contour plot Von-Mises strains. Bottom left: Scatter plot of all cracks. Bottom right: Crack-width distribution of cracks in SHCC.

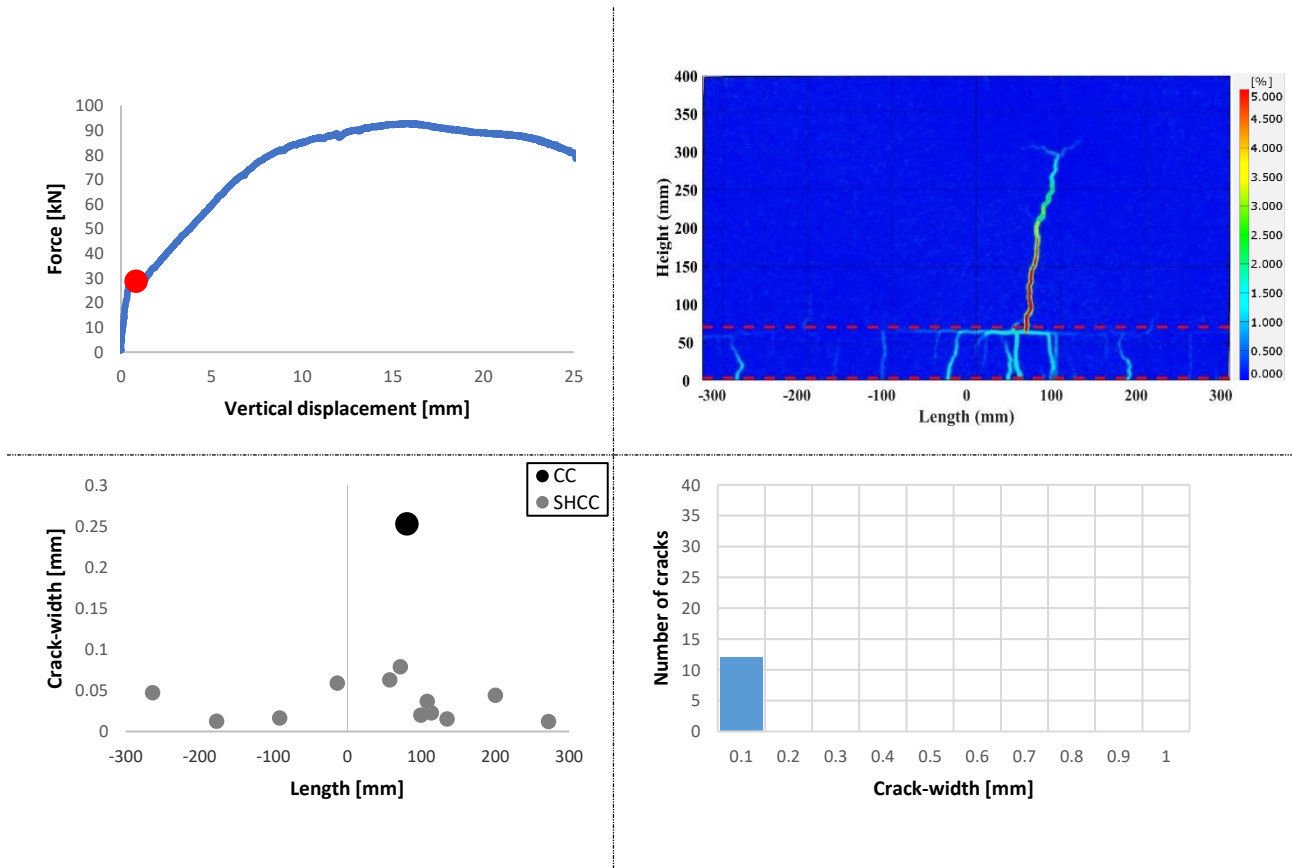


Fig. 5.5: Cracking behavior of beam PVA-RR-SI at a load of 29kN. Top left: Load-level on load-deflection curve. Top right: Contour plot Von-Mises strains. Bottom left: Scatter plot of all cracks. Bottom right: Crack-width distribution of cracks in SHCC.

## 5. Results

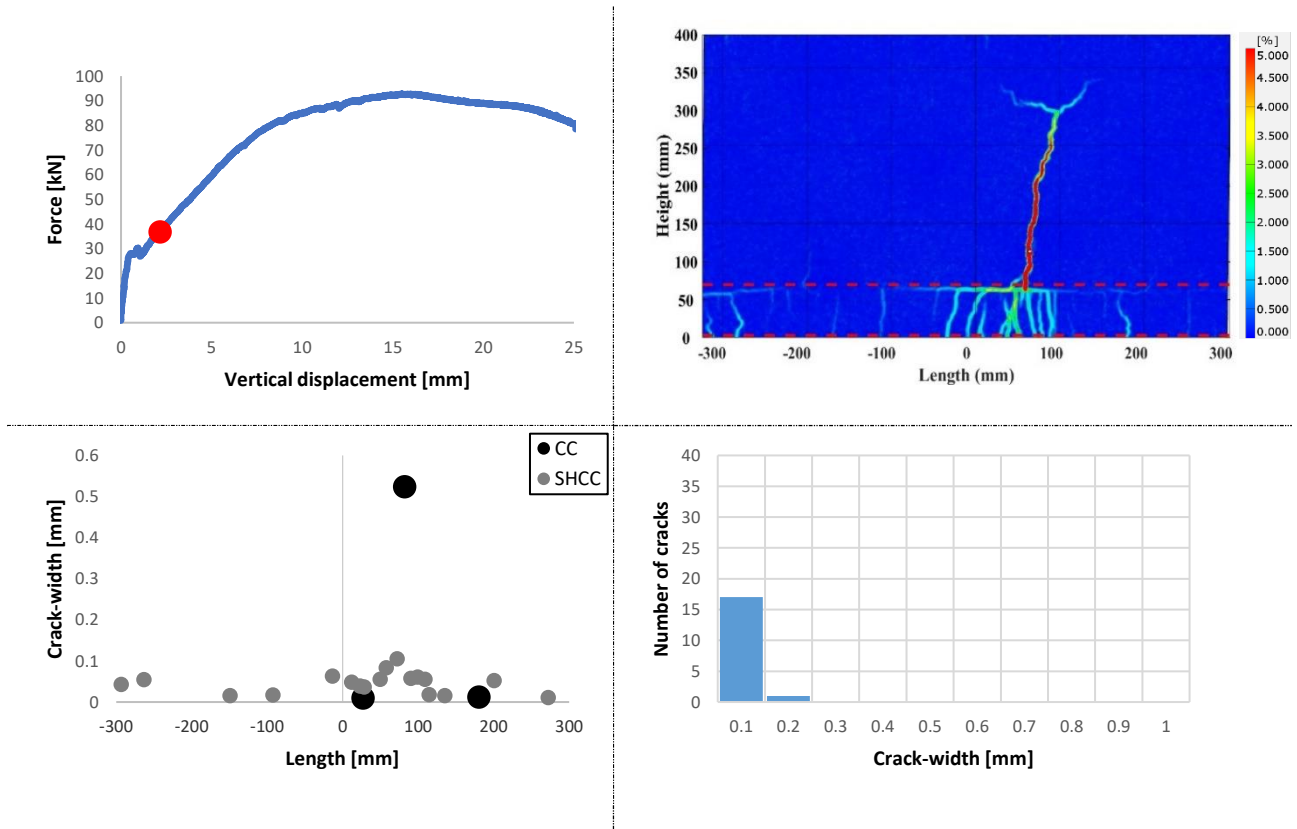


Fig. 5.6: Cracking behavior of beam PVA-RR-SI at a load of 37kN. Top left: Load-level on load-deflection curve. Top right: Contour plot Von-Mises strains. Bottom left: Scatter plot of all cracks. Bottom right: Crack-width distribution of cracks in SHCC.

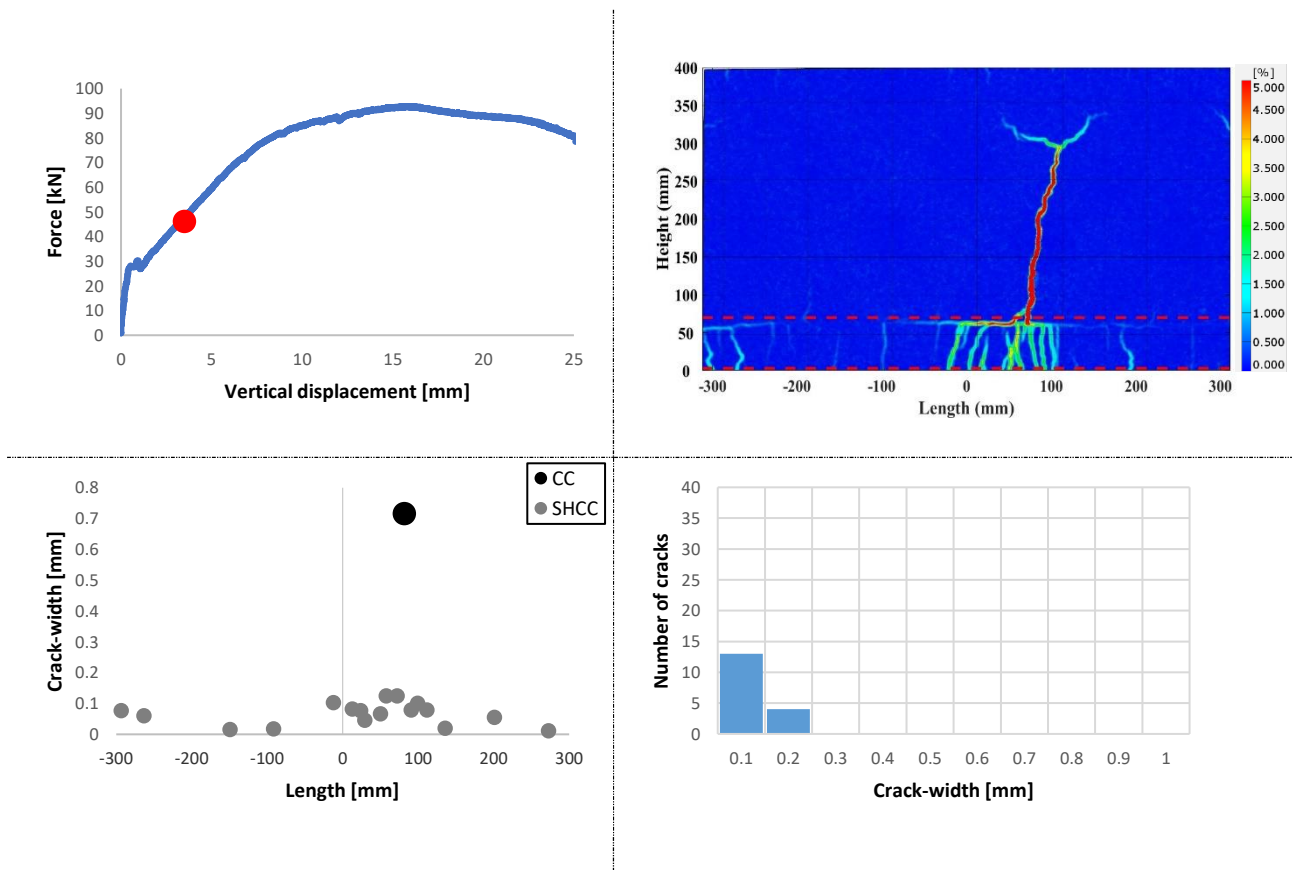


Fig. 5.7: Cracking behavior of beam PVA-RR-SI at a load of 46kN. Top left: Load-level on load-deflection curve. Top right: Contour plot Von-Mises strains. Bottom left: Scatter plot of all cracks. Bottom right: Crack-width distribution of cracks in SHCC.

## 5. Results

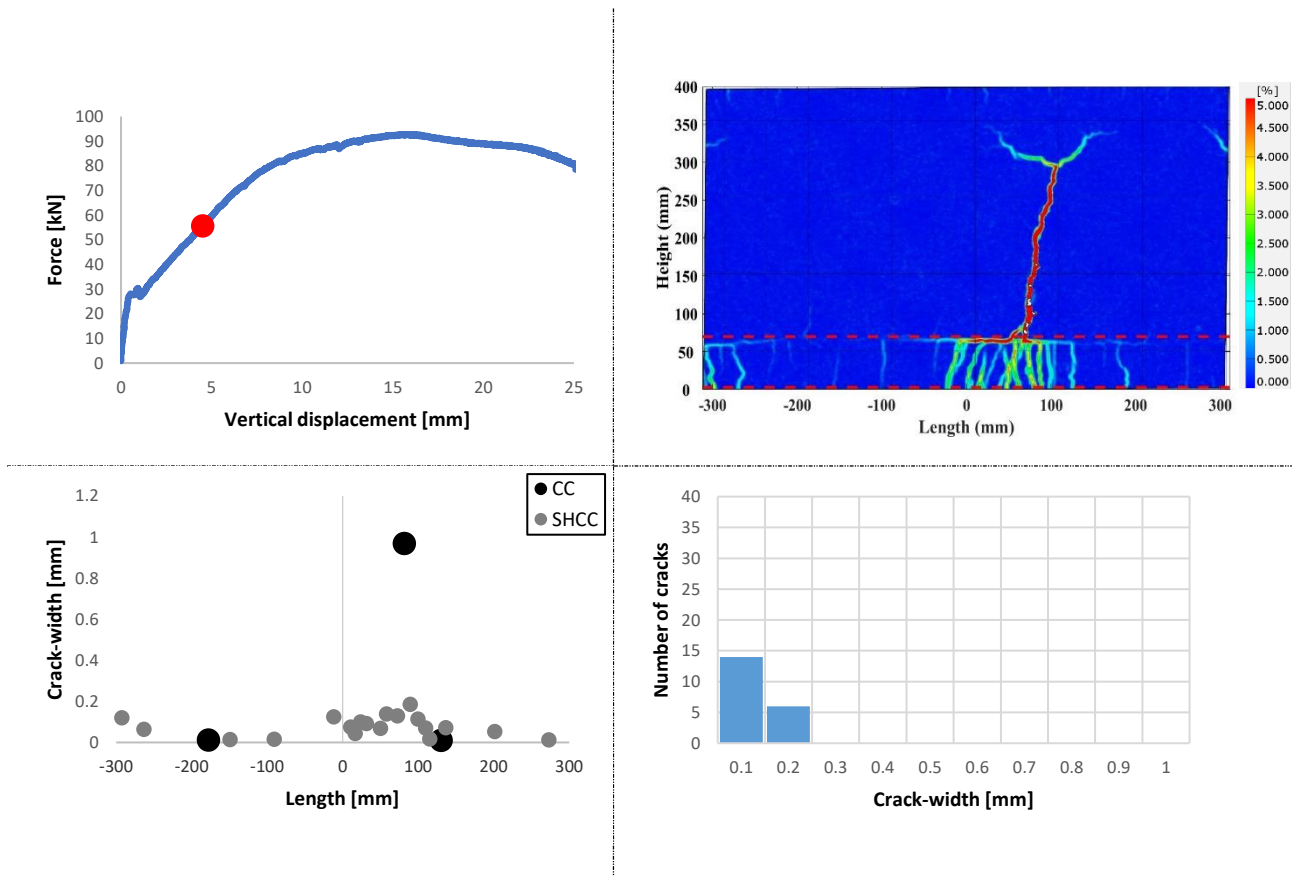


Fig. 5.8: Cracking behavior of beam PVA-RR-SI at a load of 56kN. Top left: Load-level on load-deflection curve. Top right: Contour plot Von-Mises strains. Bottom left: Scatter plot of all cracks. Bottom right: Crack-width distribution of cracks in SHCC.

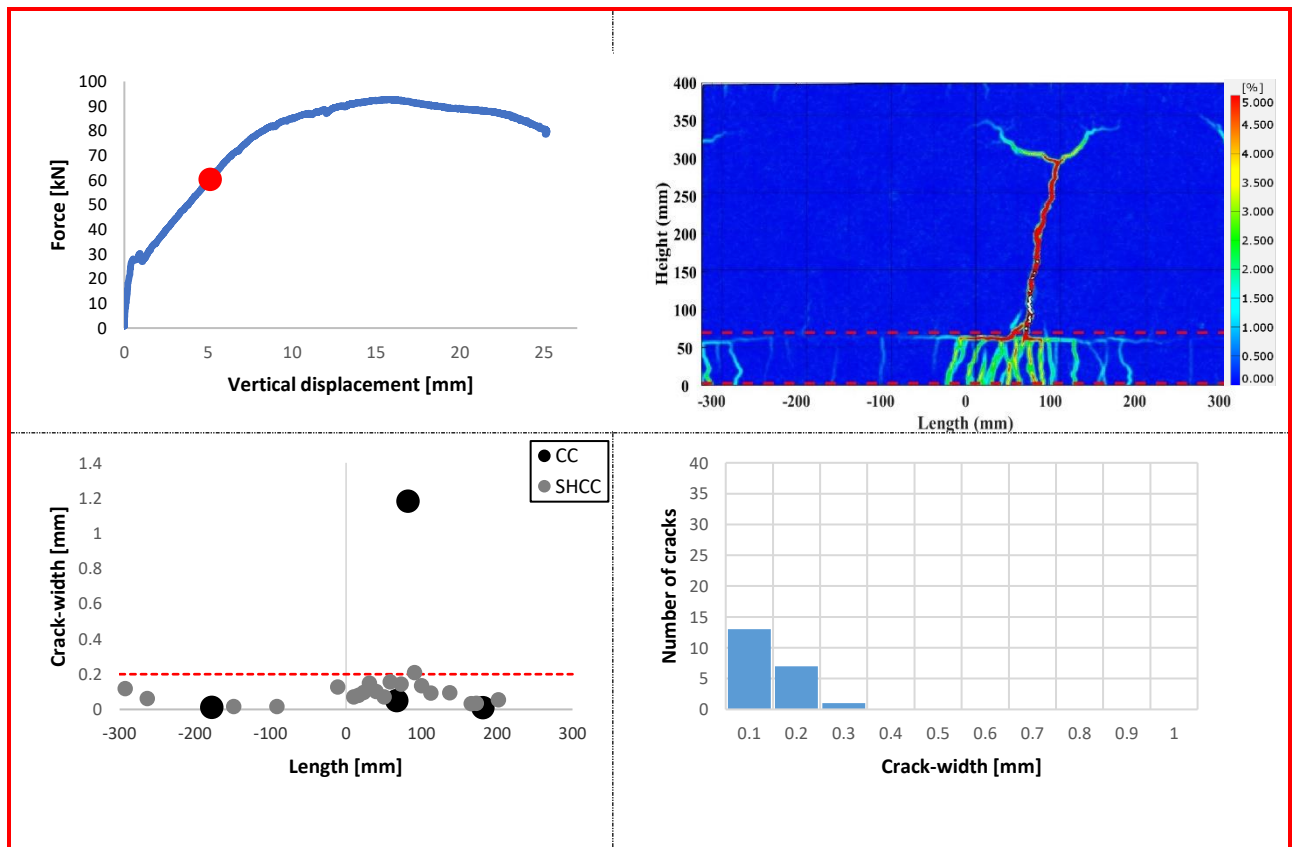


Fig. 5.9: Cracking behavior of beam PVA-RR-SI at a load of 60kN. Top left: Load-level on load-deflection curve. Top right: Contour plot Von-Mises strains. Bottom left: Scatter plot of all cracks. Bottom right: Crack-width distribution of cracks in SHCC

## 5. Results

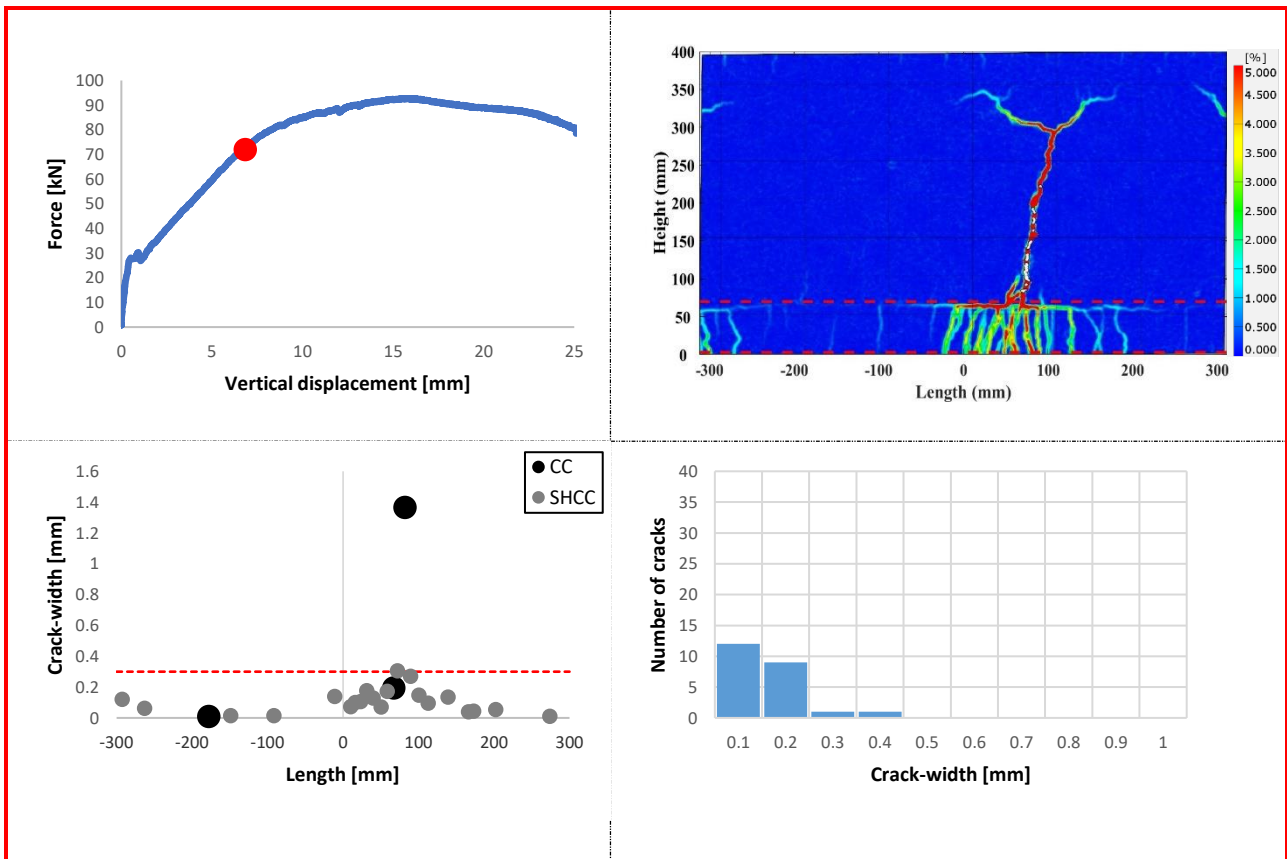


Fig. 5.10: Cracking behavior of beam PVA-RR-SI at a load of 70kN. Top left: Load-level on load-deflection curve. Top right: Contour plot Von-Mises strains. Bottom left: Scatter plot of all cracks. Bottom right: Crack-width distribution of cracks in SHCC.

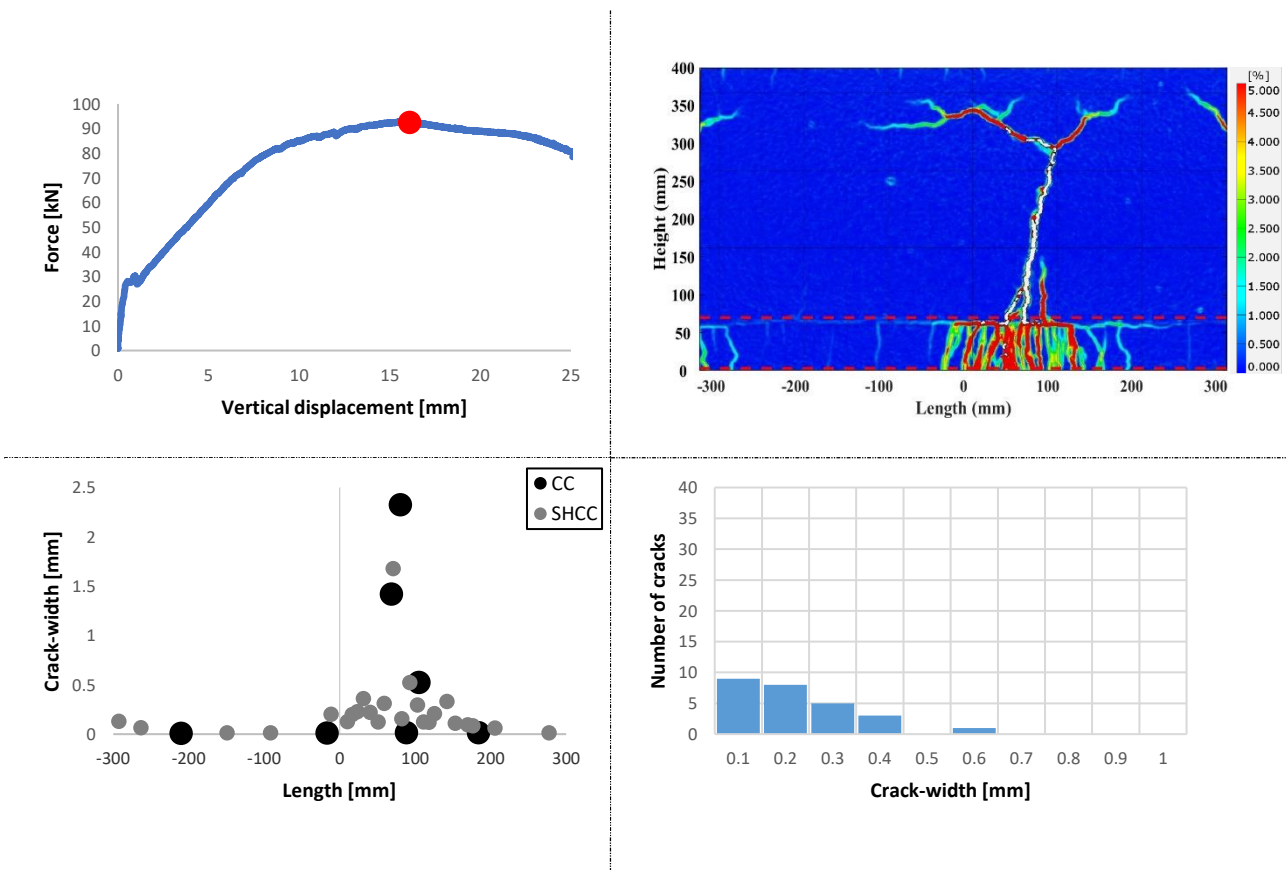


Fig. 5.11: Cracking behavior of beam PVA-RR-SI at a load of 93kN. Top left: Load-level on load-deflection curve. Top right: Contour plot Von-Mises strains. Bottom left: Scatter plot of all cracks. Bottom right: Crack-width distribution of cracks in SHCC.

Load – max. CW – deflection curve

Fig. 5.12 shows the load – max. CW - deflection curve of beam PVA-RR-SI. The maximum crack-width is determined at every load step indicated in the previous section and is illustrated with grey dots. The 0.2mm crack-width limit and the 0.3mm crack-width limit are indicated with dotted red lines. The 0.2mm crack-width limit is exceeded at a load of 57.0kN and the 0.3mm crack-width limit is exceeded at a load 69.4kN.

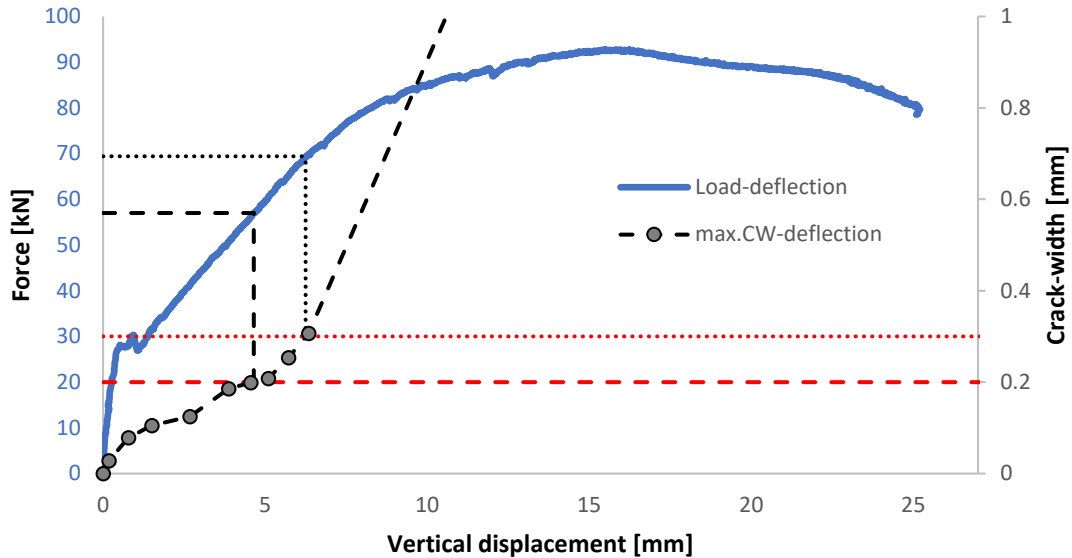


Fig. 5.12: Load - max.CW - deflection curve of beam PVA-RR-SI

Delamination & Slip

The delamination of the interface and the slip of the interface are shown in Fig. 5.13. This is done for three predefined measuring points; next to the localized propagated crack in the CC layer, 250mm left to the center of the CBMR and 250mm right to the center of the CBMR. These measuring points are indicated in Fig. 5.14, where the delamination is illustrated by contour plots of the vertical strains. It can be seen that the delamination and slip start at a load of 25kN. Upon increasing the load the delamination and slip increase. The contour plots and the delamination-curve both show that this is most evident close to the propagated crack. At the other locations delamination is insignificant. The maximum delamination (of 0.22mm) is found after yielding of the reinforcement, close to ultimate load. The contour plots reveal that full delamination of the interface does not occur in the CBMR.

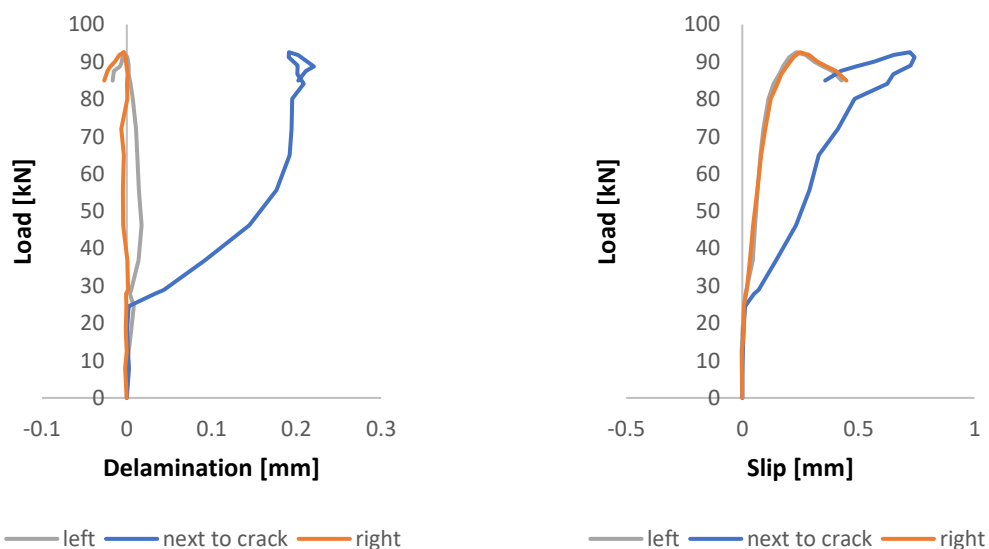


Fig. 5.13: Delamination (left) and slip (right) of interface of beam PVA-RR-SI for three measuring points

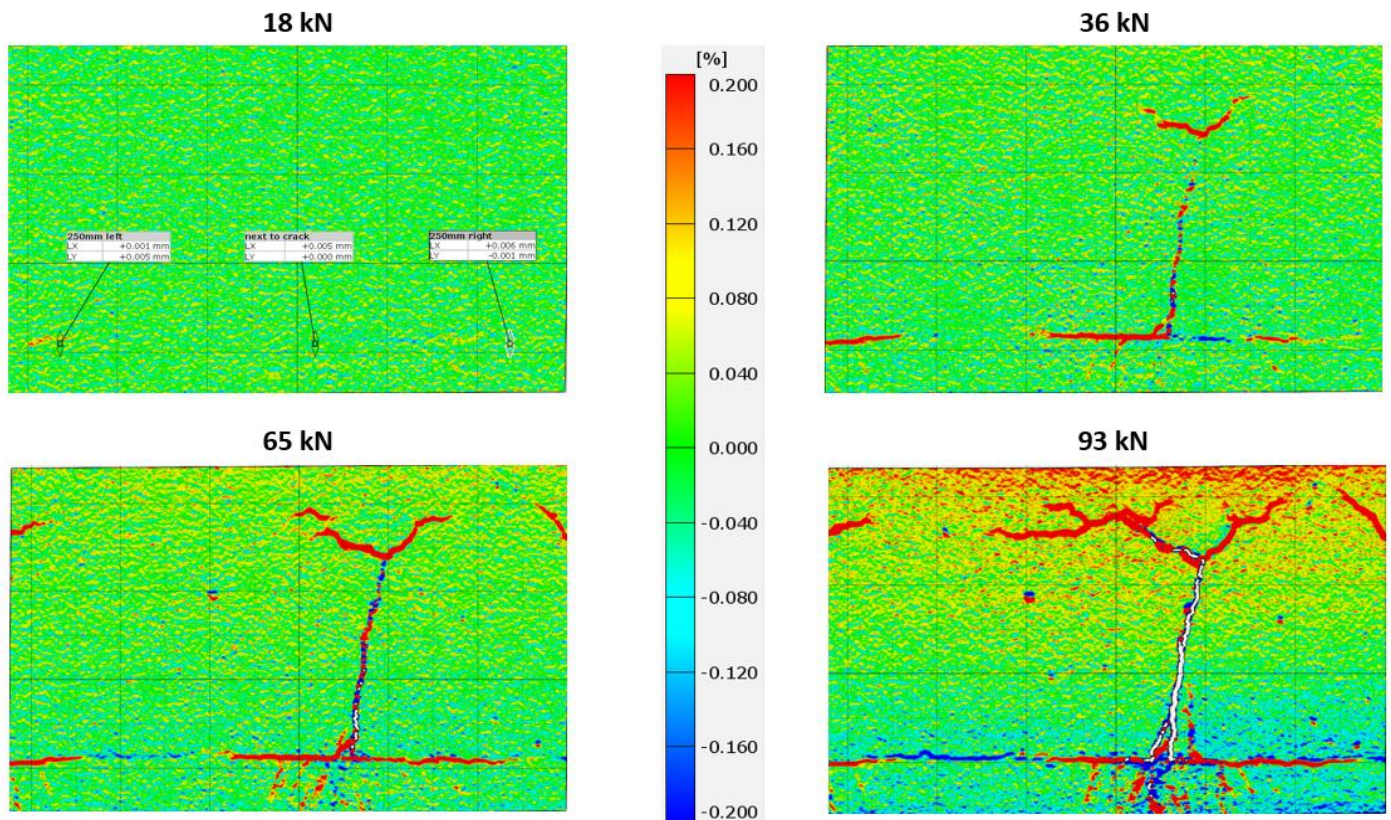


Fig. 5.14: Contour plots of vertical strains at several load levels of beam PVA-RR-SI

### Overview beam performance

Table 5.1 gives an overview of the performance of beam PVA-RR-SI.

Table 5.1: Overview beam performance of beam PVA-RR-SI

Key performance indicator	
Ultimate load	92.6kN
Maximum deflection	25.2mm
Number of cracks in CBMR in SHCC at ultimate load	27 cracks
Number of propagated cracks to CC in CBMR	1 crack
Load at 0.3mm cw-limit in CBMR	69.4kN
0.3mm load / yield load	89.9 %
Load at 0.2mm cw-limit in CBMR	57.0kN
0.2mm load / yield load	73.8 %

### 5.1.2 Beam PVA-RR-VPI

#### Load-deflection response

Fig. 5.15 illustrates the load-deflection response of beam PVA-RR-VPI. The crack formation stage started at a load of 25kN. Yielding of the reinforcement was observed at a load of 76.8kN and a deflection of 6.4mm. The ultimate load reached 90.4kN, with the beam failing at a deflection of 20.3mm due to the rupture of the reinforcement bar(s).

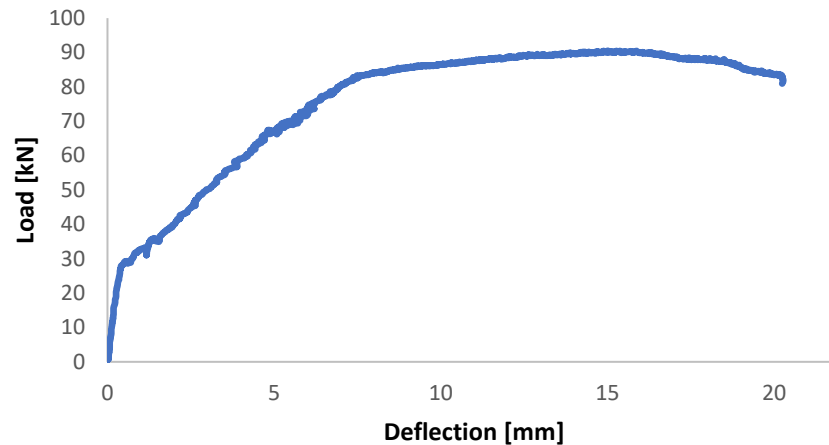


Fig. 5.15: Load-deflection response of beam PVA-RR-VPI

#### Validation GOM results

The DIC data are validated using LVDT2 and LVDT3 (located in the tension zone), as these measurements show an accurate match (Fig. 5.16). Although the laser and LVDT1 measurements also show a good correlation (Annex C), it is not accurate enough for full validation. Meanwhile, LVDT6, LVDT7, and LVDT8, positioned in the compression zone, exhibit only minimal strain, leading to a less accurate match, especially during the non-linear stage (Annex C).

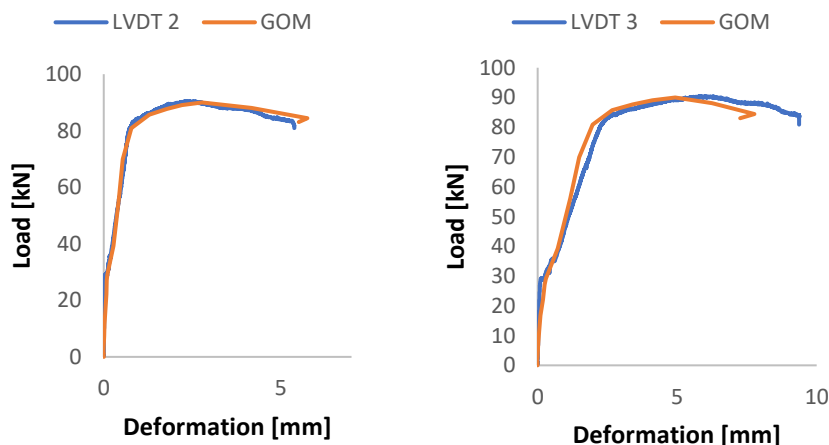


Fig. 5.16: Comparison of the measurements of LVDT2 (left) and LVDT3 (right) with the DIC measurements of beam PVA-RR-VPI

Crack pattern development

Fig. 5.17 to Fig. 5.26 shows the crack development of beam PVA-RR-VPI. It can be observed (Fig. 5.17) that cracks are detected even before the crack formation stage begins. A probable reason for this is the widening of shrinkage induced micro-cracks. However, the presence of cracks prior to testing was not investigated. As the load increases, more cracks form and existing cracks widen. The 0.2mm crack-width limit is exceeded after yielding of the reinforcement at a load level of 86kN (Fig. 5.24). The 0.3mm crack-width limit is exceeded close to the ultimate load at a load level of 89kN (Fig. 5.25). Three cracks propagate in the CC layer, with two of these cracks becoming localized. The SHCC layer is activated over the full length of the CBMR, leading to the formation of 48 cracks smaller than the 0.3mm crack-width limit and only three cracks exceeding this limit. This distribution keeps the average crack-width small, even at the ultimate load (Fig. 5.26).

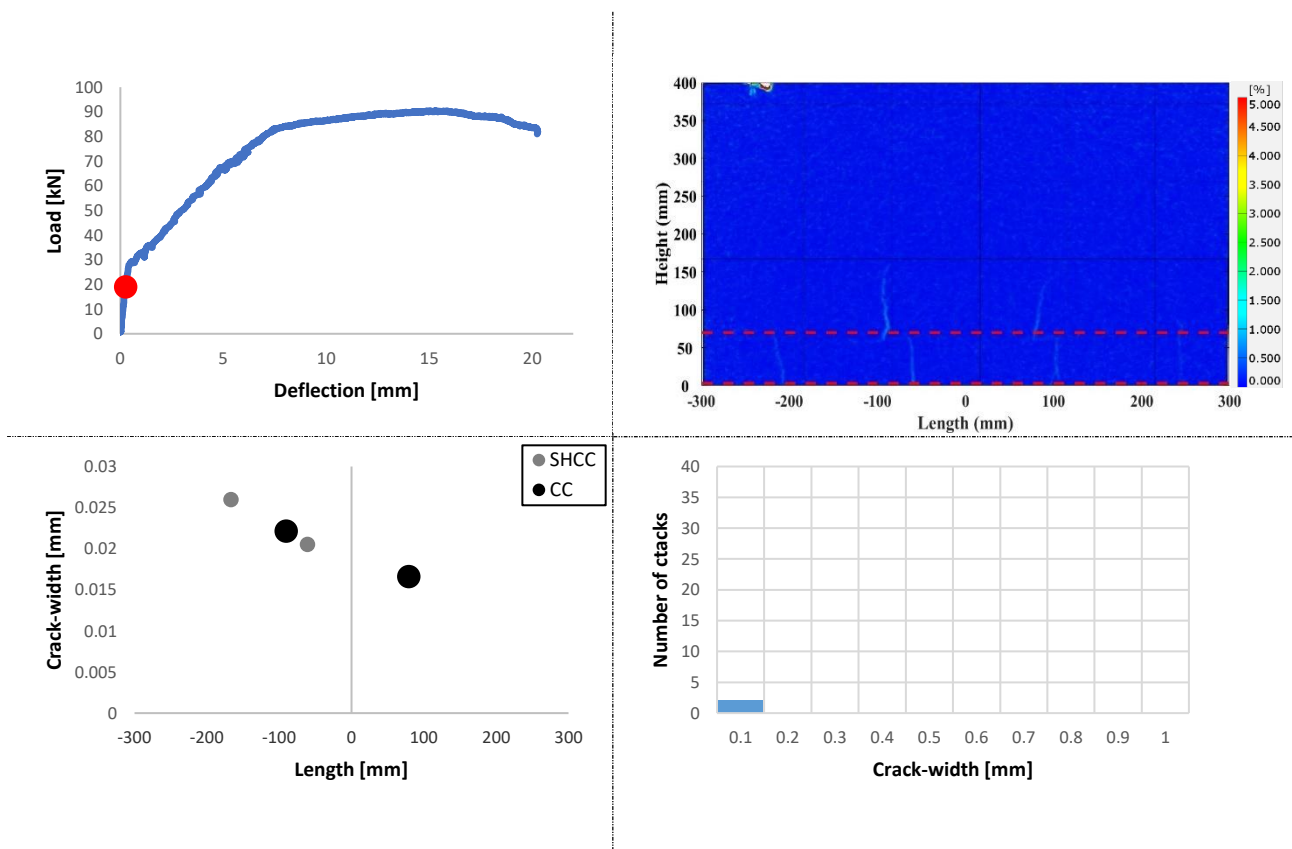


Fig. 5.17: Cracking behavior of beam PVA-RR-VPI at a load of 19kN. Top left: Load-level on load-deflection curve. Top right: Contour plot Von-Mises strains. Bottom left: Scatter plot of all cracks. Bottom right: Crack-width distribution of cracks in SHCC.

## 5. Results

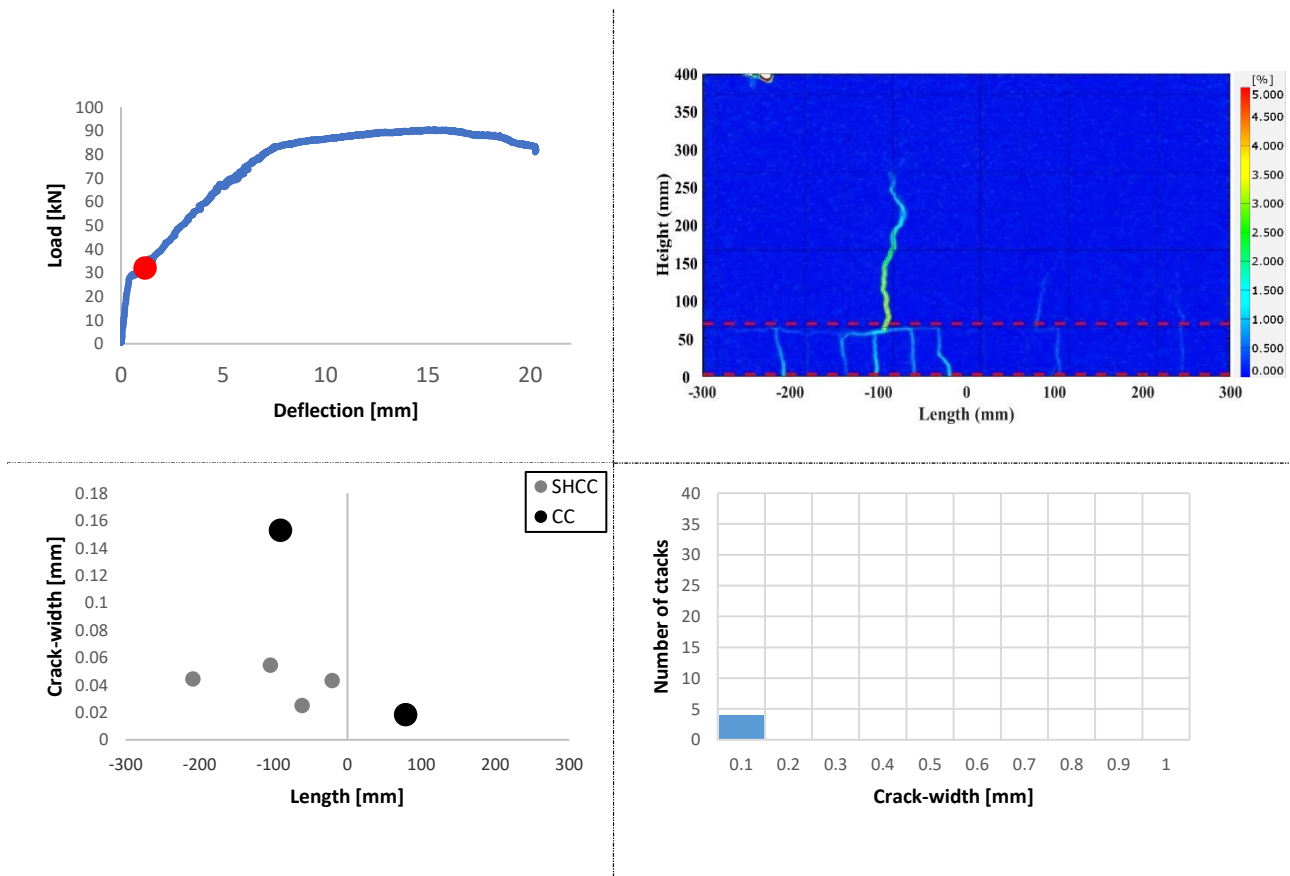


Fig. 5.18: Cracking behavior of beam PVA-RR-VPI at a load of 32kN. Top left: Load-level on load-deflection curve. Top right: Contour plot Von-Mises strains. Bottom left: Scatter plot of all cracks. Bottom right: Crack-width distribution of cracks in SHCC.

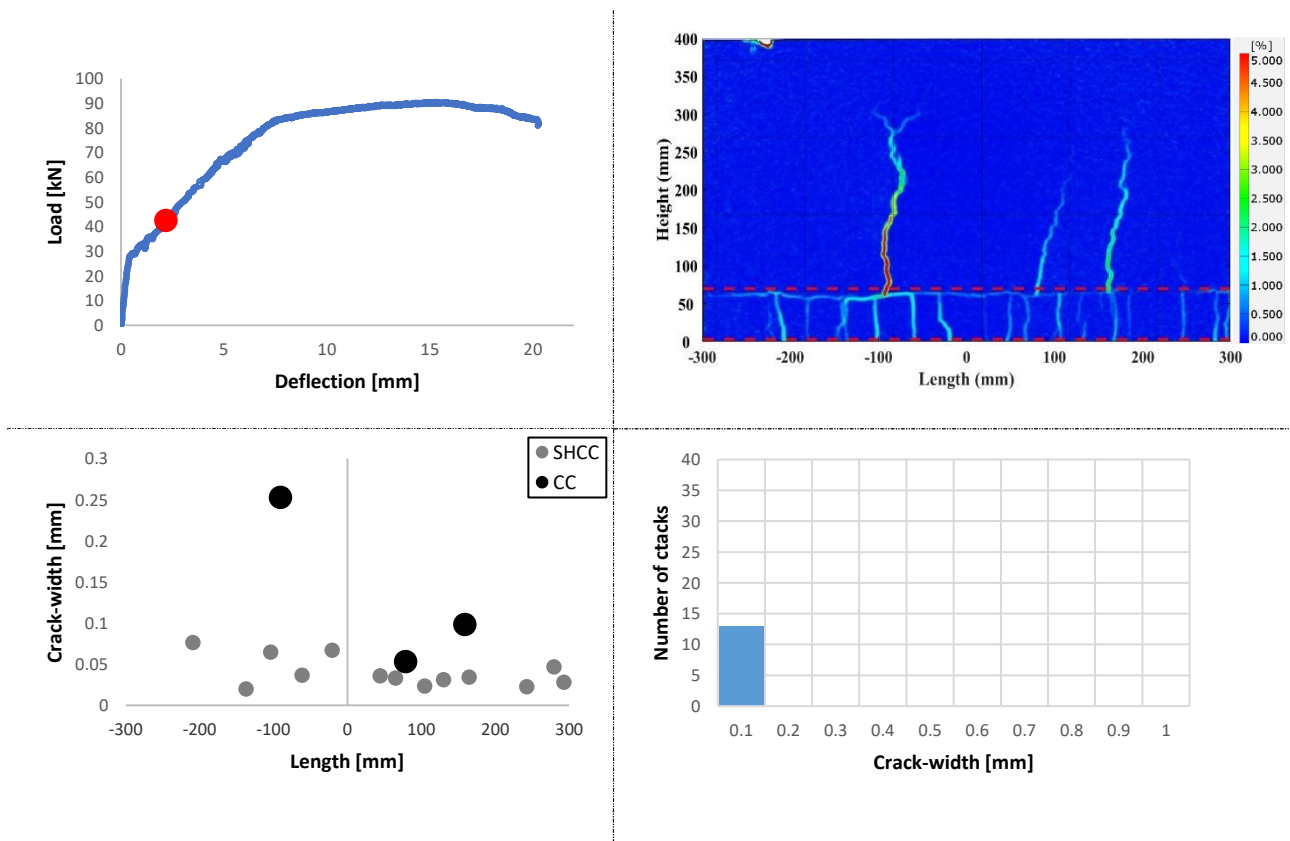


Fig. 5.19: Cracking behavior of beam PVA-RR-VPI at a load of 43kN. Top left: Load-level on load-deflection curve. Top right: Contour plot Von-Mises strains. Bottom left: Scatter plot of all cracks. Bottom right: Crack-width distribution of cracks in SHCC.

## 5. Results

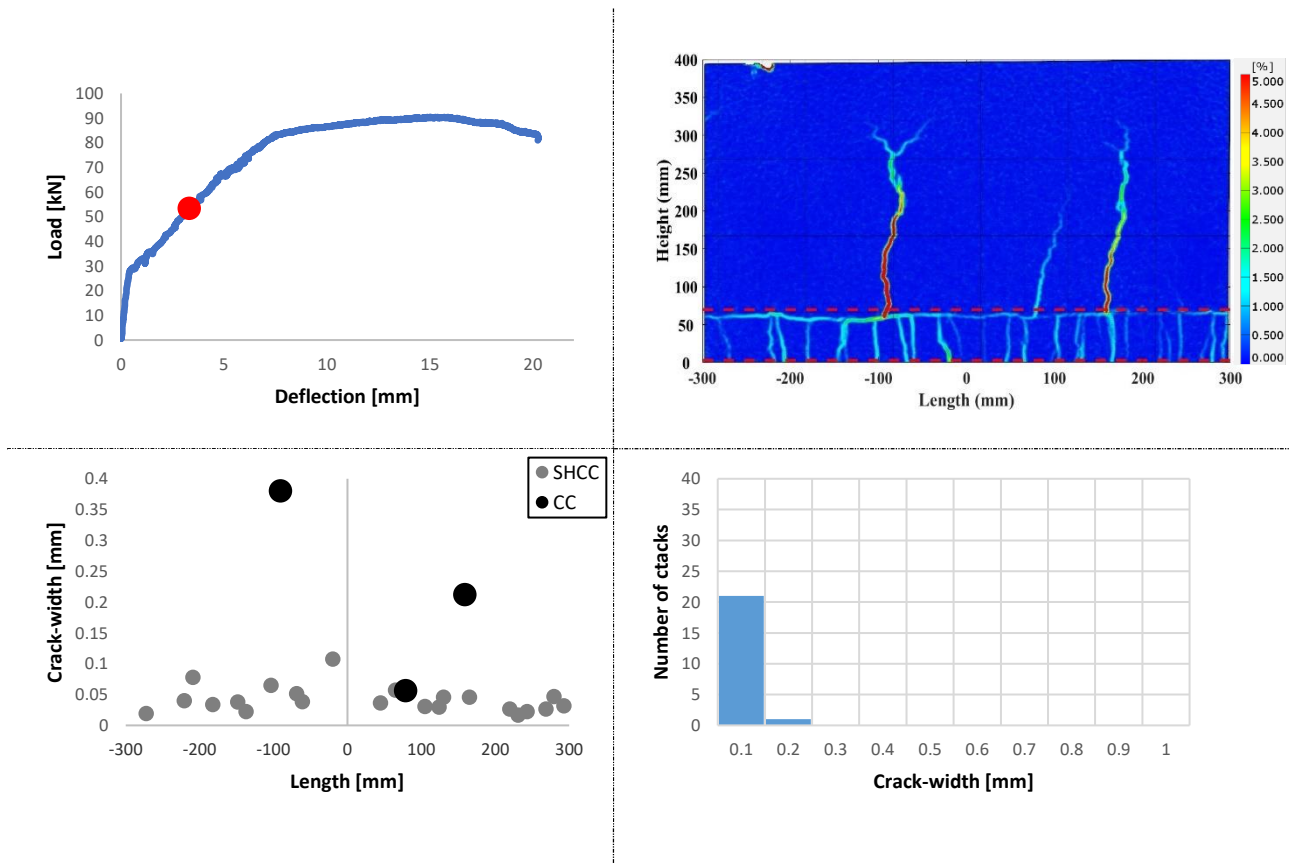


Fig. 5.20: Cracking behavior of beam PVA-RR-VPI at a load of 53kN. Top left: Load-level on load-deflection curve. Top right: Contour plot Von-Mises strains. Bottom left: Scatter plot of all cracks. Bottom right: Crack-width distribution of cracks in SHCC.

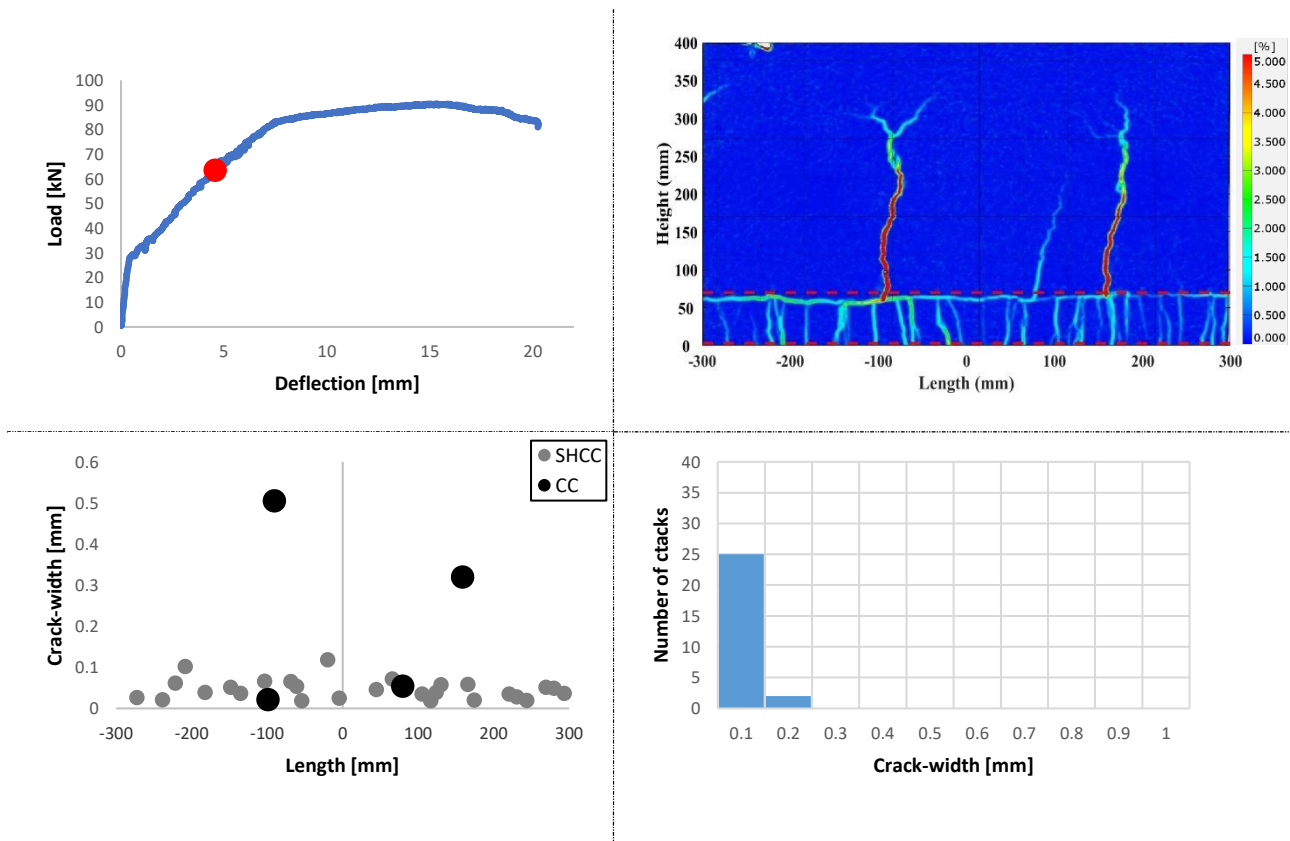


Fig. 5.21: Cracking behavior of beam PVA-RR-VPI at a load of 64kN. Top left: Load-level on load-deflection curve. Top right: Contour plot Von-Mises strains. Bottom left: Scatter plot of all cracks. Bottom right: Crack-width distribution of cracks in SHCC.

## 5. Results

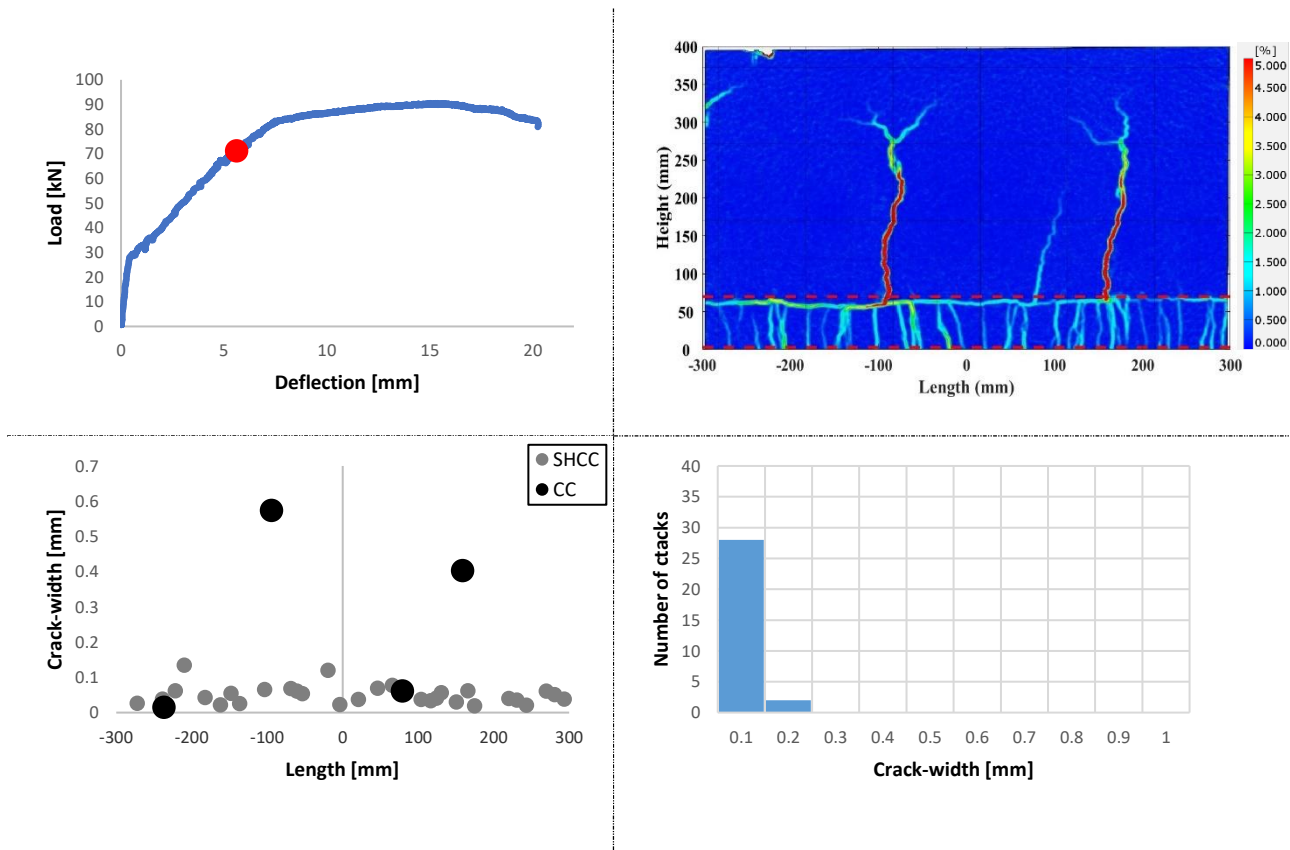


Fig. 5.22: Cracking behavior of beam PVA-RR-VPI at a load of 71kN. Top left: Load-level on load-deflection curve. Top right: Contour plot Von-Mises strains. Bottom left: Scatter plot of all cracks. Bottom right: Crack-width distribution of cracks in SHCC.

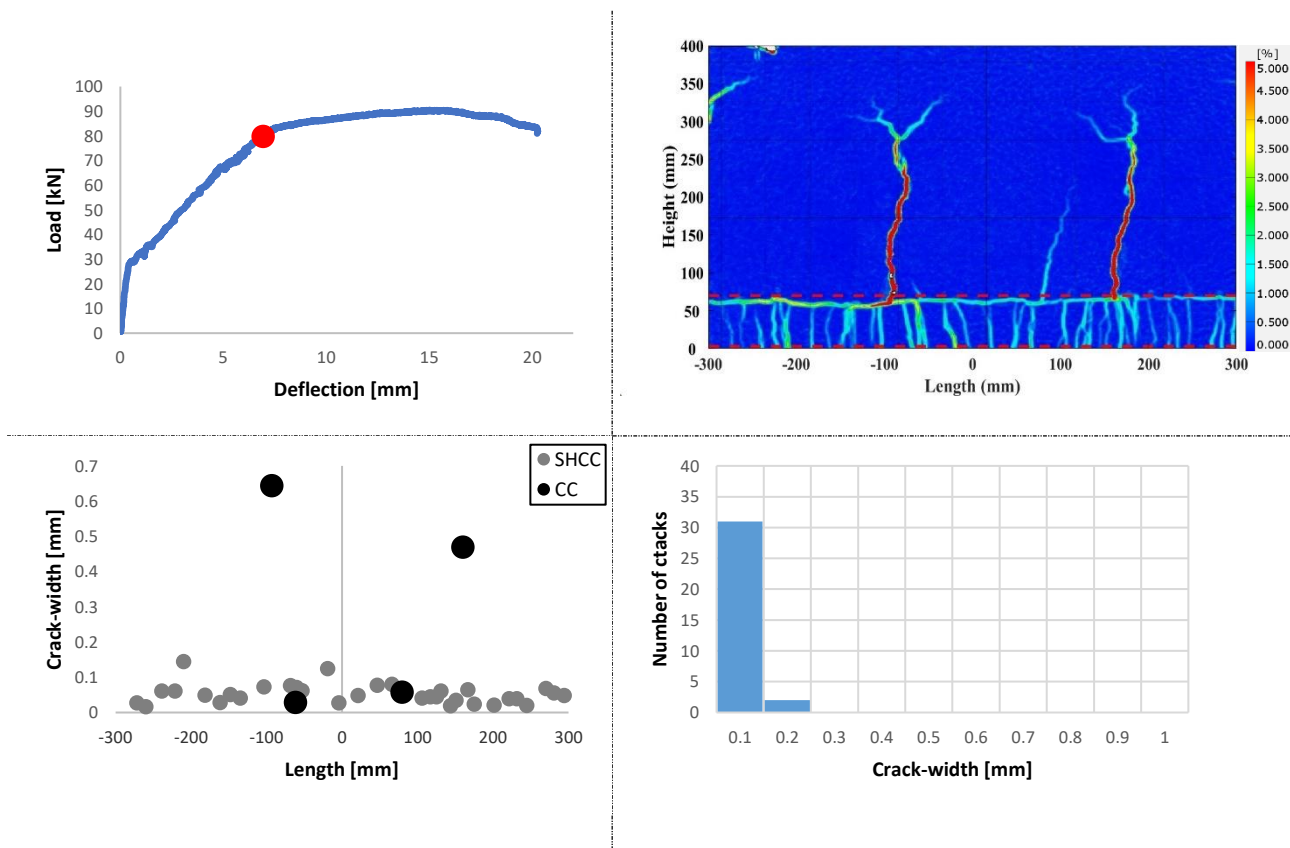


Fig. 5.23: Cracking behavior of beam PVA-RR-VPI at a load of 80kN. Top left: Load-level on load-deflection curve. Top right: Contour plot Von-Mises strains. Bottom left: Scatter plot of all cracks. Bottom right: Crack-width distribution of cracks in SHCC.

## 5. Results

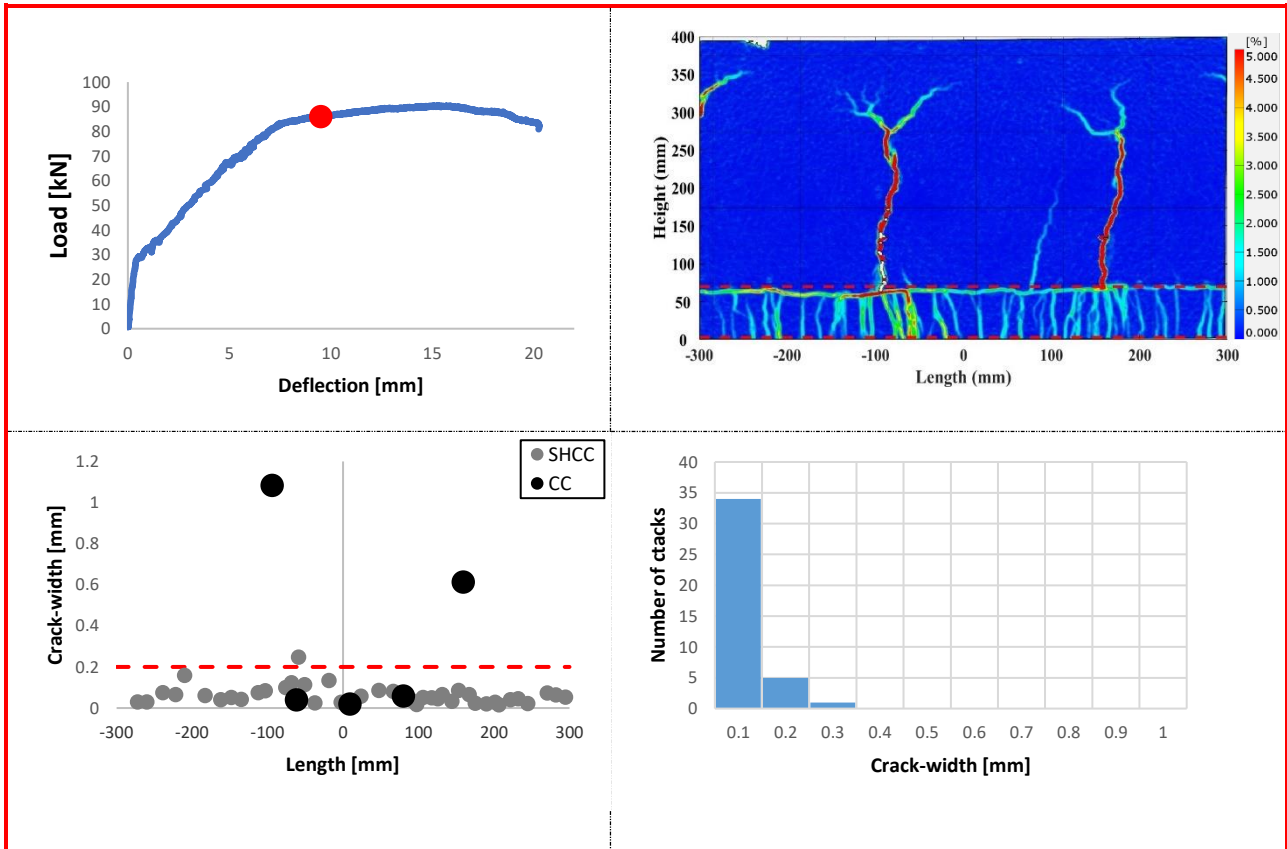


Fig. 5.24: Cracking behavior of beam PVA-RR-VPI at a load of 86kN. Top left: Load-level on load-deflection curve. Top right: Contour plot Von-Mises strains. Bottom left: Scatter plot of all cracks. Bottom right: Crack-width distribution of cracks in SHCC.

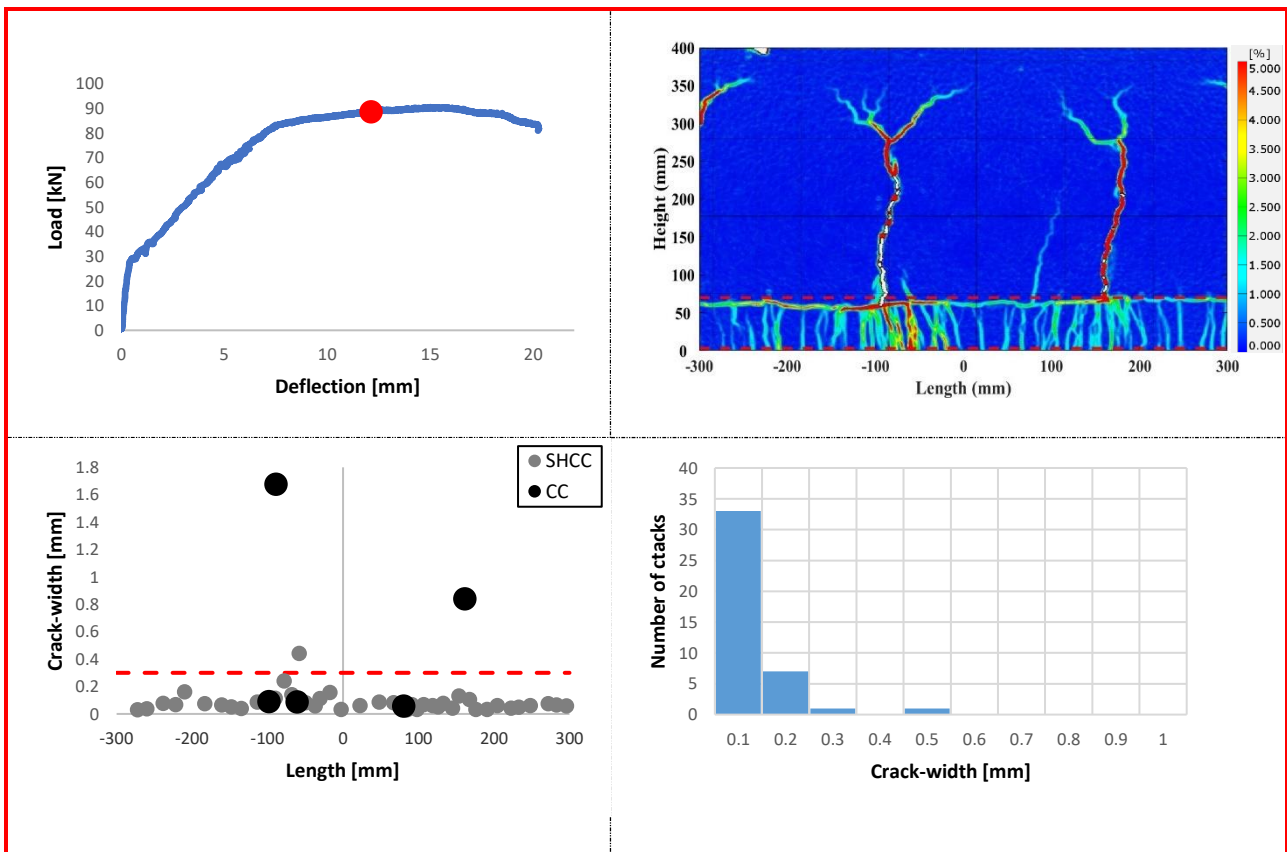


Fig. 5.25: Cracking behavior of beam PVA-RR-VPI at a load of 89kN. Top left: Load-level on load-deflection curve. Top right: Contour plot Von-Mises strains. Bottom left: Scatter plot of all cracks. Bottom right: Crack-width distribution of cracks in SHCC.

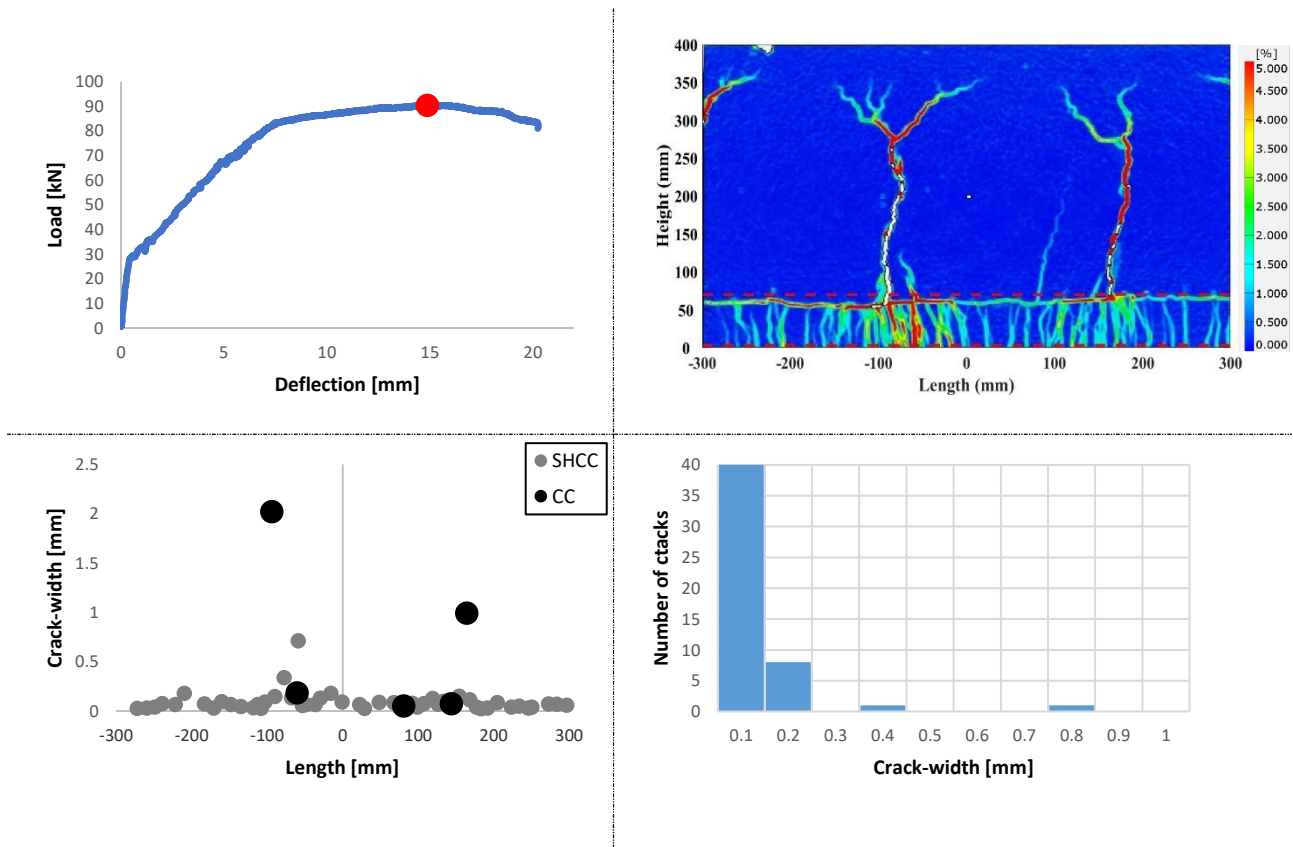


Fig. 5.26: Cracking behavior of beam PVA-RR-VPI at a load of 90kN. Top left: Load-level on load-deflection curve. Top right: Contour plot Von-Mises strains. Bottom left: Scatter plot of all cracks. Bottom right: Crack-width distribution of cracks in SHCC.

Load – max. CW – deflection curve

Fig. 5.27 shows the load – max. CW - deflection curve of beam PVA-RR-VPI. The maximum crack-width is determined at every load step indicated in the previous section and is illustrated with grey dots. The 0.2mm crack-width limit and the 0.3mm crack-width limit are indicated with dotted red lines. The 0.2mm crack-width limit and 0.3mm crack-width limit are both exceeded after yielding at a load of 85.6kN and 86.5kN, respectively.

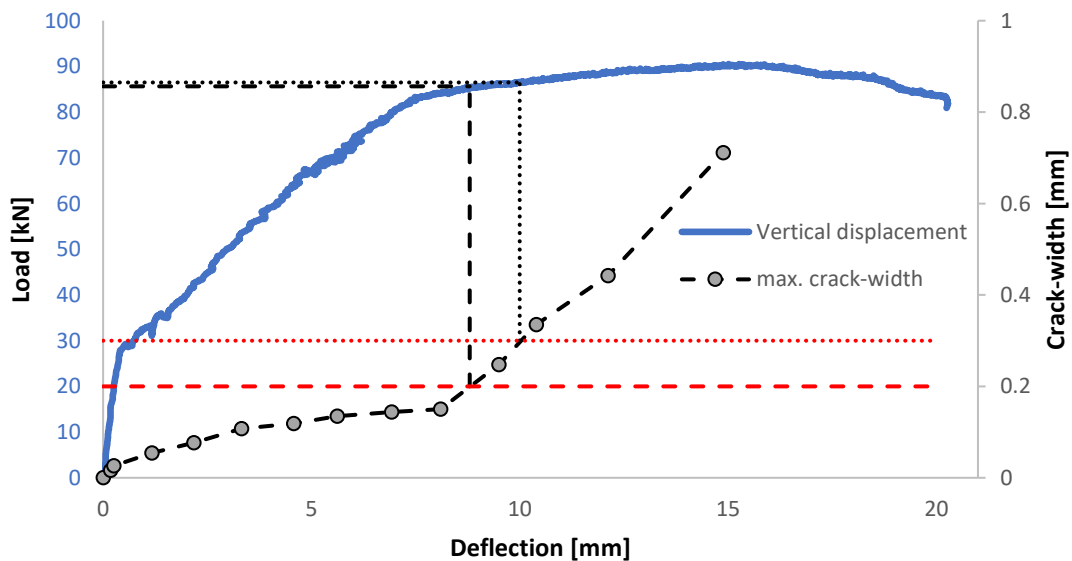


Fig. 5.27: Load - max.CW - deflection curve of beam PVA-RR-VPI

### Delamination & Slip

The delamination of the interface and the slip of the interface are shown in Fig. 5.29. This is done for three predefined measuring points; next to the most prominent localized crack in the CC layer, 250mm left to the center of the CBMR and 250mm right to the center of the CBMR. These measuring points are indicated in Fig. 5.28, where the delamination is illustrated by contour plots of the vertical strains. It can be seen that the delamination and slip start to become noticeable at a load of 19kN. Upon increasing the load the delamination and slip increase. At ultimate load the biggest delamination (0.13mm) occurs close to the crack. At failure the crack further delaminates the two concretes, reaching a delamination of 0.38mm. The contour plots show that the interface delaminates over the entire length of the CBMR; however, this delamination remains restricted well below 0.2mm at yielding (and even at ultimate load).

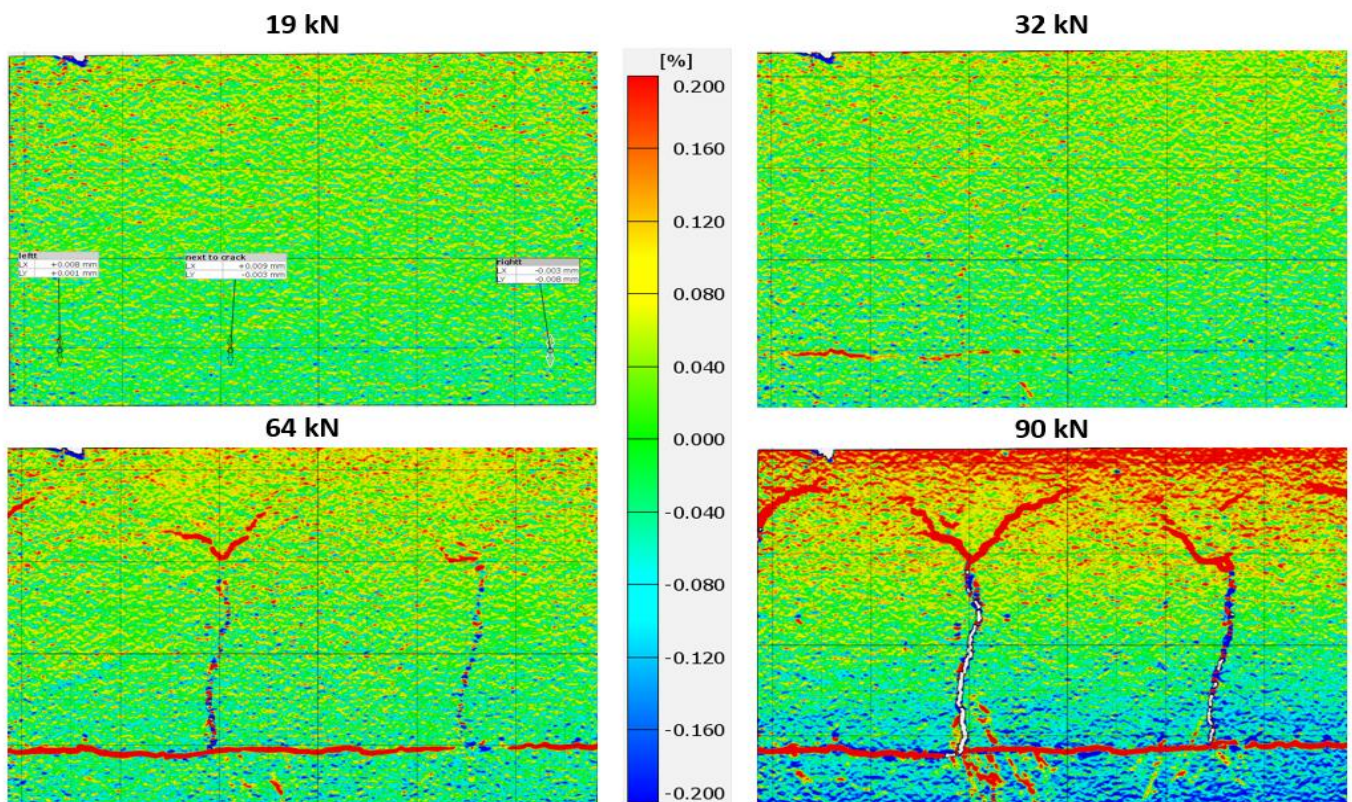
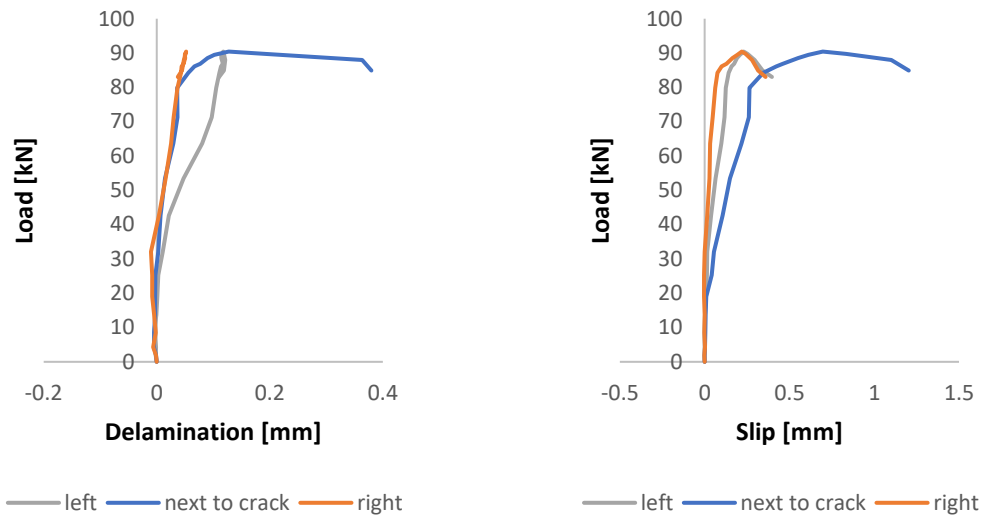


Fig. 5.28: Contour plots of vertical strains at several load levels of beam PVA-RR-VPI

Overview beam performance

Table 5.2 gives an overview of the performance of beam PVA-RR-VPI.

Table 5.2: Overview beam performance of beam PVA-RR-VPI

Key performance indicator	
Ultimate load	90.4kN
Maximum deflection	20.3mm
Number of cracks in CBMR in SHCC at ultimate load	50 cracks
Number of propagated cracks to CC in CBMR	3 cracks
Load at 0.3mm cw-limit in CBMR	86.5kN
0.3mm load / yield load	112.6 %
Load at 0.2mm cw-limit in CBMR	85.6kN
0.2mm load / yield load	111.5 %

### 5.1.3 Beam PVA-SR-VPI

#### Load-deflection response

Fig. 5.30 illustrates the load-deflection and deflection-time response of beam PVA-SR-VPI. At the beginning of the experiment the laser shows a negative deflection. This is probably caused by a slight tilting of the wooden slat on which the laser is mounted when the load cell first touched the steel beam load spreader. This error is thus corrected for (Fig. 5.31). The crack formation stage started at a load of 30kN. Yielding of the reinforcement was observed at a load of 75.9kN and a deflection of 6.8mm. At a load of 85.1kN and a deflection of 9.1mm a sudden drop occurs, attributed to the strong localization of a crack penetrating through both the SHCC and CC layers. Following this, hardening is observed. The ultimate load reached 85.8kN, with the beam failing at a deflection of 26.4mm due to the rupture of the reinforcement bar(s).

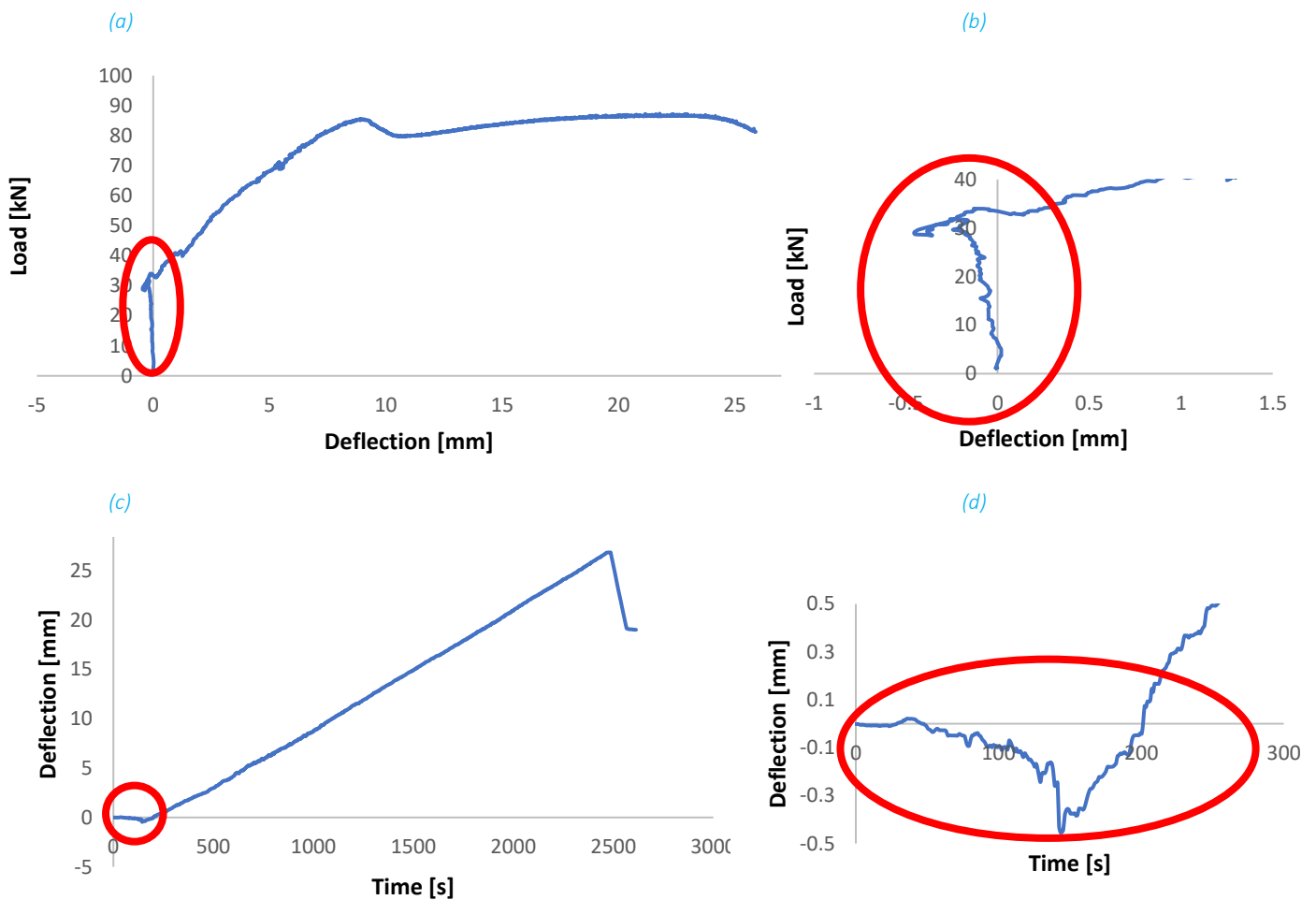


Fig. 5.30: Load-deflection response of beam PVA-SR-VPI: (a) Whole experiment and (b) Beginning stage of experiment and Deflection-time response of beam PVA-SR-VPI: (c) Whole experiment and (d) Beginning stage of experiment

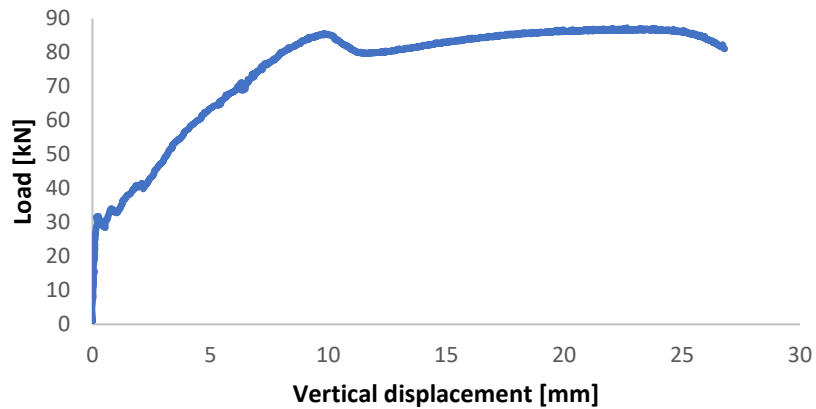


Fig. 5.31: Corrected load-deflection response of beam PVA-SR-VPI

### Validation GOM results

The DIC data are validated using LVDT3 (located in the tension zone), as these measurements show an accurate match (Fig. 5.32). Although LVDT1 and LVDT2 also demonstrate good correlation during the linear elastic stage, the data does not align well in the non-linear stage (Annex C). Meanwhile, LVDT6, LVDT7, and LVDT8, positioned in the compression zone, exhibit only minimal strain, resulting in a less accurate match, particularly during the non-linear stage (Annex C).

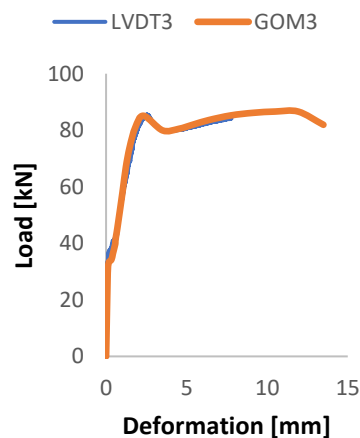


Fig. 5.32: Comparison of the measurements of LVDT3 with the DIC measurements of beam PVA-SR-VPI

### Crack pattern development

Fig. 5.33 to Fig. 5.41 shows the crack development of beam PVA-SR-VPI. As the load increases, more cracks form and existing cracks widen. The activation of SHCC is limited and concentrated around two localized and propagated cracks in the CC layer, which merge into one in the compression zone. At a load level of 58kN, SHCC cracks even close as a result of the widening of cracks around the CC crack. At this load level, the 0.2mm crack-width limit is also exceeded (Fig. 5.37). At a load level of 61kN, the 0.3mm crack-width limit is exceeded (Fig. 5.38). After a load level of 81kN (Fig. 5.39), a sudden drop in the load-deflection curve occurs, caused by the strong localization of the crack penetrating through both the SHCC and CC layer, as can be seen in Fig. 5.40. Following this drop, hardening is observed. At ultimate load, nine cracks form in the SHCC layer.

## 5. Results

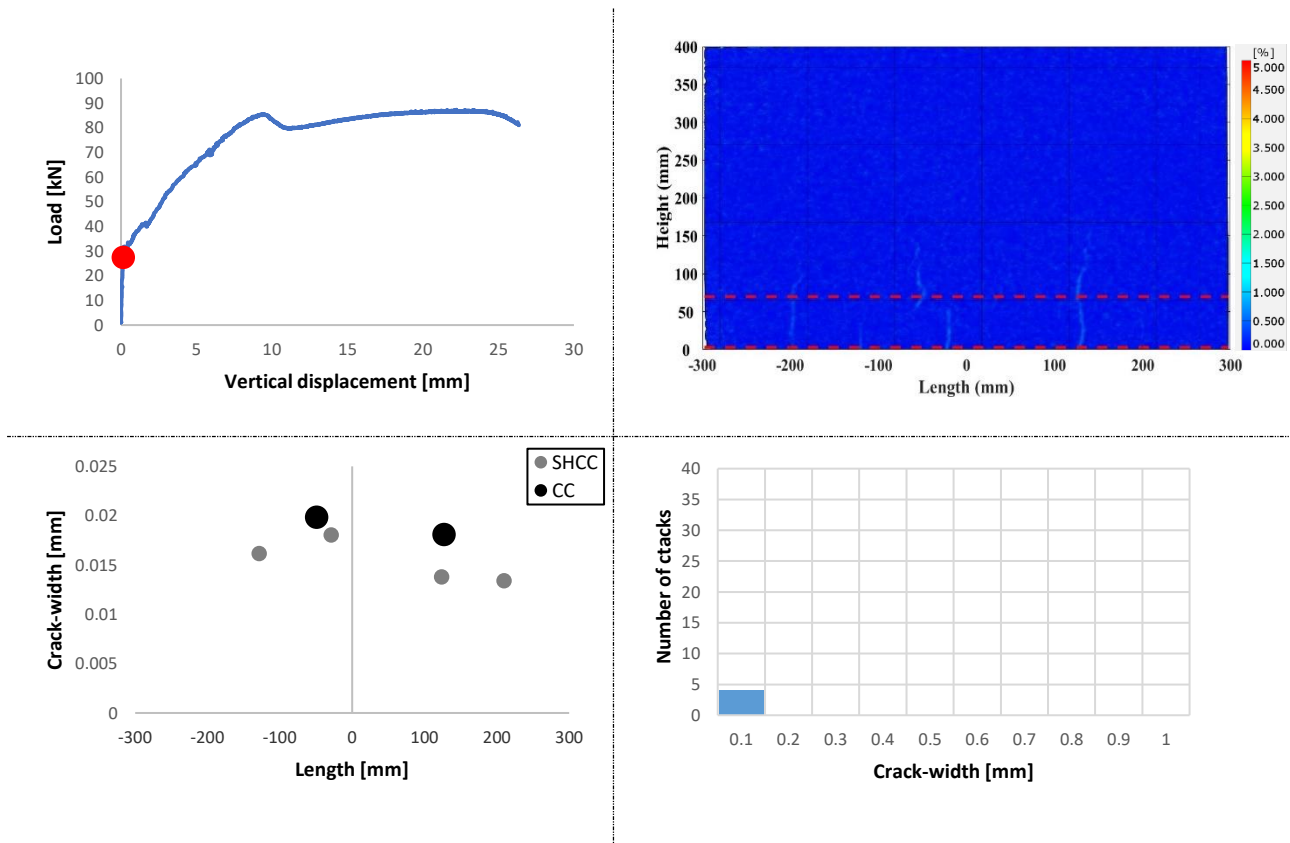


Fig. 5.33: Cracking behavior of beam PVA-SR-VPI at a load of 27kN. Top left: Load-level on load-deflection curve. Top right: Contour plot Von-Mises strains. Bottom left: Scatter plot of all cracks. Bottom right: Crack-width distribution of cracks in SHCC.

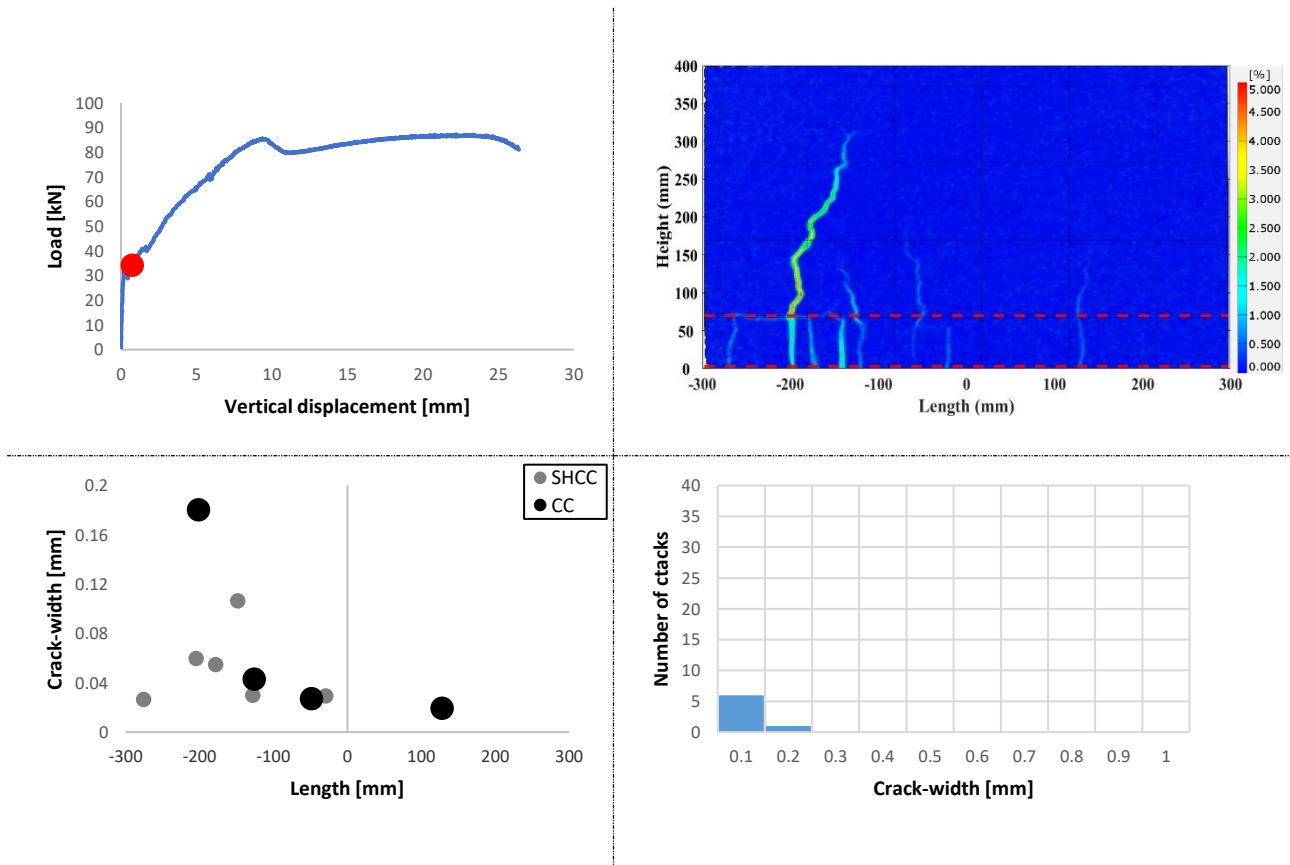


Fig. 5.34: Cracking behavior of beam PVA-SR-VPI at a load of 33kN. Top left: Load-level on load-deflection curve. Top right: Contour plot Von-Mises strains. Bottom left: Scatter plot of all cracks. Bottom right: Crack-width distribution of cracks in SHCC.

## 5. Results

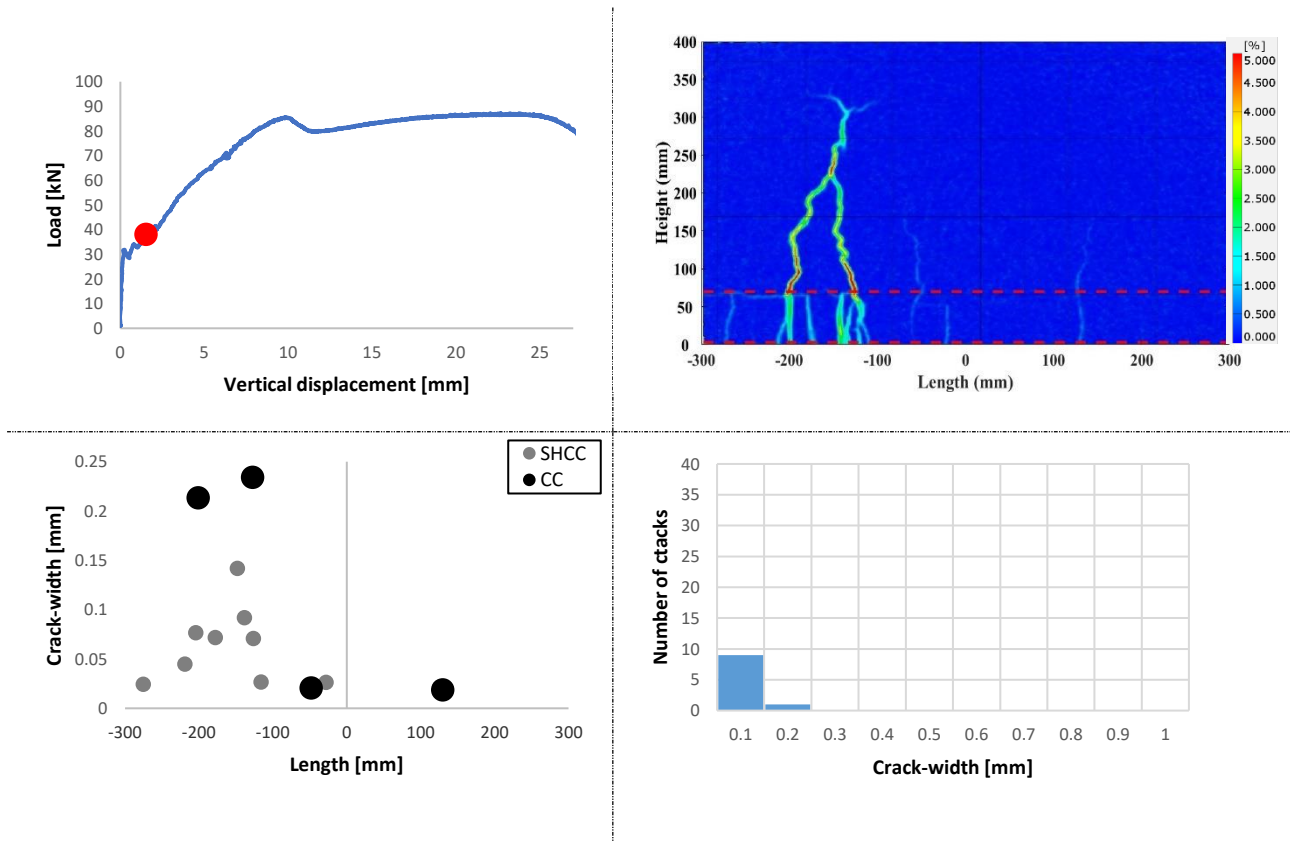


Fig. 5.35: Cracking behavior of beam PVA-SR-VPI at a load of 38kN. Top left: Load-level on load-deflection curve. Top right: Contour plot Von-Mises strains. Bottom left: Scatter plot of all cracks. Bottom right: Crack-width distribution of cracks in SHCC.

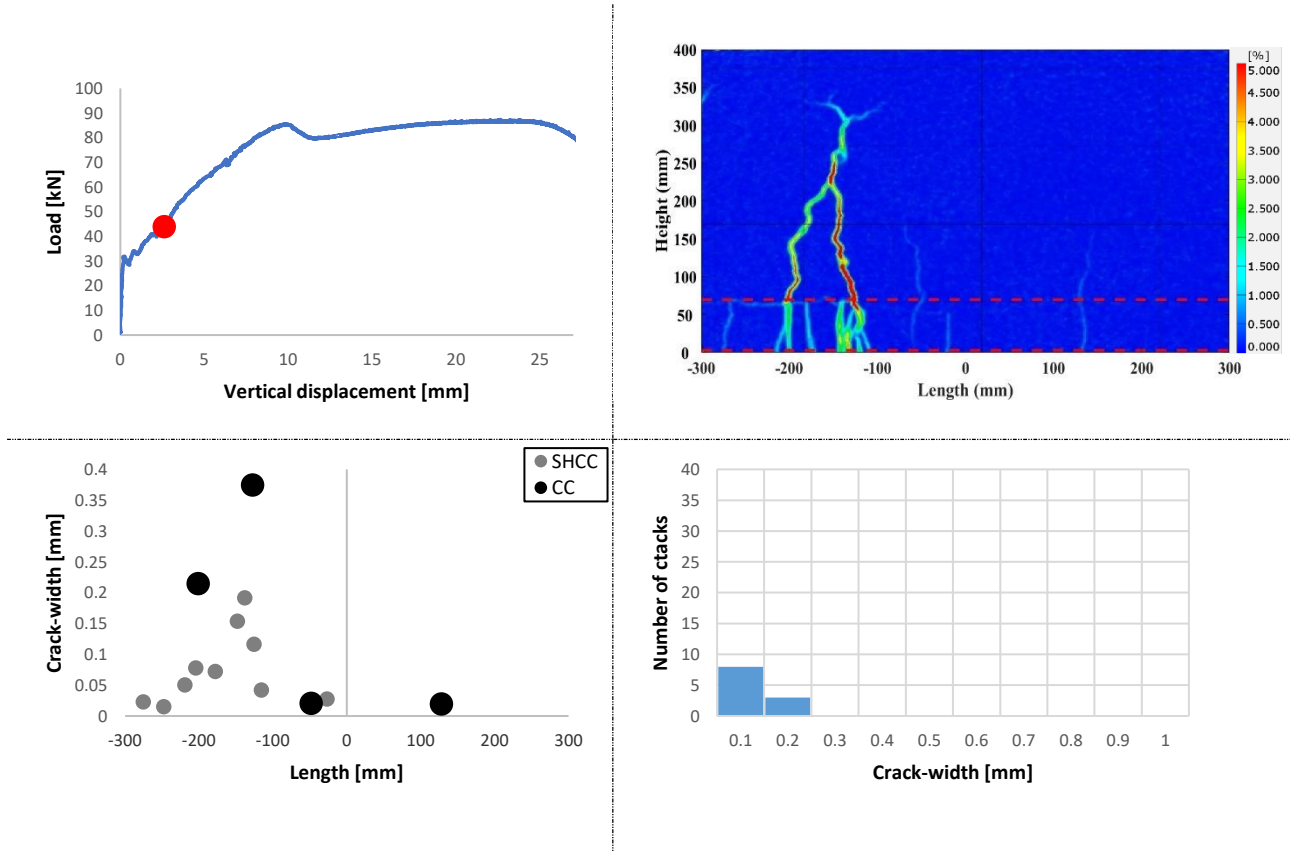


Fig. 5.36: Cracking behavior of beam PVA-SR-VPI at a load of 44kN. Top left: Load-level on load-deflection curve. Top right: Contour plot Von-Mises strains. Bottom left: Scatter plot of all cracks. Bottom right: Crack-width distribution of cracks in SHCC.

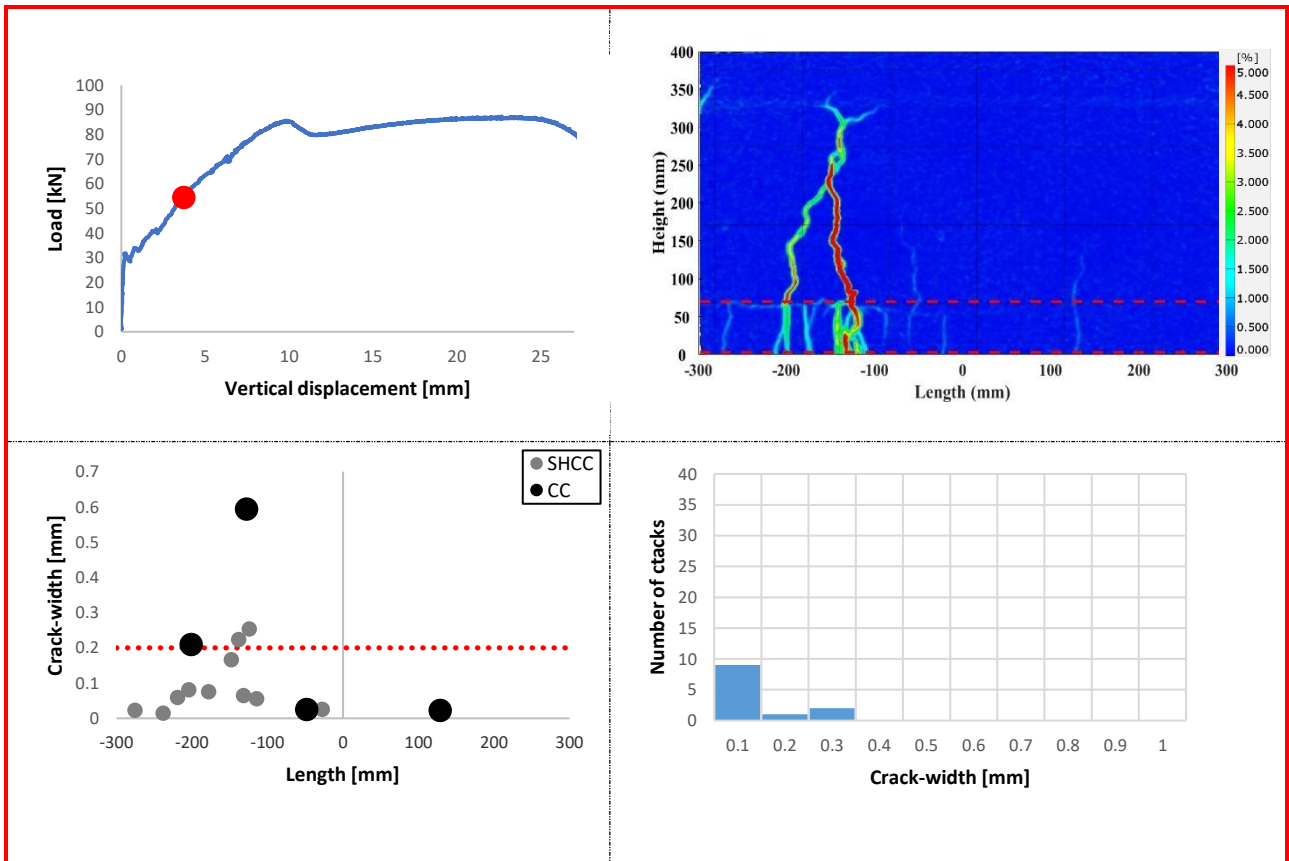


Fig. 5.37: Cracking behavior of beam PVA-SR-VPI at a load of 55kN. Top left: Load-level on load-deflection curve. Top right: Contour plot Von-Mises strains. Bottom left: Scatter plot of all cracks. Bottom right: Crack-width distribution of cracks in SHCC.

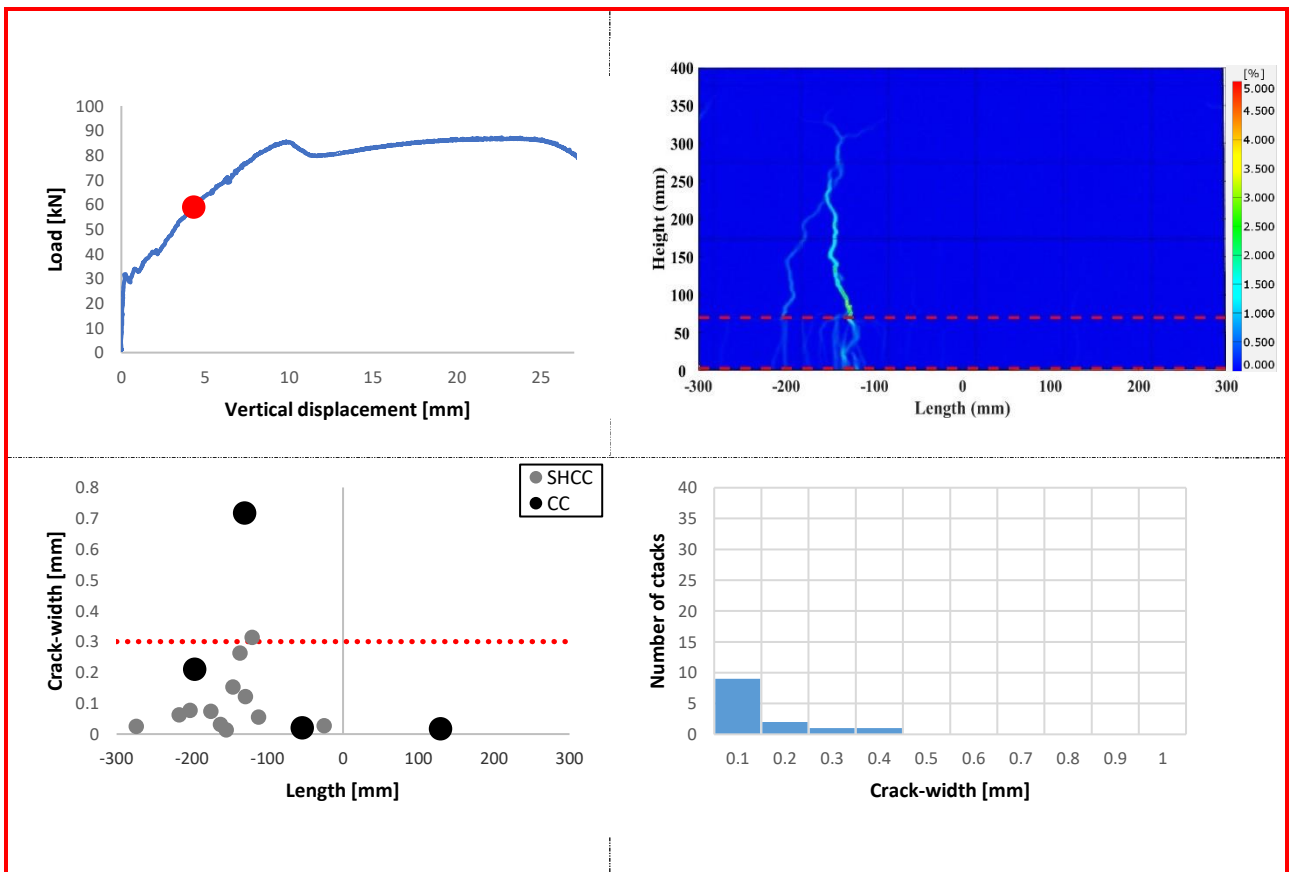


Fig. 5.38: Cracking behavior of beam PVA-SR-VPI at a load of 59kN. Top left: Load-level on load-deflection curve. Top right: Contour plot Von-Mises strains. Bottom left: Scatter plot of all cracks. Bottom right: Crack-width distribution of cracks in SHCC.

## 5. Results

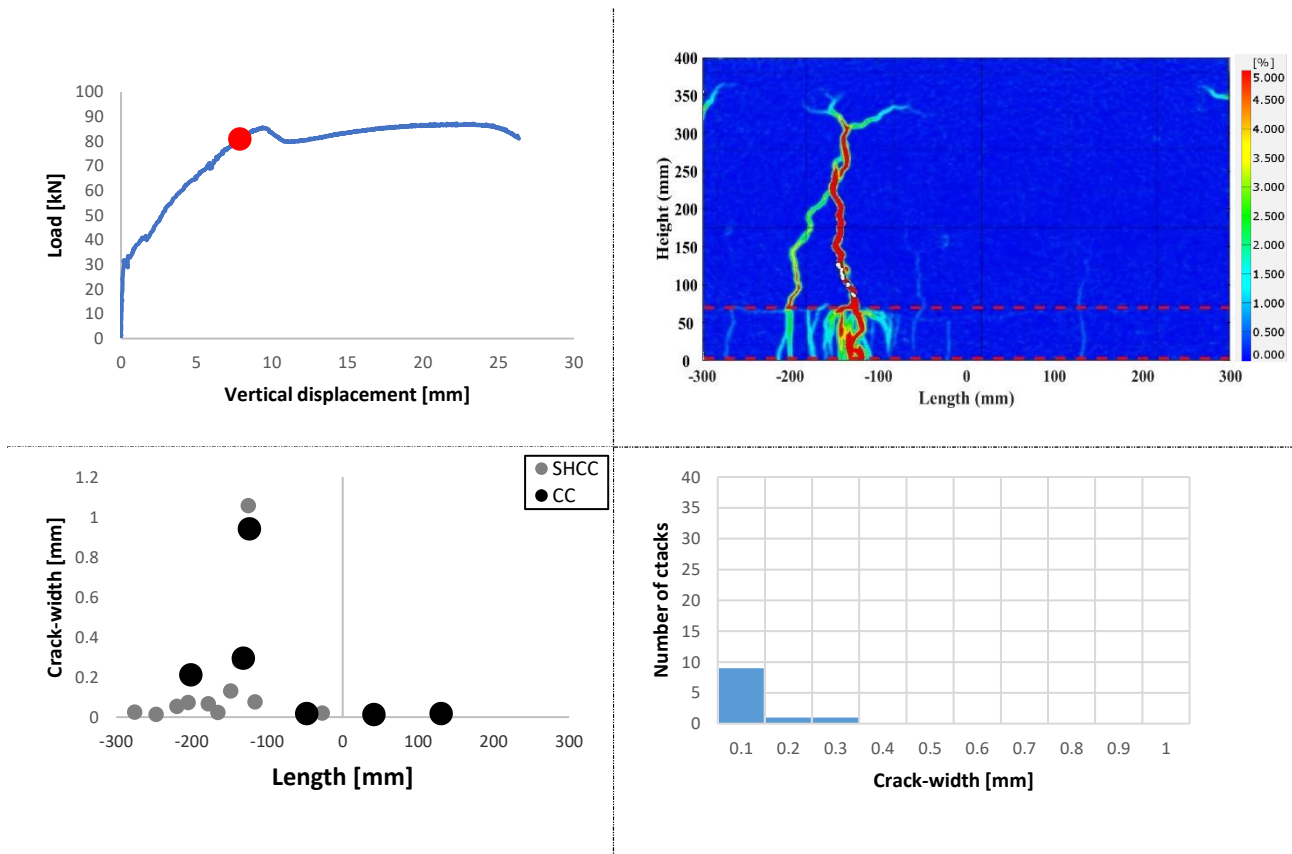


Fig. 5.39: Cracking behavior of beam PVA-SR-VPI at a load of 81N. Top left: Load-level on load-deflection curve. Top right: Contour plot Von-Mises strains. Bottom left: Scatter plot of all cracks. Bottom right: Crack-width distribution of cracks in SHCC.

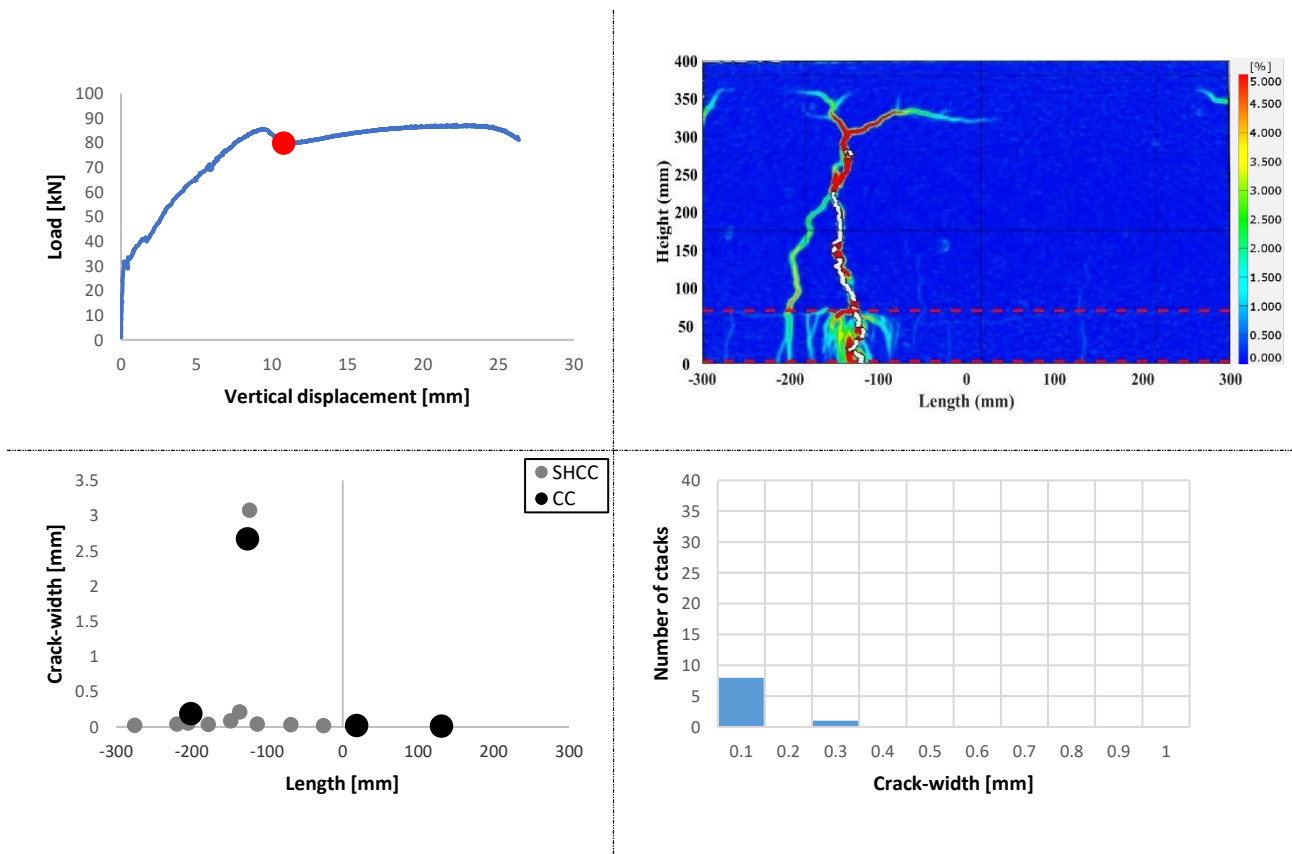


Fig. 5.40: Cracking behavior of beam PVA-SR-VPI at a load of 80kN. Top left: Load-level on load-deflection curve. Top right: Contour plot Von-Mises strains. Bottom left: Scatter plot of all cracks. Bottom right: Crack-width distribution of cracks in SHCC.

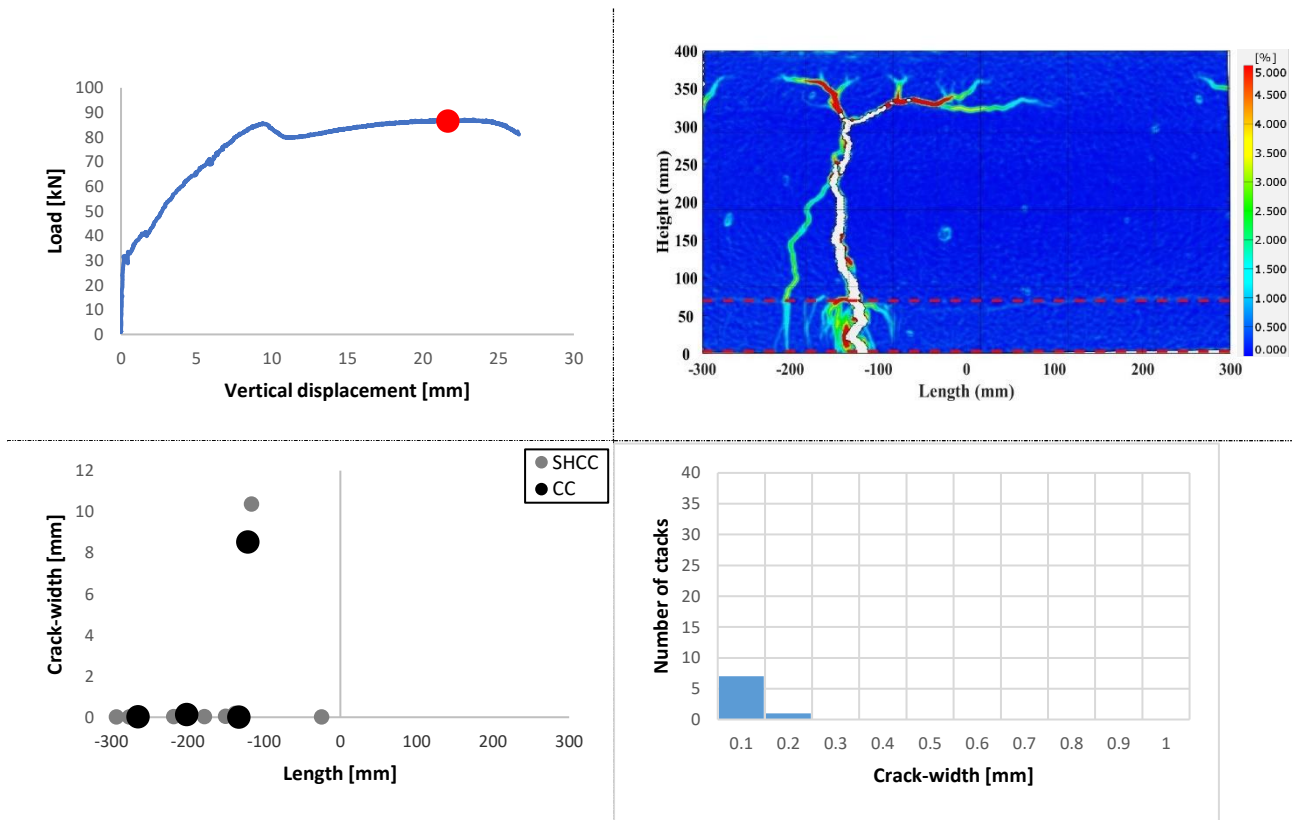


Fig. 5.41: Cracking behavior of beam PVA-SR-VPI at a load of 87kN. Top left: Load-level on load-deflection curve. Top right: Contour plot Von-Mises strains. Bottom left: Scatter plot of all cracks. Bottom right: Crack-width distribution of cracks in SHCC.

Load – max. CW – deflection curve

Fig. 5.42 shows the load – max. CW - deflection curve of beam PVA-SR-VPI. The maximum crack-width is determined at every load step indicated in the previous section and is illustrated with grey dots. The 0.2mm crack-width limit and the 0.3mm crack-width limit are indicated with dotted red lines. The 0.2mm crack-width limit is exceeded at a load of 45.9kN and the 0.3mm crack-width limit is exceeded at a load of 58.4kN.

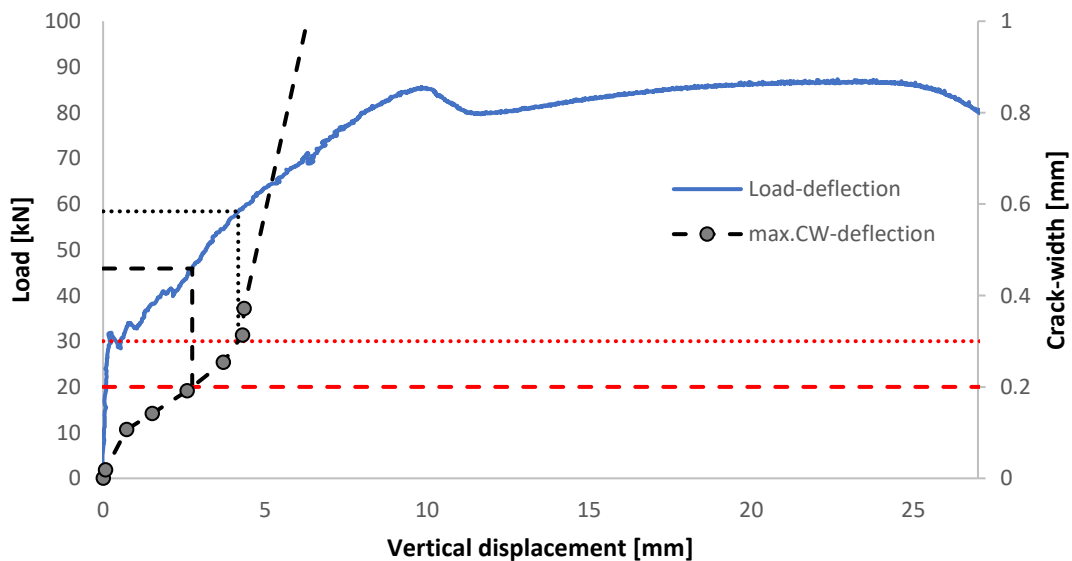


Fig. 5.42: Load - max.CW - deflection curve of beam PVA-SR-VPI

### Delamination & Slip

The delamination of the interface and the slip of the interface are shown in Fig. 5.43. This is done for four predefined measuring points; next to the localized crack in the CC layer, at the center of the CBMR, 250mm left to the center of the CBMR and 250mm right to the center of the CBMR. These measuring points are indicated in Fig. 5.44, where the delamination is illustrated by contour plots of the vertical strains. It can be seen that the delamination and slip start to become noticeable at a load of 30kN. However, upon increasing the load the delamination and slip increase limitedly. Delamination is only found to occur close the localized crack (locations 'next to crack' and 'left' in Fig. 5.44). Peak delamination was found to be 0.07mm. Thus, only partial and limited delamination occurs.

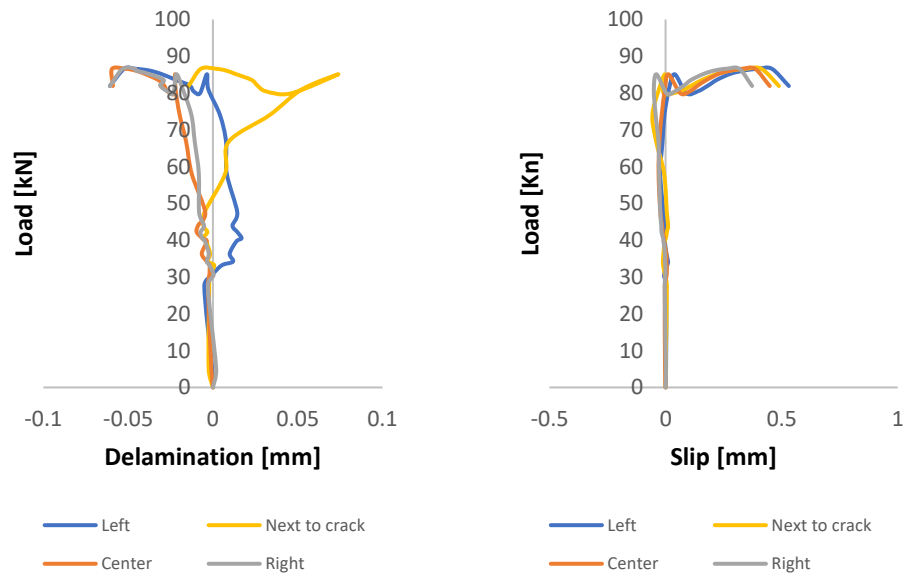


Fig. 5.43: Delamination (left) and slip (right) of interface of beam PVA-SR-VPI for four measuring points

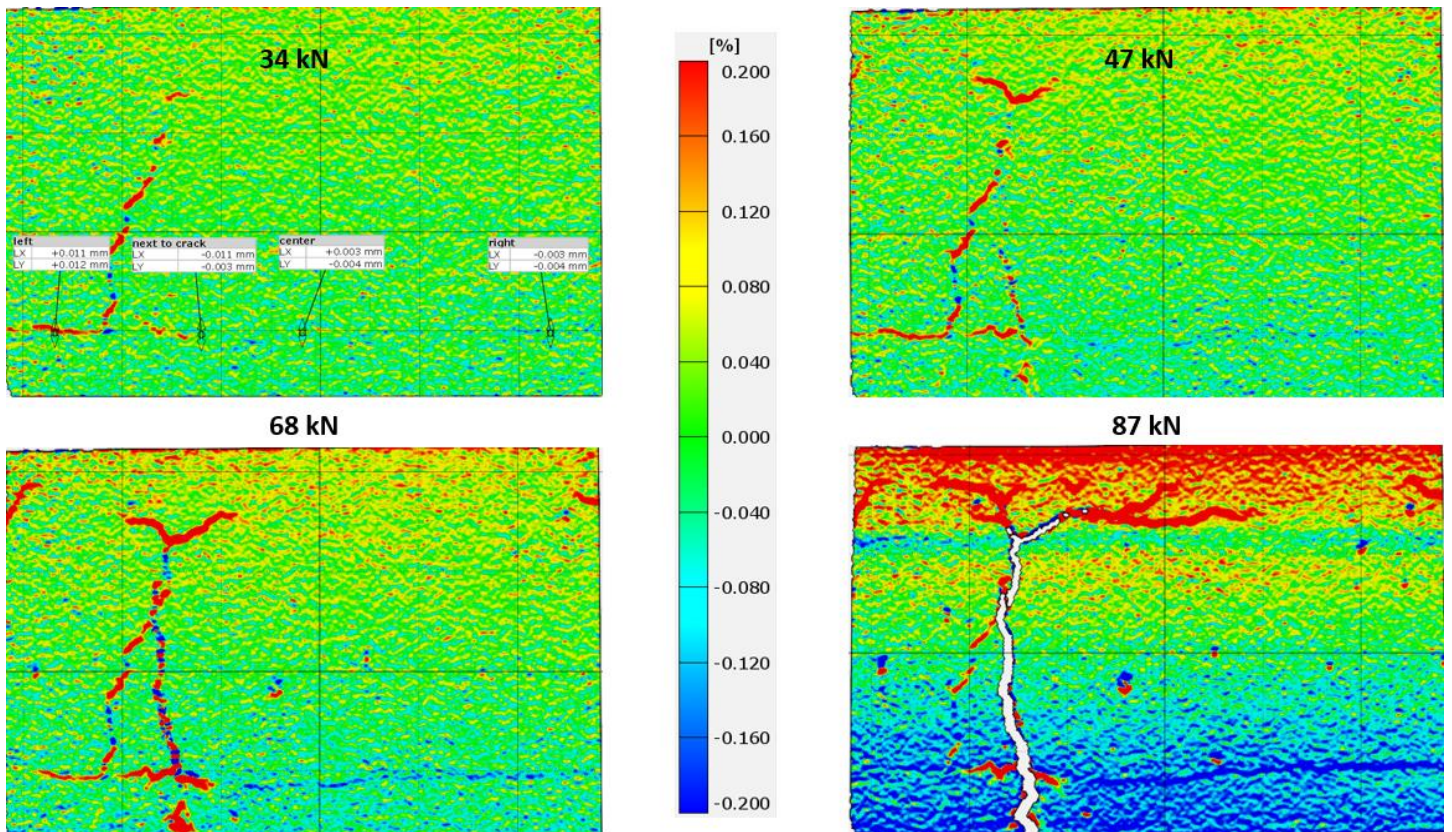


Fig. 5.44: Contour plots of vertical strains at several load levels of beam PVA-SR-VPI

### Overview beam performance

Table 5.3 gives an overview of the performance of beam PVA-SR-VPI.

Table 5.3: Overview beam performance of beam PVA-SR-VPI

Key performance indicator	
Ultimate load	87.3kN
Maximum deflection	27.3mm
Number of cracks in CBMR in SHCC at ultimate load	9 cracks
Number of propagated cracks to CC in CBMR	2 cracks
Load at 0.3mm cw-limit in CBMR	58.4kN
0.3mm load / yield load	76.9 %
Load at 0.2mm cw-limit in CBMR	45.9kN
0.2mm load / yield load	60.5 %

### 5.1.4 Beam PE-SR-VPI

#### Load-deflection response

Fig. 5.45 illustrates the load-deflection response of beam PE-SR-VPI. The crack formation stage started at a load of 29kN. Yielding of the reinforcement was observed at a load of 76.2kN and a deflection of 6.4mm. The ultimate load reached 90.4kN, with the beam failing at a deflection of 30.6mm due to the rupture of the reinforcement bar(s).

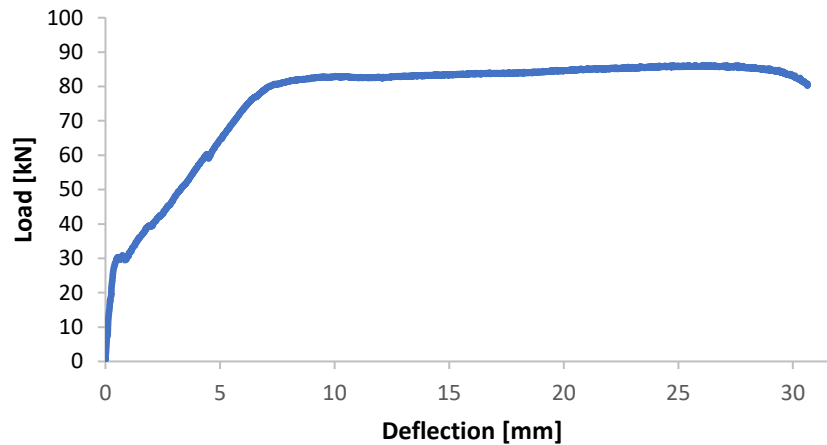


Fig. 5.45: Load-deflection response of beam PE-SR-VPI

#### Validation GOM results

The DIC data are validated based on LVDT1, LVDT2, LVDT3 (placed in the tension zone), as these measurements show an accurate match. Although the laser measurements also show a good correlation, it is not accurate enough for full validation (Annex C). LVDT6, LVDT7, and LVDT8, which were positioned in the compression zone, exhibit only minimal strain (Annex C). This led to a less accurate match, especially during the non-linear stage.

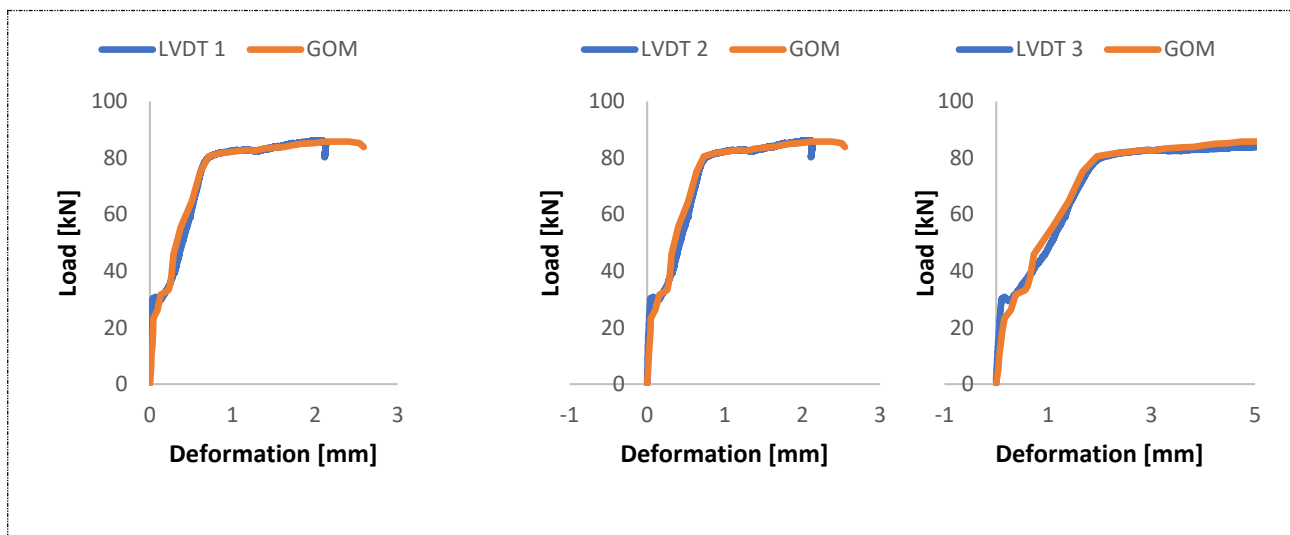


Fig. 5.46: Comparison of the measurements of LVDT1, LVDT2 and LVDT3 with the DIC measurements of beam PE-SR-VPI

### Crack pattern development

Fig. 5.47 to Fig. 5.56 shows the crack development of beam PE-SR-VPI. It can be observed (Fig. 5.47 and Fig. 5.48) that cracks are detected even before the crack formation stage begins. This is probably due to the widening of shrinkage induced micro-cracks. However, the presence of cracks prior to testing was not investigated. As the load increases, more cracks form and existing cracks widen. The 0.2mm crack-width limit is exceeded at a load level of 56kN (Fig. 5.52). The 0.3mm crack-width limit is exceeded close to the yielding load at a load level of 75kN (Fig. 5.54). Four cracks propagate in the CC layer, while SHCC is activated over the full length of the CBMR, leading to the formation of 36 cracks smaller than the 0.3mm crack-width limit and only three cracks exceeding this limit at ultimate load (Fig. 5.56).

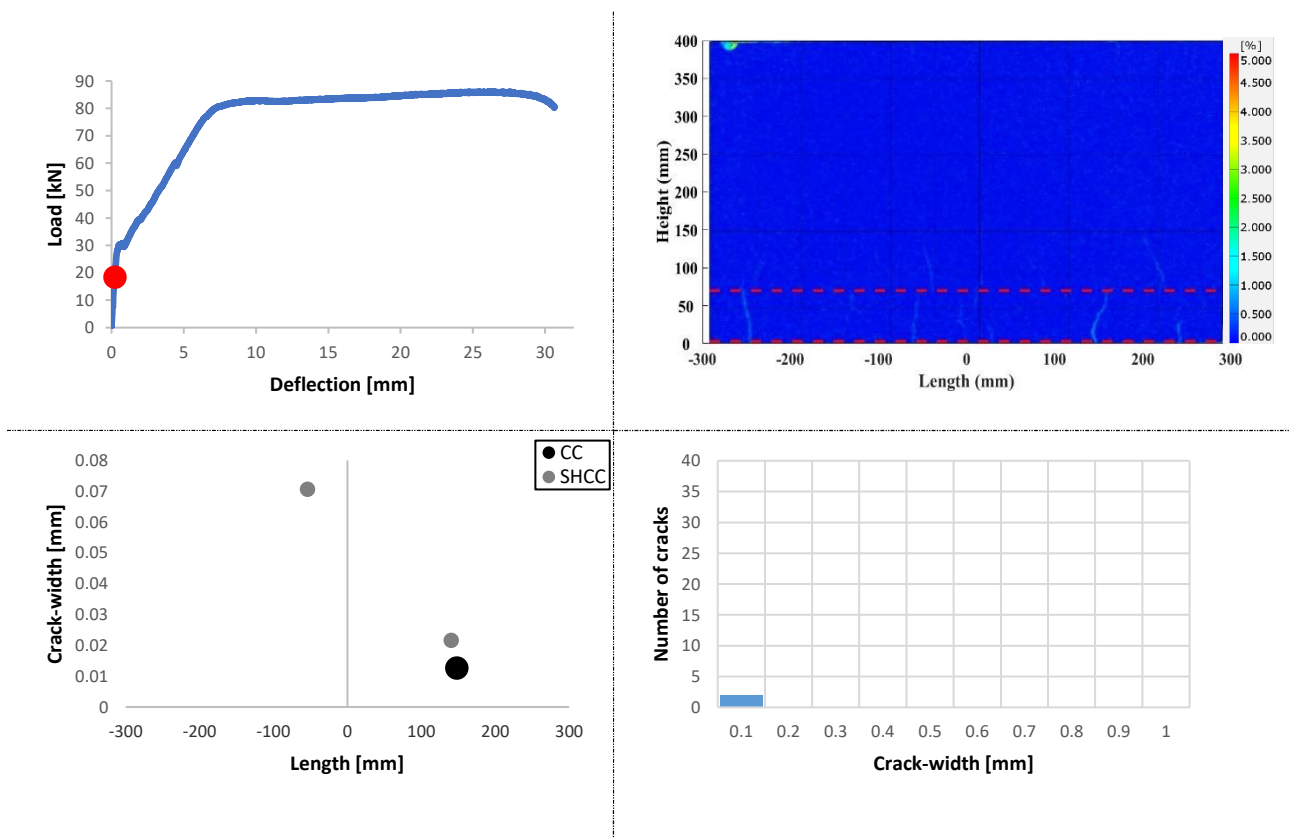


Fig. 5.47: Cracking behavior of beam PE-SR-VPI at a load of 19kN. Top left: Load-level on load-deflection curve. Top right: Contour plot Von-Mises strains. Bottom left: Scatter plot of all cracks. Bottom right: Crack-width distribution of cracks in SHCC.

## 5. Results

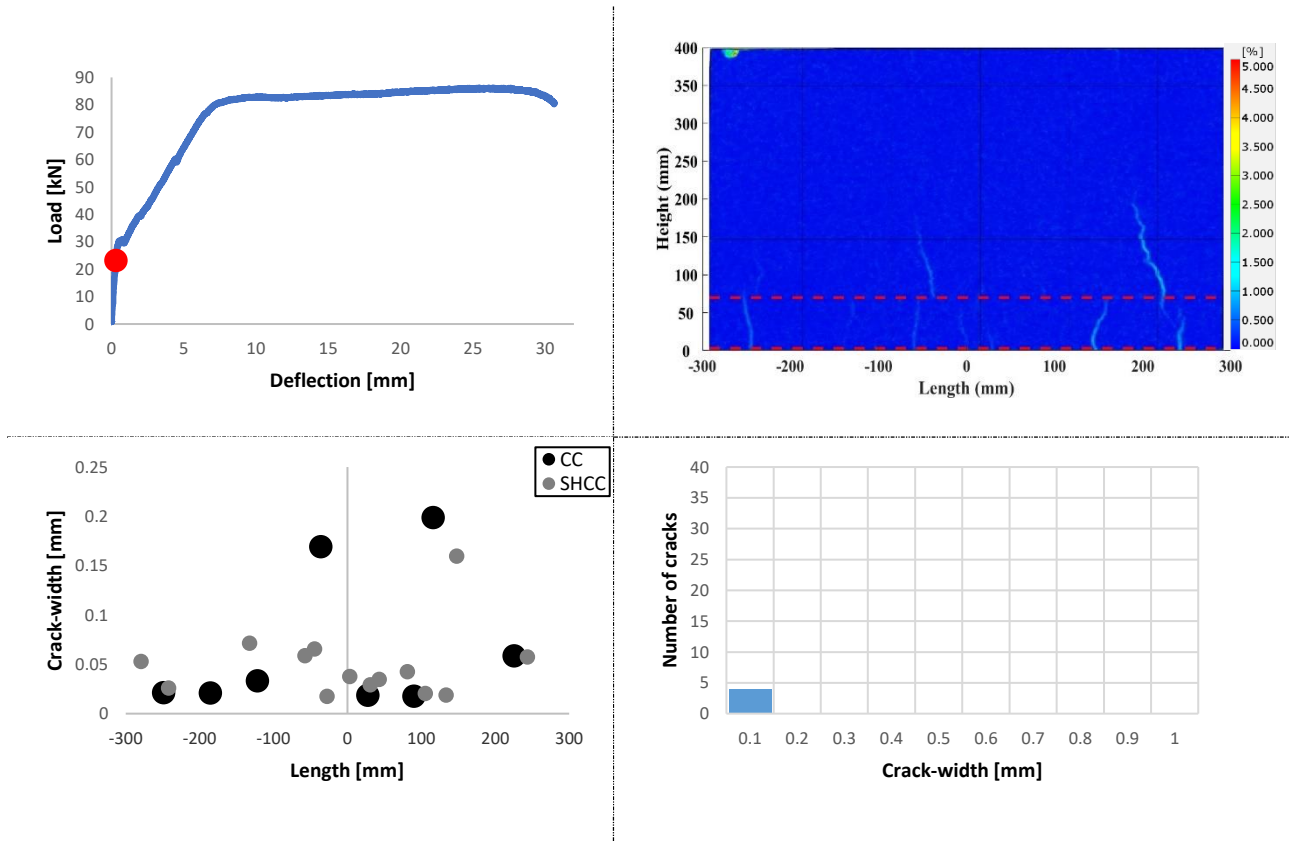


Fig. 5.48: : Cracking behavior of beam PE-SR-VPI at a load of 23kN. Top left: Load-level on load-deflection curve. Top right: Contour plot Von-Mises strains. Bottom left: Scatter plot of all cracks. Bottom right: Crack-width distribution of cracks in SHCC.

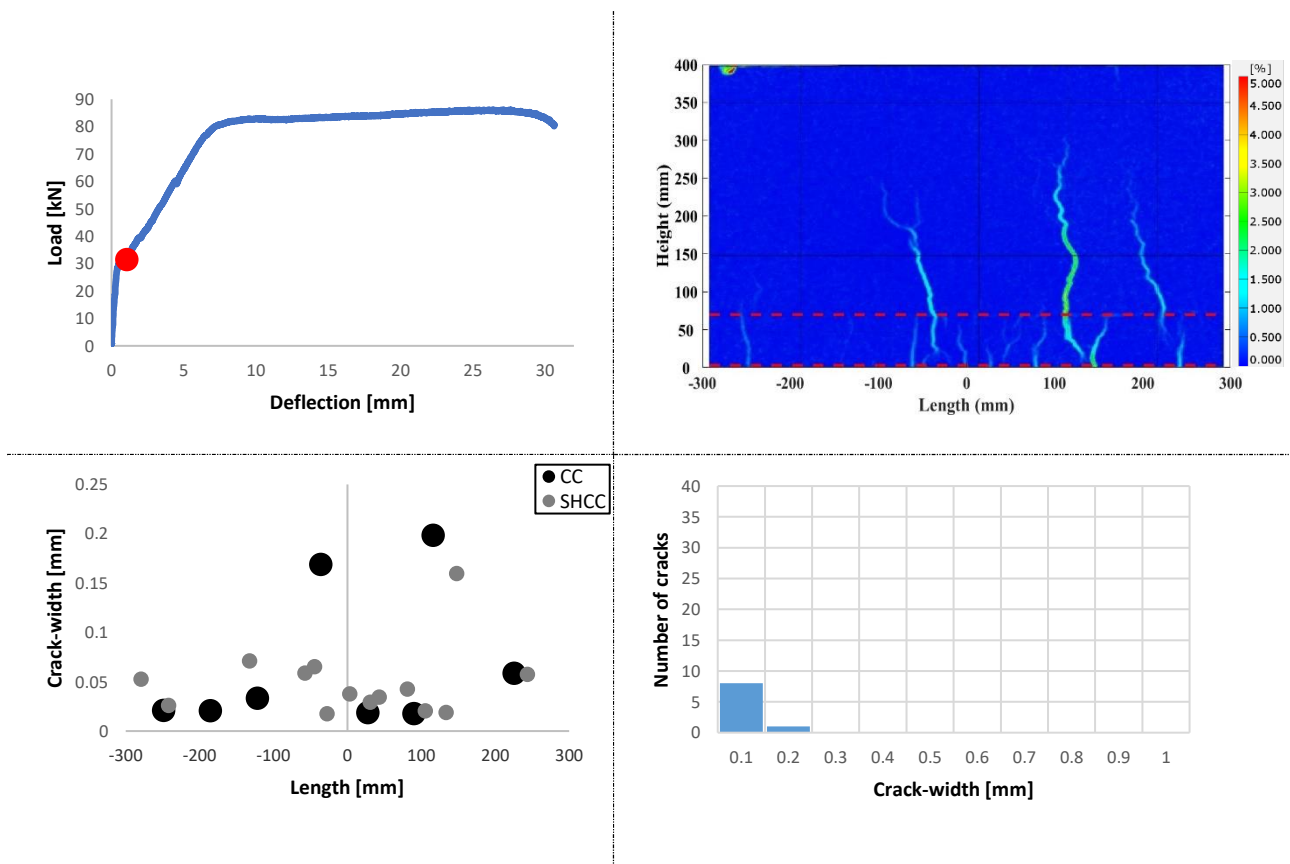


Fig. 5.49: : Cracking behavior of beam PE-SR-VPI at a load of 32kN. Top left: Load-level on load-deflection curve. Top right: Contour plot Von-Mises strains. Bottom left: Scatter plot of all cracks. Bottom right: Crack-width distribution of cracks in SHCC.

## 5. Results

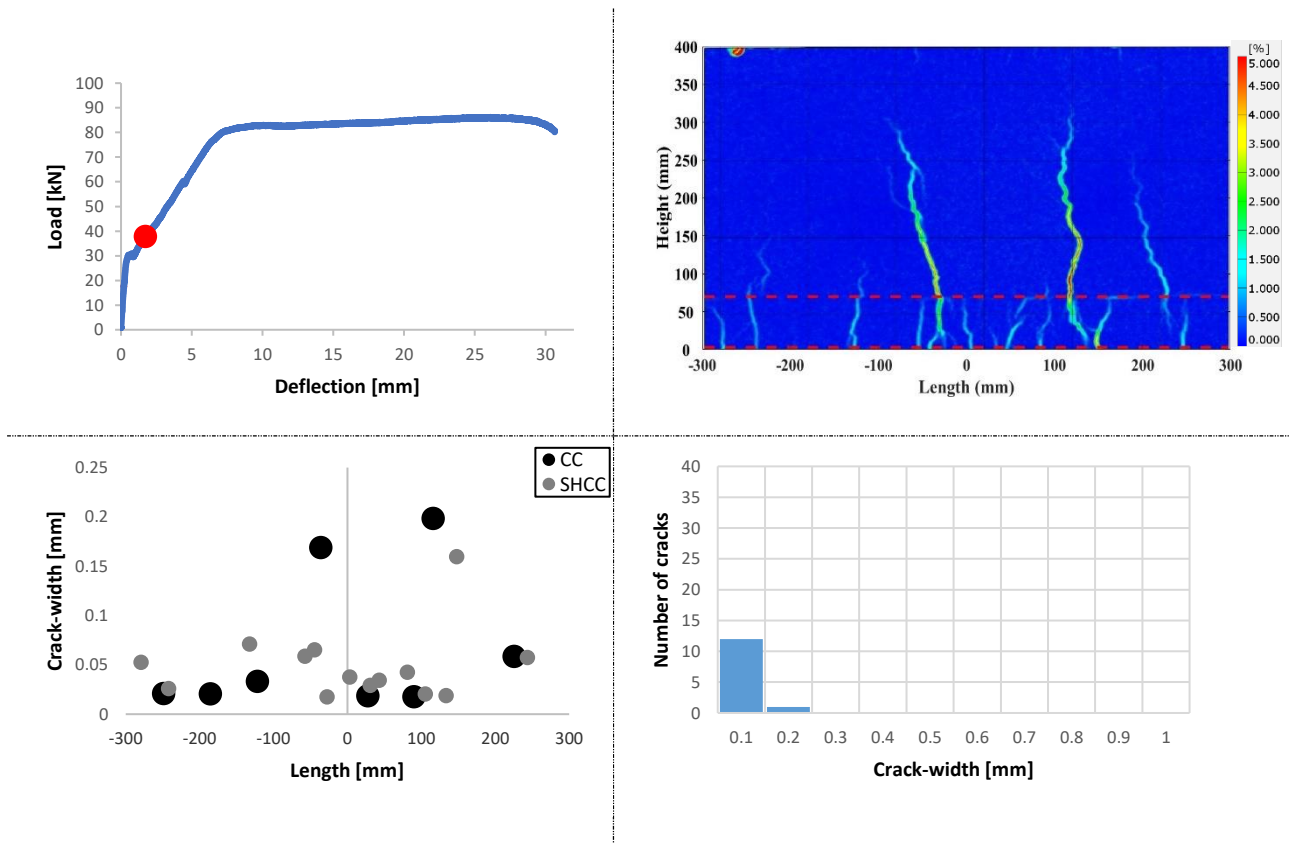


Fig. 5.50: : Cracking behavior of beam PE-SR-VPI at a load of 40kN. Top left: Load-level on load-deflection curve. Top right: Contour plot Von-Mises strains. Bottom left: Scatter plot of all cracks. Bottom right: Crack-width distribution of cracks in SHCC.

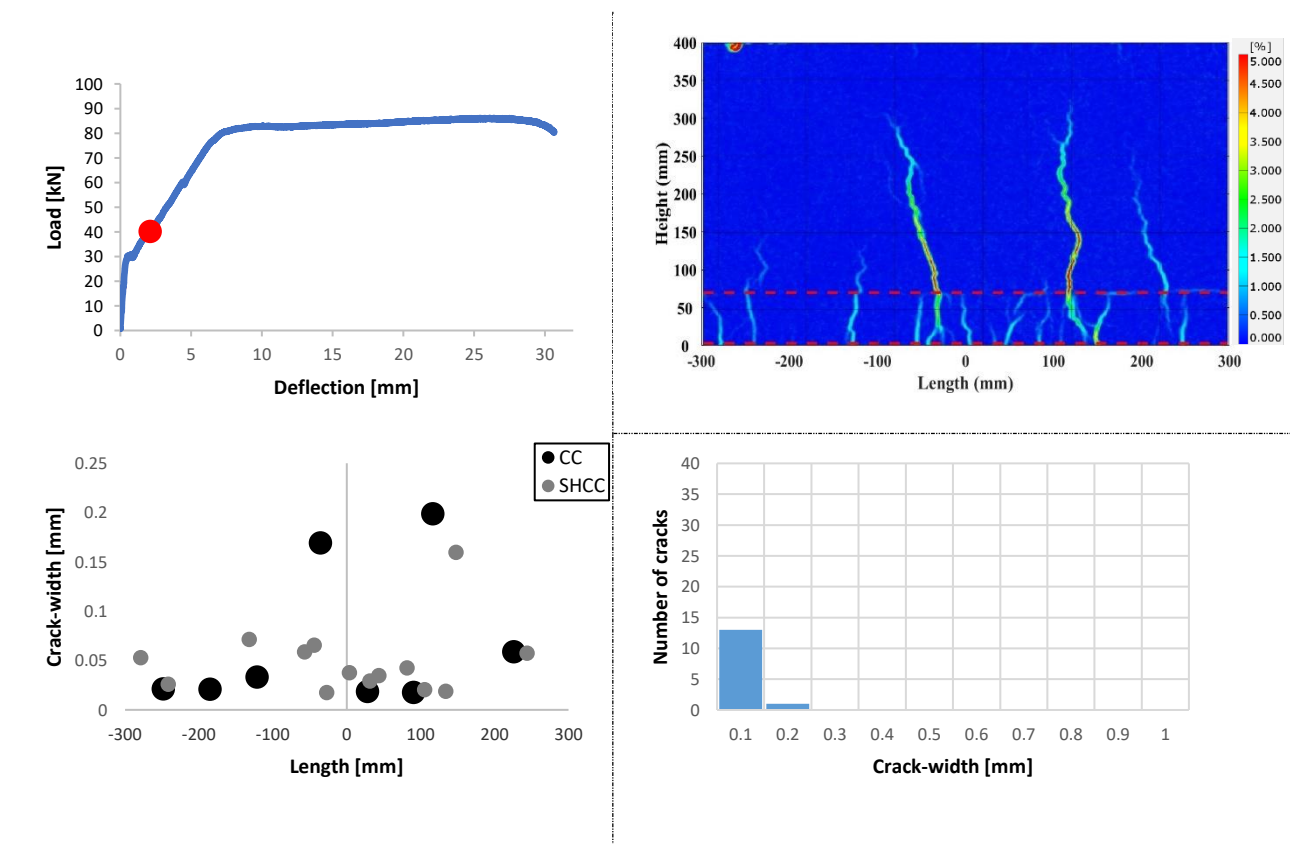


Fig. 5.51: : Cracking behavior of beam PE-SR-VPI at a load of 43kN. Top left: Load-level on load-deflection curve. Top right: Contour plot Von-Mises strains. Bottom left: Scatter plot of all cracks. Bottom right: Crack-width distribution of cracks in SHCC.

## 5. Results

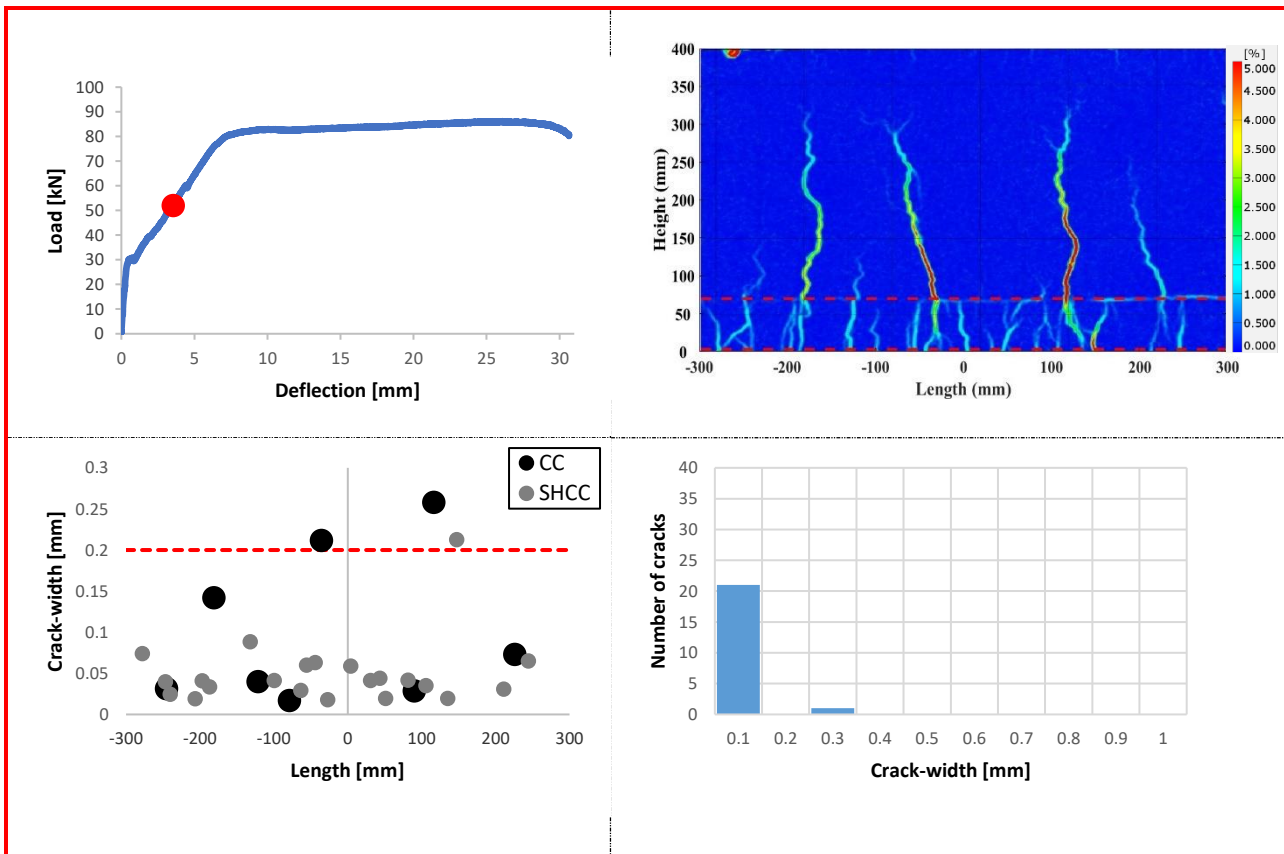


Fig. 5.52: : Cracking behavior of beam PE-SR-VPI at a load of 52kN. Top left: Load-level on load-deflection curve. Top right: Contour plot Von-Mises strains. Bottom left: Scatter plot of all cracks. Bottom right: Crack-width distribution of cracks in SHCC.

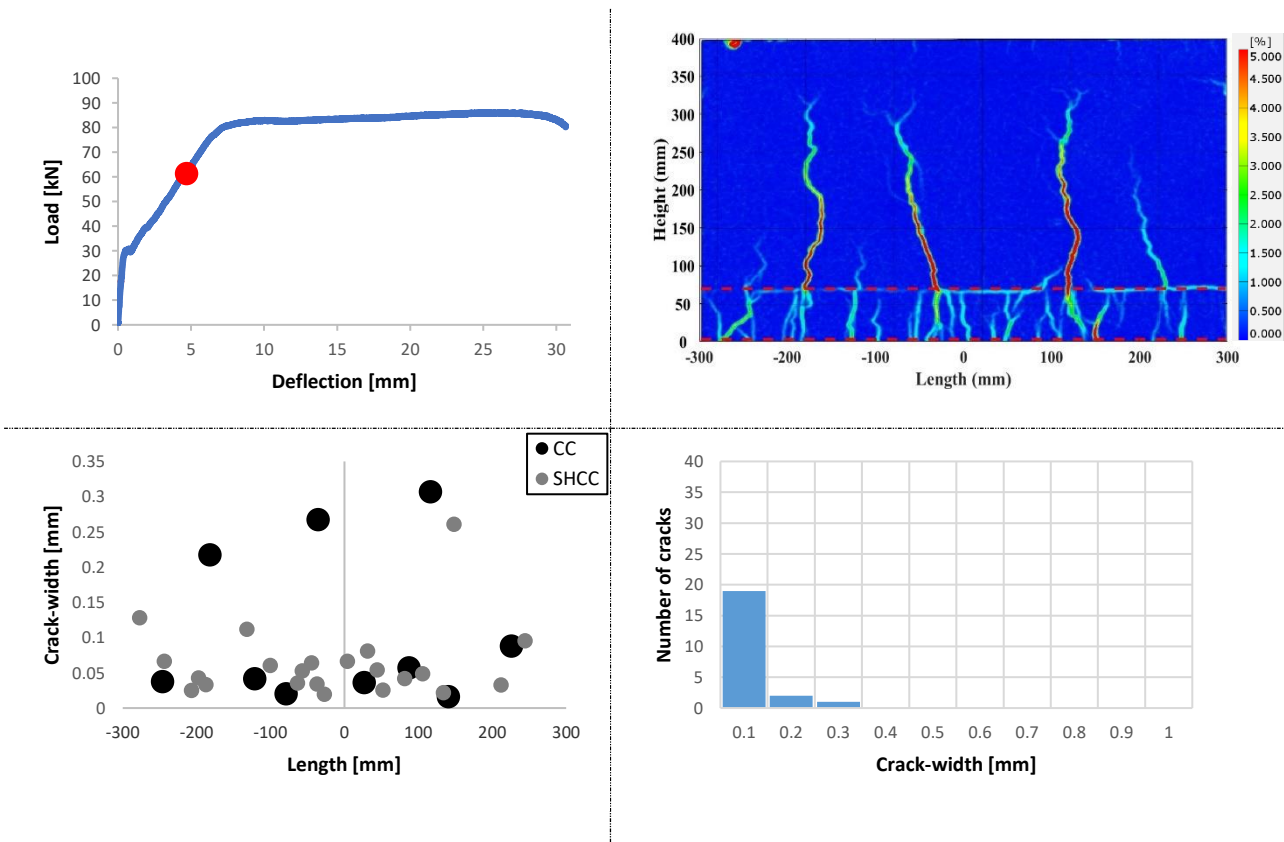


Fig. 5.53: : Cracking behavior of beam PE-SR-VPI at a load of 62kN. Top left: Load-level on load-deflection curve. Top right: Contour plot Von-Mises strains. Bottom left: Scatter plot of all cracks. Bottom right: Crack-width distribution of cracks in SHCC.

## 5. Results

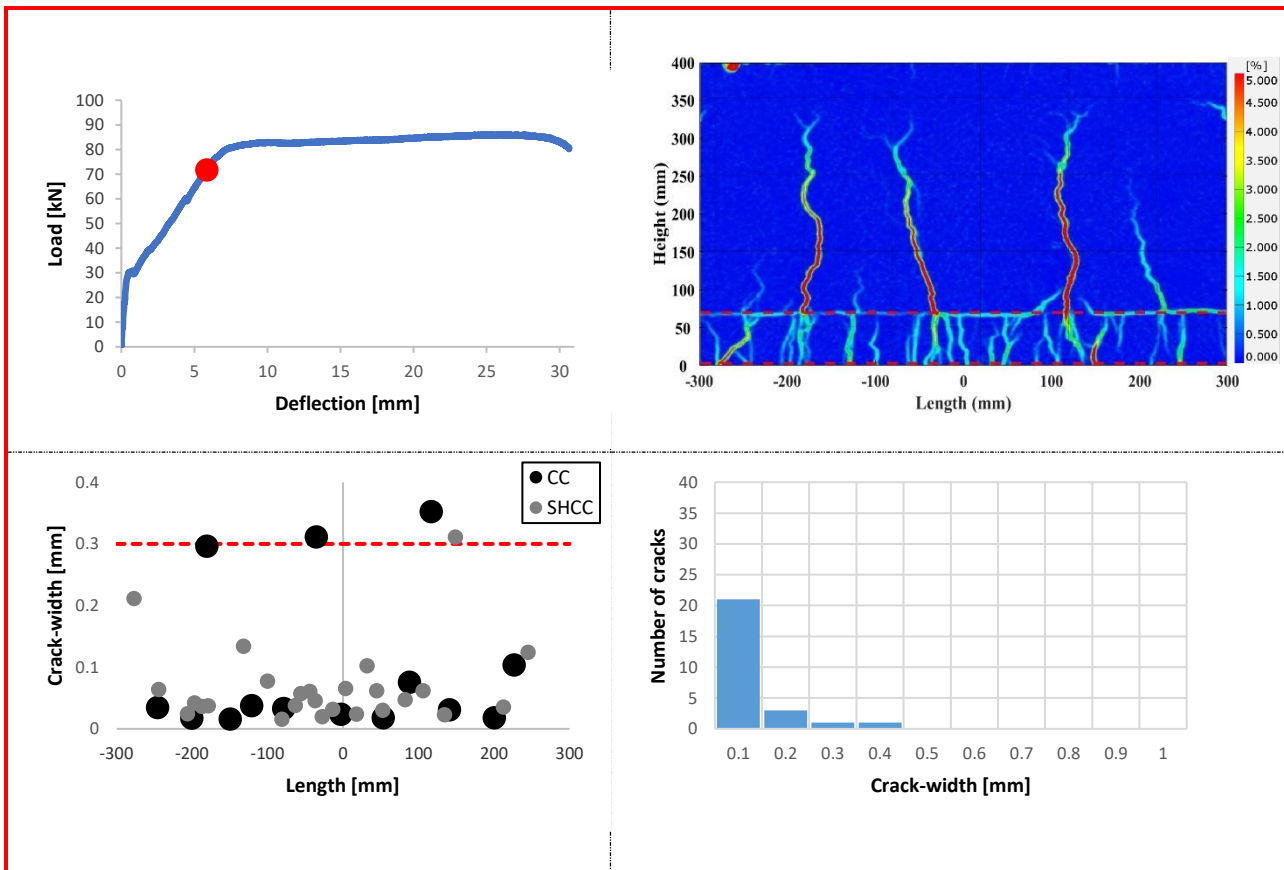


Fig. 5.54: : Cracking behavior of beam PE-SR-VPI at a load of 72kN. Top left: Load-level on load-deflection curve. Top right: Contour plot Von-Mises strains. Bottom left: Scatter plot of all cracks. Bottom right: Crack-width distribution of cracks in SHCC.

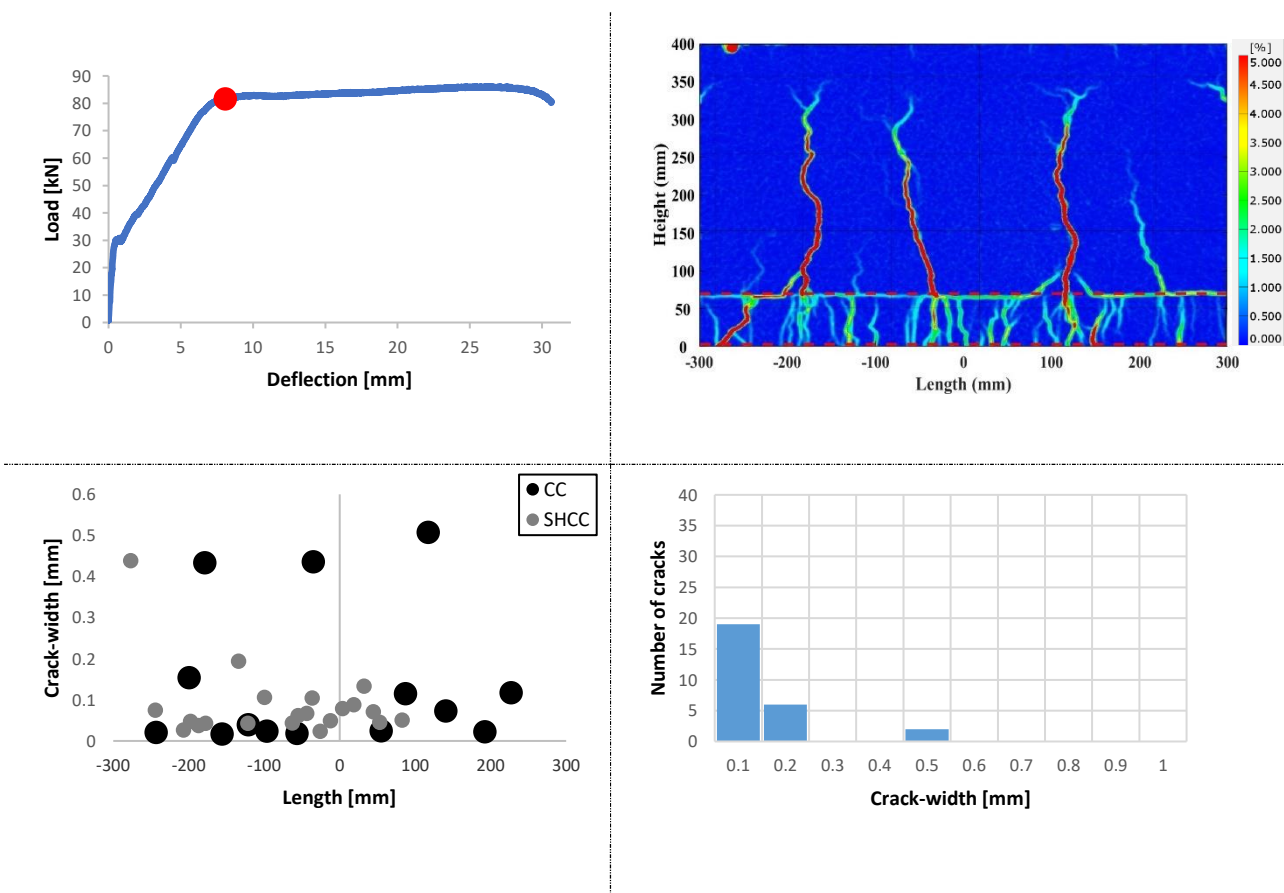


Fig. 5.55: : Cracking behavior of beam PE-SR-VPI at a load of 82kN. Top left: Load-level on load-deflection curve. Top right: Contour plot Von-Mises strains. Bottom left: Scatter plot of all cracks. Bottom right: Crack-width distribution of cracks in SHCC.

## 5. Results

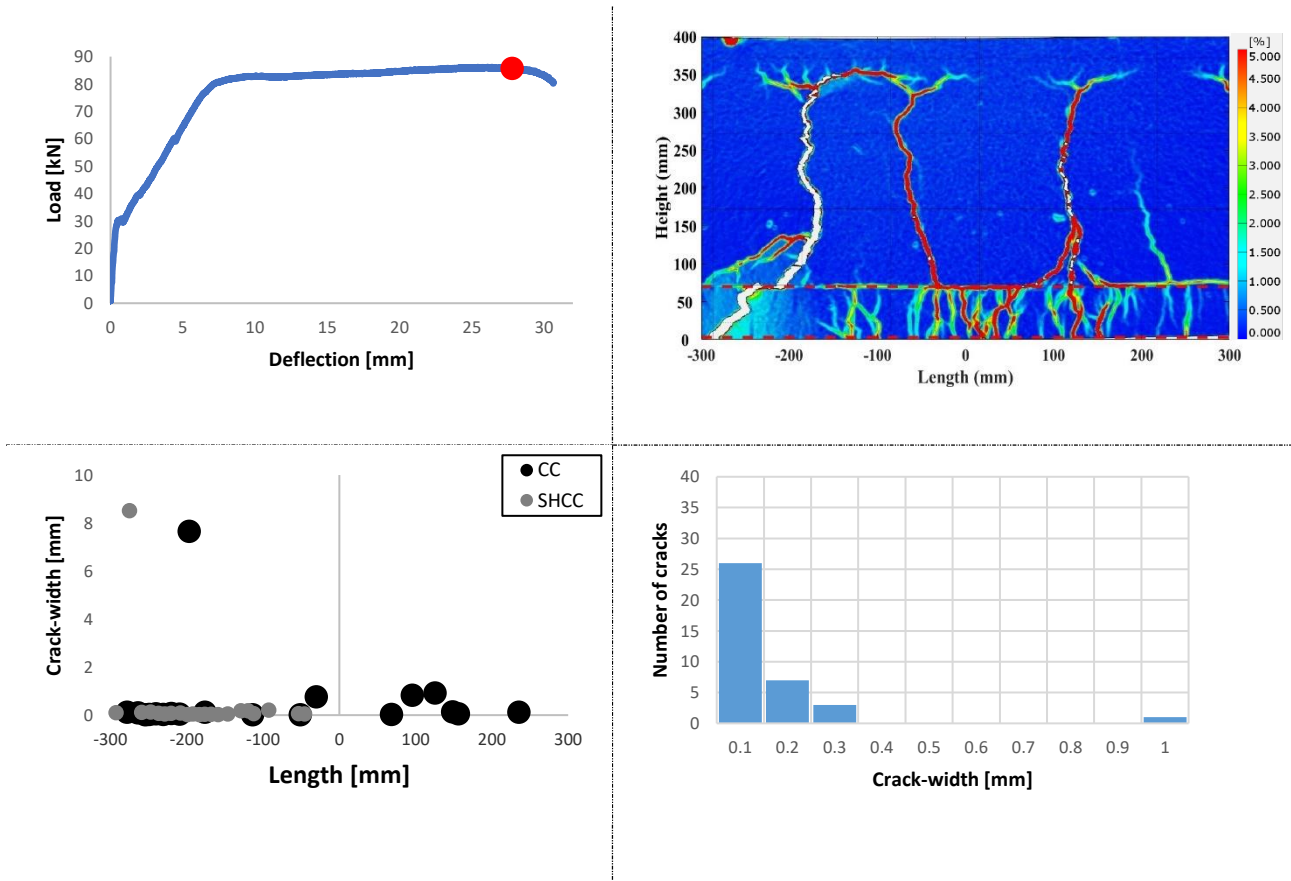


Fig. 5.56: : Cracking behavior of beam PE-SR-VPI at a load of 86N. Top left: Load-level on load-deflection curve. Top right: Contour plot Von-Mises strains. Bottom left: Scatter plot of all cracks. Bottom right: Crack-width distribution of cracks in SHCC.

### Load – max. CW – deflection curve

Fig. 5.57 shows the load – max. CW - deflection curve of beam PE-SR-VPI. The maximum crack-width is determined at every load step indicated in the previous section and is illustrated with grey dots. The 0.2mm crack-width limit and the 0.3mm crack-width limit are indicated with dotted red lines. The 0.2mm crack-width limit is exceeded at a load of 50.7kN and the 0.3mm crack-width limit is exceeded at a load of 70.0kN.

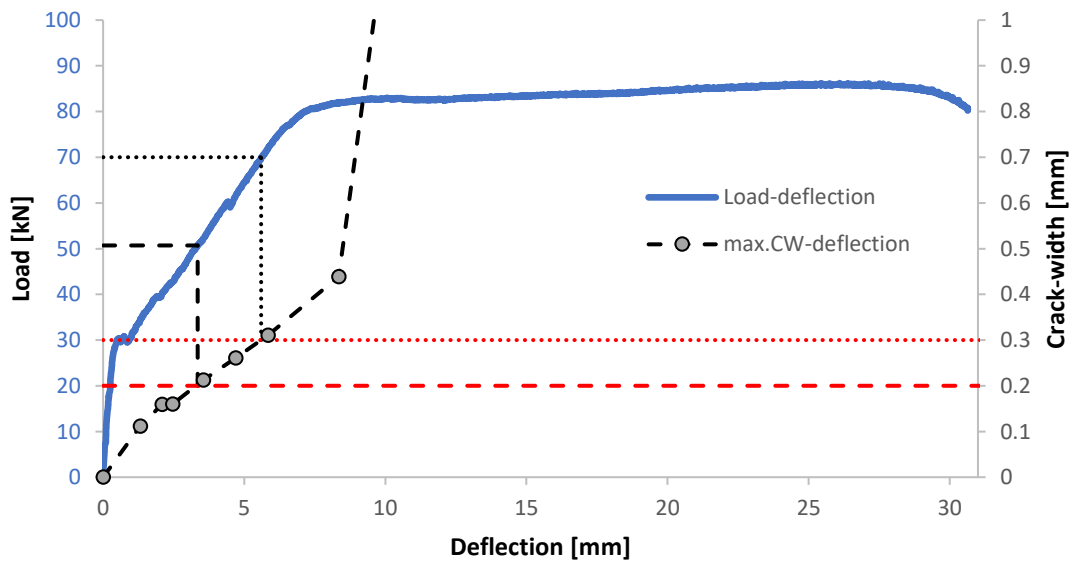


Fig. 5.57: Load - max.CW - deflection curve of beam PE-SR-VPI

Delamination & Slip

The delamination of the interface and the slip of the interface are shown in Fig. 5.58. This is done for three predefined measuring points; at the center of the CBMR, 250mm left to the center of the CBMR and 250mm right to the center of the CBMR. These measuring points are indicated in Fig. 5.59, where the delamination is illustrated by contour plots of the vertical strains. It can be seen that the delamination and slip start to become noticeable at a load of 31kN. Upon increasing the load the delamination and slip increase. At ultimate load the biggest delamination occurs close at the center, whereas the biggest slip occurs left and right of the center – as a result of the shear stresses resulting from composite behavior being low at the center. The contour plots show that the interface delaminates over the full length of the CBMR; however, this delamination remains restricted well below 0.2mm at yielding.

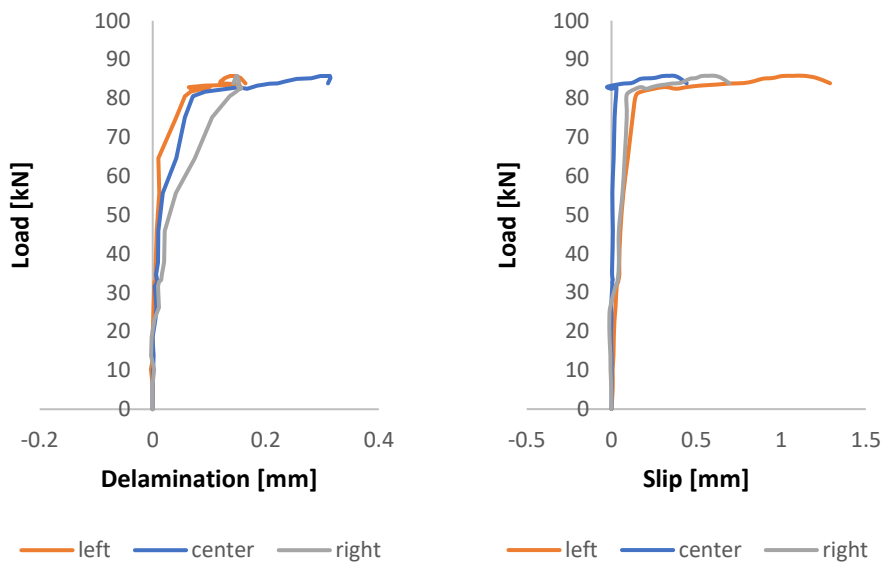


Fig. 5.58: Delamination (left) and slip (right) of interface of beam PE-SR-VPI for four measuring points

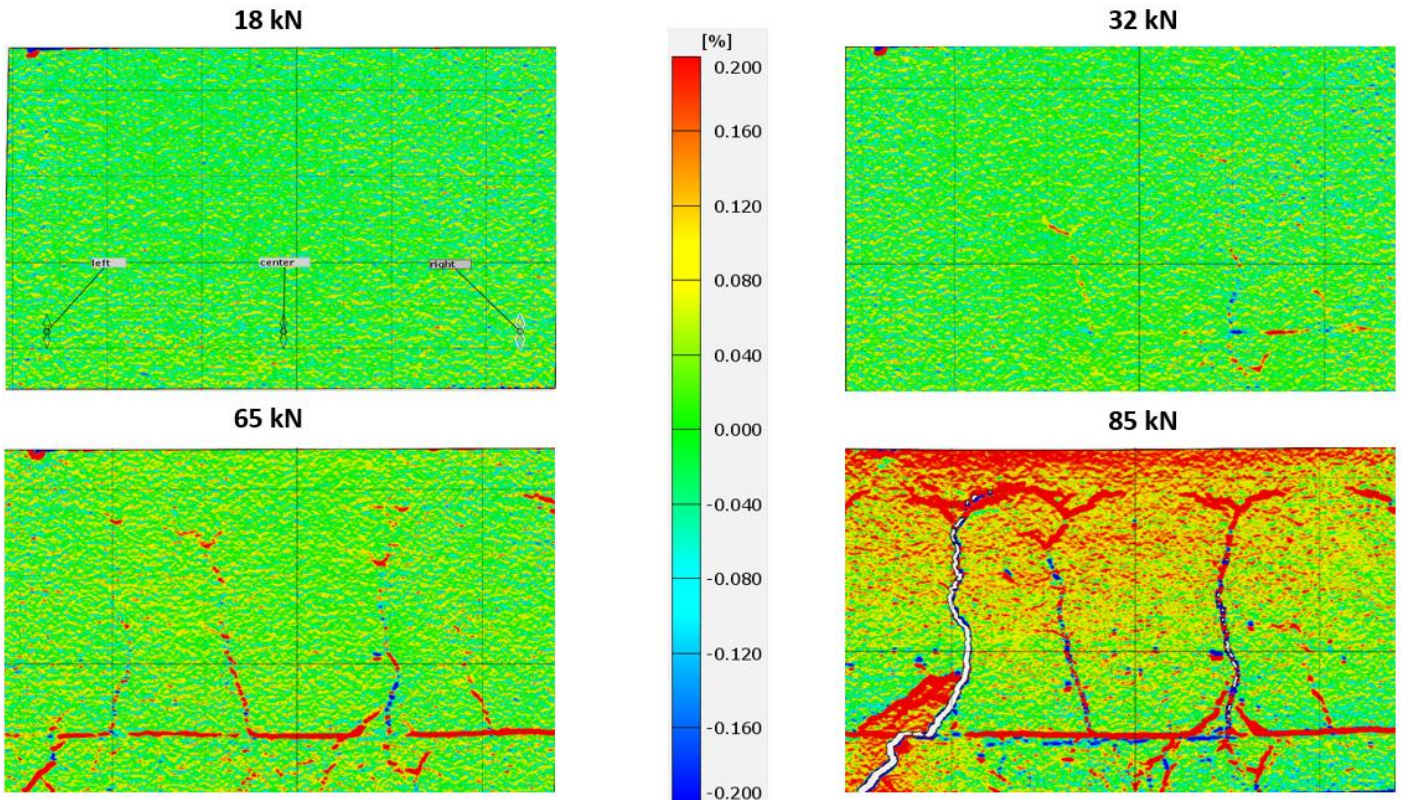


Fig. 5.59: Contour plots of vertical strains at several load levels of beam PE-SR-VPI

Overview beam performance

Table 5.4 gives an overview of the performance of beam PE-SR-VPI.

Table 5.4: Overview beam performance of beam PE-SR-VPI

Key performance indicator	
Ultimate load	85.8kN
Maximum deflection	31.1mm
Number of cracks in CBMR in SHCC at ultimate load	39 cracks
Number of propagated cracks to CC in CBMR	4 cracks
Load at 0.3mm cw-limit in CBMR	70.0kN
0.3mm load / yield load	91.8 %
Load at 0.2mm cw-limit in CBMR	50.7kN
0.2mm load / yield load	66.5 %

## 5.2 Material tests

The material properties of both SHCC and CC are evaluated on day 87 after casting of the SHCC layers. The beams are tested in the same week. For the CC, only the compressive strength is measured, while for SHCC, both compressive and tensile properties are determined. As mentioned in [Section 4.3.4](#) prisms would only be tested when significant and unaccountable results were found. The beam results are satisfactory and therefore the prism tests are cancelled. Compression tests are conducted by a compression machine with a 5000kN capacity on 150mm x 150mm x 150mm cubes, with a loading rate of 13.5kN/s (following EN12390 [57]). The samples are compressed until failure, and the maximum load exerted by the machine is recorded.

The tensile tests are performed on dogbone specimens with gauge dimensions of 110mm x 60mm x 60mm. The dogbones are glued in the setup. Once the glue hardens, the dogbones are axially pulled with a displacement rate of 0.001mm/s (similar rate used in dogbone tests in other studies). The displacement of the dogbone is measured with 2 LVDTs on one side and 2D DIC on the opposite side. Photos are taken every 10 seconds. During testing, problems arose at the SHCC-glue interface. To overcome this, several things are attempted. A description of the full testing procedure with the obtained results is given in [Section 5.2.2](#).

### 5.2.1 Compression tests

[Table 5.5](#) shows the compressive strength of the CC batches<sup>23</sup>. The largest coefficient of variance is found to be 7.59%, making the results of the compression tests acceptable. The mean compressive strength among the four batches is 50.82MPa. The characteristic compressive strength of each batch is found by [50]:

$$f_{ck} = f_{cm}(t) - 8 \quad (5.1)$$

The mix design was made for C30/37, which has a characteristic compressive strength of 37MPa. All batches obtained this strength amply.

Table 5.5: *Compressive strength of CC batches*

Batch	Cube	Compressive strength [MPa]	Mean compressive strength [MPa]	Std [MPa]	Coeff. of Variance [%]	Characteristic compressive strength [MPa]
B1	c1	47.92	50.11	1.59	3.17	42.11
	c2	51.63				
	c3	50.79				
B2	c1	49	47.45	1.81	3.82	39.45
	c2	48.44				
	c3	44.91				
B3	c1	55.08	53.92	1.46	2.71	45.93
	c2	52.28				
	c3	54.41				
B4	c1	46.83	51.79	3.93	7.59	43.79
	c2	52.09				
	c3	56.45				

<sup>23</sup> CC is casted 14 days after SHCC, so the presented strengths are the 73 day compressive strengths

Table 5.6 shows the compressive strength of the SHCCs. PVA-SHCC is found to obtain an average compressive strength of 60.18kN, whereas PE-SHCC yields a compressive strength of 68.53kN. Both results are in correspondence with results obtained in the studies of Bezemer [3] and Nuri [55], respectively. For both materials the coefficient of variance is found to be below 10%, making the compression tests' results acceptable. Given the mixture compositions, one would expect a lower coefficient of variance in the PE mixture compared to the PVA mixture, since the PE mixture includes besides CEM III/B and limestone powder, silica fume, which is a finer material, and a reduced volume fraction of fibers compared to the PVA mixture. However, the lower volume fraction of fibers in the PE mixture could also explain the almost threefold in the coefficient of variance of the PE mixture, as a lower volume fraction of fibers can lead to greater sensitivity to any uneven distribution of fibers. The distribution of fibers is, however, not monitored, so this cannot be substantiated.

Table 5.6: *Compressive strength of SHCC*

SHCC	Cube	Compressive strength [MPa]	Mean compressive strength [MPa]	Std [MPa]	Coeff. of Variance [%]
PVA	c1	58.91	60.18	1.36	2.25
	c2	58.75			
	c3	61.63			
	c4	61.44			
PE	c1	65.82	68.53	5.22	7.62
	c2	77.12			
	c3	67.91			
	c4	63.28			

### 5.2.2 Tensile tests

Two series of tests are performed, because of the problems arising at the SHCC-glue interface. In the first series several solutions are tried, yielding minimum results and damaging dogbone specimens. So, a second series is needed, where a new solution is proposed.

#### Series 1

Compared to conventional dogbone specimens, the tested dogbone specimens are bigger. This size is opted for because the dimensions of conventional dogbone specimens are too small to account for the 3D effect caused by fiber orientation (see Section 2.1.2). Not accounting for this 3D effect, will result in overestimation of the tensile properties of the material when used in larger components (as is the case with the 70mm SHCC layer in all beams). In contrast to the smaller dogbone specimens, where the SHCC-glue interface is less vulnerable, the SHCC-glue interface in the larger dogbone specimens fails consistently before a full cracking pattern can develop in the SHCC, as can be seen in Fig. 5.60.



Fig. 5.60: Failure of SHCC-glue interface in tensile test

To address the problem, several solutions are attempted. First, steel angles are added to increase the glued area (1), but this approach does not resolve the problem. In the following attempts, the steel angles are added while additional modifications are made to enhance the adhesion to the test setup. Thin grooves are cut in one direction using a saw blade (2), followed by thin grooves cut in both directions (3). Subsequently, thicker grooves are sawed in both directions (4). Finally, screws are inserted into the specimen (5).

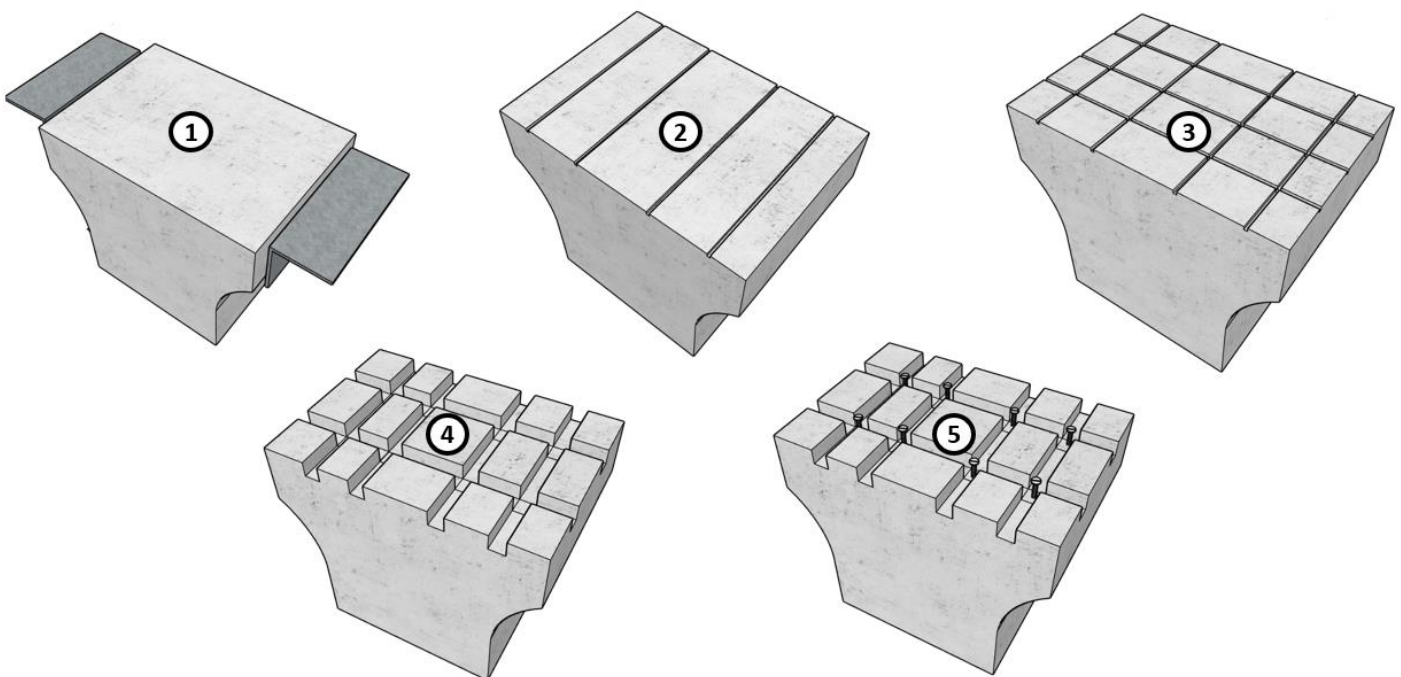


Fig. 5.61: Solutions to overcome SHCC-glue failing. (1) Steel angles. (2) Thin grooves in one direction. (3) Thin grooves in both directions. (4) Thick grooves in both directions. (5) Thick grooves in both directions + screws

Doing this, no results are obtained for the PVA specimens. For the PE-SHCC specimens, two results are obtained. Fig. 5.62 shows the stress-strain curves of the two PE-SHCC dogbone specimens of series 1. Because of the problems encountered (and the constant retesting of same specimens), no DIC measurements are made for one of the (semi-)successfully tested specimens. For the specimen where DIC measurements are performed, the DIC measurements are shown in comparison to the LVDTs' measurements. Dogbone 2 failed prematurely as a result of the failing of the SHCC-glue

## 5. Results

interface. Thus the tensile properties that are found are an underestimation of the capacity of the material.

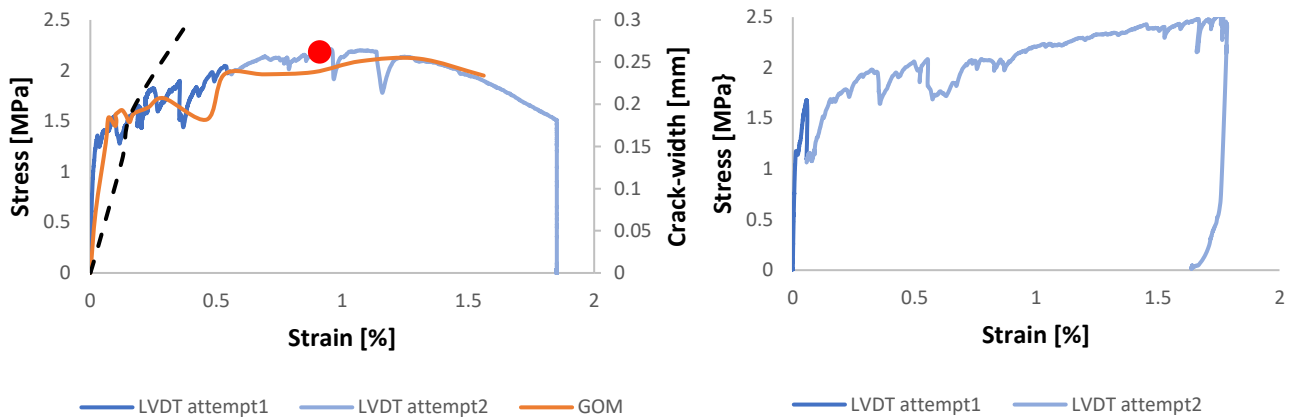


Fig. 5.62: Stress-strain-crack width curves of PE-SHCC specimens of series 1. Left: dogbone 1 Right: dogbone 2 (no DIC)

### Series 2

In series 2, steel hands (Fig. 5.63) are designed to hold the dogbone specimens. The dogbone specimens are glued inside these steel hands at both endings, and then the whole specimen (with the steel hands) is glued to the testing setup. This prevents the dogbone specimens from detaching from the test setup.



Fig. 5.63: Steel hand used in series 2 (left) and sketch of dogbone glued in the steel hand (right)

However, a new (similar) problem is encountered with this method. The SHCC-glue interface is still problematic, resulting in the SHCC detaching from the steel hand (at its flat part), see Fig. 5.64a. Due to this, a concentration of stresses develop at the neck of the dogbone – as the SHCC is now only attached to the steel hand at its side - , ultimately leading to the localization of a crack at this location and premature failure (Fig. 5.64b).



Fig. 5.64: SHCC detaching from steel hand (at its flat part) (left) and SHCC failure outside gauge area (right)

In series 2 no results are yielded for PVA-SHCC. Only one dogbone specimen (Fig. 5.65) exhibited limited strain hardening - though not sufficient to be classified as SHCC<sup>24</sup> -, before the localization of a crack at the neck occurred. In all other dogbone specimens, the SHCC detaches from the flat part of the steel hand prior to the formation of cracks in gauge zone.

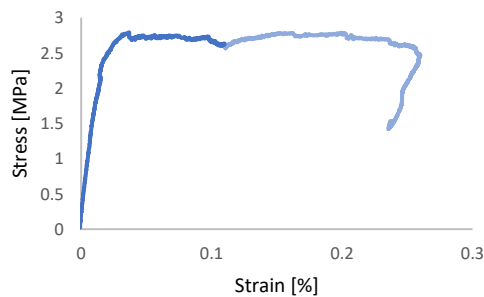


Fig. 5.65: Stress-strain curve of PVA-SHCC dogbone that showed some ductility

For the PE-SHCC specimens, three results are obtained. Fig. 5.66 shows the stress-strain curves of the three PE-SHCC dogbone specimens of series 2. All specimens exhibit strain hardening. However the exhibited response is an underestimation of the actual capacity of the material, since all specimens failed due to the localization of stresses at the neck (as a result of the detachment of the specimen from the flat part of the steel hand).

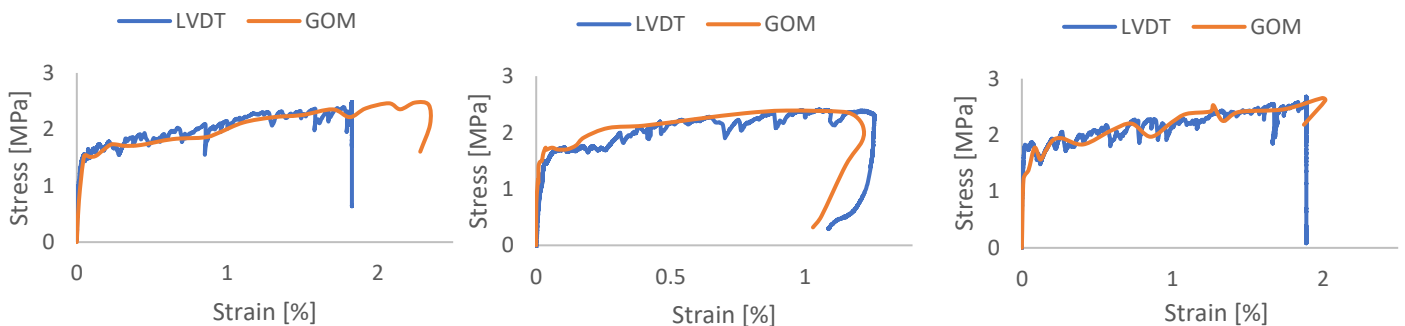


Fig. 5.66: Stress-strain curves of PE-SHCC specimens of series 2. Left to right: dogbone 1 to dogbone 3

<sup>24</sup> Specific minimum strain capacities are often implied rather than explicitly defined in literature due to the variable nature of SHCC mixtures. Generally, however, to qualify as SHCC, a minimum tensile strain capacity around 1% is widely accepted. The Japan Society of Civil Engineers even accepts a strain capacity of 0.5% [60].

Fig. 5.67 shows the stress-strain-crack width curves of all successfully tested PE-SHCC specimens. All specimens from series 2 are able to restrict crack-widths below the 0.3mm crack width limit, proving its capability of controlling crack-widths. The only dogbone of series 1 where DIC measurements are performed is unable to restrict the crack widths below the 0.3mm crack-width limit before the maximum ductility is reached. This is the result of the limited formation of cracks, as is evident from Fig. 5.68, where a contour plot of the Von-Mises strains of dogbone 1 at a load level indicated by the red dot in Fig. 5.67 is shown. A possible reason for this is a poor fiber distribution; however, this is not monitored and thus cannot be substantiated. Fig. 5.68 also shows dogbone 1 at failure.

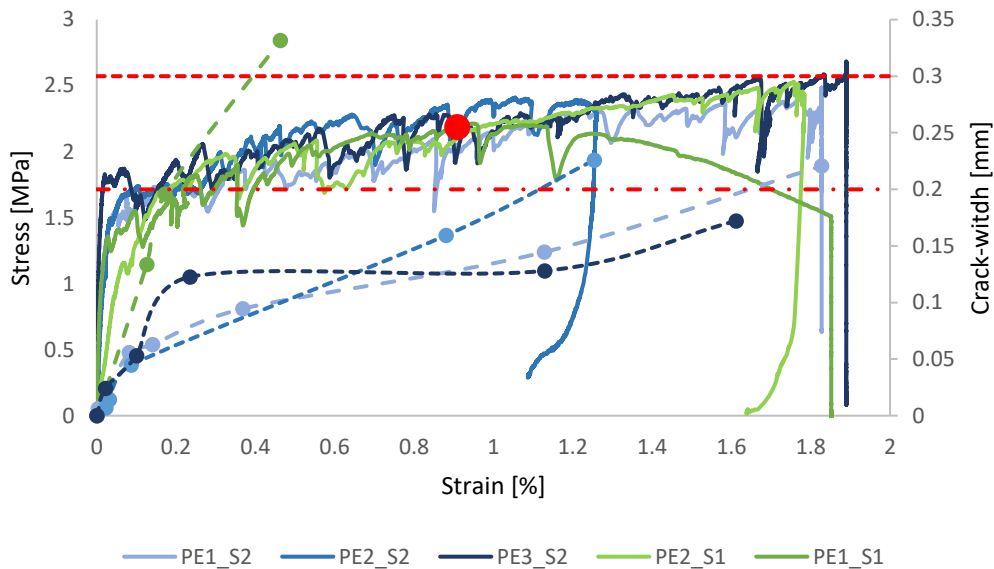


Fig. 5.67: Stress-strain-crack width curves of all PE-SHCC samples

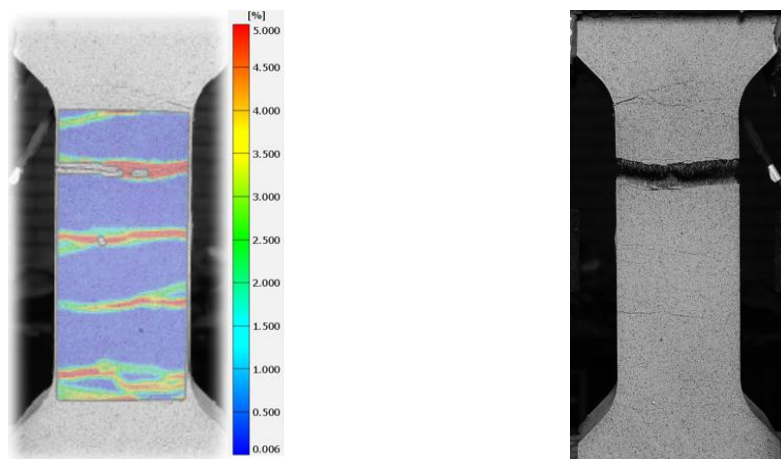


Fig. 5.68: Contour plot of Von-Mises strains of dogbone 1 of series 1 (left) and failure of dogbone 1 of series 1 (right)

The average cracking stress of the PE-SHCC specimens is found to be 1.42MPa (Table 5.7). A probable reason for the failure of the tests of the PVA-SHCC specimens, is the higher cracking stress of the material as can be seen in Fig. 5.65, not allowing for cracks to develop in the gauge section, before the detachment of the dogbone from the flat part of the steel hand.

The average ductility of the PE-specimens is found to be 1.50%. However, as 4 out of 5 dogbones failed prematurely as a result of the failure of the SHCC-glue interface, this value is a

## 5. Results

misrepresentation and underestimation of the ductility of the material. A big coefficient of variance is therefore expected. The same reasoning applies to the measured strength of the material.

Table 5.7: Overview of results of tensile tests

Sample	Cracking strain [%]	Cracking stress [MPa]	Strain at peak stress [%]	Peak stress [MPa]
PE1_S2	0.05	1.53	1.83	2.48
PE2_S2	0.02	1.25	1.05	2.41
PE3_S2	0.02	1.80	1.89	2.68
PE1_S1	0.03	1.36	0.95	2.21
PE2_S1	0.04	1.17	1.76	2.53
<b>Average</b>	0.03	1.42	1.50	2.46
<b>Std</b>	0.01	0.22	0.41	0.15
<b>Coeff. of var. [%]</b>	33.91	15.66	27.24	6.22

The PE-SHCC mixture, developed in the study by Nuri [55], demonstrates decreased tensile properties in the current study compared to those reported by Nuri [55]. Three factors could account for this difference: (1) The tensile properties found in this study are an underestimation of the actual material properties, as a full stress-strain relation cannot be achieved due to the testing challenges encountered. (2) Material samples in the current study are tested after day 85, whereas in Nuri's [55] study, tests were conducted on day 28. Although limited research exists on the time-dependent effects on the tensile properties of PE-SHCC, the literature indicates that the tensile properties of PVA-SHCC tend to degrade over time (Section 2.1.4). (3) The larger dogbone specimens used in the present study likely enables a more pronounced 3D fiber orientation, whereas the conventional dogbone specimens used by Nuri [55] had dimensions where the fiber length was similar to the specimen's thickness, potentially restricting the fiber orientation and influencing the material's tensile performance.

---

# 6. Comparison and discussion

---

## 6.1 Verification with earlier studies

Bezemer [3] studied two beams that serve as a reference for this study, beam RC400 and beam Hybrid400. Beam RC400 is a 400mm reinforced concrete beam without a layer of SHCC in the tension zone. Beam Hybrid400 is exactly similar to beam PVA-RR-SI tested in this study, as mentioned in Section 4.3.5. In the evaluation of the cracking behavior a slightly different approach was used in the study of Bezemer [3]. To have a fair comparison, the cracking behavior of the two beams studied by Bezemer [3] is re-evaluated. This is done following the exact procedure as described in Section 4.4.1 and Section 5.1.

In the analysis conducted by Bezemer [3], it was determined that the 0.2mm and 0.3mm crack-width limits for the RC400 beam were exceeded at loads of 37.0kN and 50.1kN, respectively. The re-evaluation of this beam, using the procedure employed in this study, yields similar results, with the 0.2mm and 0.3mm crack-width limits being exceeded at loads of 36.5kN and 49.8kN, respectively. The load – max. CW – deflection curve of beam RC400 is shown in Fig. 6.1.

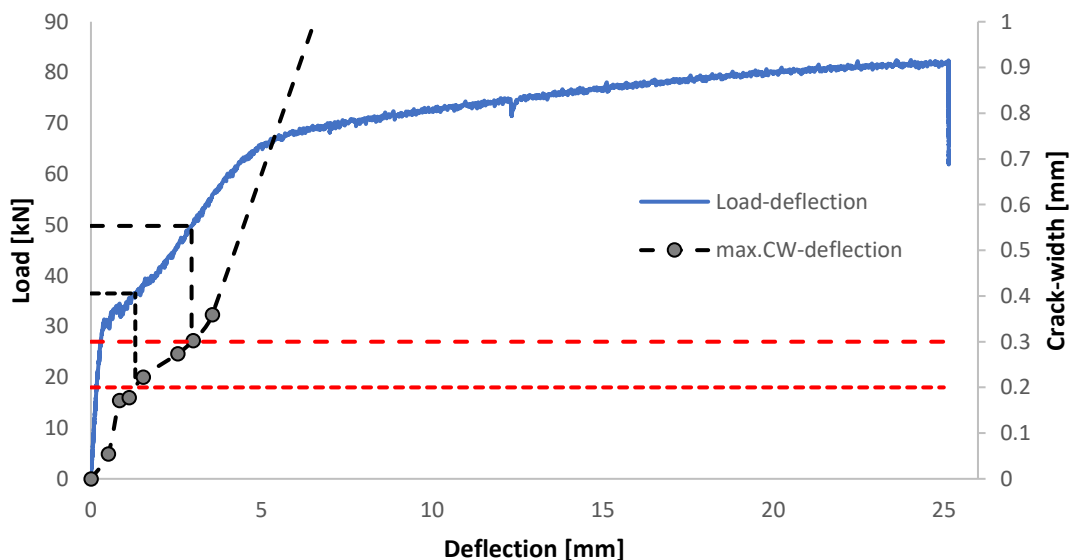


Fig. 6.1: Load - max. CW - deflection curve of beam RC400 (tested by Bezemer [4])

The re-evaluation of beam Hybrid400, however, does not yield matching results. The 0.2mm and 0.3mm crack-width limit were found to be exceeded at a load of 50.0kN and 69.9kN, respectively, in the study of Bezemer [3]. The re-evaluation of this beam, reveals that the 0.2mm crack-width limit is already exceeded at a load level of 49.8kN - as is shown in Fig. 6.2 where all SHCC cracks are drawn in a scatter plot next to the contour plot of the Von-Mises strains at this load level. Similarly, the 0.3mm crack-width limit is found to be exceeded prior to the 69.9kN found in the study of Bezemer [3], as is shown in Fig. 6.3 where the cracking behavior of the beam is shown at a load level of 68.2N.

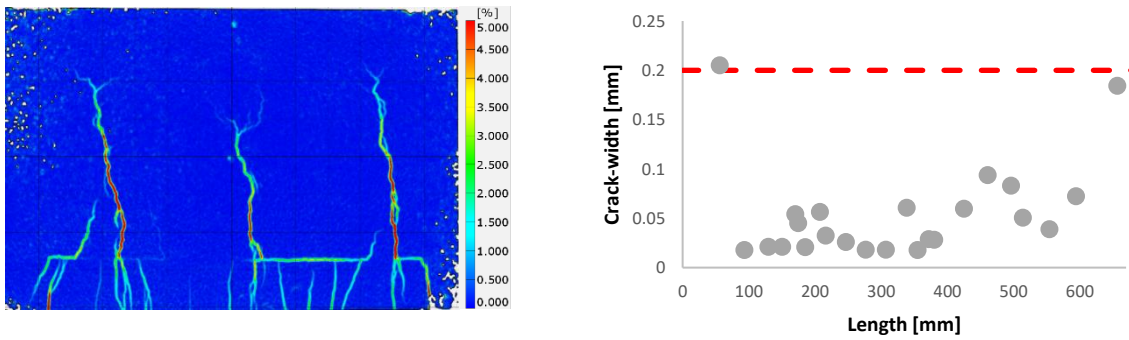


Fig. 6.2: Cracking behavior of beam hybrid400 at a load of 49.8kN. Left: Contour plot Von-Mises strains. Right: Scatter plot of all SHCC cracks

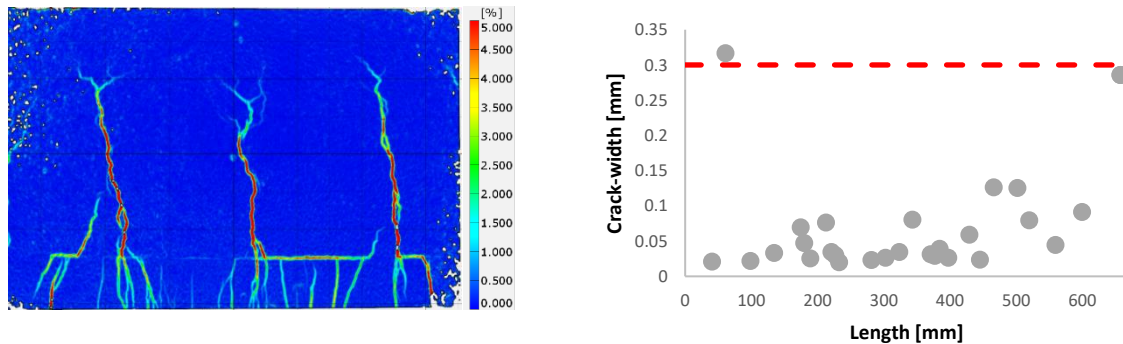


Fig. 6.3: Cracking behavior of beam hybrid400 at a load of 68.2kN. Left: Contour plot Von-Mises strains. Right: Scatter plot of all SHCC cracks

Fig. 6.4 presents the load-max crack-width-deflection curve for beam Hybrid400. The 0.2mm and 0.3mm crack-width limits are exceeded at 49.0kN and 65.4kN, respectively. The significant difference between these results and those of Bezemer [3], particularly the load at which the 0.3mm crack-width limit is exceeded, cannot be attributed solely to the slightly different procedure employed for evaluating the crack-widths. Instead, this discrepancy arises from differences in how deflections at each photo are determined.

There are three methods for determining the deflection at each photo. In method 1, the deflection/load is directly read from a display installed on the load spreader (Section 4.4). However, this display only serves as an indicator of the actual deflection at every photo as the display lacks behind the actual load. In method 2, the deflection is taken from the GOM evaluation, but this method tends to overestimate the actual beam deflection as it measures the total deflection rather than the beam deflection alone. In method 3, the deflection is determined using a photo counter recorded with the test data (at every instance a photo is made, the trigger signal of the camera is recorded), allowing for more accurate determination of the actual deflection at every photo. Bezemer [3] used method 2 in his study, leading to a slight overestimation of the deflection at each load step for beam Hybrid400, and consequently, an overestimation of the loads at which the crack-width limits were exceeded. In this thesis, method 3 is employed to achieve more accurate results.

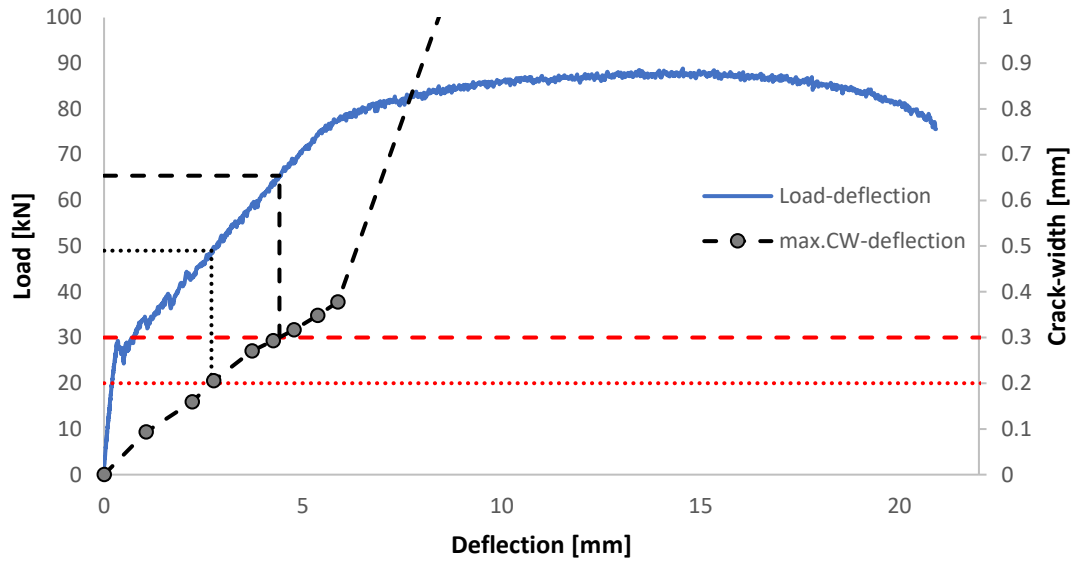


Fig. 6.4: Load - max. CW - deflection curve of beam Hybrid400 (tested by Bezemer [4])

## 6.2 Influence of curing time

As stated earlier beam PVA-RR-SI, tested in this study at 85 days of SHCC age, is a replica of beam Hybrid400, which was tested in Bezemer's [3] study at 55 days of SHCC age. This difference in testing age presents an opportunity to examine the influence of curing time on the crack-controlling ability of the 70mm SHCC layer. Fig. 6.5 shows a comparison of the load – max. CW – deflection curves for both beams. Beam Hybrid400 is referred to as PVA-RR-SI (55) and beam PVA-RR-SI tested in this study is referred to as beam PVA-RR-SI (85).

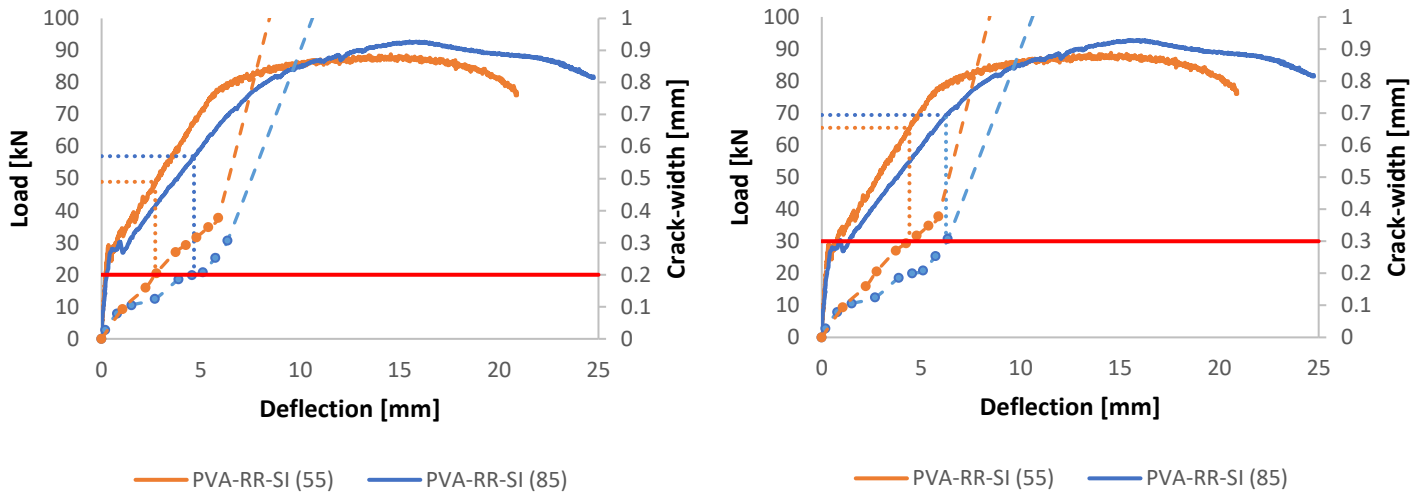


Fig. 6.5: Comparison of load - max. CW - deflection curves of beams PVA-RR-SI (55) and PVA-RR-SI (85) along with the 0.2mm crack-width limit (left) and 0.3mm crack-width limit (right)

The first observation that can be made is the lower stiffness of beam PVA-RR-SI (85) compared to beam PVA-RR-SI (55). This lower stiffness can be explained by the lesser amount of cracks (Fig. 6.6) formed in the CBMR of beam PVA-RR-SI (85) – in both the SHCC layer as well as the CC layer - and the distribution of these cracks (Fig. 6.7) – with beam PVA-RR-SI (55) showing a better distribution of the SHCC cracks across the CBMR. The formation of a greater number of cracks (and a better distribution of these cracks) typically enhances tension stiffening<sup>25</sup>, which in turn improves the overall stiffness of the beam. Another possible reason for the lower tension stiffening observed in beam PVA-RR-SI (85) is the impact of shrinkage induced cracks. Shrinkage induced cracks typically reduce tension stiffening in concrete structures [58]. Beam PVA-RR-SI (85) which has a higher curing time, probably contained more shrinkage induced cracks. For better understanding of hybrid R/SHCC structures it is thus good to consider and monitor shrinkage (induced cracks).

The greater number of cracks observed in beam PVA-RR-SI (55) compared to beam PVA-RR-SI (85) may be attributed to the more pronounced delamination of the SHCC-CC interface in beam PVA-RR-SI (55), which may have facilitated more activation of SHCC.

<sup>25</sup> Tension stiffening in reinforced concrete refers to the ability of uncracked concrete between cracks to contribute to the stiffness of the structure, even after cracking has occurred [61].

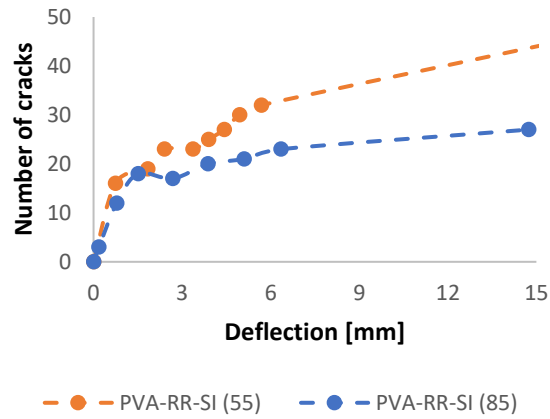


Fig. 6.6 Comparison of number of developed cracks between beams PVA-RR-SI and PVA-RR-VPI

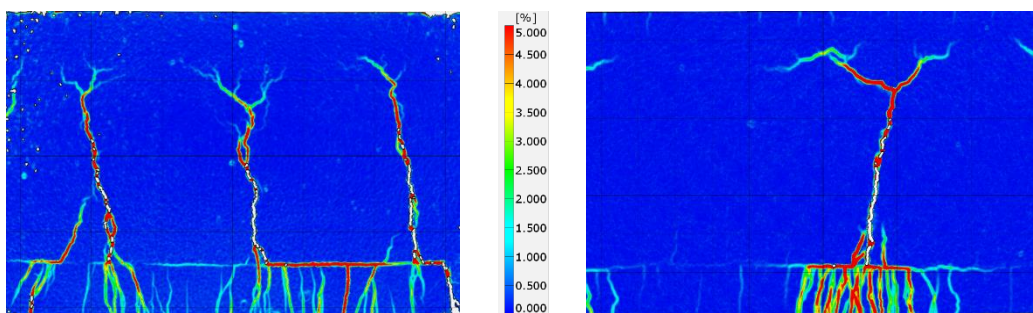


Fig. 6.7: Contour plot of Von Mises strains at a load of 82kN for beam PVA-RR-SI (55) (left) and beam PVA-RR-VPI (85) (right)

Despite the reduced crack formation in the CBMR of beam PVA-RR-SI (85), the crack-width limits are exceeded at a higher load compared to beam PVA-RR-SI (55). In particular, the 0.2mm crack-width limit is exceeded at a load of 57.0kN, representing a 16.3% increase compared to beam PVA-RR-SI (55), in which this limit was exceeded at a load of 49.0kN. The 0.3mm crack-width limit is exceeded at a load of 69.4kN, representing a slight increase of 6.1% compared to beam PVA-RR-SI (55), in which this limit was exceeded at a load of 65.4kN. This result is counterintuitive, as the formation of more cracks would typically suggest improved crack-width control. A possible reason for the earlier crack-localization in beam PVA-RR-SI (55) is the higher tensile strength of the SHCC. The literature review highlighted that the tensile strength of PVA-SHCC decreases with time and that in a numerical simulation of SHCC beams, higher strength of SHCC led to earlier crack localization. To further understand why the crack-widths are less effectively controlled in beam PVA-RR-SI (55) at lower loads compared to beam PVA-RR-SI (85), the delamination behavior of the SHCC-CC interface is investigated (Fig. 6.8).

It can be observed that at a similar load step of 42kN (just prior to the exceeding of the 0.2mm crack-width limit in beam PVA-RR-SI (55)), that a greater portion of the interface of beam PVA-RR-SI (55) has delaminated (indicated by red) compared to beam PVA-RR-SI (85). The more extensive debonding between the SHCC and CC layers in beam PVA-RR-SI (55) leads to greater stresses in the SHCC layer<sup>26</sup>. However, due to the higher strength of the SHCC in beam PVA-RR-SI (55), the number of cracks developed up to a deflection of 2.5mm (just prior to the moment the 0.2mm crack-width limit is

<sup>26</sup> Singh [2] showed that beams with completely or partially debonded SHCC-CC interfaces (achieved by taping the surface of the SHCC) exhibited earlier crack localization - as a result of higher stresses acting in the SCC at lower loads - compared to beams with smooth interfaces, despite good activation of SHCC in all cases.

exceeded in beam PVA-RR-SI (55)) is similar to beam PVA-RR-SI (85). Meaning that the supposedly higher stresses acting in the SHCC cause more widening of the cracks in PVA-RR-SI (55)) compared to beam PVA-RR-SI (85), where a SHCC layer with a similar amount of cracks experiences less stress. As a result of the stronger interface bond in beam PVA-RR-SI (85), the action of SHCC as effective reinforcement of the concrete is more pronounced in this beam. After a deflection of 2.5mm, the greater delamination in beam PVA-RR-SI (55) facilitates the formation of additional (and more distributed) cracks compared to beam PVA-RR-SI (85), which is why the 0.3mm crack-width limit is exceeded at a similar load in both beams. The more pronounced delamination of beam PVA-RR-SI (55) – facilitating the formation of more (distributed) cracks – suggests that curing time influences the bond behavior of SHCC-CC, with the bond strengthening over time. The influence of the SHCC-CC interface is further discussed in the next section.

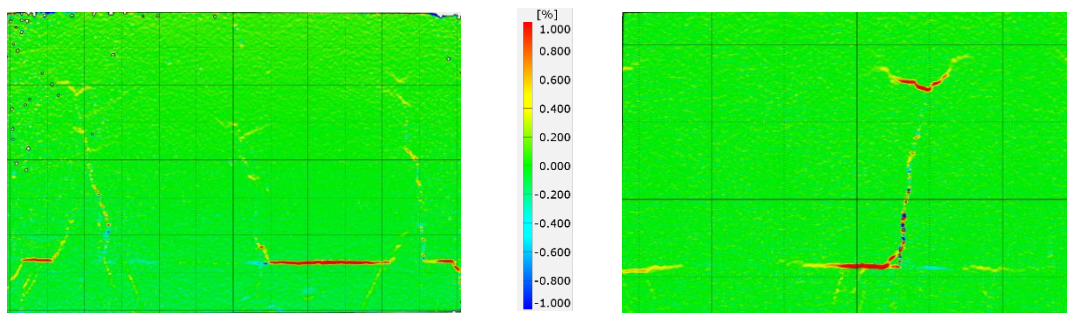


Fig. 6.8: Comparison of interface behavior of (left) beam PVA-RR-SI (55) and (right) beam PVA-RR-VPI at a load level of 42kN

### 6.3 Influence of SHCC-CC interface roughness

Fig. 6.9 presents the load – maximum crack-width – deflection curves for beams PVA-RR-SI and PVA-RR-VPI, where the only altered parameter is the interface roughness. A first observation that can be made is the difference in stiffness between the two beams, with beam PVA-RR-VPI exhibiting higher stiffness compared to beam PVA-RR-SI. This difference can be attributed to the number and distribution of cracks formed in both beams. Beam PVA-RR-VPI develops more cracks in both the SHCC and CC layers, as shown in Fig. 6.10a. Additionally, beam PVA-RR-VPI demonstrates a more uniform crack distribution in the SHCC layer than beam PVA-RR-SI, as illustrated in Fig. 6.11. The increased number of cracks and the improved distribution of these cracks in beam PVA-RR-VPI lead to more pronounced tension stiffening, resulting in a stiffer beam compared to PVA-RR-SI.

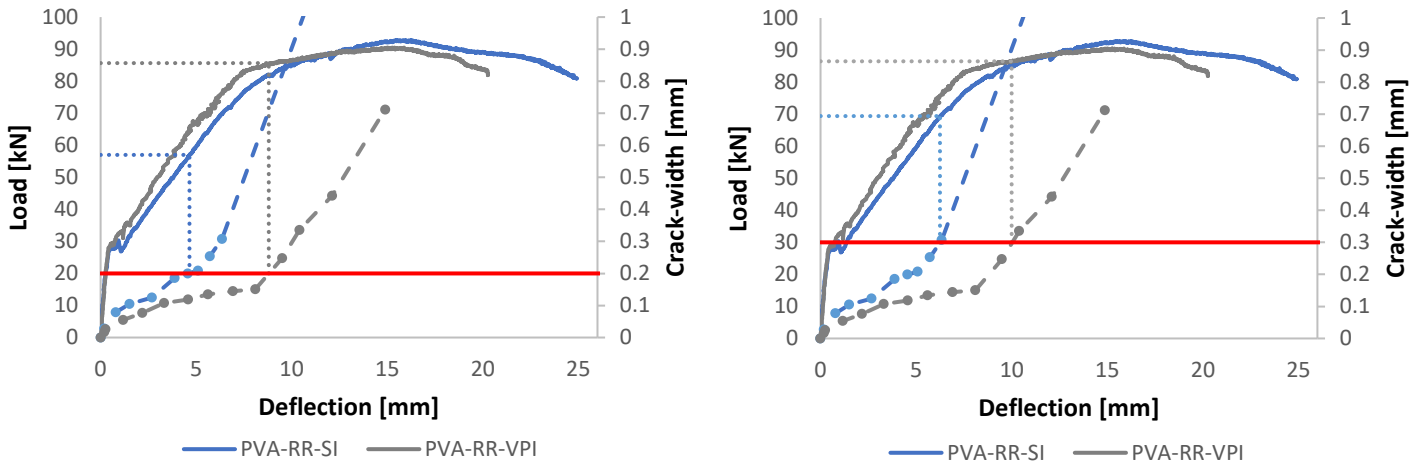


Fig. 6.9: Comparison load - max. crack-width - deflection curves of beams PVA-RR-SI and PVA-RR-VPI along with the 0.2mm crack-width limit (left) and 0.3mm crack-width limit (right)

More importantly for the aim of this study, the dashed lines in Fig. 6.9 show the maximum crack-width development of both beams. It can be observed that beam PVA-RR-SI is unable to control crack-widths beyond yielding of the rebars. The 0.2mm and 0.3mm crack-width limits are exceeded at loads of 57.0kN and 69.4kN, respectively, in beam PVA-RR-SI. Beam PVA-RR-VPI, however, is able to control crack-widths beyond yielding for both crack-width limits. The 0.2mm and 0.3mm crack-width limits are exceeded at loads of 85.6kN and 86.5kN, respectively, in beam PVA-RR-VPI. Thus, changing the smooth interface (SI) to a Vaseline-treated profiled interface (VPI), results in an increase at which the 0.2mm and 0.3mm crack-width limit are exceeded of 50.2% and 24.6%, respectively.

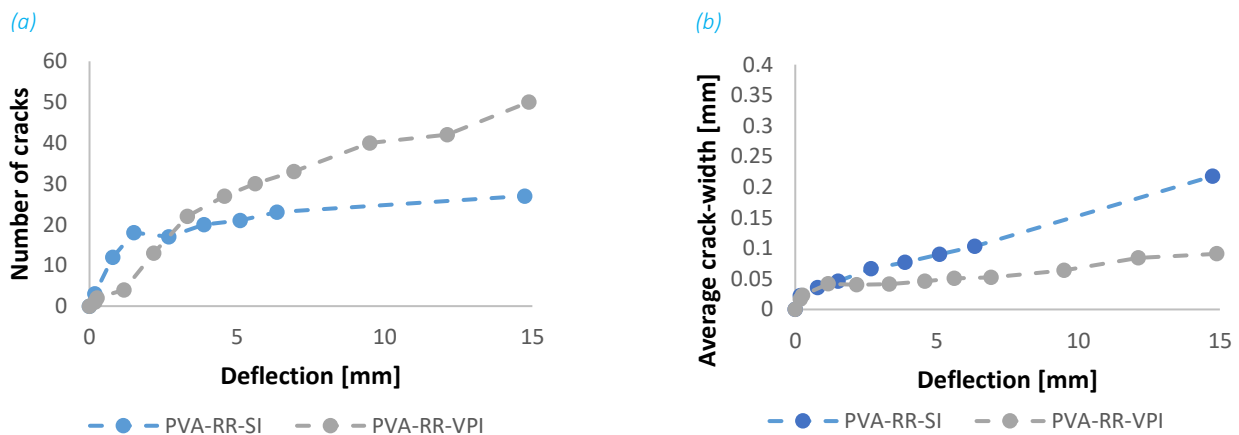


Fig. 6.10: Comparison of (a) number of developed cracks and (b) average crack-width between beams PVA-RR-SI and PVA-RR-VPI

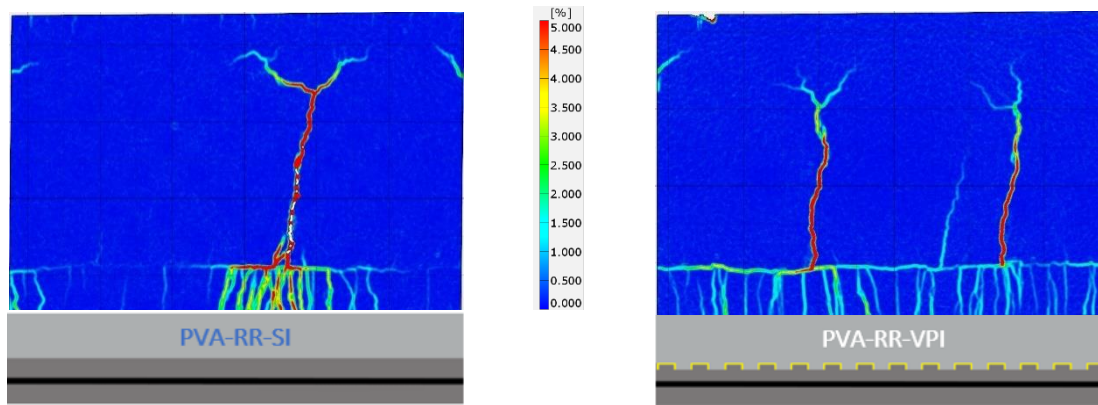


Fig. 6.11: Contour plot of Von Mises strains at a load of 72kN for beam PVA-RR-SI (left) and beam PVA-RR-VPI (right)

To understand why the Vaseline-treated profiled interface (VPI) results in improved crack-width control compared to the smooth interface (SI), the delamination behavior of both interfaces is compared (Fig. 6.12). As shown in Fig. 5.13 (SI) and Fig. 5.29 (VPI), the smooth interface partially delaminates from a low load onwards, while the Vaseline-treated profiled interface exhibits controlled delamination until ultimate load. At ultimate load, the maximum delamination of the VPI is 0.13mm, whereas this degree of delamination is already observed in the SI at a load of 35kN (Fig. 5.13). The contour plots of the vertical strains of beams PVA-RR-SI and PVA-RR-VPI (Fig. 6.12) also highlight this. For the SI, significant delamination (indicated by redness along the interface) occurs at a load level of 28kN, (also evident from Fig. 5.13) . At a similar load level of 32kN profound delamination of the VPI is still not observable. At a load level of 55kN, it can be seen that beam PVA-RR-VPI shows controlled delamination over the full length of the CBMR, whereas in beam PVA-RR-SI the interface displays only partial delamination, but to a greater extent. The limited amount of delamination at lower loads and the controlled delamination over the full length of the CBMR at higher loads of the Vaseline-treated profiled interface, allow for the SHCC to be activated over the full length of the CBMR (as can be seen from the cracking pattern in Fig. 6.11), resulting in a greater amount of cracks and a lower average crack-width (Fig. 6.10). Whereas, the profound delamination at lower loads - resulting in higher stresses in the SHCC layer at lower loads - and the partial delamination - resulting in partial activation of SHCC (Fig. 6.11) - of the smooth interface, lead to earlier crack localization and ultimately worse crack-width controlling ability.

Thus, it can be suggested that when delamination occurs over the full length of the CBMR (facilitated by the chemical debond with the application of Vaseline), but is controlled and remains limited (facilitated by the mechanical interlock through the shear keys), crack-widths are better controlled. This is in accordance with the findings of He [53].

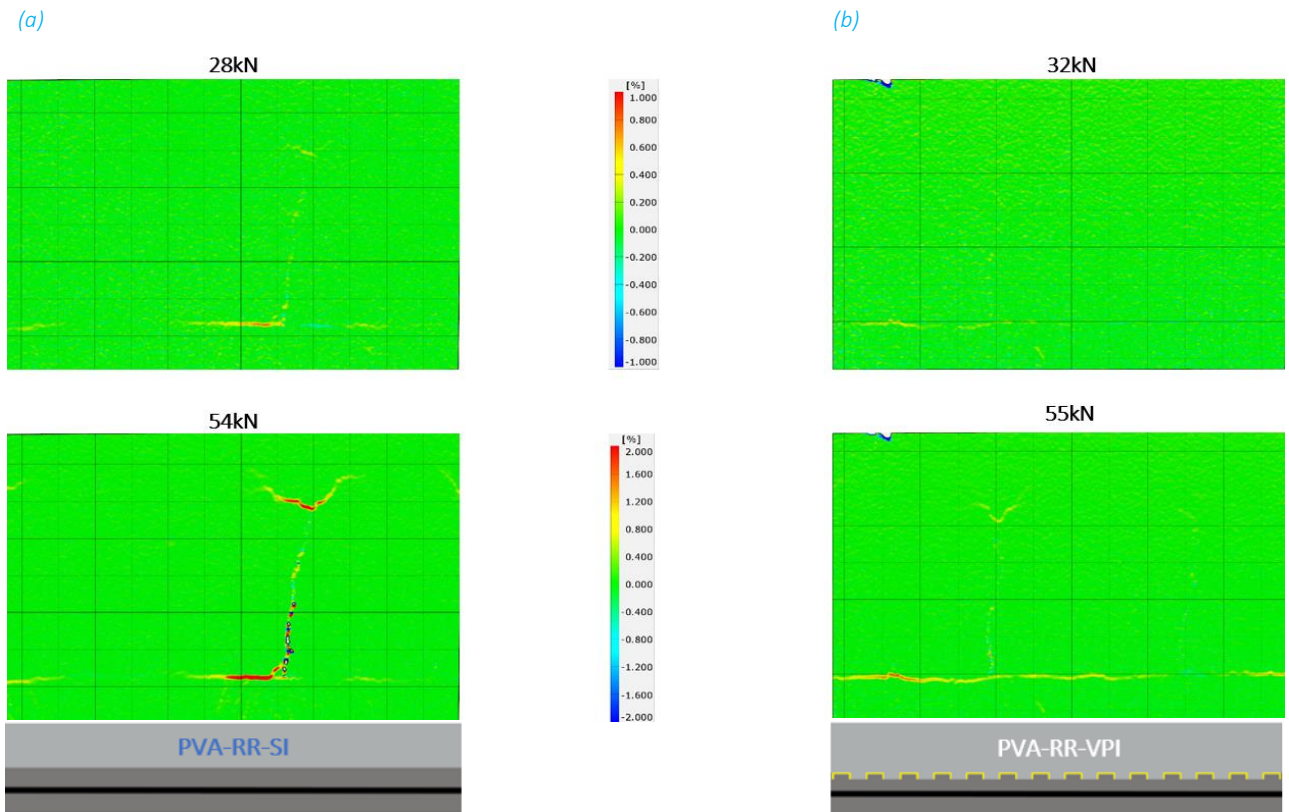


Fig. 6.12: Comparison of interface behavior of (a) beam PVA-RR-SI and (b) beam PVA-RR-VPI at different loads

### 6.4 Influence of reinforcement-SHCC bond

Fig. 6.13 presents the load – maximum crack-width – deflection curves for beams PVA-RR-VPI and PVA-SR-VPI, which differ in the rebar type. Based on the number of developed cracks (Fig. 6.15a) and the distribution of these cracks (Fig. 6.14), one would expect the stiffness of beam PVA-RR-VPI to be significantly higher than the stiffness of beam PVA-SR-VPI. The stiffnesses of the beams, however, seem to be similar. A probable explanation of the unexpectedly higher stiffness of beam PVA-SR-VPI is the slightly higher SHCC layer in this beam due to a casting error, as was explained in Section 4.3.5. The tension stiffening effect in beam PVA-SR-VPI becomes smaller at higher loads - as was also observed in beam PVA-RR-SI – due to the distribution of the cracks (Fig. 6.14).

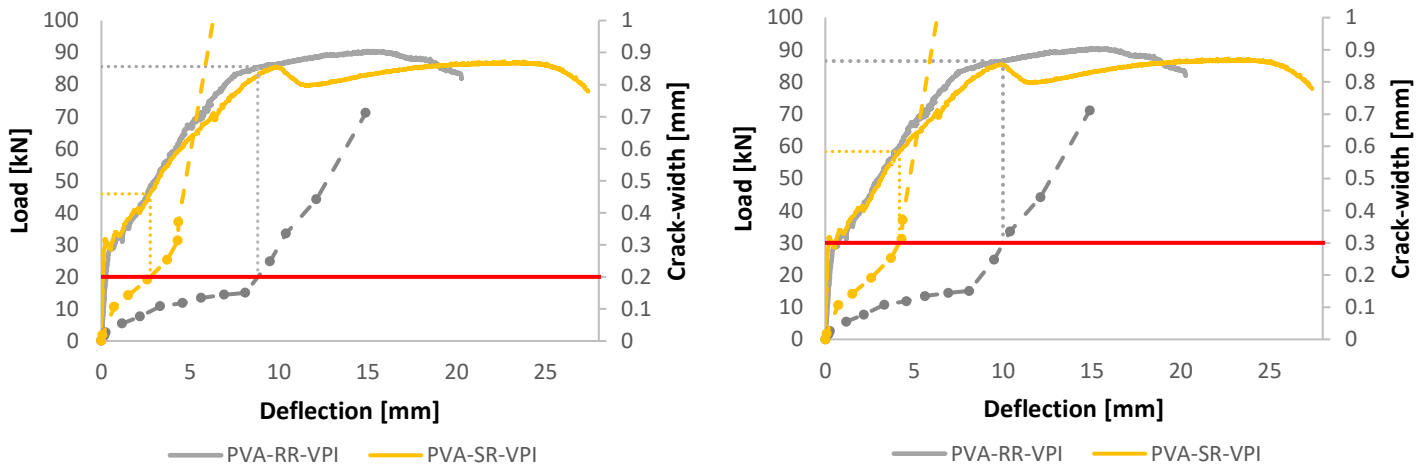


Fig. 6.13: Comparison load - max. crack-width - deflection curves of beams PVA-RR-VPI and PVA-SR-VPI along with the 0.2mm crack-width limit (left) and 0.3mm crack-width limit (right)

Moreover, it can also be observed that the beam with smooth rebars (SR) exhibits higher ductility compared to the beam with rough rebars (RR). The deflection at ultimate load for beam PVA-SR-VPI is 8.3mm higher than the deflection at ultimate load in beam PVA-RR-VPI. A likely reason for this is that smooth rebars allow for more redistribution of stress through bar slip, ultimately delaying the point of failure. This finding is in accordance with the findings of Bandelt & Billington [54].

This supposed better redistribution of stresses along the rebars, however, does not yield a better crack-width controlling ability of beam PVA-SR-VPI compared to beam PVA-RR-VPI. Rather, the replacement of rough rebars (RR) by smooth rebars (SR) considerably compromises the beam's ability to control crack-widths. Beam PVA-SR-VPI exhibits a 39.5kN reduction in the load at which the 0.2mm crack-width limit is exceeded and a 28.1kN reduction for the 0.3mm crack-width limit, compared to beam PVA-RR-VPI. Both limits are exceeded prior to reinforcement yielding. SHCC is activated to a limited extent in the beam with smooth rebars, as is evident from the number of cracks developed (Fig. 6.15a). The distribution of cracks (Fig. 6.14) also shows a very strong localization of the cracks in beam PVA-SR-VPI. This observation aligns with the findings of Bezemer [3], where a further weakened rebar-SHCC bond (achieved by coating smooth rebars with Vaseline) caused crack localization in the SHCC and even more limited SHCC activation in a 300mm hybrid R/SHCC beam. The findings of the current study indicate that a rebar-SHCC bond established solely through friction and chemical adhesion results in reduced activation of the SHCC, thereby negatively impacting its crack-width controlling ability.

The strong localization of cracks in the SHCC layer in beam PVA-SR-VPI cannot, however, solely be attributed to the weakening of the rebar-SHCC bond. Due to an error during casting, a dent formed in the interface at the exact location where cracks in the SHCC localize (as described in Section 4.3.5).

## 6. Comparison and discussion

This dent leads to more pronounced delamination at this specific location, with (almost) no delamination elsewhere, further contributing to the limited SHCC activation. Assessing the observations of the current study in light of the observations of the study of Bezemer [3], it is unlikely that the dent significantly impacted the displayed cracking behavior and consequently the crack-controlling ability of beam PVA-SR-VPI. Moreover, the increased thickness of the SHCC layer in beam PVA-SR-VPI, resulting from the casting error, likely did not result in an underestimation of the crack-width controlling ability of the beam. In fact, under ideal experimental conditions—where the SHCC layer would have been 70mm thick—it is expected that a lower stiffness would have been observed, likely causing the crack-width limits to be exceeded at even lower loads than those recorded in the study (i.e., the results would likely have been even more pronounced).

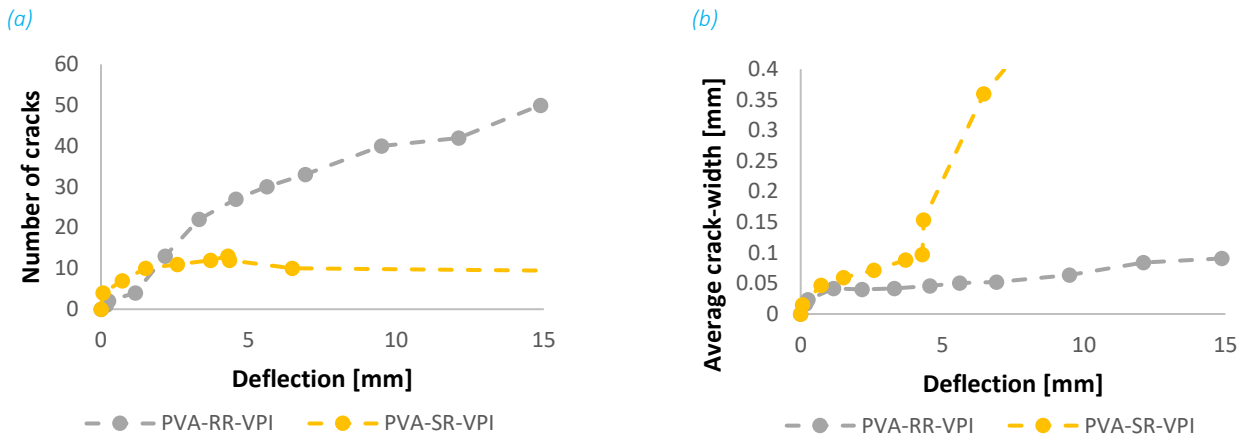


Fig. 6.15: Comparison of (a) number of developed cracks between beams PVA-RR-VPI and PVA-SR-VPI and (b) average crack-width between beams PVA-RR-VPI and PVA-SR-VPI

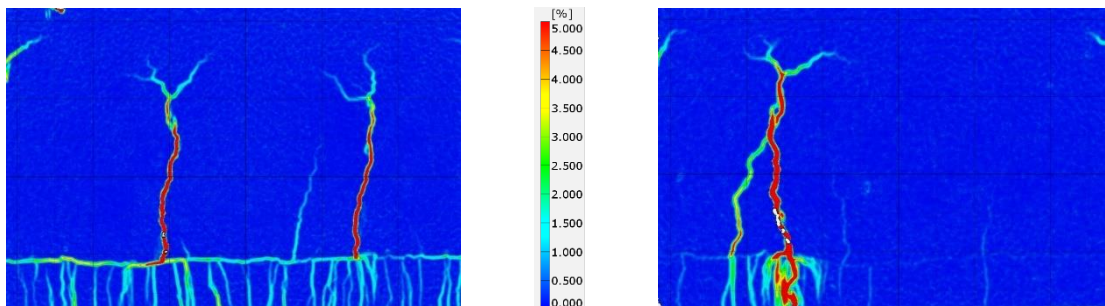


Fig. 6.14: Contour plot of Von Mises strains at a load of 80kN for beam PVA-RR-VPI (left) and beam PVA-SR-VPI (right)

It is also interesting to note that the Vaseline-treated profiled interface (which is implemented in both beams) does not yield similar interface behavior. This suggests that roughening the interface is beneficial only when a sufficient rebar-SHCC bond is established. If the rebar-SHCC bond is too weak, cracks will localize quickly, diminishing the significance of the interface.

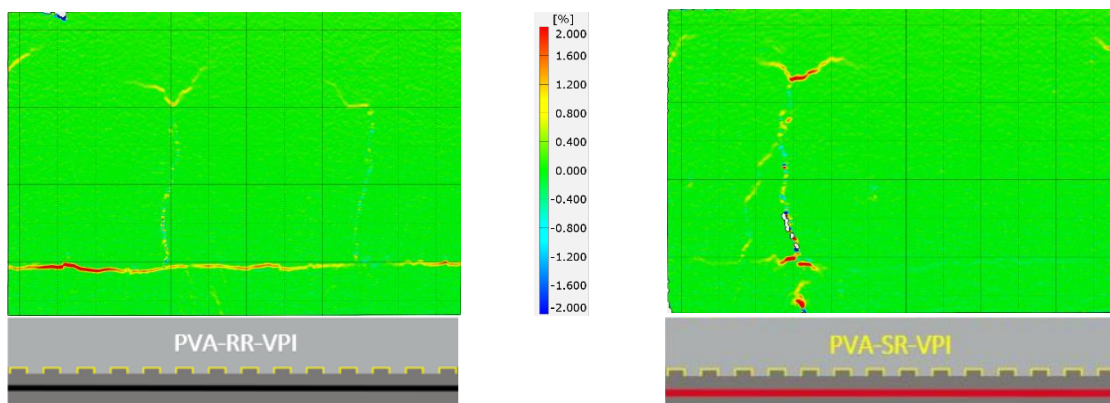


Fig. 6.16: Comparison of interface behavior of (left) beam PVA-RR-VPI (55) and (right) beam PVA-SR-VPI at a load level of 71kN

## 6.5 Influence of SHCC-type

Fig. 6.17 presents the load – maximum crack-width – deflection curves for beams PVA-SR-VPI and PE-SR-VPI, where two different SHCC-types are employed, one based on PVA fibers and the other based on PE fibers. The unexpectedly higher stiffness of beam PVA-SR-VPI compared to beam PE-SR-VPI is for the same reasons already discussed in the previous section. The beam with PE-SHCC shows higher ductility compared to the beam with PVA-SHCC – as a result of the higher ductility of PE-SHCC compared to PVA-SHCC<sup>27</sup>, with the deflection at ultimate load being 3.4mm higher in beam PE-SR-VPI compared to beam PVA-SR-VPI.

More importantly for the aim of this study, the dashed lines in Fig. 6.17 show the maximum crack-width development of both beams. It can be observed that beam PE-SR-VPI shows superior crack-width control compared to beam PVA-SR-VPI. The 0.2mm and 0.3mm crack-width limits are exceeded at loads of 50.7kN and 70.0kN, respectively, in beam PE-SR-VPI. Thus, substituting PVA-SHCC by PE-SHCC, results in an increase at which the 0.2mm and 0.3mm crack-width limit are exceeded of 10.5% and 19.9%, respectively. This enhanced crack-width control when using PE-SHCC compared to PVA-SHCC can directly be attributed to the increased number of cracks formed (Fig. 6.18a) and the improved distribution (Fig. 6.19) of these cracks in beam PE-SR-VPI compared to beam PVA-SR-VPI, thereby keeping the maximum and average crack-width small (Fig. 6.18b).

It is important to note that the benefits of PE-SHCC cannot be solely attributed to the fiber type but rather to the overall SHCC mix, as the mixtures differ in more than just fiber composition. The PE mixture contained slightly more fine material, featured fibers that were 2mm shorter than those in the PVA mixture, and had a lower fiber volume. Viewed holistically, these parameters collectively influence the resulting tensile properties. Comparing the tensile properties of the two mixtures, it is suggested that one of the reasons for the superior crack-width controlling ability of beam PE-SR-VPI is the lower tensile strength combined with a higher tensile strain capacity of the PE-mixture.

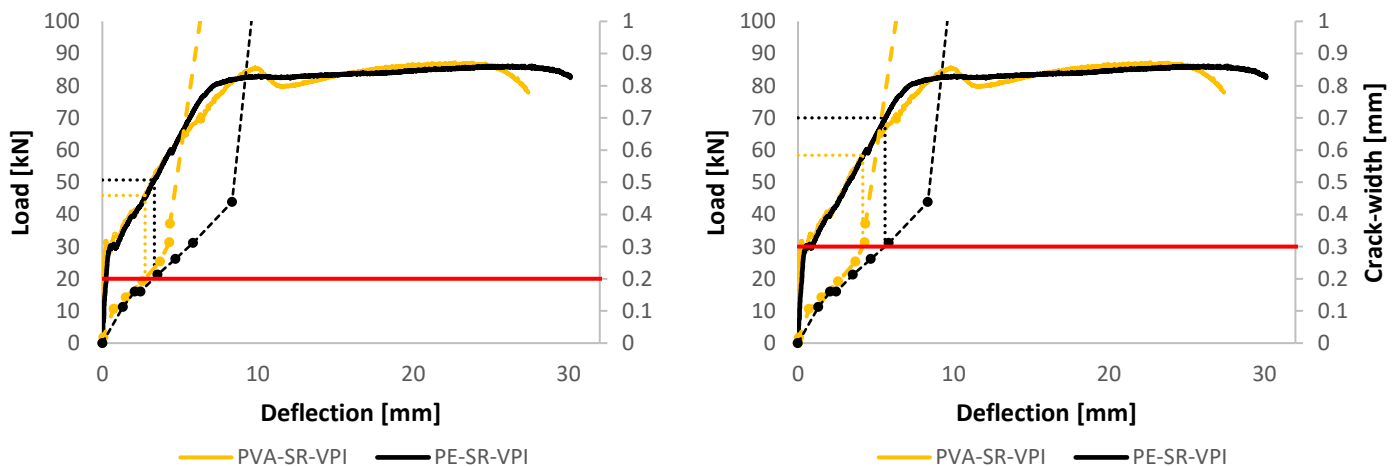


Fig. 6.17: Comparison load - max. crack-width - deflection curves of beams PVA-SR-VPI and PE-SR-VPI along with the 0.2mm crack-width limit (left) and 0.3mm crack-width limit (right)

<sup>27</sup> In the current study, testing of PVA-SHCC was not succeeded in. However, a direct comparison of the ductility of both mixtures can be made based on previous studies [3] where these mixtures were used and tested.

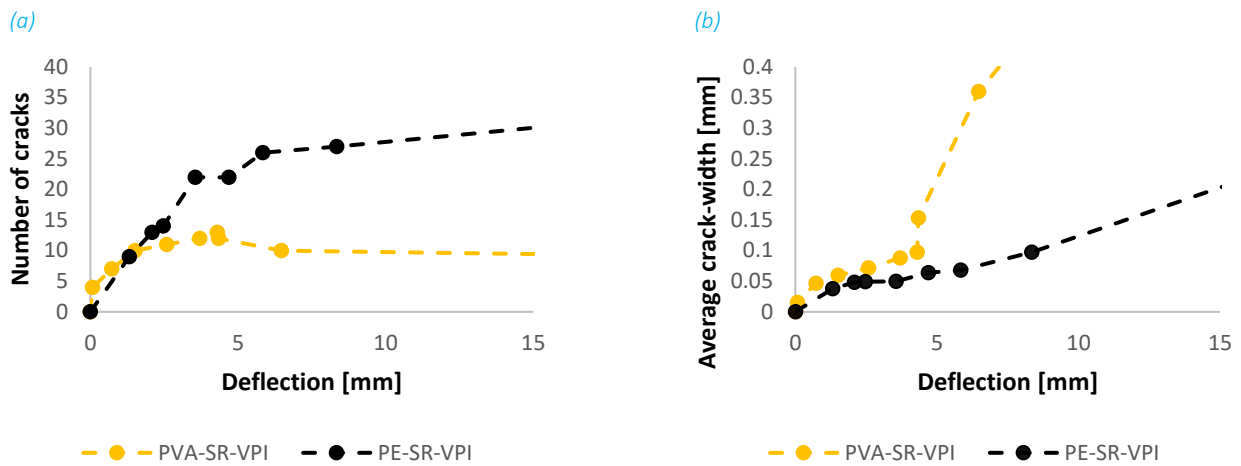


Fig. 6.18: Comparison of (a) number of developed cracks between beams PVA-SR-VPI and PE-SR-VPI and (b) average crack-width between beams PVA-SR-VPI and PE-SR-VPI

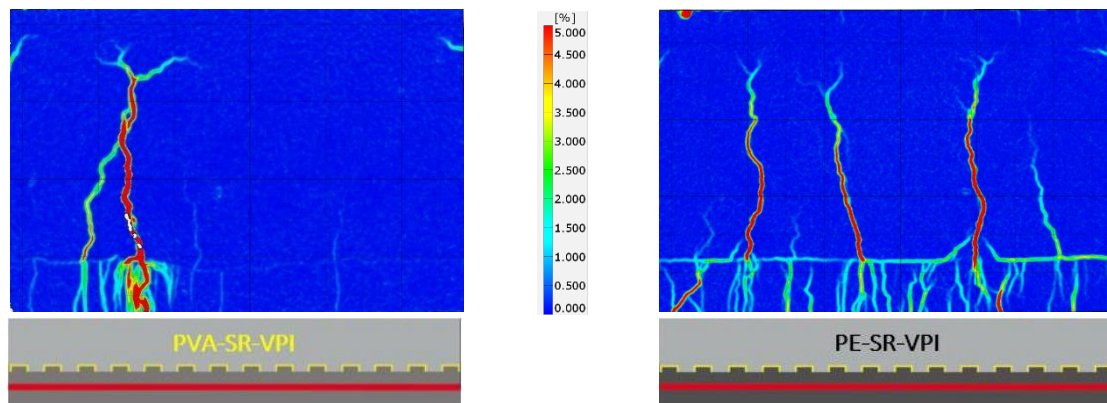


Fig. 6.19: Contour plot of Von Mises strains at a load of 80kN for beam PVA-SR-VPI (left) and beam PE-SR-VPI (right)

Moreover, in discussing the influence of the rebar-SHCC bond, it was noted that a weaker bond resulted in lower activation of the SHCC due to the fast localization of cracks. Consequently, the advantages of the Vaseline-treated interface (VPI) could not be fully realized. However, a comparison of the interface behavior (Fig. 6.20) between beams PVA-SR-VPI and PE-SR-VPI reveals that the benefits of using a VPI are achieved with PE-SHCC. This suggests that the significantly enhanced activation of SHCC in beam PE-SR-VPI, compared to beam PVA-SR-VPI, is likely due to the strengthened rebar-SHCC bond associated with PE-SHCC.

This suggestion is supported by the findings of Deng et al. [59], who examined the bond behavior of similar mixtures containing PVA and PE fibers under both monotonic and cyclic loading conditions. Their research demonstrated that the rebar-SHCC bond strength in the PE fiber samples was at least twice as high as in the PVA fiber samples for both loading types. However, there remains limited comparative research specifically addressing the rebar-SHCC bond behavior in PE-SHCC as compared to PVA-SHCC. Most studies, as discussed in the literature review in Section 2.1.3, focus predominantly on PVA-SHCC – mainly due to its lower cost –, leaving the bond behavior of PE-SHCC relatively underexplored.

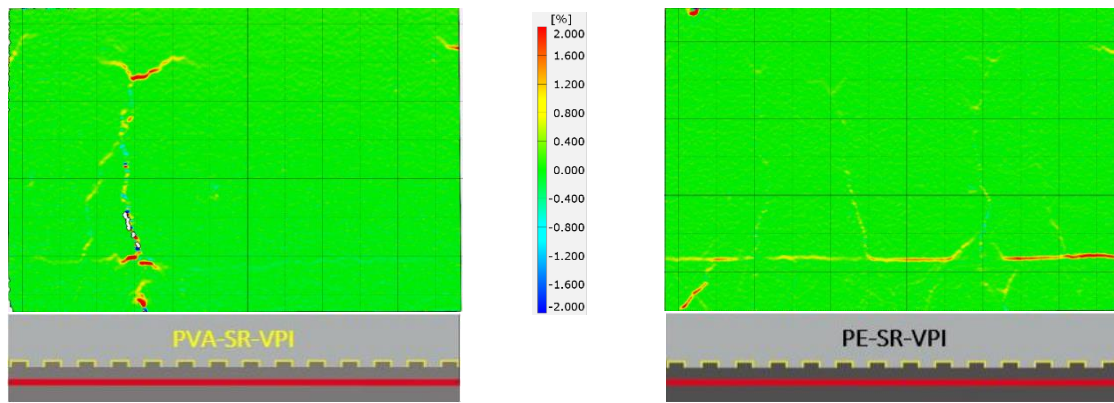


Fig. 6.20: Comparison of interface behavior of (left) beam PVA-SR-VPI (55) and (right) beam PE-SR-VPI at a load level of 71kN

The potentially stronger rebar-SHCC bond when using PE-SHCC raises an important question regarding the performance of a hybrid R/SHCC beam with PE-SHCC and ribbed rebars, a configuration not examined in the current study. While the present study has established that for PVA-SHCC, mechanical interlock is necessary to achieve sufficient bond strength and activate the SHCC, excessively high bond strength—such as that potentially created by combining PE-SHCC with ribbed rebars—could present challenges in strain redistribution in the reinforcement. This may lead to stress localization, which could, in turn, promote premature crack localization. However, further research would be needed to confirm this hypothesis.

## 6.6 Efficiency of all tested beams

Fig. 6.21 shows the efficiency of all tested beams – including the beams tested by Bezemer [3] – in limiting the crack-widths below the 0.2mm and 0.3mm crack-width limits.

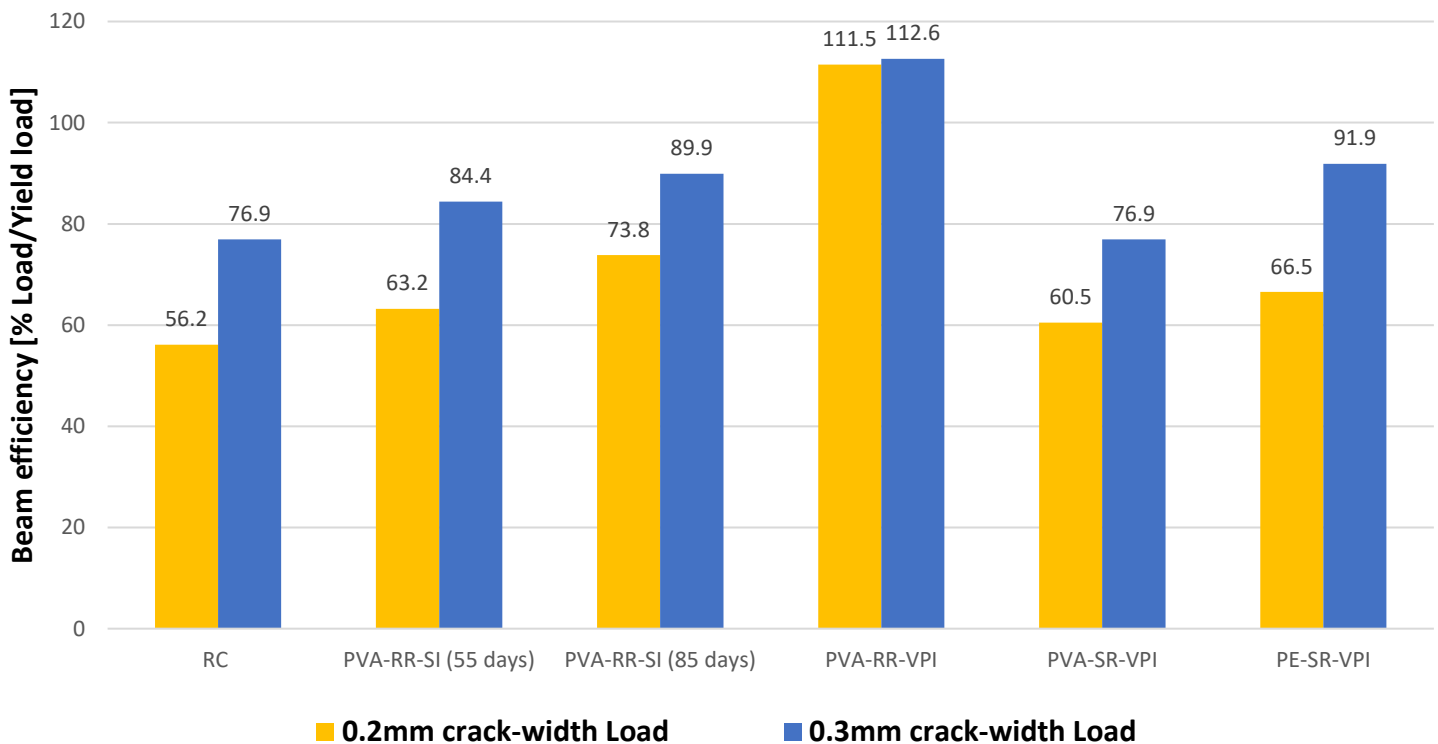


Fig. 6.21: Efficiency of all tested beams expressed as the percentage relative to the yield load at which the 0.2mm and 0.3mm crack-width limits are exceeded. Beams RC and PVA-RR-SI (55) are tested by Bezemer [3].

The observations indicate that only beam PVA-RR-VPI effectively limits crack widths beyond the yielding point of the reinforcement. The implementation of a 70mm thick SHCC layer shows a modest benefit when comparing the RC beam to PVA-RR-SI(55). A similar modest improvement is also observed with extended curing time, as seen when comparing PVA-RR-SI(55) to PVA-RR-SI(85). In contrast, the application of a Vaseline-coated profiled interface yields a significant improvement in crack-width control, as evident in the comparison between PVA-RR-SI(85) and PVA-RR-VPI. However, the use of smooth rebars reduces the effectiveness of the beam in controlling crack widths, as seen when comparing PVA-RR-VPI to PVA-SR-VPI. Lastly, using PE-SHCC instead of PVA-SHCC notably enhances the beam's crack-width control efficiency.

## 6.7 Behavior outside CBMR

Although this study primarily focuses on the flexural cracking behavior within the CBMR, it is also insightful to analyse the behavior outside the CBMR, as the bending moment remains significant in areas adjacent to the CBMR. Consequently, the cracking behavior 200mm to the left and right of the CBMR is evaluated for two beams: PVA-RR-SI and PE-SR-VPI. Furthermore, the behavior of the SHCC-CC interface outside the CBMR is assessed for all beams in the study.

### 6.7.1 Cracking behavior

#### Beam PVA-RR-SI

At a load level of 60kN, it was determined (Section 5.1) that the 0.2mm crack-width limit had been exceeded within the CBMR. To further investigate this, the same load level is analysed, but this time including the regions outside the CBMR. As shown in Fig. 6.22, at this load level, the 0.2mm crack-width limit is also exceeded in the areas outside of the CBMR.

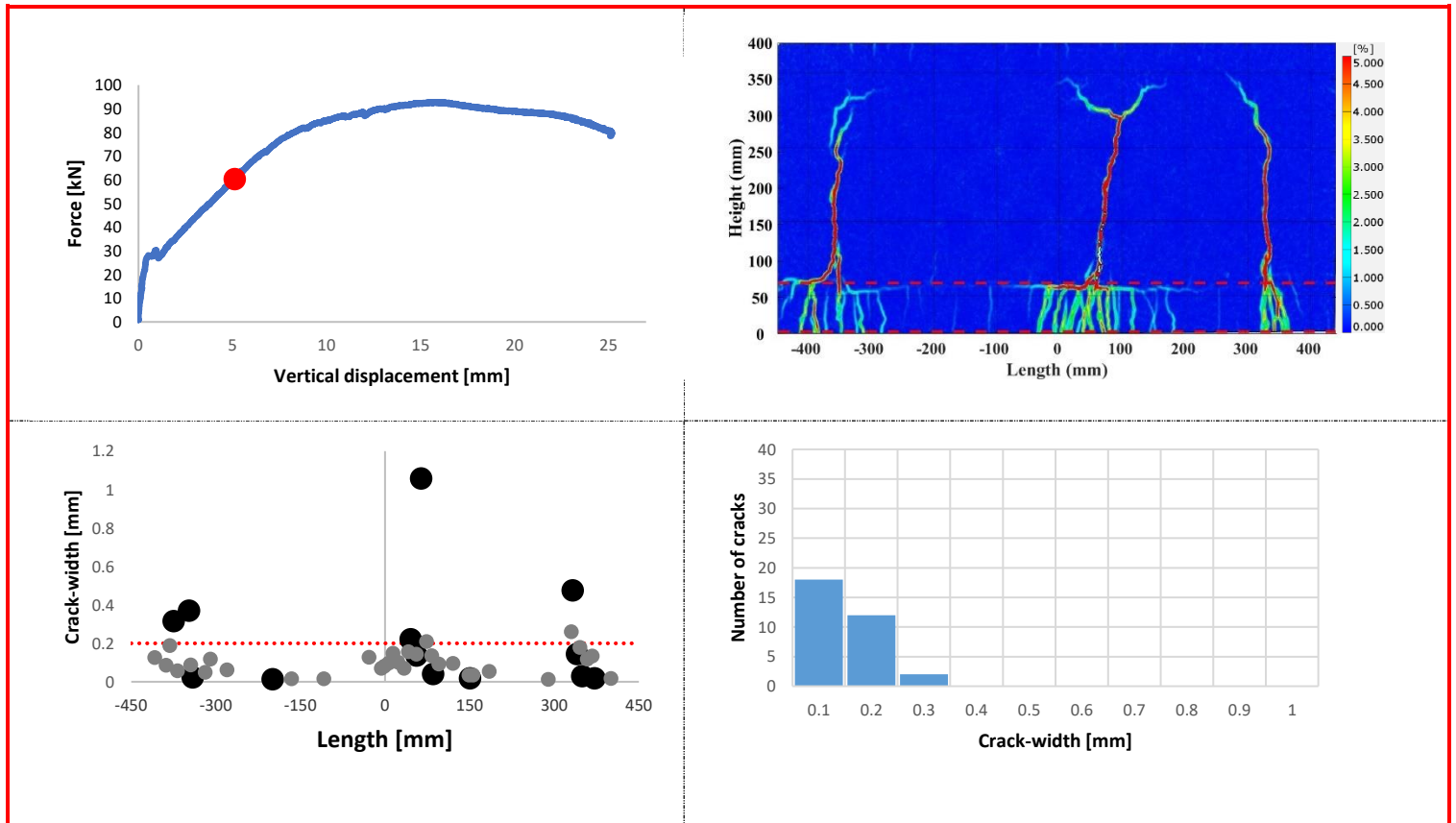


Fig. 6.22: Cracking behavior of beam PVA-RR-SI at a load of 60kN with the inclusion of the areas adjacent to the CBMR. Top left: Load-level on load-deflection curve. Top right: Contour plot Von-Mises strains. Bottom left: Scatter plot of all cracks. Bottom right: Crack-width distribution of cracks in SHCC.

Fig. 6.23 demonstrates that at a significantly earlier load step of 41kN, the 0.2mm crack-width limit is exceeded outside of the CBMR. At the location where this happens a stirrup is present. The stress concentrations at this transition zone are probably caused by a combination of reasons. The cracking patterns observed near the stirrups—particularly the merging of cracks propagating into the CC—suggest that the influence of the acting shear force in this region should not be overlooked. Inadequate vibration during casting may also have resulted in improper compaction of the SHCC around the stirrups, creating a weak zone. Additionally, the confinement effect of the stirrups could create a locally slightly stiffer zone, leading to increased stress concentrations at this transition point. The 0.3mm crack-width limit was determined to be exceeded at a load level of 70kN. To further investigate this, the same load level was analysed, but this time including the regions outside the

## 6. Comparison and discussion

CBMR. As shown in Fig. 6.24, at this load level, the 0.3mm crack-width limit is not exceeded in the areas outside of the CBMR.

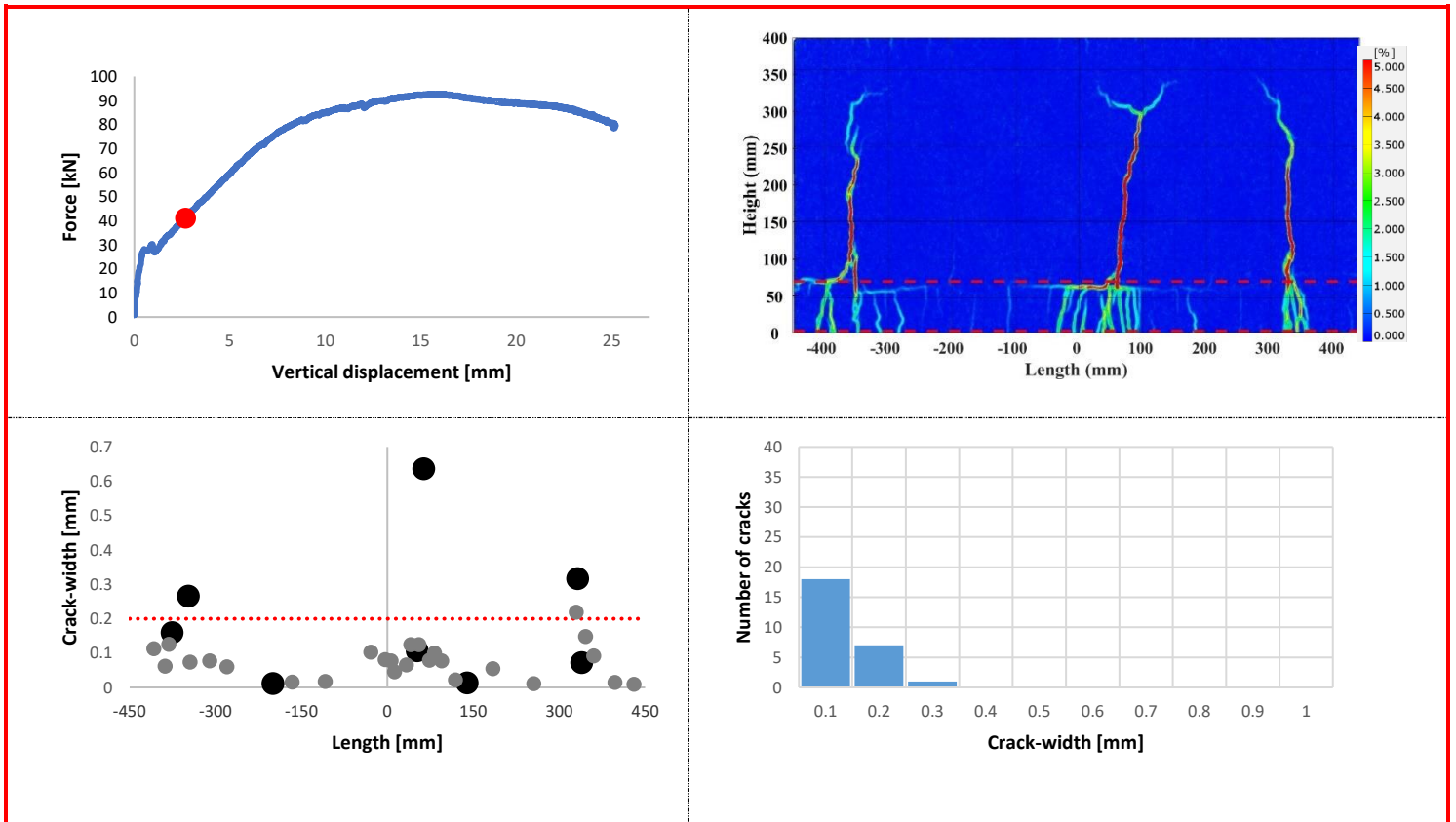


Fig. 6.23: Cracking behavior of beam PVA-RR-SI at a load of 41kN (outside CBMR). Top left: Load-level on load-deflection curve. Top right: Contour plot Von-Mises strains. Bottom left: Scatter plot of all cracks. Bottom right: Crack-width distribution of cracks in SHCC.

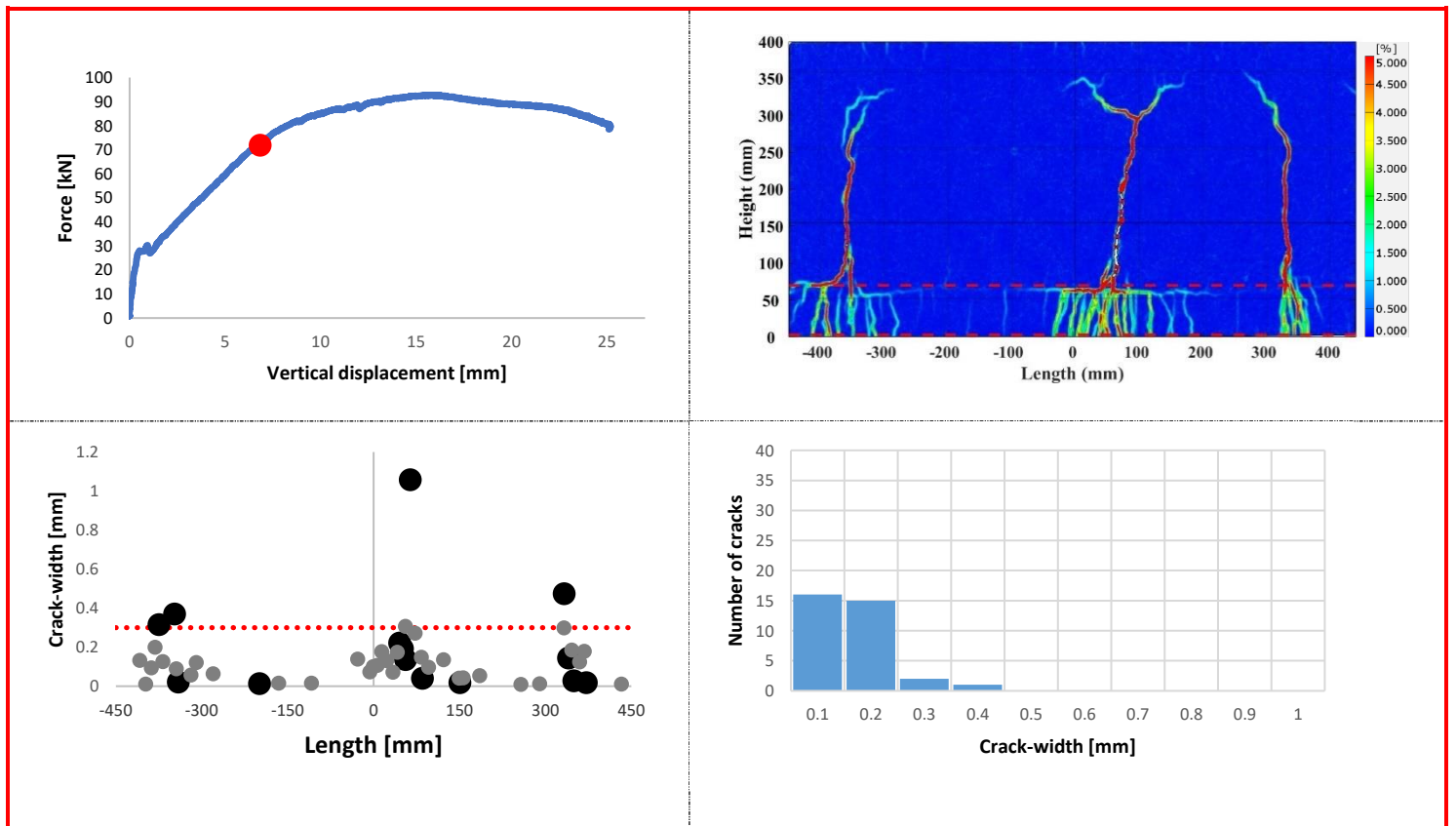


Fig. 6.24: Cracking behavior of beam PVA-RR-SI at a load of 70kN (outside CBMR). Top left: Load-level on load-deflection curve. Top right: Contour plot Von-Mises strains. Bottom left: Scatter plot of all cracks. Bottom right: Crack-width distribution of cracks in SHCC.

## 6. Comparison and discussion

The load-max. CW-deflection curve for beam PVA-RR-SI, which includes data from both inside and outside the CBMR, is presented in Fig. 6.25. It shows that the 0.2mm crack-width limit is exceeded at a load of 39.9kN, representing a decrease of 17.1kN compared to the load required for the same limit within only the CBMR. The 0.3mm crack-width limit is exceeded at a load of 69.9kN, which remains unchanged from the value observed within the CBMR alone.

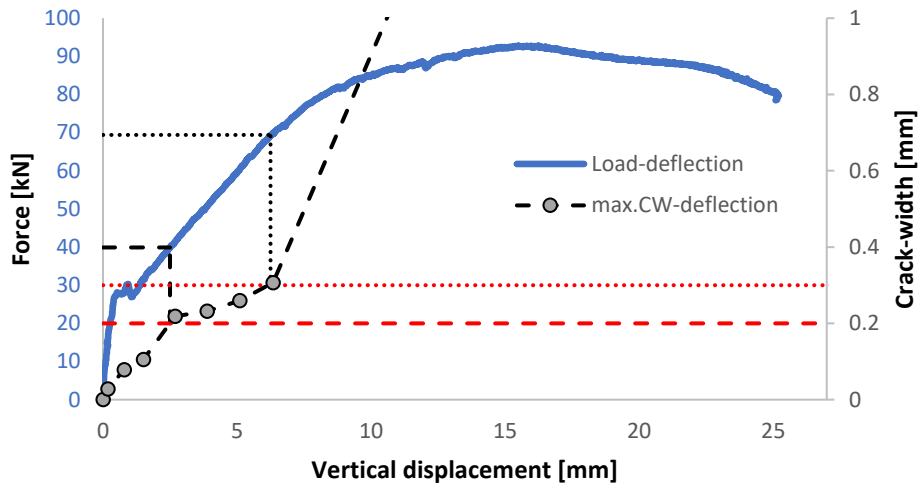


Fig. 6.25: Load - max.CW - deflection curve of beam PVA-RR-SI (including region outside CBMR)

### Beam PE-SR-VPI

At a load level of 52kN, it was determined (Section 5.1) that the 0.2mm crack-width limit had been exceeded within the CBMR. To further investigate this, the same load level is analysed, but this time including the regions outside the CBMR. As shown in Fig. 6.26, at this load level, the 0.2mm crack-width limit is also exceeded in the areas outside of the CBMR. Furthermore it can also be seen that even the 0.3mm crack-width limit is exceeded at this load level.

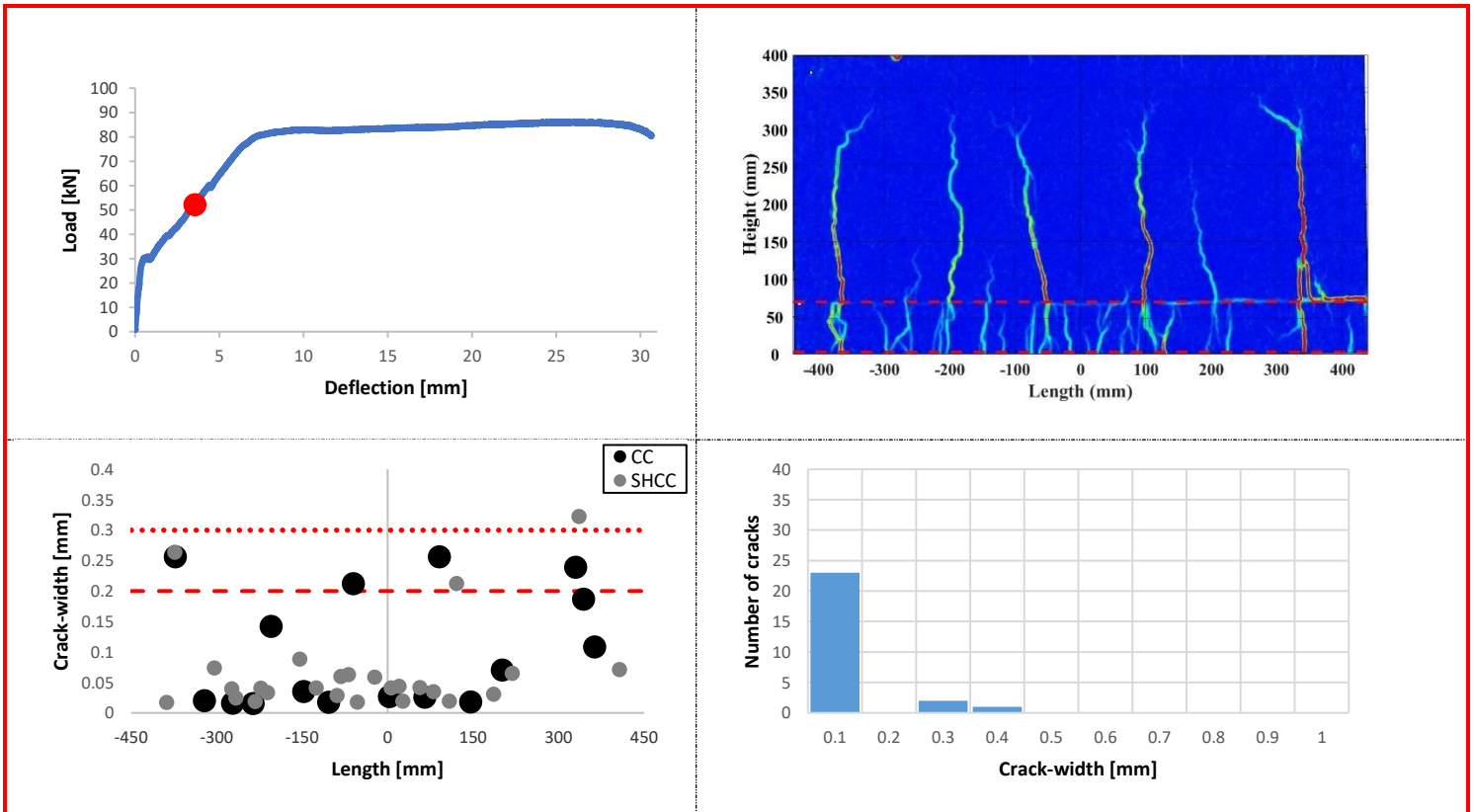


Fig. 6.26: Cracking behavior of beam PE-SR-VPI at a load of 52kN (outside CBMR). Top left: Load-level on load-deflection curve. Top right: Contour plot Von-Mises strains. Bottom left: Scatter plot of all cracks. Bottom right: Crack-width distribution of cracks in SHCC.

Fig. 6.27 demonstrates that at a significantly earlier load step of 40kN, the 0.2mm crack-width limit is exceeded outside of the CBMR.

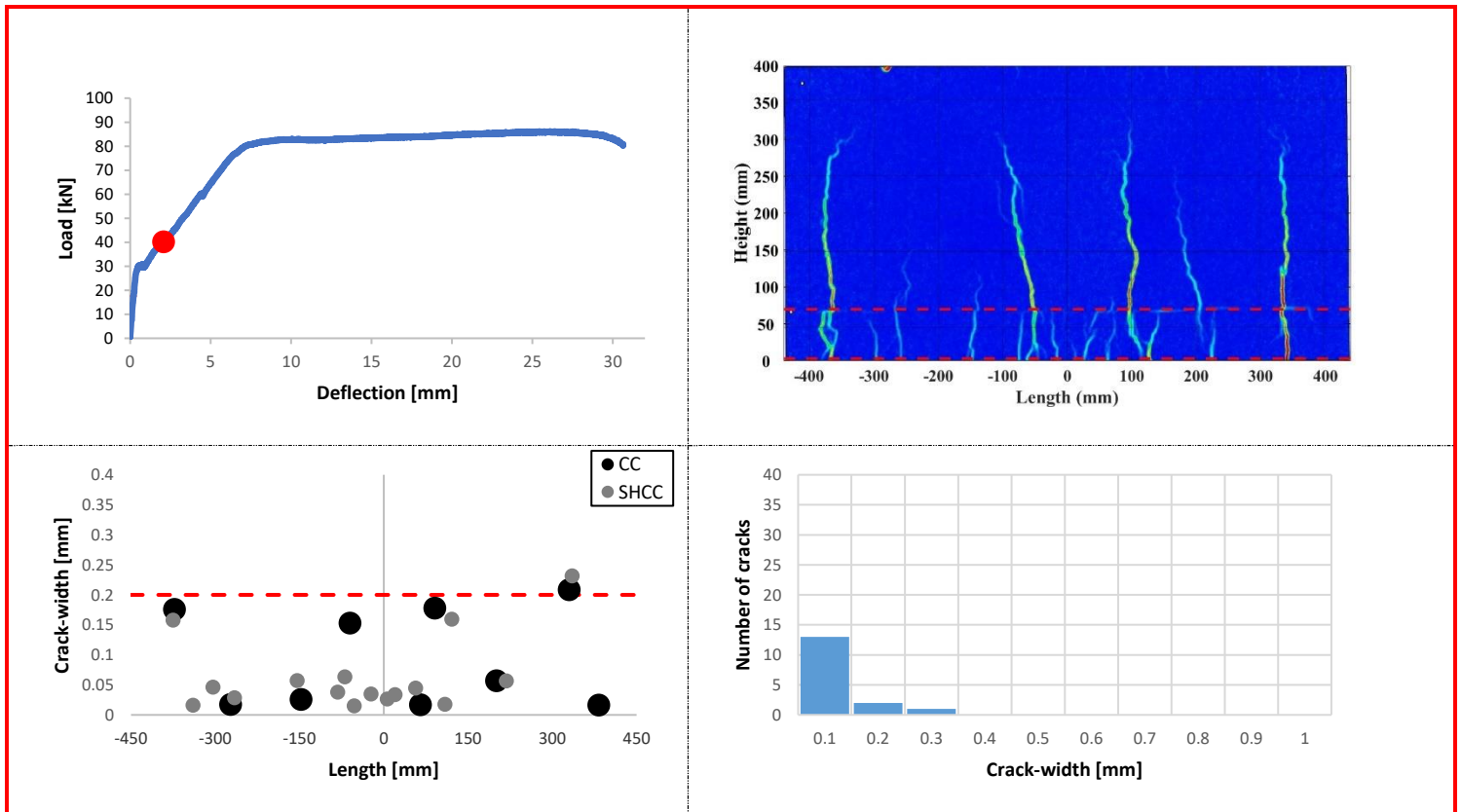


Fig. 6.27: Cracking behavior of beam PE-SR-VPI at a load of 40kN with the inclusion of the areas adjacent to the CBMR. Top left: Load-level on load-deflection curve. Top right: Contour plot Von-Mises strains. Bottom left: Scatter plot of all cracks. Bottom right: Crack-width distribution of cracks in SHCC.

The load-max. CW-deflection curve for beam PE-SR-VPI, which includes data from both inside and outside the CBMR, is presented in Fig. 6.28. It shows that the 0.2mm crack-width limit is exceeded at a load of 39.5kN, a decrease of 11.2kN compared to the load required for this limit when considering only the CBMR. Similarly, the 0.3mm crack-width limit is exceeded at a load of 49.1kN, representing a decrease of 20.9kN from the corresponding load in the CBMR alone. In addition to the reasons previously discussed regarding the cracking behavior of beam PVA-RR-SI outside the CBMR, the location where crack localization occurs in beam PE-SR-VPI is particularly vulnerable due to the transition of the interface.

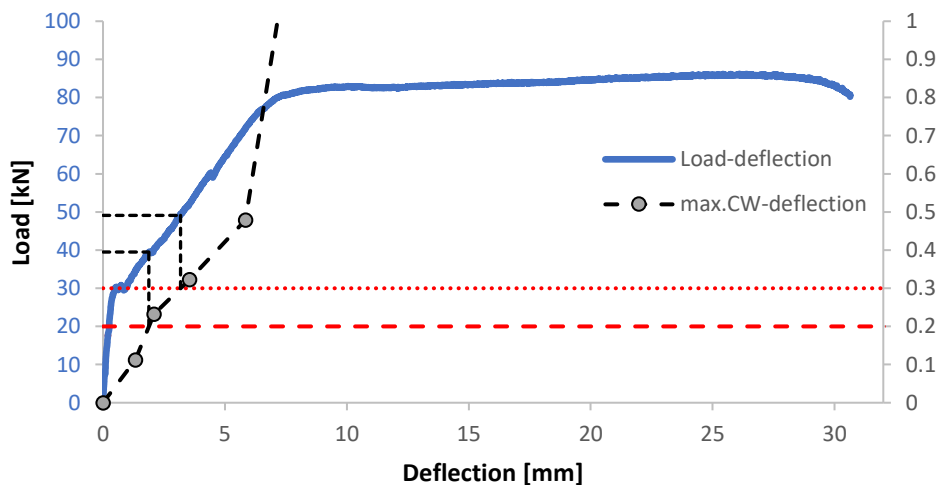


Fig. 6.28: Load - max.CW - deflection curve of beam PVA-RR-SI (including region outside CBMR)

### 6.7.2 Delamination & Slip outside CBMR

The delamination and slip inside the CBMR has already been presented in Chapter 5. The delamination and slip outside the CBMR is monitored on the opposite side of the beam (see Fig. 4.9), to ensure the interface crack does not exceed the crack-width limits and full delamination of the interface across the whole beam does not occur. For all beams it is found that delamination cracks do not exceed the 0.3mm crack-width limit prior to yielding (Fig. 6.29 - Fig. 6.32). The 0.2mm crack-width limit, however, is exceeded prior to yielding in beam PVA-SR-VPI at a load of 71.5kN and in beam PE-SR-VPI at a load of 56.5kN. These loads are larger than the loads at which the 0.2mm crack-width limit is exceeded by a flexural crack for both beams.

#### Beam PVA-RR-SI

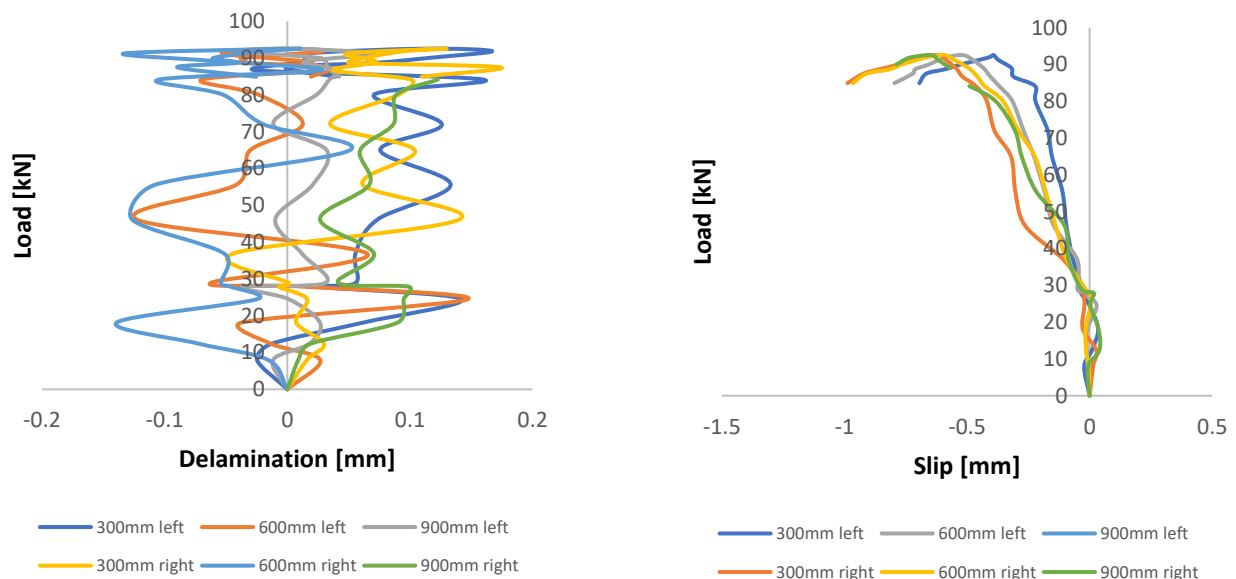


Fig. 6.29: Delamination (left) and slip (right) of beam PVA-RR-SI outside CBMR

#### Beam PVA-RR-VPI

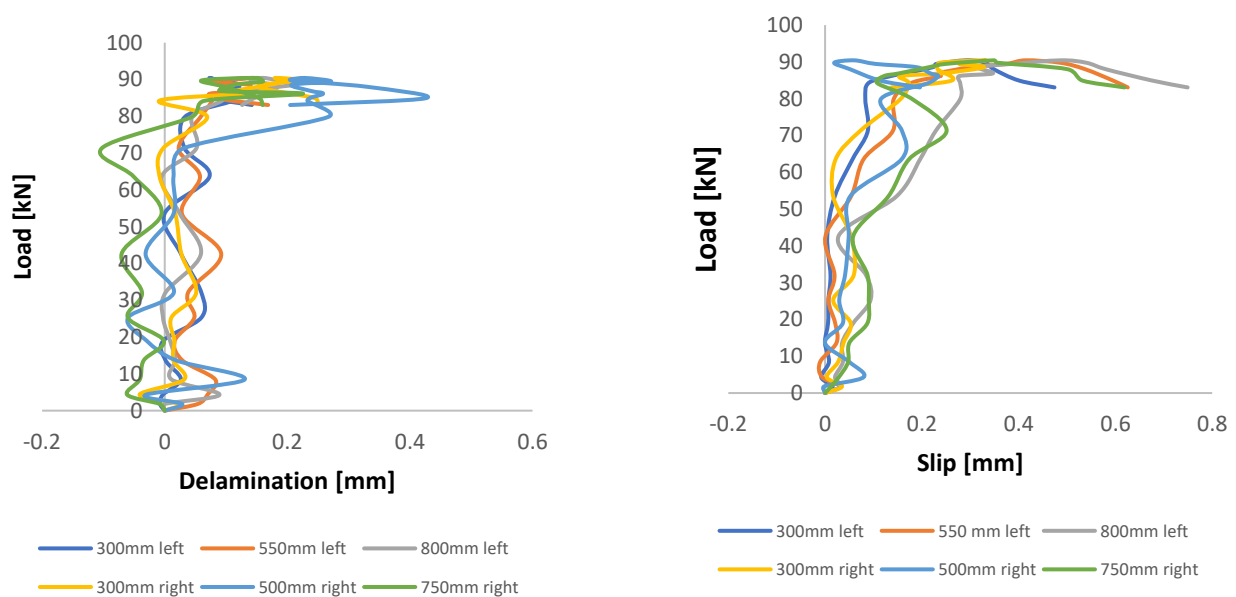


Fig. 6.30: Delamination (left) and slip (right) of beam PVA-RR-VPI outside CBMR

6. Comparison and discussion

Beam PVA-SR-VPI

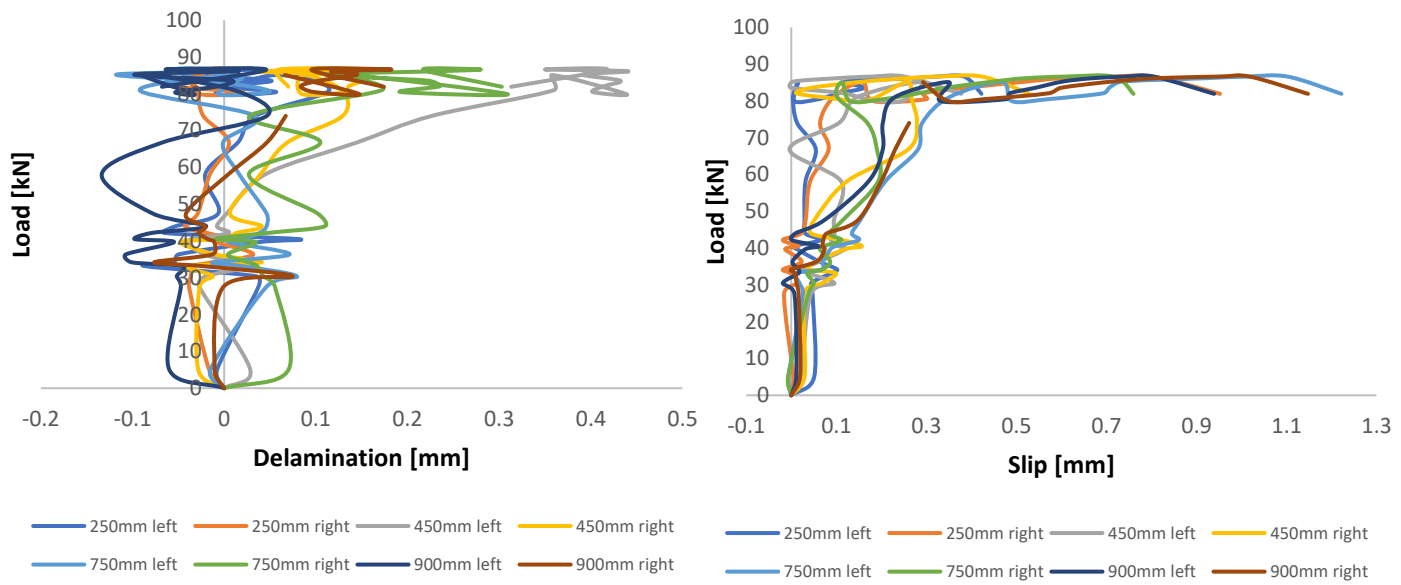


Fig. 6.31: Delamination (left) and slip (right) of beam PVA-SR-VPI outside CBMR

Beam PE-SR-VPI

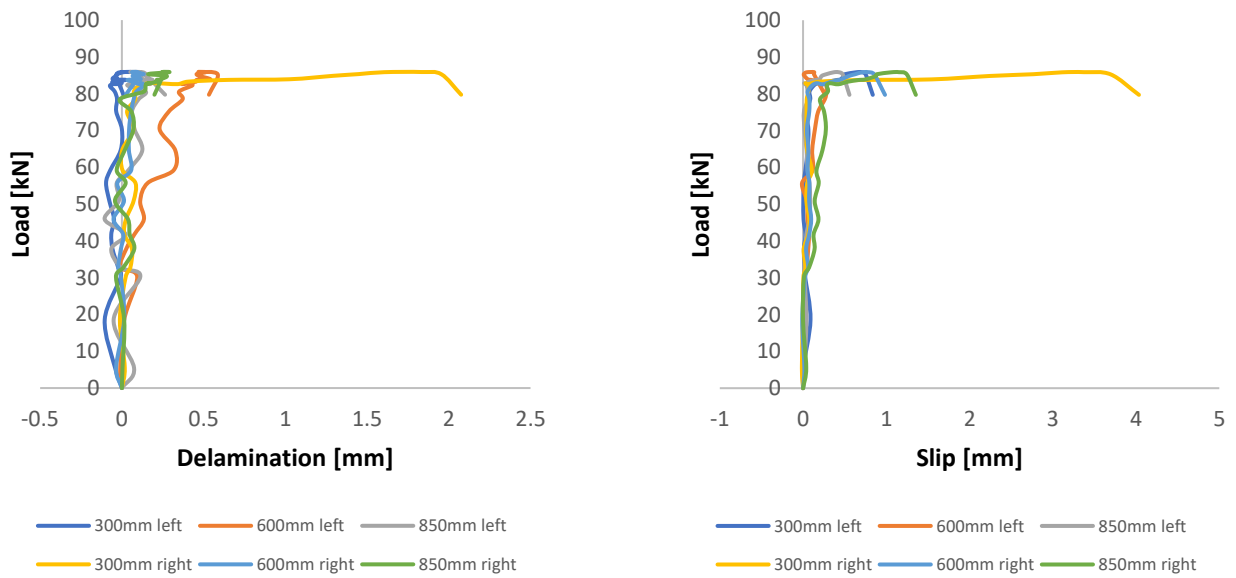


Fig. 6.32: Delamination (left) and slip (right) of beam PE-SR-VPI outside CBMR

# Part III

## Conclusion & Recommendation

---

# 7. Conclusion and recommendation

---

## 7.1 Conclusions

The primary objective of this research is to investigate the crack-width controlling ability of hybrid R/SHCC beams, with a focus on understanding how various parameters such as SHCC-CC interface, rebar-SHCC bond, and SHCC-type impact crack-width control. Thereby the following hypothesis was postulated:

*'The crack-width control in hybrid R/SHCC beams can be improved such that the 0.2mm crack-width limit is not exceeded up until reinforcement yielding by using a roughened SHCC-concrete interface, modifying the steel-SHCC bond by using smooth steel rebars, and choosing PE-based SHCC over PVA-based SHCC.'*

To test the hypothesis, a set of four 400mm high R/SHCC hybrid beams with a 70mm SHCC-layer in the tension zone have been designed and experimentally tested. The main findings from the current study can be summarized as follows:

- Mechanical interlock of the SHCC-CC interface bond — while preventing bond formation through chemical adhesion by applying Vaseline—results in superior crack-width control in R/SHCC beams. In a 400mm hybrid beam with an interface purely based on mechanical interlock (achieved by constructing shear keys), the 0.2mm and 0.3mm crack-width limits were exceeded at 111.5% and 112.6% of the yield load, respectively. In contrast, for a 400mm hybrid beam with an interface based on chemical adhesion and friction, these limits were exceeded at 73.8% and 89.9% of the yield load, respectively. By preventing chemical adhesion, the interface's delamination is promoted. This delamination activates the SHCC across the entire constant bending moment region. Mechanical interlock then controls the delamination, keeping it limited, and allows the SHCC to function as effective reinforcement. In contrast, a bond based on chemical adhesion and friction cannot adequately control the delamination, resulting in higher stresses in the SHCC and, ultimately, earlier crack localization. These findings are in accordance with the findings from the study of He on hybrid beams of 200mm [53], which was elaborated on in the literature study ([Section 2.3.2](#))
- Weakening the reinforcement-SHCC bond by preventing mechanical interlock compromises the crack-width controlling ability of hybrid R/SHCC beams. In a 400mm hybrid beam where the rebar-SHCC bond was formed through a combination of mechanical interlock, friction, and chemical adhesion (ribbed rebars), the 0.2mm and 0.3mm crack-width limits were exceeded at 111.5% and 112.6% of the yield load, respectively. In contrast, for a similar beam with a rebar-SHCC bond based solely on chemical adhesion and friction (smooth rebars), these limits were exceeded at 60.5% and 76.9% of the yield load, respectively. While preventing mechanical interlock enhances ductility, it limits the activation of SHCC and leads

to rapid crack localization. Without a sufficient rebar-SHCC bond, the advantages of a roughened interface cannot be fully realized, indicating the importance of both bond mechanisms working in tandem.

- Hybrid beams incorporating PE-based SHCC demonstrate superior crack-width controlling ability compared to those with PVA-based SHCC when combined with smooth rebars (where the rebar-SHCC bond relies on chemical adhesion and friction). In a 400mm hybrid beam with PE-based SHCC, the 0.2mm and 0.3mm crack-width limits were exceeded at 66.5% and 91.8% of the yield load, respectively. In contrast, for a similar beam with PVA-based SHCC, these limits were surpassed at 60.5% and 76.9% of the yield load. This enhanced performance in PE-SHCC beams is likely due to a significantly stronger rebar-SHCC bond compared to PVA-SHCC. With the use of PE-based SHCC the advantage of a roughened interface was able to be realized, in contrast to PVA-based SHCC. Additionally, PE-SHCC provides a more ductile response in hybrid beams. However, it remains uncertain whether these advantages would hold when rough rebars are used, as excessively high bond strength from mechanical interlock (which may well be the case when using PE-SHCC) could hinder strain redistribution, potentially leading to premature crack localization.
- Curing time has a notable positive effect on the crack-width controlling ability of R/SHCC beams. The findings of the current study suggest that hybrid beams tested at a later age exhibit superior crack-width controlling ability. In a 400mm hybrid beam tested on 85 days of SHCC age, the 0.2mm and 0.3mm crack-width limits were exceeded at 73.8% and 89.9% of the yield load, respectively. In contrast, for a 400mm hybrid beam tested by Bezemer [3] on 55 days of SHCC age, these limits were exceeded at 63.2% and 84.4% of the yield load, respectively. The primary factor driving the improved crack-width control in more cured hybrid beams is the behavior of the SHCC-CC interface. The interface—which, in the assessment of the influence of the curing time in the current study, relied on friction and chemical adhesion—tends to strengthen over time. While a weaker bond may allow for more delamination and thus promote the formation of additional (and better distributed) cracks, it also reduces the SHCC's ability to act as effective reinforcement, ultimately leading to earlier crack localization. Furthermore, curing time affects the strain-hardening properties of SHCC. Younger SHCC exhibits higher tensile strength, which can result in earlier crack localization. Based on the findings of the current study, the behavior of the SHCC-CC interface appears to be the governing mechanism through which curing time influences crack-width control.

The above conclusions are illustrated in

[Fig. 7.1](#), where an overview is given of the influence of certain parameters on the load at which the 0.2mm and 0.3mm crack-width limits are exceeded as a percentage of the yield load.

## 7. Conclusion and recommendation

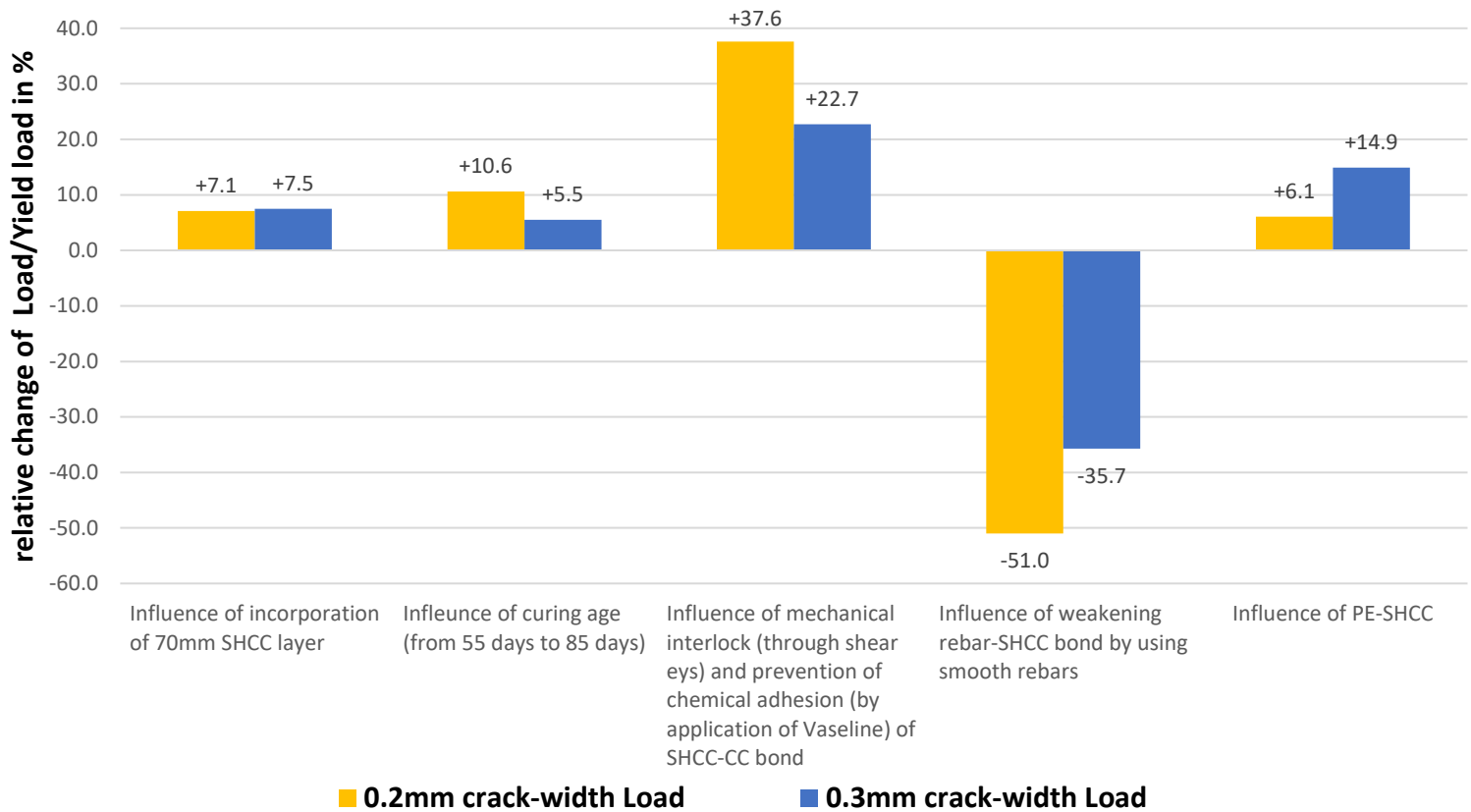


Fig. 7.1: Relative influence of certain parameters on the load at which the 0.2mm and 0.3mm crack-width limits are exceeded as a percentage of the yield load in the 400mm hybrid R/SHC beams

Based on the monitoring of the beams' behavior outside of the CBMR, the following additional conclusions can be drawn:

- The crack-widths outside of the CBMR play a significant role, particularly when employing a profiled interface. The likelihood of crack localization just outside the CBMR, where the bending moment remains substantial, is high. In the examined beams, this localization coincides with the zone where a transition (of the SHCC-CC interface and presence of a stirrup) occurs.
- No beam exhibited complete delamination of the SHCC-CC interface. At all deflections, the two layers remained securely bonded at certain points along the interface. The delamination cracks do not pose a significant concern in any of the beams, as the crack-width limits are found to be either exceeded after reinforcement yielding or after these limits have been exceeded by a flexural crack.

Secondary to the main objective of this thesis, the tensile tests conducted on material samples also yielded some noteworthy conclusions, which can be summarized as follows:

- Compared to the conventionally used dogbone specimens for testing tensile properties, the larger dogbone specimens used in this study, which aimed to better capture the 3D effect of fiber orientation, exhibits vulnerability at the SHCC-glue interface during testing. This results in the failure of the interface before the full (or even partial) development of a cracking pattern. Although glueing the dogbone specimen to a steel hand (specifically designed to

overcome this problem) before attaching it to the test setup improves this issue to some extent, it shifts the problem to the flat part of the steel hand, ultimately causing crack localization at the neck of the dogbone. However, this method allows for a full cracking pattern to form in the tested PE specimens. In contrast, the PVA specimens, which have a higher first-cracking stress, have been shown to not be able to overcome this issue, and thus, the method does not yield any viable results for the PVA specimens.

- The tensile properties of SHCC seem to decrease after a certain age, for both PVA-SHCC (confirmed in the study of Bezemer [3]) as well as PE-SHCC. However, the decrease of the properties of PE-SHCC found in this study, cannot only be attributed to the testing age, as the dogbone specimen size – effecting the 3D orientation of fibers - was increased in this study compared to the study of Nuri [55].

### 7.2 Recommendations

Based on the conclusions, the following recommendations are made:

- The literature review revealed uncertainty regarding the impact of incorporating fine aggregates into SHCC on its strain hardening properties. At the same time, the inclusion of fine aggregates reduces shrinkage and is more cost-effective. Therefore, investigating the effect of fine aggregates on both the strain hardening properties of SHCC and the crack-width controlling ability of hybrid R/SHCC beams is of interest. Additionally, incorporating fine aggregates would likely facilitate the execution of tensile dogbone tests on the larger specimens used in this study, enabling further exploration of the 3D effects of fiber orientation.
- The tensile properties of SHCC seem to decrease after a certain age. The effect of time on the tensile properties of PVA-SHCC have been well documented. However, still few studies have been performed on the effect of time on PE-SHCC. It is, therefore, recommended to study the effect of age on the tensile properties of PE-SHCC.
- The Vaseline-coated, profiled SHCC-CC interface in this study was limited to the region of interest (i.e., the constant bending moment region) due to the complexity of constructing this interface outside this zone, particularly where stirrups are present. It is therefore recommended to investigate methods for constructing a similar interface along the full length of the beam.
- This experimental study emphasized the critical role of achieving sufficient bond strength between reinforcement and SHCC. However, the bond strength was only manipulated by using smooth and rough rebars in combination with PVA-SHCC. It remains uncertain whether an intermediate bond strength (such as by using ribbed, Vaseline-coated rebars to prevent chemical adhesion) could further enhance the crack-width controlling ability of hybrid beams with PVA-SHCC. Additionally, the study revealed that for regions where a more ductile beam response is desired (such as earthquake-prone areas), smooth rebars combined with PE-SHCC are recommended over PVA-SHCC. However, it is still uncertain whether the superior crack-width control observed with PE-SHCC extends to configurations using ribbed rebars. Further investigation is needed to explore this potential.
- The comparison with the hybrid beam tested by Bezemer [3] revealed that curing age has a substantial effect on the crack-width controlling ability of hybrid beams. The reason behind this difference is still not fully understood. Further research on the effect of curing time on the crack-width controlling ability of hybrid beams is needed. It is recommended to monitor the shrinkage behavior of the beams to also understand the contribution of this parameter to the effect of the curing time.

- The study of crack widths outside the constant bending moment region revealed a vulnerability to cracking at the stirrup locations. One possible cause is poor SHCC compaction in these areas. The limited-length vibration table used in this study required the beam to be moved along its length for vibration, which may have led to uneven compaction. For future studies, it is crucial to ensure consistent vibration across the entire beam to avoid compaction issues.



---

# 8. Bibliography

---

- [1] Z. Huang, "flexural behaviour of reinforced concrete beams with a layer of shcc in the tension zone," 2017.
- [2] S. Singh, "Influence of Interface and Type of Strain Hardening Cementitious Composite (SHCC) on Crack Control in SHCC-Concrete Hybrid Beams," 2019.
- [3] H. J. Bezemer, "The Effect of Height Scaling on the Flexural Crack Width Controlling Behavior of Hybrid R/SHCC Beams A Numerical and Experimental Study," 2022. [Online]. Available: <http://repository.tudelft.nl/>.
- [4] M. Lukovic, "Influence of interface and strain hardening cementitious composite (shcc) properties on the performance of concrete repairs," 2016.
- [5] M. Lukovic, D. Hordijk, Z. Huang, and E. Schlangen, "Strain hardening cementitious composite (SHCC) for crack width control in reinforced concrete beams," 2019. [Online]. Available: <http://heronjournal.nl/64-12/10.html>
- [6] N. F. Chamasemani, M. Kelishadi, H. Mostafaei, M. A. D. Najvani, and M. Mashayekhi, "Environmental Impacts of Reinforced Concrete Buildings: Comparing Common and Sustainable Materials: A Case Study," *Construction Materials*, vol. 4, no. 1, pp. 1–15, Dec. 2023, doi: 10.3390/constrmater4010001.
- [7] Eurocode 2: Design of concrete structures. (2004). European Committee of Standardization
- [8] G. Van Zijl and F. Wittmann, "Durability of Strain-Hardening Fibre-Reinforced Cement-Based Composites (SHCC)," 2011. [Online]. Available: [www.springer.com/series/8780](http://www.springer.com/series/8780)
- [9] P. Wang *et al.*, "Research on bonding and shrinkage properties of SHCC-repaired concrete beams," *Materials*, vol. 13, no. 7, Apr. 2020, doi: 10.3390/ma13071757.
- [10] V. Li, "Engineered Cementitious Composites (ECC)-Material, Structural, and Durability Performance," 2011. [Online]. Available: <https://www.researchgate.net/publication/268273534>
- [11] G. P. A. G. van Zijl *et al.*, "A Framework for Durability Design with Strain-Hardening Cement-Based Composites (SHCC) - Influence of Elevated Temperatures," in *Durability of Strain-Hardening Fibre-Reinforced Cement-Based Composites (SHCC)*, Springer Netherlands, 2011, pp. 1–8. doi: 10.1007/978-94-007-0338-4\_1.
- [12] Z. Pan, C. Wu, J. Liu, W. Wang, and J. Liu, "Study on mechanical properties of cost-effective polyvinyl alcohol engineered cementitious composites (PVA-ECC),"

- Construction and Building Materials*, vol. 78, pp. 397–404, Mar. 2015, doi: 10.1016/j.conbuildmat.2014.12.071.
- [13] S. Wang, Y. Wang, M. Gao, and Y. Huang, “Aging Effect of Plasma-Treated Carbon Fiber Surface: From an Engineering Point,” *Coatings*, vol. 14, no. 1, Jan. 2024, doi: 10.3390/coatings14010080.
- [14] I. Curoşu, “Influence of fiber type and matrix composition on the tensile behavior of strain-hardening cement-based composites (shcc) under impact loading,” 2017.
- [15] I. Curosu, V. Mechtcherine, and O. Millon, “Effect of fiber properties and matrix composition on the tensile behavior of strain-hardening cement-based composites (SHCCs) subject to impact loading,” *Cement and Concrete Research*, vol. 82, pp. 23–35, Apr. 2016, doi: 10.1016/j.cemconres.2015.12.008.
- [16] A. V. Georgiou and S. J. Pantazopoulou, “Effect of fiber length and surface characteristics on the mechanical properties of cementitious composites,” *Construction and Building Materials*, vol. 125, pp. 1216–1228, Oct. 2016, doi: 10.1016/j.conbuildmat.2016.09.009.
- [17] A. Bentur and S. Mindess, “Fibre Reinforced Cementitious Composites,” 2007.
- [18] R. K. Tai and Ricky, “The effect of upscaling element size on composite performance,” 2015.
- [19] Arnon. Bentur and Sidney. Mindess, *Fibre reinforced cementitious composites*. CRC Press, 2014.
- [20] V. Mechtcherine, V. Slowik, and P. Kabele, “RILEM Bookseries Strain-Hardening Cement-Based Composites SHCC4,” 2018. [Online]. Available: <http://www.springer.com/series/8781>
- [21] A. G. Van Zijl, “The Role of Aggregate in High Performance, Fibre-Reinforced, Cement-based Composites,” 2005. [Online]. Available: [www.concretesociety.co.za](http://www.concretesociety.co.za)
- [22] V. C. Li, D. K. Mishra, and H.-C. Wu, “Matrix design for pseudo-strain-hardening fibre reinforced cementitious composites,” 1995.
- [23] A. Carlos, I. Masumi, M. Hiroaki, M. Maki, and O. Takahisa, “The effects of limestone aggregate on concrete properties,” *Construction and Building Materials*, vol. 24, no. 12, pp. 2363–2368, 2010, doi: 10.1016/j.conbuildmat.2010.05.008.
- [24] D. Wang, C. Shi, N. Farzadnia, Z. Shi, H. Jia, and Z. Ou, “A review on use of limestone powder in cement-based materials: Mechanism, hydration and microstructures,” Aug. 30, 2018, *Construction and Building Materials*. doi: 10.1016/j.conbuildmat.2018.06.075.
- [25] J. Yu and C. K. Y. Leung, “RILEM Bookseries Calcined Clays for Sustainable Concrete Proceedings of the 3rd International Conference on Calcined Clays for Sustainable Concrete - Using Limestone Calcined Clay to Improve Tensile Performance and

- Greenness of High-Tensile Strength Strain-Hardening Cementitious Composites (SHCC)," 2020. [Online]. Available: <http://www.springer.com/series/8781>
- [26] S. Qian, J. Zhou, M. R. de Rooij, E. Schlangen, G. Ye, and K. van Breugel, "Self-healing behavior of strain hardening cementitious composites incorporating local waste materials," *Cement and Concrete Composites*, vol. 31, no. 9, pp. 613–621, Oct. 2009, doi: 10.1016/j.cemconcomp.2009.03.003.
- [27] L. Wang *et al.*, "On the use of limestone calcined clay cement (LC3) in high-strength strain-hardening cement-based composites (HS-SHCC)," *Cement and Concrete Research*, vol. 144, Jun. 2021, doi: 10.1016/j.cemconres.2021.106421.
- [28] A. Jain and N. P. Y. Pawade, "Characteristics of Silica Fume Concrete," 2015.
- [29] P. Wang *et al.*, "Research on bonding and shrinkage properties of SHCC-repaired concrete beams," *Materials*, vol. 13, no. 7, Apr. 2020, doi: 10.3390/ma13071757.
- [30] V. S. Ramachandran and V. M. Malhotra, *Concrete Admixtures Handbook*, Second. 1996.
- [31] V. K. Singh, "Portland cement additives," in *The Science and Technology of Cement and Other Hydraulic Binders*, Elsevier, 2023, pp. 499–570. doi: 10.1016/b978-0-323-95080-0.00014-5.
- [32] R. Tepfers, "A theory of bond applied to overlapped tensile reinforcement splices for deformed bars," 1973.
- [33] S. W. Lee, S. B. Kang, K. H. Tan, and E. H. Yang, "Experimental and analytical investigation on bond-slip behaviour of deformed bars embedded in engineered cementitious composites," *Construction and Building Materials*, vol. 127, pp. 494–503, Nov. 2016, doi: 10.1016/j.conbuildmat.2016.10.036.
- [34] Y. Chen, J. Yu, H. Younas, and C. K. Leung, "Experimental and numerical investigation on bond between steel rebar and high-strength Strain-Hardening Cementitious Composite (SHCC) under direct tension," *Cement and Concrete Composites*, vol. 112, Sep. 2020, doi: 10.1016/j.cemconcomp.2020.103666.
- [35] J. Cai, J. Pan, J. Tan, and X. Li, "Bond behaviours of deformed steel rebars in engineered cementitious composites (ECC) and concrete," *Construction and Building Materials*, vol. 252, Aug. 2020, doi: 10.1016/j.conbuildmat.2020.119082.
- [36] M. Deng, J. Pan, and H. Sun, "Bond behavior of steel bar embedded in Engineered Cementitious Composites under pullout load," *Construction and Building Materials*, vol. 168, pp. 705–714, Apr. 2018, doi: 10.1016/j.conbuildmat.2018.02.165.
- [37] P. Gao, G. Ye, J. X. Wei, Q. J. Yu, "Prediction of the chemical shrinkage of Portland cement." , 4th International Rilem Conference on Microstructure Related Durability of Cementitious Composites: Microdurability, 2020.

- [38] J. Zhang, C. Gong, Z. Guo, and M. Zhang, "Engineered cementitious composite with characteristic of low drying shrinkage," *Cement and Concrete Research*, vol. 39, no. 4, pp. 303–312, Apr. 2009, doi: 10.1016/j.cemconres.2008.11.012.
- [39] K. H. Yang, E. A. Seo, and S. H. Tae, "Carbonation and CO<sub>2</sub> uptake of concrete," *Environmental Impact Assessment Review*, vol. 46, pp. 43–52, 2014, doi: 10.1016/j.eiar.2014.01.004.
- [40] P. Van den Heede, A. Mignon, G. Habert, and N. De Belie, "Cradle-to-gate life cycle assessment of self-healing engineered cementitious composite with in-house developed (semi-)synthetic superabsorbent polymers," *Cement and Concrete Composites*, vol. 94, pp. 166–180, Nov. 2018, doi: 10.1016/j.cemconcomp.2018.08.017.
- [41] V. C. Li, "Engineered Cementitious Composites (ECC) Bendable Concrete for Sustainable and Resilient Infrastructure."
- [42] M. Luković, B. Budnik, J. Dragaš, V. Carević, and I. Ignjatović, "Contribution of strain-hardening cementitious composites (SHCC) to shear resistance in hybrid reinforced concrete beams," *Building Materials and Structures*, vol. 66, no. 3, pp. 145–155, 2023, doi: 10.5937/grmk2300006l.
- [43] M. D. Lepech and V. Li, "Long Term Durability Performance of Engineered Cementitious Composites," 2011. [Online]. Available: <https://www.researchgate.net/publication/267819443>
- [44] W.L. Xu, "The development of ultra-high ductility cementitious composites and the establishment of an analytic model based on micro-mechanics," Tongji University, Shanghai, 2016.
- [45] Q. Wang, Y. Zhou, M. Lai, M. Gu, and J. C. M. Ho, "Carbon fiber to improve the resistance of high strength PVA-ECC to elevated temperatures," *Journal of Building Engineering*, vol. 71, Jul. 2023, doi: 10.1016/j.jobbe.2023.106475.
- [46] K. Yu, L. Li, J. Yu, Y. Wang, J. Ye, and Q. F. Xu, "Direct tensile properties of engineered cementitious composites: A review," Mar. 20, 2018, *Construction and Building Materials Ltd*. doi: 10.1016/j.conbuildmat.2017.12.124.
- [47] M. Chen, Y. Wang, T. Zhang, and M. Zhang, "Behaviour of structural engineered cementitious composites under dynamic tensile loading and elevated temperatures," *Engineering Structures*, vol. 280, Apr. 2023, doi: 10.1016/j.engstruct.2023.115739.
- [48] J. Luo, Z. Cai, K. Yu, W. Zhu, and Z. Lu, "Temperature impact on the micro-structures and mechanical properties of high-strength engineered cementitious composites," *Construction and Building Materials*, vol. 226, pp. 686–698, Nov. 2019, doi: 10.1016/j.conbuildmat.2019.07.322.
- [49] A. E. H. Khalil, E. Etman, A. Atta, and M. Essam, "Behavior of RC beams strengthened with strain hardening cementitious composites (SHCC) subjected to monotonic and

- repeated loads,” *Engineering Structures*, vol. 140, pp. 151–163, Jun. 2017, doi: 10.1016/j.engstruct.2017.02.049.
- [50] CEN, “EN 1992-1-1: Eurocode 2: Design of concrete structures - Part 1-1: General rules and rules for buildings,” 2004.
- [51] N. Jayananda, “Flexural behaviour of reinforced concrete beams with a layer of shcc in the tension zone,” 2017.
- [52] S. Mustafa, S. Singh, D. Hordijk, E. Schlangen, and M. Luković, “Experimental and numerical investigation on the role of interface for crack-width control of hybrid SHCC concrete beams,” *Engineering Structures*, vol. 251, Jan. 2022, doi: 10.1016/j.engstruct.2021.113378.
- [53] S. He, S. Mustafa, Z. Chang, M. Liang, E. Schlangen, and M. Luković, “Ultra-thin Strain Hardening Cementitious Composite (SHCC) layer in reinforced concrete cover zone for crack width control,” *Engineering Structures*, vol. 292, Oct. 2023, doi: 10.1016/j.engstruct.2023.116584.
- [54] M. J. Bandelt and S. L. Billington, “Simulation of Deformation Capacity in Reinforced High-Performance Fiber-Reinforced Cementitious Composite Flexural Members,” *Journal of Structural Engineering*, vol. 144, no. 10, Oct. 2018, doi: 10.1061/(asce)st.1943-541x.0002174.
- [55] S. M. Nuri, “Strain-Hardening Cementitious Composite as Lost Formwork for Reinforced Concrete Beams.”
- [56] M.-H. Shih and W.-P. Sung, “Application of digital image correlation method for analysing crack variation of reinforced concrete beams,” Indian Academy of Sciences, 2013.
- [57] CEN, *Testing hardened concrete. Part 3, Compressive strength of test specimens*. BSI, 2002.
- [58] R. I. Gilbert, “Shrinkage, Cracking and Deflection-the Serviceability of Concrete Structures,” *Electronic Journal of Structural Engineering*, 2001.
- [59] M. Deng, J. Pan, and H. Sun, “Bond behavior of deformed bar embedded in Engineered Cementitious Composites under cyclic loading,” *Construction and Building Materials*, vol. 197, pp. 164–174, Feb. 2019, doi: 10.1016/j.conbuildmat.2018.11.200.
- [60] Japan Society of Civil Engineers, “Recommendations for Design and Construction of High Performance Fiber Reinforced Cement Composites with Multiple Fine Cracks (HPFRCC),” 2008.
- [61] S. M. Allam, M. S. Shoukry, G. E. Rashad, and A. S. Hassan, “Evaluation of tension stiffening effect on the crack width calculation of flexural RC members,” *Alexandria Engineering Journal*, vol. 52, no. 2, pp. 163–173, 2013, doi: 10.1016/j.aej.2012.12.005.



# A. Top view profiled interface

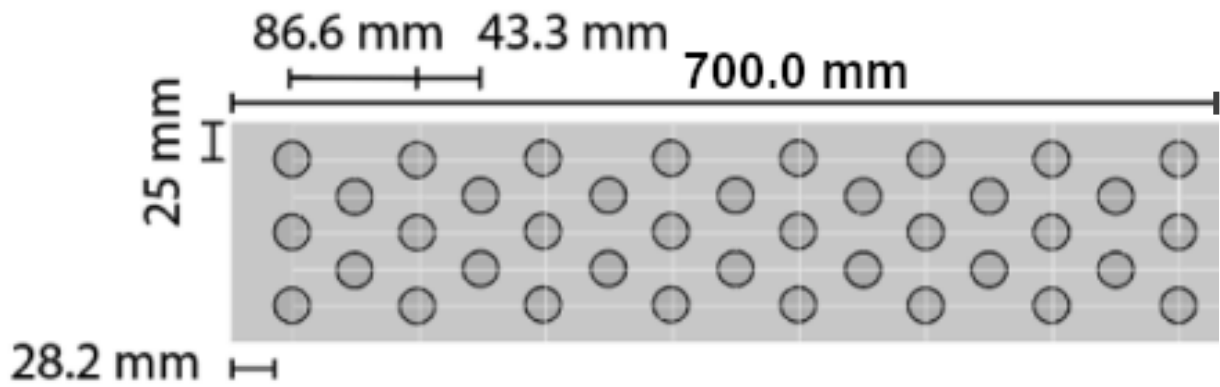


Fig. A. 1: Top view of profiled interface



Fig. A. 2: Silicon mold used to construct profiled interface

# B. Design checks

## B.1. Concrete cover

To ensure full load transfer between steel and concrete, sufficient concrete cover is needed. According to Eurocode 2 [50] the minimum required concrete cover is:

$$c_{min} = c_{nom} + \Delta dev = 10 + 5 = 15 \text{ mm}$$

The following covers are present in the design of the beams:

$$c_{bottom,cbma} = 35 - \frac{\phi_{long}}{2} = 35 - \frac{8}{2} = 31 \text{ mm}$$

$$c_{bottom,ss} = 35 - \phi_{long} - \frac{\phi_{shear}}{2} = 35 - 8 - \frac{8}{2} = 23 \text{ mm}$$

$$c_{side,cbma} = 39 - \frac{\phi_{long}}{2} = 39 - \frac{8}{2} = 35 \text{ mm}$$

$$c_{side,ss} = 39 - 2 * \phi_{long} - \frac{\phi_{shear}}{2} = 39 - 2 * 8 - \frac{8}{2} = 19 \text{ mm}$$

Since none of the designed covers subceeds the minimum required cover, full load transfer between steel and concrete can be ensured.

## B.2. Flexural capacity

To prevent failure of the steel prior to cracking of the concrete, sufficient longitudinal reinforcement needs to be applied. Eurocode 2 [50] prescribes a minimum amount of longitudinal reinforcement to prevent this brittle failure as follows:

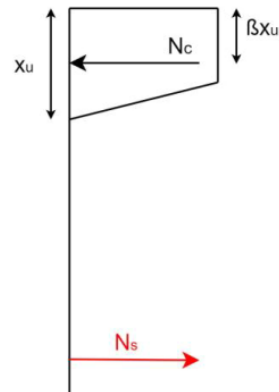
$$\begin{aligned} A_{s,min} &= \max\left(\frac{0,26f_{ctm}}{f_{yk}}bd ; 0,0013bd\right) \\ &= \max\left(\frac{0,26 * 3}{500} * 150 * (400 - 35) ; 0,0013 * 150 * (400 - 35)\right) \\ &= 112,74 \text{ mm}^2 \end{aligned}$$

Additionally, the steel should yield before the compressive zone fails, which limits the amount of reinforcement that can be applied. The maximum allowable reinforcement can be determined by solving the horizontal equilibrium of the tensile steel force and compressive concrete force:

$$N_s = A_{s,max}f_{yd}$$

$$N_c = 0,75bx_{u,max}f_{cd}$$

$$N_s = N_c$$



$$\rightarrow A_{s,max} = \frac{0,75bx_{u,max}f_{cd}}{f_{yd}} = \frac{0,75 * b * 0,456 * d * f_{cd}}{f_{yd}}$$

$$A_{s,max} = \frac{0,75 * 150 * 0,456 * (400 - 35) * \frac{30}{1,5}}{\frac{500}{1,15}} = 651,29 \text{ mm}^2$$

All beams are reinforced with 3 longitudinal rebars with a diameter of 8mm, this results in the following applied longitudinal reinforcement:

$$A_{s,applied} = 3 * \frac{1}{4} \pi \phi_{long}^2 = 3 * \frac{1}{4} * \pi * 8^2 = 150,80 \text{ mm}^2$$

Since it holds that  $A_{s,min} \leq A_{s,applied} \leq A_{s,max}$ , the applied reinforcement is sufficient.

### B.3. Shear capacity

The inclusion of stirrups is essential in the design due to the presence of shear forces beyond the region of constant bending moment. To adequately design the shear reinforcements, the maximum shear force must be determined initially. This determination assumes a uniform tensile capacity for the SHCC-layer when the ultimate moment capacity is reached.

$$x_u = \frac{A_{s,applied}f_{yk} + f_{ctm,SHCC}b_{SHCC}h_{SHCC}}{0,75bf_{ck}}$$

$$= \frac{150,80 * 500 + 3 * 150 * 70}{0,75 * 150 * 30} = 31,67 \text{ mm}$$

$$M_{ult} = 0,75bx_u f_{ck} * (d - \beta x_u)$$

$$= 0,75 * 150 * 31,67 * 30 * (400 - 35 - 0,389 * 31,67) = 37.696.682 \text{ Nmm}$$

$$V_{Ed} = \frac{M_{ult}}{a_{shear\_span}} = \frac{37.696.682}{913} = 41.289 \text{ N}$$

$$v_{Ed} = \frac{V_{Ed}}{bd} = \frac{41.289}{150 * (400 - 35)} = 0,75 \text{ N/mm}^2$$

$$k = \min\left(\sqrt{\frac{200}{d}}; 2\right) = 1,74$$

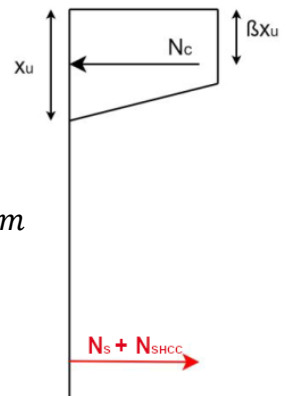
$$v_{rdc} = 0,18k(100p_l f_{ck})^{\frac{1}{3}} = 0,18 * 1,74 * \left(100 * \frac{150,80}{150 * (400 - 35)} * 30\right)^{\frac{1}{3}} = 0,63 \text{ N/mm}^2$$

$v_{rdc} \leq v_{Ed}$ , thus stirrups are needed and will be calculated following:

$$\frac{A_{sw}}{s} = \frac{V_{Ed}}{f_{ywd}z \cot \theta}$$

With  $s = 175 \text{ mm}$  &  $\theta = 45^\circ$ , the required  $A_{sw}$  becomes:

$$A_{sw,required} = \frac{V_{Ed}s}{f_{ywd}z \cot \theta} = \frac{41.289 * 175}{500 * (400 - 35 - 0,389 * 31,67 * \cot(45))} = 40,43 \text{ mm}^2$$



The applied  $A_{sw,applied} = 10 * \frac{1}{4} * \pi * \phi_{sw}^2 = 10 * \frac{1}{4} * \pi * 8^2 = 502,65 \text{ mm}^2$  and is ample.

Maximum distance from support =  $z * \cot(\theta) = 217,73 \text{ mm} \geq 213 \text{ mm}$

# C. Comparison GOM data and LVDT data

## C.1 Beam PVA-RR-SI

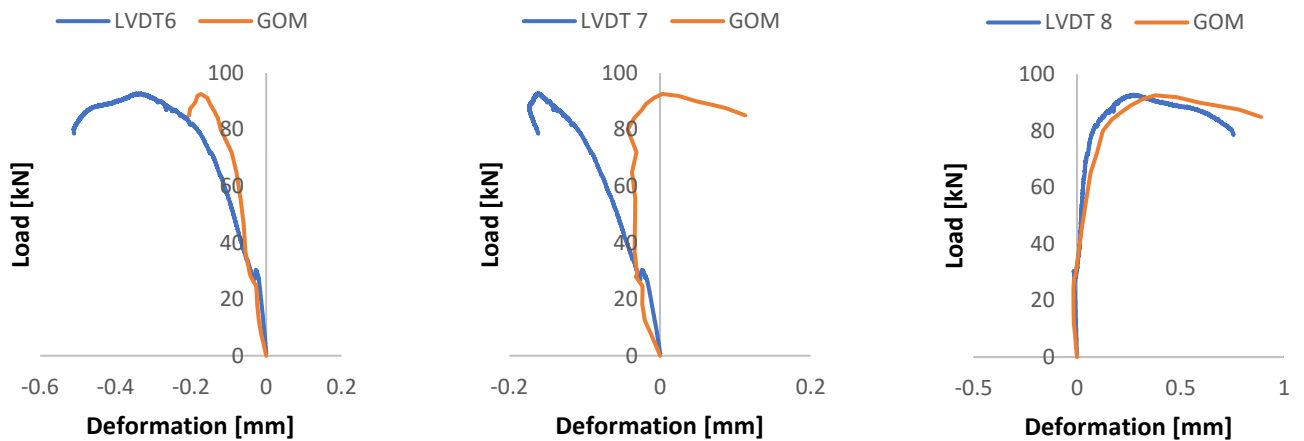


Fig. C. 1: Comparison of DIC data with LVDT6, LVDT7 and LVDT8 of beam PVA-RR-SI

## C.2 Beam PVA-RR-VPI

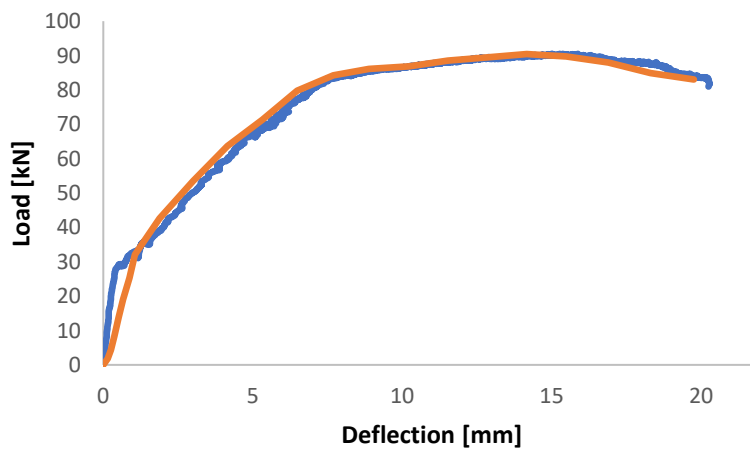


Fig. C. 2: Comparison DIC data with laser of beam PVA-RR-VPI

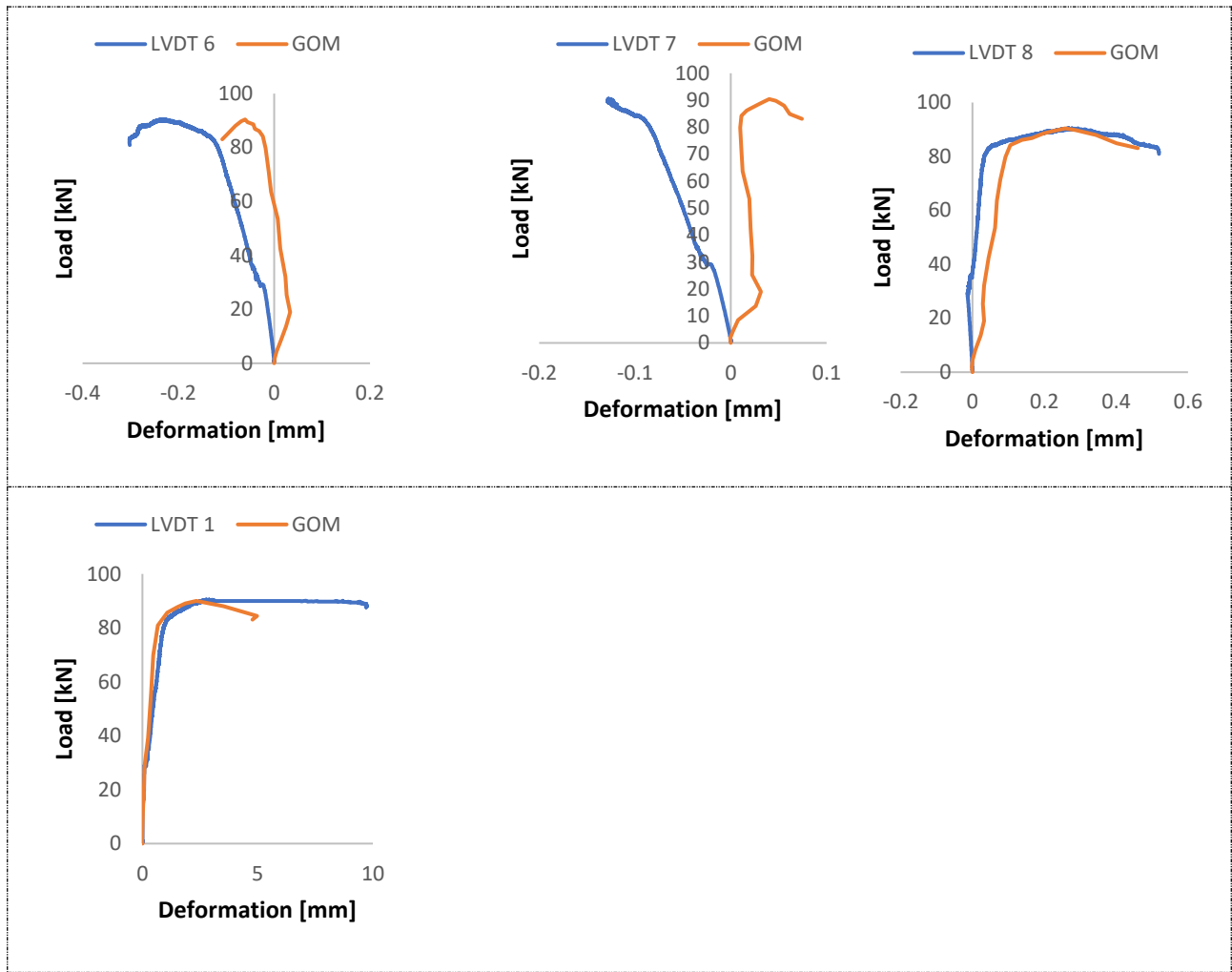


Fig. C. 3: Comparison of DIC data with LVDT1, LVDT6, LVDT7 and LVDT8 of beam PVA-RR-VPI

### C.3 Beam PVA-SR-VPI

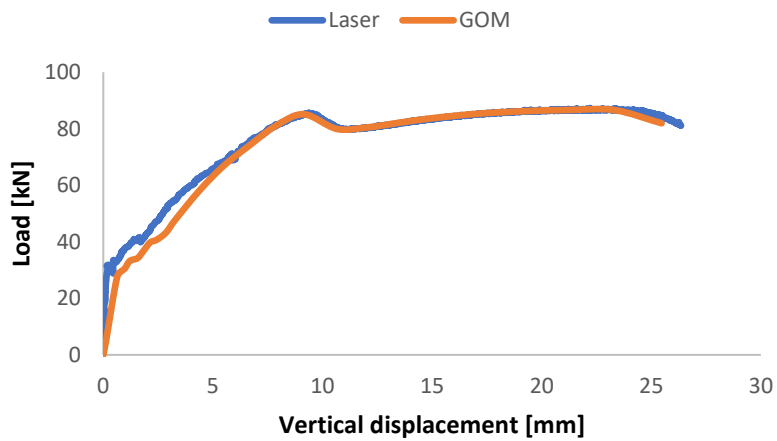


Fig. C. 4: Comparison of DIC data with laser of beam PVA-SR-VPI

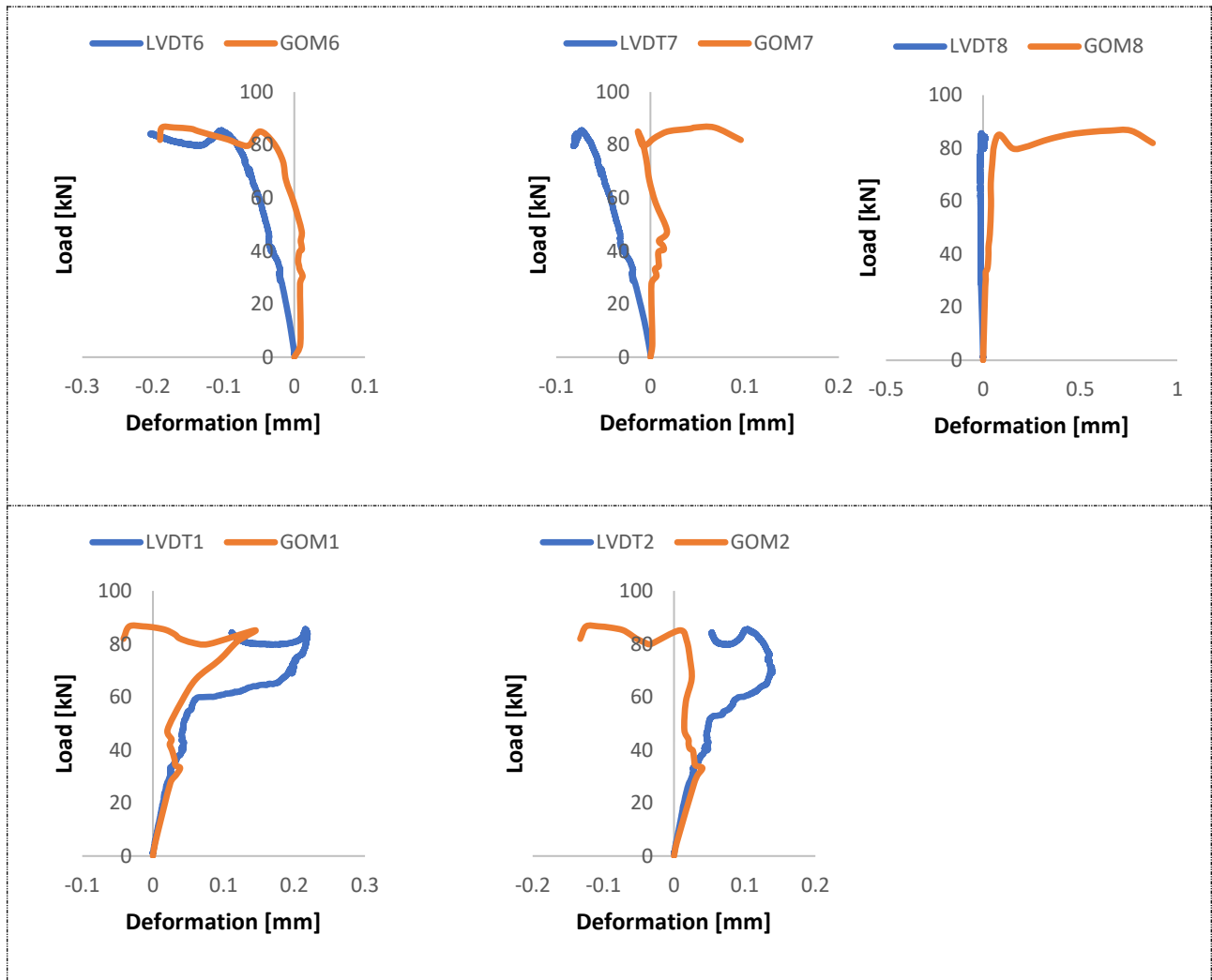


Fig. C. 5: Comparison of DIC data with LVDT1, LVDT2, LVDT6, LVDT7 and LVDT8

### C.4 Beam PE-SR-VPI

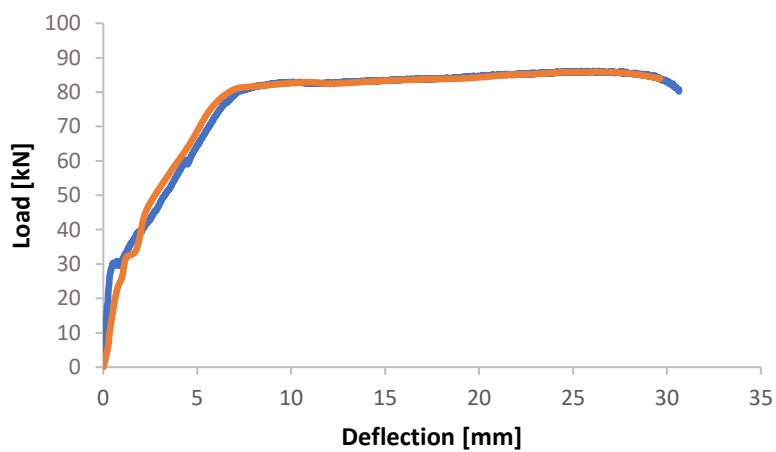


Fig. C. 6: Comparison of DIC data with laser of beam PE-SR-VPI

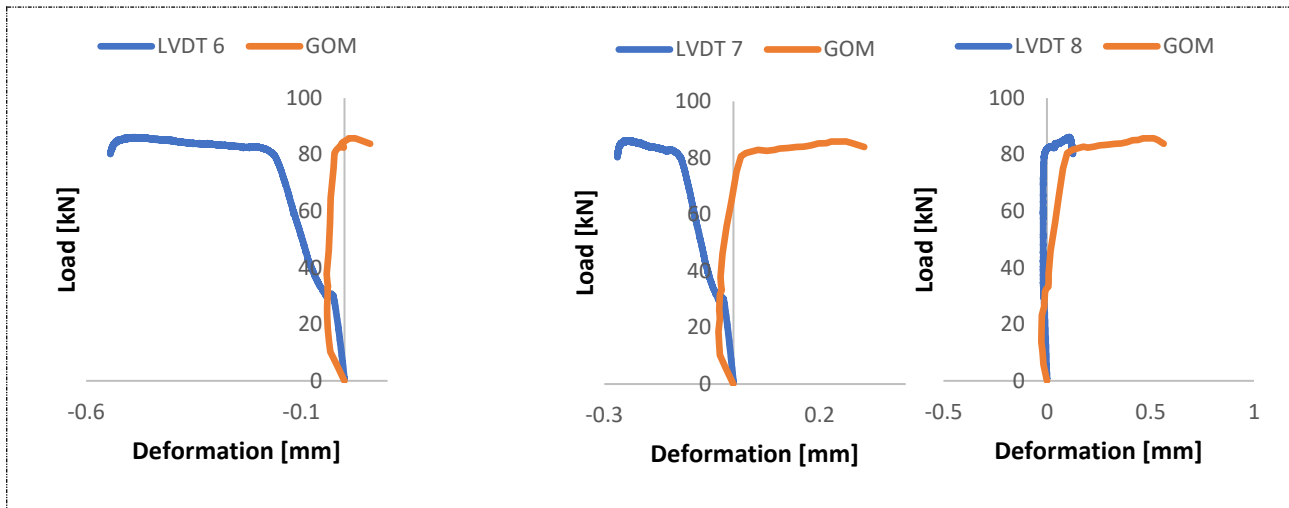


Fig. C. 7: Comparison of DIC data with LVDT6, LVDT7 and LVDT8 of beam PE-SR-VPI

